High Resolution Secondary Ion Mass Spectrometry Analysis of Boron in High Strength Steels and Polycrystalline Superalloys

Hanis Ayuni Mohd Yusof

St. Cross College



A thesis submitted for the degree of Doctor of Philosophy in the University of Oxford

Hilary Term 2020

ABSTRACT

High Resolution Secondary Ion Mass Spectrometry Analysis of Boron in High Strength Steels and Polycrystalline Superalloys

Hanis Ayuni Mohd Yusof
St. Cross College

A thesis submitted for the degree of Doctor of Philosophy in the University of Oxford
Hilary Term 2020

Boron is added to high strength steels to increase hardenability and as grain strengthener in polycrystalline superalloys, but is difficult to study by many conventional techniques. The main aim of this study was to explore the application of high resolution secondary ion mass spectrometry (NanoSIMS) to analyse boron distributions in a range of high strength steels after different commercial heat treatments. New findings on the behaviour of boron at four stages of the manufacturing process (as-rolled, as-quenched, quenched and tempered and direct quenched) are demonstrated, and particularly information on how Ti plays an important role in maximising the beneficial effect of boron on hardenability. Boron was found to segregate at prior austenite grain boundaries during isothermal heat treatments by equilibrium segregation, and also during cooling by non-equilibrium segregation. In hot rolled samples, boron particles started to precipitate out during the hot rolling process, and during subsequent air cooling boron also segregated to prior austenite grain boundaries. Strong grain boundary segregation was observed in the as-quenched samples, with small precipitates near the grain boundaries as well as in the grain interiors. Finally, in quenched and tempered samples, small boron-containing precipitates were created during the tempering stage that were not visible in other samples. A longer heating time in the austenite region also gives higher boron segregation at grain boundaries. As a result, the direct quenching method can be an alternative process to reduce costs and increase overall efficiency in steel manufacturing as it shows a similar boron distribution to that developed by the conventional thermomechanical process. As well as these qualitative observations, quantitative analysis of boron segregation to a large number of grain

boundaries has been demonstrated using the NanoSIMS, because it can map large areas in a short time. This is the only extensive quantification of grain boundary segregation performed with a NanoSIMS instrument to date with 100s of grain boundaries analysed. Quantification of boron-containing precipitate densities and size has also been reported. In another set of experiments on samples of a new polycrystalline Ni superalloy, the primary effect of boron addition has been shown to be the suppression of Cr-rich $M_{23}C_6$ carbides and the formation of Cr-rich M_5B_3 borides. NanoSIMS analysis of these superalloys was shown to provide complementary information to SEM, APT and TEM studies carried out by other researchers on the same alloys. The data presented in this thesis shows that NanoSIMS can be added to and can complement conventional techniques to guide the development of materials for industrial applications and understand the affect that heat treatments have on microstructure and materials properties.

PREFACE

This thesis is submitted for the degree of Doctor of Philosophy at the University of Oxford. The work was carried out in the Department of Materials under the supervision of Prof. Chris R. M. Grovenor and Dr. Katie L. Moore. No part of this thesis has been previously submitted for a degree at this or any other university. The work of other authors has been duly acknowledged in the text. A list of cited references is given at the end of each chapter.

Some of the work described in this thesis has been presented in the following publications and conferences:

Paraskevas Kontis, **Hanis A. Mohd Yusof,** Stella Pedrazzini, Katie L. Moore, Paul A.J. Bagot, Michael P. Moody, Chris R. M. Grovenor and Roger C. Reed, On The Effect Of Boron On Grain Boundary Character In A New Polycrystalline Superalloy, Acta Materialia, Vol. 103 (2016) pp. 688-699

Paraskevas Kontis, **Hanis A. Mohd Yusof,** Katie L. Moore, Chris R. M. Grovenor and Roger C. Reed, On The Effect Of Boron On The Mechanical Properties Of A New Polycrystalline Superalloy, MATEC Web of Conferences, Vol. 14 (2014) pp. 17003

Hanis Ayuni Mohd Yusof, Katie Moore and Chris Grovenor. (2015) High-Resolution Imaging And Quantification Of Boron Segregation To Austenite Grain Boundaries In High-Strength Steels Using Combined Nanosims/EBSD Analysis. 144th Annual Meeting & Exhibition of The Minerals, Metals & Materials Society (TMS 2015) at Orlando, Florida, USA.

Hanis Ayuni Mohd Yusof, Katie Moore and Chris Grovenor. (2014) Combined Nanosims/EBSD Analysis Of Boron Segregation In High Strength Steels. 4th International NanoSIMS Workshop. 13-14 October 2014. Paris, France.

Hanis Ayuni Mohd Yusof, Katie Moore and Chris Grovenor. (2014) Characterisation Of Grain Boundary Segregation In Metals Using High-Resolution Imaging By Nanosims. 9th International Materials Technology Conference and Exhibition (IMTCE 2014). 13-16 May 2014. Kuala Lumpur, Malaysia.

Paraskevas Kontis, **Hanis A. Mohd Yusof,** Katie L. Moore, Chris R. M. Grovenor and Roger C. Reed. (2014) On The Effect Of Boron On The Mechanical Properties Of A New Polycrystalline Superalloy. 2nd European Symposium on Superalloys and their Applications (EUROSUPERALLOYS 2014). 12-16 May 2014. French Riviera, France.

Hanis Ayuni Mohd Yusof, Katie Moore, and Chris Grovenor. (2013) Nanosims Analysis Of Boron Segregation To Austenite Grain Boundaries In High Strength Steels. 8th International Conference on Processing & Manufacturing of Advanced Materials (THERMEC 2013). 2-6 December 2013. Las Vegas, USA.

This thesis is approximately 40,000 words.

ACKNOWLEDGEMENTS

In the name of Allah, the Most Gracious and the Most Merciful.

All praises to Allah for His greatness and giving me His blessing for the completion of this thesis. I thank Allah for all the opportunities, trials and strength that have been showered on me during my DPhil study. I am truly blessed and beyond grateful for the gift of wonderful people I have met along this journey. Some of them inspire me, stretch me, challenge me, love me and encourage me.

I would like to express my sincere gratitude to my supervisors, Prof. Chris R. M. Grovenor and Dr. Katie L. Moore for their endless support, excellent supervision and advice throughout the course. Most importantly, they have provided positive encouragement and a warm spirit to finish this thesis. It has been a great pleasure and honour to have them as my supervisors.

I am immensely grateful to Dr. Matthew Green of Tata Steel for providing the steel samples and fruitful discussion of the project. I would also like to thank Dr. Paraskaves Kontis and Prof. Roger Reed for sharing the superalloy samples and meaningful discussion.

I am very grateful for the technical support from Oxford Materials, Laurie Walton in the workshop, Greg Cook, Steve Lett, Chris Salter, Dr. Sverre Myra and not to forget the late Gabriella Chapman for SEM and EBSD training.

I am most appreciative to Dr. Kexue Li for the help in acquiring the second set of NanoSIMS data on steel sample 12AM24.

I am grateful to have known all the members of CRMG Group, particularly Haibo Jiang, Tayebeh Mousavi, Greg Brittles and Canan for being awesome officemates. A special thank you goes to my lovely best friend Juliana M. Januruddin for always checking on me and being a great listener. You simply make everything brighter. May our friendship last forever.

I would like to thank the Malaysian Government and University Malaysia Pahang for the SLAB/SLAI scholarship that they awarded in which has allowed me to undertake this research at Oxford.

My deepest gratitude goes to all my family members for their unconditional love and support.

I am eternally grateful to my parents, Abah and Umi who their love and prayers has kept me going when the journey got tough, and without them I'm pretty sure this thesis would not have happened.

Thank you to Aizat my loving husband, for all you have sacrificed so I could live out my dream. It will always be remembered. To my dear children, Hannah and Ashraf, you have made me stronger, better and more fulfilled than I could ever imagined. I love you to the moon and back.

TABLE OF CONTENTS

ABSTRACT ..... **I**

PREFACE ..... **III**

ACKNOWLEDGEMENTS ..... **IV**

TABLE OF CONTENTS ..... **V**

1 INTRODUCTION **1**

1.1 BACKGROUND 1

1.2 AIM OF THE RESEARCH 2

1.2.1 High Strength Steels *2*

1.2.2 Polycrystalline Ni-based Superalloys *3*

1.3 STRUCTURE OF THESIS 3

1.4 REFERENCES 4

2 LITERATURE REVIEW **6**

2.1 INTRODUCTION 6

2.1.1 Techniques for Localising Grain Boundary Segregation *7*

2.2 SECONDARY ION MASS SPECTROMETRY (SIMS) 10

2.2.1 Introduction to SIMS *10*

2.2.2 The Sputtering Process *11*

2.2.3 Instrumentation *11*

2.2.4 Types of SIMS Instruments *18*

2.2.5 Technical Details *19*

2.2.6 The CAMECA NanoSIMS 50 ..... *28*

2.3 BORON HARDENABILITY EFFECT 31

2.3.1 Grain Boundary Segregation *32*

2.3.2 Quantification of Grain Boundary Segregation *38*

2.3.3 Boron Grain Boundary Segregation Studies using SIMS or NanoSIMS *41*

2.4 SUMMARY AND CONCLUSIONS 45
2.5 REFERENCES 46
3 EXPERIMENTAL TECHNIQUES 56
3.1 INTRODUCTION 56
3.2 SAMPLE PREPARATION 56
3.3 STANDARDS FOR NANOSIMS ANALYSIS 58
3.4 LIGHT MICROSCOPY 59
3.5 SCANNING ELECTRON MICROSCOPY (SEM) 61
3.6 ELECTRON BACKSCATTER DIFFRACTION (EBSD) 63
3.7 NANOSIMS ANALYSIS 65
3.7.1 NanoSIMS Primary Ion Sources 66
3.7.2 Tuning the Instrument 68
3.7.3 Resolving Mass Overlaps 73
3.7.4 Lateral Resolution 75
3.7.5 Data Analysis and Presentation 75
3.7.6 Quantification 76
3.8 CORRELATION AFTER NANOSIMS ANALYSIS 77
3.9 REFERENCES 80
4 BORON SEGREGATION IN STEEL 82
4.1 INTRODUCTION 82
4.2 MATERIALS AND METHODS 83
4.2.1 Full Manufacturing Sequence 84
4.2.2 Materials Composition 85
4.3 MICROSTRUCTURE 87
4.3.1 As-rolled Samples 90
4.3.2 As-quenched Samples 91
4.3.3 Quenched and Tempered Samples 95
4.4 BORON DISTRIBUTION IN STEELS 96
4.4.1 Reference Sample 12AN15 – Al protected, as-quenched 96

4.4.2 Comparison of Al Protected Steels with Different Heat Treatments (12AM22, 12AM22AA, 12AM22F, 12AM22G and 12AM24) *103*

4.4.3 Comparison of Ti Protected Steels with Different Heat Treatments (12AM23, 12AM23AA and 12AM25) *133*

4.4.4 Comparison of As-quenched (12AM16) and Direct Quenched (12AM15D) Samples *149*

4.4.5 Comparison of Samples 13ZZ6ZBM, 13ZZ9ZBM and 13ZZ12ZBM *152*

4.4.6 Discussion and Summary of Boron Distributions *155*

4.5 QUANTITATIVE ANALYSIS OF BORON IN STEELS 162

4.5.1 Ion-implanted Standard Samples *162*

4.5.2 Quantitative Analysis of Total Boron Counts *166*

4.5.3 Quantification of Grain Boundary Concentration *170*

4.5.4 Quantification of Particle Sizes and Size Distributions *182*

4.5.5 Discussion and Summary of Quantitative Analysis *188*

4.6 CONCLUSIONS 192

4.7 REFERENCES 195

5 GRAIN BOUNDARY ANALYSIS IN A NEW POLYCRYSTALLINE SUPERALLOY 197

5.1 INTRODUCTION 197

5.1.1 Applications of Nickel-based Superalloys *197*

5.1.2 Metallurgy of Nickel-based Superalloys *198*

5.1.3 Carbon and Boron as Grain Boundary Strengtheners *199*

5.2 MATERIALS AND METHODS 201

5.2.1 Materials Composition *201*

5.2.2 Heat Treatment *201*

5.2.3 Sample Preparation for NanoSIMS Analysis *202*

5.3 RESULTS AND DISCUSSION 203

5.3.1 Microstructure *203*

5.3.2 NanoSIMS Analysis *205*

5.4 DISCUSSION AND SUMMARY 219

5.5 CONCLUSIONS 220

5.6 REFERENCES 221

6 CONCLUSIONS AND SUGGESTIONS FOR FUTURE WORK 225

6.1 CONCLUSIONS 225

6.1.1 High Strength Steels 225

6.1.2 Polycrystalline Ni-based Superalloys 228

6.2 FUTURE WORK 229

6.3 REFERENCES 230

1 Introduction

1.1 Background

The addition of minute amounts of boron to steels has a positive effect on the hardenability, and can also act as a grain boundary strengthener in Ni-based superalloys, hence improving the properties of both materials. The effect of boron on the hardenability of steels has been extensively studied by many researchers (He et al., 1989, Hara et al., 2004, Grange and Mitchell, 1961, Ueno and Itoh, 1988, Li et al., 2015a, Li et al., 2015b, Da Rosa et al., 2020), is explained by boron segregation to austenite grain boundaries delaying the transformation of austenite to ferrite or bainite during cooling. During heat treatment, boron diffuses to the austenite grain boundaries, where it reduces the grain boundary energy. This means that the grain boundary nucleation mechanism is ineffective and retards the formation of bainite or ferrite (Simcoe et al., 1955).

The segregation of boron can be controlled either by equilibrium segregation or non-equilibrium segregation. Equilibrium segregation involves boron redistribution driven by thermodynamics to minimize the total Gibbs free energy of the system (McLean, 1957, Aust, 1974). Non-equilibrium segregation describes the enrichment of grain boundaries by diffusion of boron atom-vacancy complexes to the vacancy sinks (i.e. grain boundaries) during cooling (Karlsson et al., 1988).

In order to maximise this beneficial effect, it is essential to prevent boron precipitating into nitrides or carbides because its positive effect on hardenability requires it to be in solid solution. The addition of titanium to steels as a nitride former gives boron protection from reaction with nitrogen by leading to the formation of more stable TiN (Sharma et al., 2019).

To understand the mechanisms involved in how heat treatments can alter the effect of boron on hardenability, it is necessary to develop techniques to localise boron in steel samples to determine if it is present in precipitates or segregated at grain boundaries. The difficulty in detecting boron, especially small amounts of boron (Cameron, 1979) and a strong tendency for the formation of boron

carbides and boron nitrides makes it difficult to use conventional analysis techniques to clearly identify the mechanisms responsible for the beneficial boron effect.

Auger electron spectroscopy (AES) has proved invaluable in determining the species segregated to embrittled boundaries (Hondros and Seah, 1972, Larere et al., 1982), while microanalysis within a transmission electron microscope (Williams and Edington, 1976, Wittry, 1979) and atom probe tomography (Waugh and Southon, 1979, Miller et al., 1978) have helped in the overall understanding of segregation processes. A review of possible techniques for the analysis of grain boundary segregation is given in (Lejček, 2010). This work aims to show how NanoSIMS can be added to this list of state-of-the-art techniques.

The concept of applying the NanoSIMS to the analysis of boron in steels is based on the fact that it is one of the most sensitive elemental and isotopic surface analysis techniques. The lateral resolution can be as good as 50 nm (Stadermann et al., 1999, Horreard, 2000), and the very high sensitivity to trace elements is due to the very high transmission of the secondary ion optics (Slodzian et al., 1992).

1.2 Aim of the Research

1.2.1 High Strength Steels

The main aim of this study was to explore the application of high-resolution secondary ion mass spectrometry (NanoSIMS) to analyse boron distributions in a range of high strength steels after different commercial heat treatments. This thesis was designed to provide new insights, and further understanding of scientific questions, including:

1. Comparison between Al-protected steels and Ti-protected steels at three processing stages (as-rolled, as-quenched and quenched and tempered). What is the role of Al and Ti in the steels? How does boron behave at the early stage of processing (as-rolled), after water quenching from the austenite region (as-quenched), and after the tempering process (quenched and tempered)?

Does it exist in solid solution or segregate at the grain boundary or precipitate as a second phase? How do the heat treatments alter the effect of boron on hardenability in these steels?

2. Comparison of two Al-protected steel samples at different reheating times in the austenite region. Does reheating time at the austenite region have an impact on the behaviour of boron in the steels?
3. Comparison of direct quenched steel and the conventional as-quenched steel. Do the processing conditions play a significant role in controlling the location of boron in these steels?
4. Comparison between Mo alloyed steel and two other Al-protected steels with different Al concentrations. What is the effect of Mo on boron distribution in the steel?
5. How can NanoSIMS data be used for quantitative analysis of boron in steels?

1.2.2 Polycrystalline Ni-based Superalloys

The purpose of this research was to extend our knowledge using the capability of the NanoSIMS to show the distribution of grain boundary elements (boron and carbon) in a new polycrystalline Ni-based superalloy, and to compare this data with SEM, APT and TEM analysis of the same alloys. Hence, this experiment was to provide information on the role of boron and carbon in controlling grain boundary character in this class of Ni-based superalloys.

1.3 Structure of Thesis

Chapter 2 begins with an overview of elements that can have a strong effect on mechanical properties by segregation at grain boundaries, and how boron is an important element in certain materials. A review of the literature and detailed description of secondary ion mass spectrometry including its technical details, in depth explanation of the CAMECA NanoSIMS 50, and the mechanism of grain boundary segregation are given here.

Chapter 3 describes the sample preparation and instruments used to carry out the work reported in this thesis. As the main technique used was the NanoSIMS, the details of how to perform the instrumental alignment are described.

Chapter 4 presents the main work of this thesis on high strength boron treated steels. The main aim of this study was to explore the application of high-resolution secondary ion mass spectrometry (NanoSIMS) to analyse boron distributions in a range of high strength steels after different commercial heat treatments. 15 different steels samples were provided by Dr Matthew Green of Tata Steel, and formed part of the set of materials studied in the EU OPTIBOS project entitled 'New developments and optimisation of high strength boron treated steels through the application of advanced boron monitoring techniques' with partners in Germany, Belgium and Spain.

Chapter 5 will demonstrate the capability of the NanoSIMS to provide detailed information on the distribution and behaviour of boron in a new polycrystalline superalloy. It will be shown that the NanoSIMS provides information on the boron distribution complementary to parallel SEM, APT and TEM analysis of the same alloys. This project was a collaboration with Dr. Paraskevas Kontis and his supervisor Professor Roger Reed.

Finally, Chapter 6 will give overall conclusions of the most significant findings, along with suggestions for future work.

1.4 References

AUST, K. T. 1974. Selective segregation at grain boundaries. *Canadian Metallurgical Quarterly,* 13**,** 133-143.

CAMERON, T. B. 1979. Methods of detecting boron in steel. *Journal of Metals,* 31**,** F31-F31.

DA ROSA, G., MAUGIS, P., PORTAVOCE, A., DRILLET, J., VALLE, N., LENTZEN, E. & HOUMMADA, K. 2020. Grain-boundary segregation of boron in high-strength steel studied by nano-SIMS and atom probe tomography. *Acta Materialia,* 182**,** 226-234.

GRANGE, R. A. & MITCHELL, J. B. 1961. On the hardenability effect of boron in steel. *Trans. Am. Soc. Metals***,** Medium: X; Size: Pages: 157-85.

HARA, T., ASAHI, H., UEMORI, R. & TAMEHIRO, H. 2004. Role of Combined Addition of Niobium and Boron and of Molybdenum and Boron on Hardnenability in Low Carbon Steels. *ISIJ International,* 44**,** 1431-1440.

HE, X. L., CHU, Y. Y. & JONAS, J. J. 1989. Grain boundary segregation of boron during continuous cooling. *Acta Metallurgica,* 37**,** 147-161.

HONDROS, E. D. & SEAH, M. P. 1972. Grain-boundary activity measurements by Auger Electron Spectroscopy. *Scripta Metallurgica,* 6**,** 1007-1012.

HORREARD, F. 2000. Recent developments in SIMS instrumentation. *Elektronika,* 41**,** 7-1010.

KARLSSON, L., NORDÉN, H. & ODELIUS, H. 1988. Overview no. 63 Non-equilibrium grain boundary segregation of boron in austenitic stainless steel—I. Large scale segregation behaviour. *Acta Metallurgica,* 36**,** 1-12.

LARERE, A., GUTTMANN, M., DUMOULIN, P. & ROQUES-CARMES, C. 1982. Auger electron spectroscopy study of the kinetics of intergranular and surface segregations in nickel during annealing. *Acta Metallurgica,* 30**,** 685-693.

LEJČEK, P. 2010. Grain Boundary Segregation in Metals. Berlin, Heidelberg: Springer Berlin Heidelberg.

LI, Y. J., PONGE, D., CHOI, P. & RAABE, D. 2015a. Atomic scale investigation of non-equilibrium segregation of boron in a quenched Mo-free martensitic steel. *Ultramicroscopy,* 159**,** 240-247.

LI, Y. J., PONGE, D., CHOI, P. & RAABE, D. 2015b. Segregation of boron at prior austenite grain boundaries in a quenched martensitic steel studied by atom probe tomography. *Scripta Materialia,* 96**,** 13-16.

MCLEAN, D. 1957. *Grain boundaries in metals,* Oxford, Clarendon Press.

MILLER, M. K., BEAVEN, P. A., LEWIS, R. J. & SMITH, G. D. W. 1978. Atom probe microanalytical studies of some commercially important steels. *Surface Science,* 70**,** 470-484.

SHARMA, M., ORTLEPP, I. & BLECK, W. 2019. Boron in Heat-Treatable Steels: A Review. *Steel Research International,* 90.

SIMCOE, C. R., ELSEA, A. R. & MANNING, G. K. 1955. Study of the Effect of Boron on The Decomposition of Austenite. *JOM,* 7**,** 193-200.

SLODZIAN, G., DAIGNE, B., GIRARD, F., BOUST, F. & HILLION, F. 1992. Scanning secondary ion analytical microscopy with parallel detection. *Biology of the Cell,* 74**,** 43-50.

STADERMANN, F. J., WALKER, R. M. & ZINNER, E. 1999. Nanosims: The next generation ion probe for the microanalysis of extraterrestrial material. *Meteoritics & Planetary Science,* 34**,** A111-A112.

UENO, M. & ITOH, K. 1988. Optimum condition to obtain the maximum hardenability effect of boron. *Tetsu-To-Hagane/Journal of the Iron and Steel Institute of Japan,* 74**,** 910-917.

WAUGH, A. R. & SOUTHON, M. J. 1979. Surface-analysis and grain-boundary segregation measurements using atom-probe techniques. *Surface Science,* 89**,** 718-724.

WILLIAMS, D. B. & EDINGTON, J. W. 1976. High resolution microanalysis in materials science using electron energy loss measurements. *Journal of Microscopy-Oxford,* 108**,** 113-145.

WITTRY, D. B. 1979. Local characterization of solids by electron-energy loss spectrometry. *Journal of Microscopy-Oxford,* 117**,** 175-184.

2 Literature Review

2.1 Introduction

Impurity segregation and its influence on the mechanical properties of metals and alloys has been studied for many years. Segregation to grain boundaries can lead to many problems such as grain boundary fracture as a result of temper brittleness (Wu et al., 2008, Phythian and English, 1993, McMahon Jr, 2003), creep embrittlement (Eggeler and Dlouhy, 2005, Fujiwara et al., 1994, Laha et al., 2012, Swindeman et al., 1983), stress relief cracking of welds (Ishikawa et al., 1999, Shin and McMahon Jr, 1984, Hippsley et al., 1984), environmentally assisted fatigue (Briant and Banerji, 1978, Daniel et al., 2007), grain boundary corrosion (Krahe and Guttmann, 1974, Ogura et al., 1978), and some forms of intergranular stress corrosion cracking (Akhurst et al., 1980, McMahon and Truax, 1973, Moloznik et al., 1979) .

Sulphur is known to segregate to grain boundaries and cause brittle intergranular fracture in nickel, iron, stainless steels, and other alloys (Larere et al., 1982, Mostefa et al., 1990, Tehovnik et al., 2011, Shin and Meshii, 1983b, Shin and Meshii, 1983c, Shin and Meshii, 1983a, Bruemmer et al., 1980b, Bruemmer et al., 1980a, Hanninen and Minni, 1982). It is believed that the intergranular embrittlement is due to a decrease in the cohesive strength caused by impurity segregation at grain boundaries (Doherty et al., 1974). Phosphorus grain boundary segregation contributes to the degradation of mechanical properties of iron and steels (Naudin et al., 1999, Mulford et al., 1976, Christien et al., 2003, Hashimoto et al., 1984). Therefore, diffusion and segregation data concerning sulphur and phosphorous in metals are of great importance.

Unlike many other segregants, boron is an element that does not cause grain boundary embrittlement, instead it is known to be a grain boundary strengthener in polycrystalline nickel-based superalloys (Ladna and Birnbaum, 1988, Kontis et al., 2017) and greatly increases the hardenability in heat treatable steels (Sharma et al., 2019). The difficulty in detecting boron, in particular the small

amounts of boron involved (Cameron, 1979) and the strong tendency for the formation of boron-containing precipitates such as boron carbides (BC) and boron nitrides (BN) during processing of heat-treatable steels, have made it challenging to clearly identify the mechanisms involved in the beneficial boron effect.

2.1.1 Techniques for Localising Grain Boundary Segregation

Auger electron spectroscopy (AES) has proved invaluable in determining the species segregated to embrittled boundaries (Larere et al., 1982, Liu et al., 1992, Mega et al., 1996, Christien et al., 2010, Song et al., 2011). AES is recognised as a true surface analysis technique, has the advantage of analysing material surfaces to depths of only a few nm. However, to achieve very clean sample surface and accurate results, a sample would need to be inside high vacuum chamber and requires *in-situ* grain boundary fracture. This sample preparation can be challenging and only a few grain boundaries can be analysed (Lejcek and Hofmann, 1994, Sharma et al., 2019). An additional problem is that only brittle grain boundaries can be analysed which limits the analysis to solute segregation problems which embrittle the grain boundaries and within one system only those grain boundaries which fracture can be analysed.

AES instruments use a high-energy primary electron beam as an excitation source to ionize atomic core level electrons. When the primary electron beam bombards the sample surface, Auger electrons are excited by the energy released which are characteristic of elements present at the surface. Therefore, the characteristic energy of emitted Auger electrons can be used for elemental analysis (except H and He) (O'Connor et al., 1992). Due to the low energy of the Auger electrons the technique is extremely surface sensitive as Auger electrons have a very short mean free path. Figure 2.1 illustrates the basic principle of AES showing the primary electrons directed to the sample surface and Auger electrons are ejected only from the surface according to their characteristic energy based on the elements in the sample.

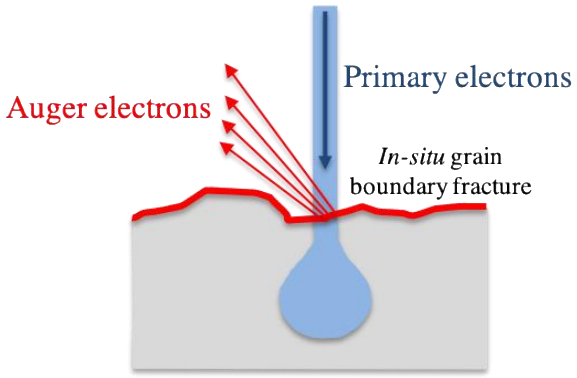


Figure 2.1: Basic principle of Auger electron spectroscopy (AES).

The use of transmission electron microscopy (TEM) together with energy dispersive x-ray spectroscopy (EDS) (Alber et al., 1997) or electron energy loss spectroscopy (EELS) is another method to investigate grain boundary segregation (Herbig et al., 2014, Keast and Williams, 2001, Muller et al., 1996). In TEM, as shown schematically in Figure 2.2, a high energy primary electron beam is accelerated through a thin sample typically less than 80 nm thickness. In EDS mode, the detector collects the signal of characteristic x-ray energies emitted by the atoms of different elements present in the sample and provide information on the chemical composition of the sample. However, light elements such as B, C and N are difficult to detect by TEM-EDS (Sharma et al., 2019).

On the other hand, in EELS detection mode, the energy of the incident electrons is reduced caused by inelastic scattering of electrons as they pass through the sample. EELS provides elemental information of the sample by detecting the energy distribution of the electrons or the energy change in the primary electron beam while passing through the sample. EELS is superior to EDS at detecting light elements such as B. However, studies by Bok Sel et al. conclude that EELS is not suitable to detect boron at lower levels than 100 ppm (Bok Seol et al., 2010).

In the TEM there is no requirement to carry out grain boundary fracture which makes these techniques preferable to AES. Additionally, by performing electron diffraction, the crystallography of the grain boundary can be ascertained (Li and Williams, 2003). However, TEM sample preparation and quantification can be very challenging and is only limited to few grain boundaries.

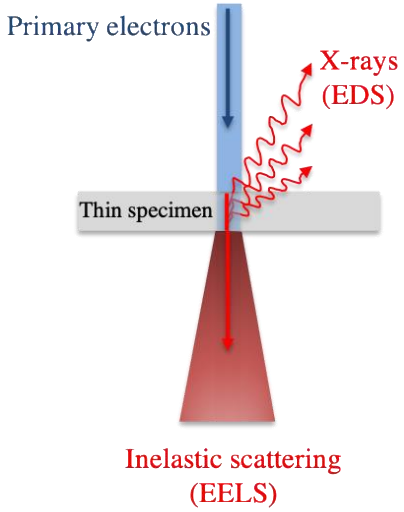


Figure 2.2: Basic principle of transmission electron microscopy (TEM) with electron dispersive x-ray spectroscopy (EDS) and electron energy loss spectroscopy (EELS).

In addition, atom probe tomography (APT) is recognised as a technique that can study interface segregation (Haslberger et al., 2015, Bok Seol et al., 2010, Alam et al., 2012). APT is an analytical technique that combines the capabilities of atomic scale imaging of the field ion microscope (FIM) and time-of-flight mass spectrometry that provides high chemical sensitivity (Cerezo et al., 1988). This technique can give accurate concentrations of segregated elements and all elements including light elements can be detected. Nevertheless, the analysis only limited to one grain boundary per sample and the sample preparation is very time consuming. Figure 2.3 shows the basic principle of APT where the individual atoms are evaporated at the tip of the needle-shaped specimen in a strong electric field and accelerated towards a position-sensitive detector.

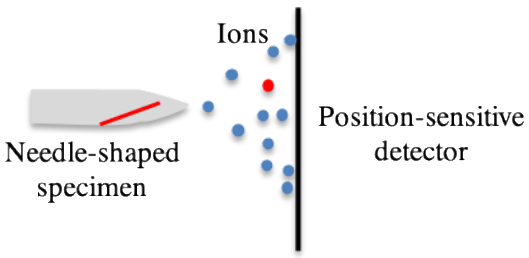


Figure 2.3: Basic principle of atom probe tomography (APT) with the red line in the sample indicating a grain boundary.

A review of common techniques to study grain boundary segregation such as AES, SIMS, TEM and APT is given in (Lejček, 2010) based on two groups of methods; surface analysis and microscopic techniques. My project aims to show how NanoSIMS can be added to this list of state-of-the-art techniques.

There are a limited number of publications that have used NanoSIMS analysis to determine grain boundary segregation on simple polished cross-sections (Lozano-Perez et al., 2008, Valle et al., 2011, Christien et al., 2012, Seol et al., 2013, Da Rosa et al., 2020). The NanoSIMS is one of the most sensitive elemental and isotopic surface analysis techniques due to the very high transmission efficiency of the secondary ion optics (Slodzian et al., 1992) allowing trace elements to be detected. The lateral resolution can be as good as 50 nm (Stadermann et al., 1999, Horreard, 2000) and it is simultaneously able to achieve high mass resolution, allowing peaks which have nominally the same mass to be separated.

2.2 Secondary Ion Mass Spectrometry (SIMS)

2.2.1 Introduction to SIMS

Secondary ion mass spectrometry (SIMS) is a surface analysis technique in which charged particles, ejected from the surface after bombardment with a primary ion beam, are separated by a mass analyser and compositional data is collected. Since its inception over 100 years ago (Thomson, 1910, Dempster, 1918), SIMS has undergone tremendous technological improvements and today is a technique recognised, both scientifically and commercially, as a valuable tool for surface analysis due to its combination of excellent depth resolution and very high chemical sensitivity.

2.2.2 The Sputtering Process

The erosion of a target by high energy particle bombardment is referred to as sputtering and is schematically displayed in Figure 2.4. A cascade of collisions occurs after ion bombardment resulting in the ejection of atoms and atomic clusters from the surface. Some ejected atoms and atomic clusters are automatically ionized during the ejection process, either positively or negatively depending on their chemical nature. These ejected species are called secondary ions, and contain chemical information on the analysed area. They are eventually collected and separated based on their mass-to-charge ratio.

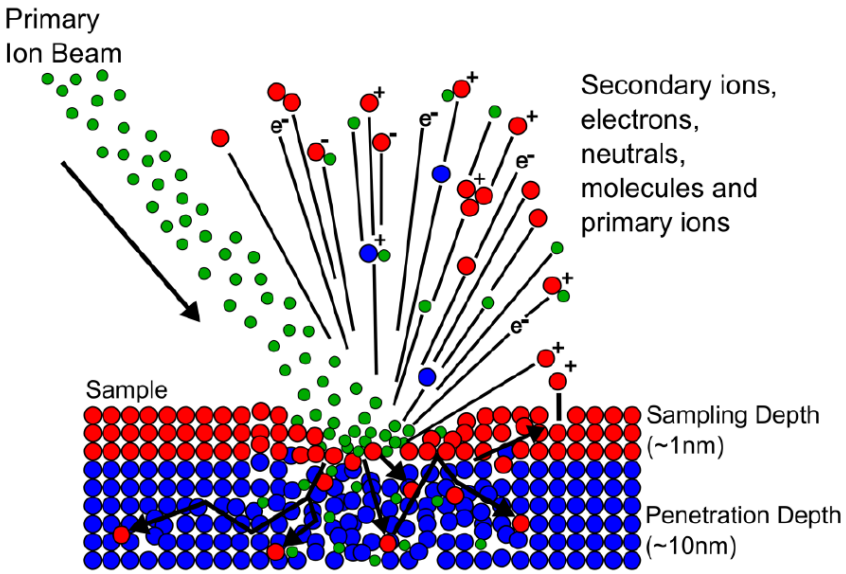


Figure 2.4: A schematic showing the erosion of a target's surface by sputtering and the generation of secondary ions. Reproduced from (Moore, 2011).

2.2.3 Instrumentation

The key components of modern SIMS instruments are shown in Figure 2.5. Primary ion beams are produced by ion sources, focused through the primary ion column onto the sample to generate secondary ions. These secondary ions will be collected by extraction optics and separated based on to their mass-to-charge ratio in the energy analyser and mass analyser. Ultimately, the signals are

collected by ion detectors. These signals are processed according to the operating method chosen (i.e. imaging, line scan, depth profile, mass spectrum, or isotopic ratio).

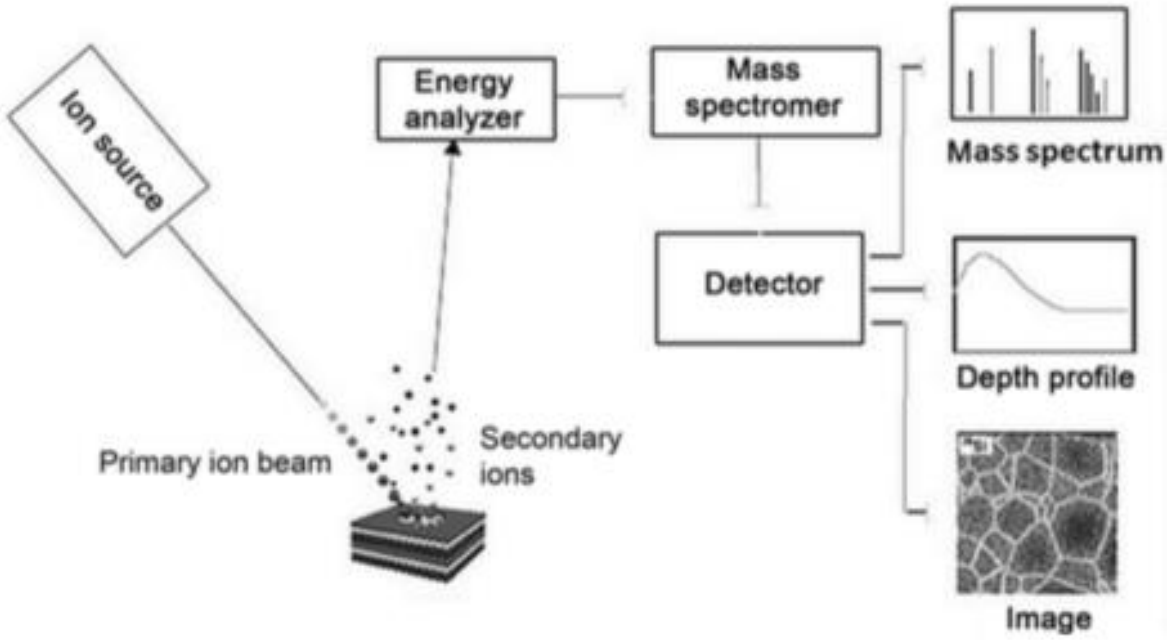


Figure 2.5: Overview of basic components of a SIMS instrument. Reproduced with permission from (Tanzi et al., 2019). Copyright © 2019 Elsevier.

2.2.3.1 Primary Ion Sources

To produce a high quality primary ion beam, the ion source must produce a high purity ion beam of high current density with small energy spread and a constant ion current density throughout the beam cross-section. The simplest ion gun consists of a source of primary ions and an extractor-accelerator lens combination to reduce energy spread. If there are impurities in the source feed material, a Wien filter, which employs crossed electrostatic and magnetic fields to allow selection of a particular m/z value, may be introduced (Vickerman et al., 1989).

When choosing the type of ion species or ion gun, factors such as type of elements, current (pulsed or continuous), and beam diameter are important. Primary beam species used frequently in SIMS analysis include Cs^+, O^-, Ga^+, and C_{60}^+, at energies between 1 and 30 keV. During analysis, the samples will be implanted with primary ions to depths of 1 to 10 nm (van der Heide, 2014).

The NanoSIMS instruments used in this study requires a Cs^+ microbeam ion source that generates negative ions and an O^- duoplasmatron source that generates positive ions due to the co-axial optics used in the instrument. It can only detect secondary ions which have opposite polarity to the primary ions. The creation of primary ion sources that is used in the NanoSIMS will be described in section 3.7.1.

2.2.3.2 Mass Analyser

Once the secondary ions have been generated, they need to be separated using a mass analyser. There are three type of mass analyser that are widely used in SIMS; magnetic sector, quadrupole and time-of-flight. The types of SIMS instruments can be categorised into dynamic and static SIMS depending on the choice of mass analysers and the duty cycle (what fraction of the time the beam is incident on the sample surface). The types of SIMS instruments will be discussed in section 2.2.4.

Dynamic SIMS instruments can have two types of mass analysers, magnetic sector and quadrupole. The most common mass analyser used in dynamic SIMS instruments is magnetic sector. As the name implies, the magnetic field is used to separate the ions according to their mass to charge ratios (*m/z*). As the primary ions enter the magnetic field, the secondary ions are deflected according to Fleming's left hand rule based on their *m/z* value where lighter ions will be deflected more. The ions are acted on by two equal forces due to magnetic field (F_B = Lorentz force) and direction of motion (F_C = centrifugal force). The following equation shows the relationship of both forces:

$$\boldsymbol{F_B = Bzev = F_C = \frac{mv^2}{r}} \qquad \textbf{(2.1)}$$

where *B* is magnetic flux density, *z* is charge of the ion, *e* is elementary charge, *v* is velocity of the ion, *m* is the mass of the ion and *r* is the curved path radius where the ions travel before they reach the detector.

Consider the ions are accelerated by potential voltage *V*, the electric potential energy is equal to kinetic energy and given by:

$$\mathbf{E}_{el} = \mathbf{E}_k = zeV = \frac{1}{2}mv^2 \qquad \textbf{(2.2)}$$

By eliminating the velocity (*v*) of the ion from equation 2.1 and 2.2, the equations can be simplified to find the *m/z* ratios:

$$\frac{m}{z} = \frac{eB^2r^2}{2V} \qquad \textbf{(2.3)}$$

The *m/z* value is depending on the curved path radius (*r*) if the magnetic flux density (*B*) and the voltage (*V*) are held constant. The ions that are not selected by *B* and *V* value, will not pass to the detector.

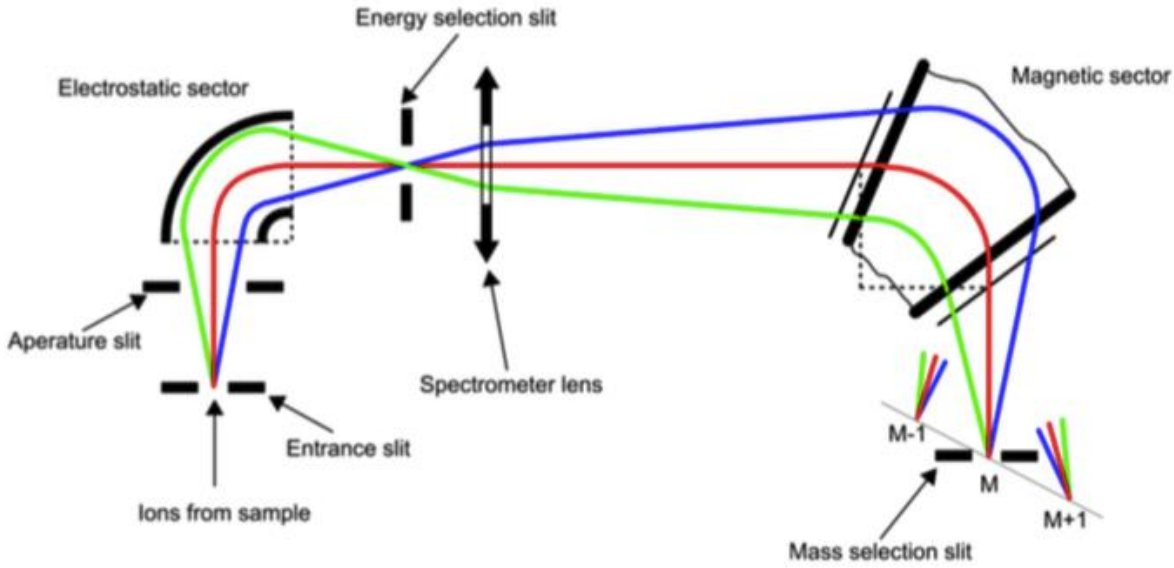


Figure 2.6: Schematic diagram of double focusing mass spectrometer showing the electrostatic and magnetic sectors. Reproduced with permission from (Moore et al., 2012). Copyright © 2012 John Wiley and Sons.

The magnetic sector mass spectrometers consist of single or double focussing magnetic sector. The single magnetic sector analysers introduce chromatic aberrations into the ion beams which reduces mass resolution, and are used as mass focussing where they focus angular dispersions. In order to achieve higher mass resolution, a mass spectrometer can combine a magnetic sector analyser and an

electrostatic filter because when they are used together, both the angular dispersion and the energies are focussed which is then called double focussing instrument. The high resolution SIMS instrument (NanoSIMS) that is used in this study is an example of the double focusing magnetic sector instrument which is illustrated in Figure 2.6.

The quadrupole mass analyser uses resonant electric fields that are tuned to preferred masses to separate the secondary ions. It consists of four parallel metal rods of circular or hyperbolic cross-section as shown in Figure 2.7. The opposing pairs of the rods are connected to each other with direct current (DC = U) and radio frequency (RF = $V \cos \omega t$) voltages. An oscillating electrical field is generated when a DC voltage is superimposed on the RF voltage where it is used to selectively stabilize or destabilize ions in the quadrupole. The equations of motion describing the series of oscillations produced when the ions enter the quadrupole is discussed in detail by (Miller and Denton, 1986). Only ions of a certain *m/z* value will have a stable trajectory through the quadrupole, which allow them to reach the detector while the other ions will have unstable trajectories, and consequently collide with the rods and be neutralised. The mass spectrum can be acquired by changing the DC and RF voltages and polarity applied to the rods while keeping their ratio constant. Due to its ability to select ions of a single *m/z* value, the quadrupole mass analyser is also referred to as a mass filter.

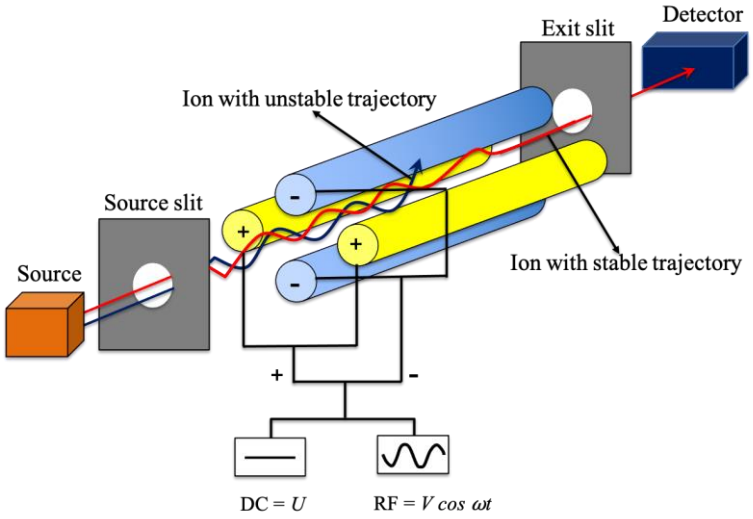


Figure 2.7: Schematic diagram of quadrupole mass analyser. Adapted with permission from (Kicman et al., 2007). Copyright © 2007 Elsevier.

Figure 2.8 shows an illustration of the principle of a time-of-flight mass analyser. The ion source produce pulses of primary ions in bundles and the secondary ions are accelerated towards the free-field region called a flight tube through the extraction electrode. The time-of-flight mass analyser uses the velocity of the ions in a field-free drift path to separate them. All ions will have approximately the same kinetic energy so their velocities are determined by their mass. Mass to charge ratios (*m/z*) are determined by the time it takes for the ions to travel through the field-free drift region in the flight tube to the detector. The *m/z* ratios and the time taken by the ions to travel through the field-free drift region in the time-of-flight analyser to the detector can be derived from equations 2.4 to 2.10 adapted from (Hoffmann and Stroobant, 2007).

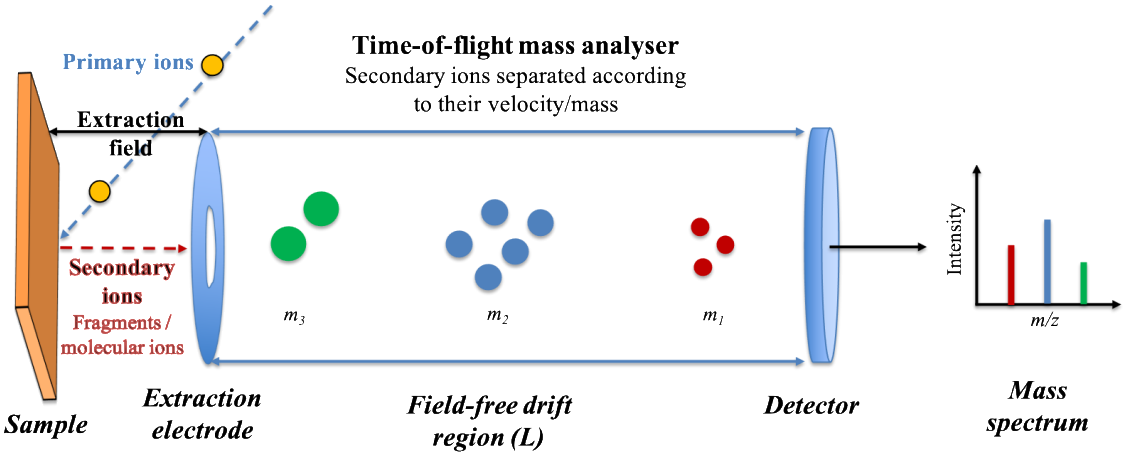


Figure 2.8: Schematic diagram of time-of-flight mass analyser. Redrawn with permission from (Hoex, 2018).

The electric potential energy, E_{el} of the ions in the extraction field is given by:

$$\mathbf{E_{el} = qV = zeV} \qquad \textbf{(2.4)}$$

where *q* is the total charge of the particle equal to the product of charge number, *z*, and elementary-charge constant, *e*, and *V* is potential acceleration voltage.

All of the ions acquire the same kinetic energy, E_k which is given by:

$$\mathbf{E}_k = \frac{\mathbf{1}}{\mathbf{2}} mv^2 \tag{2.5}$$

where *m* is mass, and *v* is velocity.

The electric potential energy is converted into kinetic energy:

$$\mathbf{E}_{el} = \mathbf{E}_k = zeV = \frac{\mathbf{1}}{\mathbf{2}} mv^2 \tag{2.6}$$

The velocity of the ions is given by rearranging the equation above:

$$v = \sqrt{\frac{2zeV}{m}} \tag{2.7}$$

As the ions travel at a constant velocity to the detector, the time taken by ions to reach the detector to cover the drift path length, *L* is given by:

$$t = \frac{L}{v} \tag{2.8}$$

The time is described by replacing *v* with its value from equation 2.4 gives:

$$t = L\left(\frac{m}{2zeV}\right)^{\frac{1}{2}} \tag{2.9}$$

By rearranging the equation above, *m/z* ratios can be calculated as:

$$\frac{m}{z} = \left(\frac{2eV}{L^2}\right) t^2 \tag{2.10}$$

This equation shows ions with lower *m/z* will travel the fastest and will arrive first at the detector compared to the ions with the larger *m/z*.

In this kind of system, the analyser needs a pulsed primary gun or pulsed secondary ion extraction to define the start of the flight time. All secondary ions produced can be identified (Vickerman, 2009). Initially, in the 1970s most static SIMS used a quadrupole mass analyser but since the introduction of time-of-flight mass analyser in 1978, it has been recognised as the standard analyser for static SIMS instruments because of its combination of high mass resolution and high transmission in the high mass range (Benninghoven, 1994).

2.2.4 Types of SIMS Instruments

2.2.4.1 Dynamic SIMS

Dynamic SIMS employs a high primary ion dose (above 10^{12} ions cm^{-2}) which results in fast surface erosion (Vickerman et al., 1989). Because of the high dose and high sensitivity, the main use for dynamic SIMS is depth profiling and measuring the chemical distribution of dopants in semiconductors and related devices. Modern dynamic SIMS equipment offers parts per billion sensitivity, tens of nanometre lateral resolution and sub-nanometre depth resolution. They have been widely applied in the areas of materials science (Christien et al., 2012, Lozano-Perez et al., 2008, Lozano-Perez et al., 2009), geology (Oehler et al., 2006, Oehler et al., 2010, Sugitani et al., 2009), cell biology (Boxer et al., 2009, Guerquin-Kern et al., 2005) and microbiology (Li et al., 2008, Wagner, 2009). For quantitative analysis, dynamic SIMS is the preferred instrument as it is able to achieve a much faster sputtering rates from the high primary ion current and produce a more efficient ion yield and thus it gives better counting statistics. The high resolution SIMS (NanoSIMS) that is used in this study is categorised as a dynamic SIMS instrument. The characteristics of the NanoSIMS will be described in detail in section 2.2.6.

2.2.4.2 Static SIMS

Static SIMS instruments generally use low primary ion doses (less than 10^{12} ions cm^{-2}). As the interactions between the primary ion beam and sample are essentially limited to the top monolayer of the surface and signals originate from previously undisturbed areas, the surface is said to be static (Vickerman et al., 1989). Static SIMS is normally utilized to study the composition of surface impurities or molecular information, the much lower doses employed means that much larger molecular fragments are emitted than for dynamic SIMS. These instruments generally use a time of flight tube. Figure 2.9 demonstrates a pulse of primary ion beam bombardment on a targeted area

which receives a very low primary ion current density, and displays the spectrum recorded from ions of various masses.

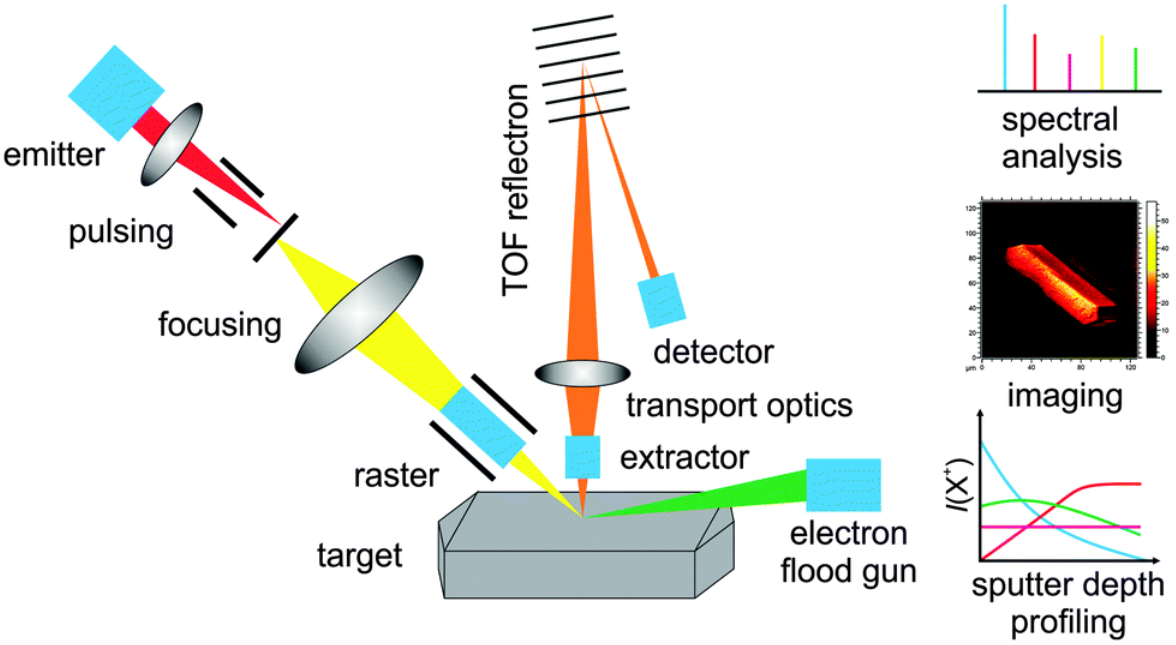


Figure 2.9: Schematic diagram of the operation of a static SIMS instrument. Reproduced with permission from (Hofmann et al., 2014) published by the PCCP Owner Societies. Copyright © 2014 PCCP Owner Societies, licensed under a Creative Commons Attribution 3.0 Unported Licence.

2.2.5 Technical Details

2.2.5.1 Sputter Yield and Preferential Sputtering

The erosion rate is quantitatively described by sputter yield, Y_{SP} , which is defined as the number of secondary particles removed per primary ion (Wilson et al., 1989, Vickerman et al., 1989). Sputter yield is dependent both on the primary ion beam parameters and target material properties. The mass, energy, angle of incidence and current density of the primary ion beam all affect the sputter rate (Dowsett et al., 2003). Even for well-defined, constant primary ion conditions, a variation of a factor of five in sputter rate is observed between targets of different elements across the periodic table due to different surface binding energies. Furthermore, within targets of the same atomic number, different crystallographic planes give rise to varying sputter rates (Stark et al., 2009). Topography

also has a major effect on the yield and is enhanced by roughness of similar scale to the collision cascade, or reduced by holes or porosity which may trap sputtered particles (Kita et al., 2009).

Significant changes in local structure and surface composition of the target occur due to atomic mixing and preferential sputtering. Strong atomic displacement and diffusion take place during the collision cascade, and the implantation of primary ions into the bulk causes atomic mixing in the target surface. In this altered layer, the material properties (such as binding energy, distribution of elements, density etc.) are considerably changed, and this effects subsequent collision cascades and sputter rates. The difference in sputter yields between various elements in a multi-elemental target causes preferential sputtering. Obviously the material properties within the altered layer are changed and a composition gradient exists between the preferentially sputtered surface and the unchanged bulk which affects the sputter rate (Hofmann et al., 2019).

2.2.5.2 Resolution

2.2.5.2.1 Mass Resolution

The ability of an instrument to separate ions of different masses is defined as the mass resolution.

Mass resolution *R* is defined as:

$$\boldsymbol{R = \frac{M_1}{M_1 - M_2} = \frac{M}{\Delta M}} \qquad \textbf{(2.11)}$$

Where M_1 is the mass of the ion of interest and M_2 is the mass of an adjacent interference peak (van der Heide, 2014, Moore et al., 2012). When peaks are not fully mass resolved it is common to measure mass resolution based on the width of the ion signal at half its height and this is known as full width at half maximum (FWHM) rule (Hoffmann and Stroobant, 2007). In a magnetic sector SIMS, high mass resolution can be achieved by using slits to cut off the edges of the secondary ion

beam which reduces the width (in mass) of the peaks but then will reduce the chemical sensitivity by lowering the transmission of secondary ions to the detectors (Moore et al., 2012).

As examples of signals of interest in this work, let us consider the problem separating $^{31}P^{12}C$, $^{27}Al^{16}O$ and $^{11}B^{16}O_2$ molecular secondary ions that have masses close to 43 amu. The true masses of these species are 42.9737620 amu, 42.9764526 amu and 42.9991348 amu, respectively. The minimum mass resolution required to separate $^{11}B^{16}O_2$ and $^{27}Al^{16}O$ would be 1896 and to separate $^{31}P^{12}C$ and $^{27}Al^{16}O$ would be 15973. These numbers are illustrated in Table 2.1.

Table 2.1: The true masses of $^{31}P^{12}C$, $^{27}Al^{16}O$ and $^{11}B^{16}O_2$ and the mass resolution to separate the ions

Ion	Mass (a.m.u)	Mass resolution (M/ΔM)	
$^{31}P^{12}C$	42.9737620	15973	
$^{27}Al^{16}O$	42.9764526		1896
$^{11}B^{16}O_2$	42.9991348		

If the instrument is tuned to a mass resolution of $\frac{M}{\Delta M} > 1900$ then it will be possible to eliminate the $^{11}B^{16}O_2$ interference from the $^{27}Al^{16}O$ signal. The NanoSIMS can thus easily distinguish $^{11}B^{16}O_2$ and $^{27}Al^{16}O$ but not resolve $^{27}Al^{16}O$ and $^{31}P^{12}C$ which requires a mass resolution of 15973. Figure 2.10 shows the NanoSIMS mass spectra around mass 43 from three separate scans taken from a steel sample (black dotted line) and the Al (red line) and B standards (blue line). The NanoSIMS can reach mass resolution as high as 3500 with 100% transmission (Oxford NanoSIMS, 2010), and higher mass resolutions if the transmission efficiency is reduced.

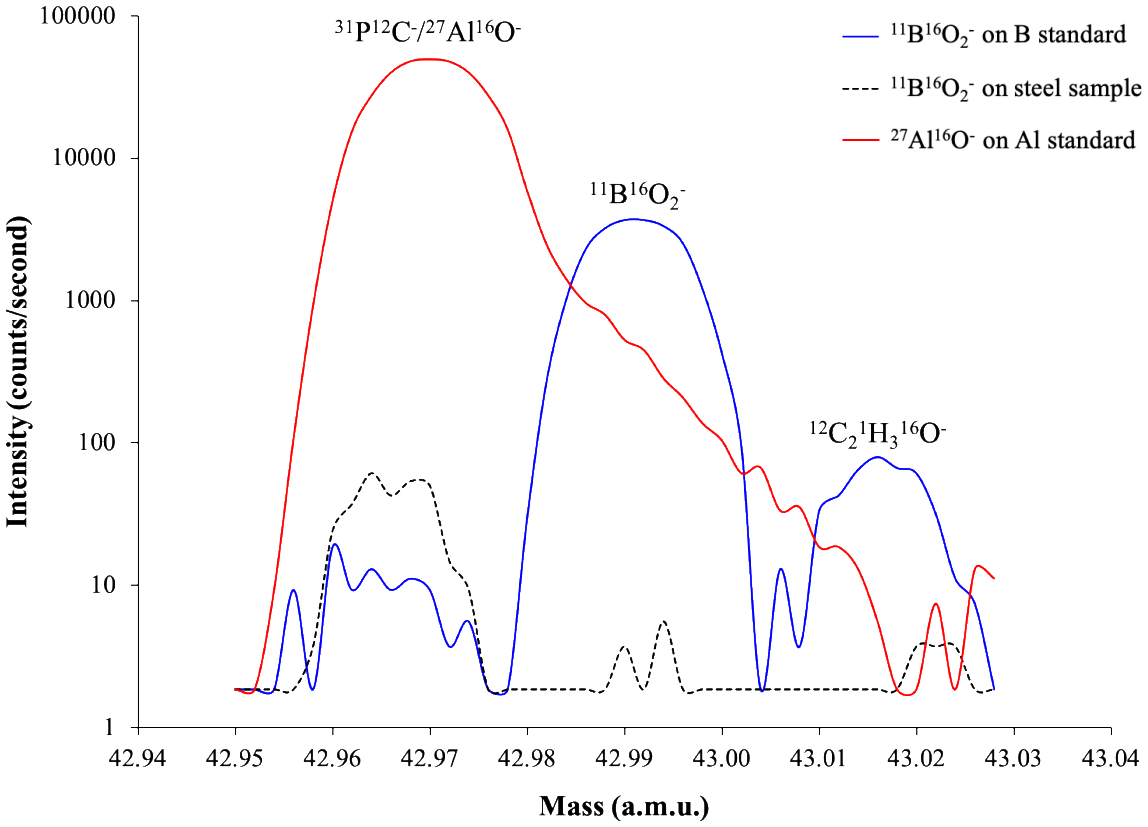


Figure 2.10: The NanoSIMS HMR scans for mass 43 from Al standard (red line), B standard (blue line) and steel sample (black dotted line).

2.2.5.2.2 Lateral Resolution

The extent of the collision cascade created by the impact of a single ion will affect the lateral resolution of all SIMS experiments. The sputtered ions can also be generated from a depth of about 1 nm, and from Monte Carlo simulations of a collision cascade the best lateral resolution that can be achieved from a single primary ion generating secondary ions from 1 nm depth is about 2 nm (Wilson et al., 1989). In addition, we must consider that to obtain a quantifiable secondary ion signal the primary ion beam will normally have to have a high current and so produce a large number of incident primary ions per second (Moore et al., 2012).

Under real experimental conditions, the diameter of the primary beam decides the lateral resolution; i.e when the beam size is 100 nm, the lateral resolution will be around 100 nm. To maximise the

useful resolution in chemical mapping experiments, the beam size and image pixel size should match as closely as possible. Unfortunately, SIMS users will need to choose either high sensitivity or high lateral resolution because aiming for a smaller primary beam diameter will also reduce the primary beam intensity (Ladna and Birnbaum, 1988, Moore et al., 2012).

2.2.5.2.3 Depth Resolution

Depth resolution is the ability to differentiate features and different signal intensities at various depths into the sample surface. Due to the fact that secondary ions come from the top few monolayers of the sample, the depth resolution of the SIMS technique is limited to ˜1 nm. There are a number of factors contributing to the depth resolution like primary ion type, impact energy, impact angle and the nature of the substrate which includes composition, crystalline structure and orientation (van der Heide, 2014). It is also affected by broadening effects, chemical segregation from the sample bulk, surface charging and sample topography (Tomita et al., 2012). Mixing effects from beam sputtering, in particular, cause redistribution that limit the depth resolution. Depth profiles are often calibrated by measuring the depth of the final sputter crater by surface profilometry and by assuming the sputter rate is consistent (Liebl, 1975).

2.2.5.3 Detection Limits and Sensitivity

The detection limit for a given element or its ability to detect elements present at low concentrations is determined by the number of atoms available in the analysed volume and also the useful yield. For a given detection limit, a compromise between lateral and depth resolution may be set, depending on the needs of the precise experiment being attempted. The detection limits also depend on factors including the type of instrumentation, the primary ion beam and the area of analysis. In SIMS, the detection limits range between 10^{12} and 10^{16} atoms/cm^3. Figure 2.11 shows a list of approximate best detection limits of both static and dynamic SIMS, compared with similar data for other analytical

techniques, presented in *volume density* (atoms/cm^3) and *surface density* (atoms/cm^2) on the silicon (110) surface. The efficiency of elemental ionization during analysis and the transmission efficiency of the ion optics will both influence the SIMS instrument's sensitivity (van der Heide, 2014).

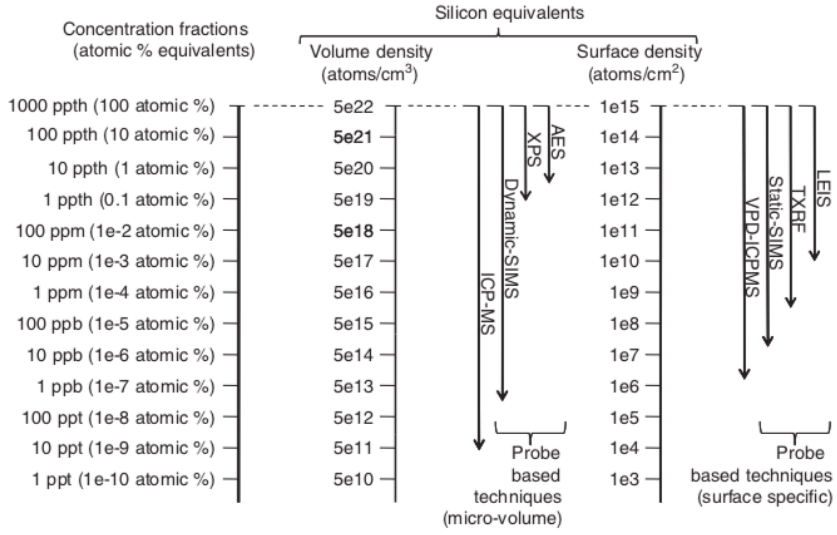


Figure 2.11: List of approximate best detection limits of both static and dynamic SIMS along with other analytical technique in volume density (atoms/cm^3) and surface density (atoms/cm^2) on silicon (110) surface. Reproduced with permission from (van der Heide, 2014). Copyright © 2014 John Wiley and Sons.

2.2.5.4 Quantification

In SIMS, direct comparison between the concentration of two elements in a sample surface cannot be done simply by comparing signal intensities because each element has different ion yield, thus providing a challenge to the quantification of SIMS data. The relative sensitivity factor, RSF, can be used as a method to quantify SIMS data by relating the number of counts from SIMS analysis to the actual concentration of the element in the sample. A low RSF value means a high yield, which therefore indicates a higher sensitivity to detect that particular species.

The use of the RSF is defined by:

$$C_E = RSF \cdot \frac{I_E}{I_M} \tag{2.12}$$

Where C_E is the concentration of an element of interest, I_E is the detected ion count from the element of interest and I_M is the detected ion count from the matrix element (Wilson et al., 1989, van der Heide, 2014).

In order to determine the RSF on unknown sample, a careful experimental setup is needed by calibrating with a standard material of known composition at the same time as the unknown sample is analysed. This is because the instrument conditions will greatly influence the RSF values. Reference materials of homogeneous bulk sample or ion implanted sample are preferred to determine RSF value due to the fact the ion yields varies for each matrix (Wilson et al., 1989). Figure 2.12 and Figure 2.13 show the RSF values for each element in a silicon matrix (EAG Laboratories, 2017). Whilst the solute segregation problems to be analysed in this project are not in a silicon matrix, these RSF values are still useful as they give an indication of the likely ion yield.

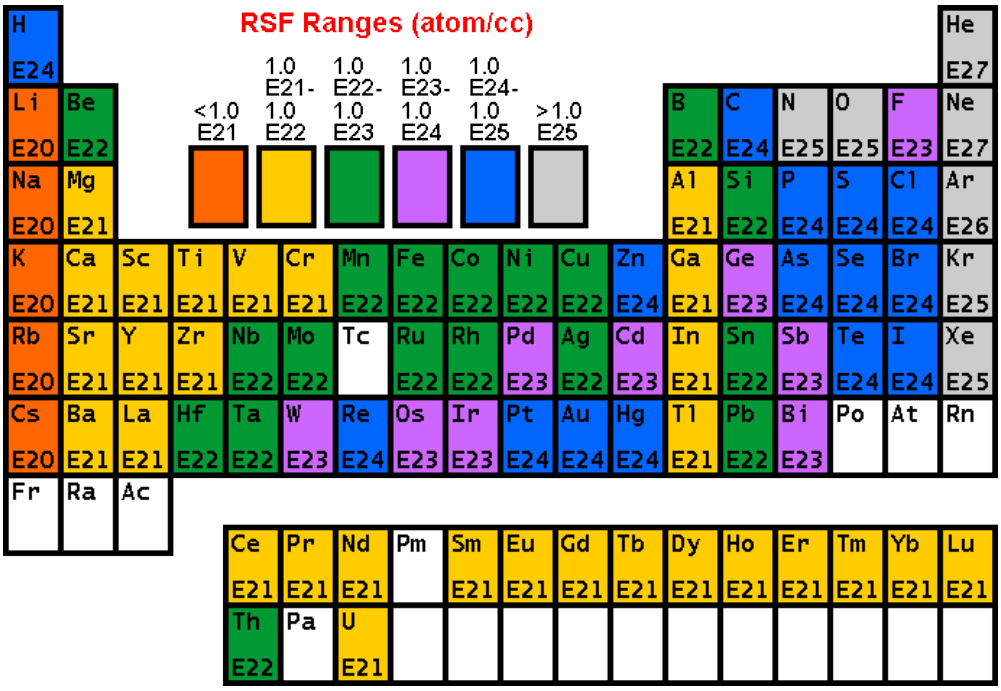


Figure 2.12: RSF values for negative ions under oxygen primary ion bombardment, positive secondary ions on a silicon matrix. Reproduced with permission from (EAG Laboratories, 2017). Copyright © 2015-2021 Eurofins Scientific.

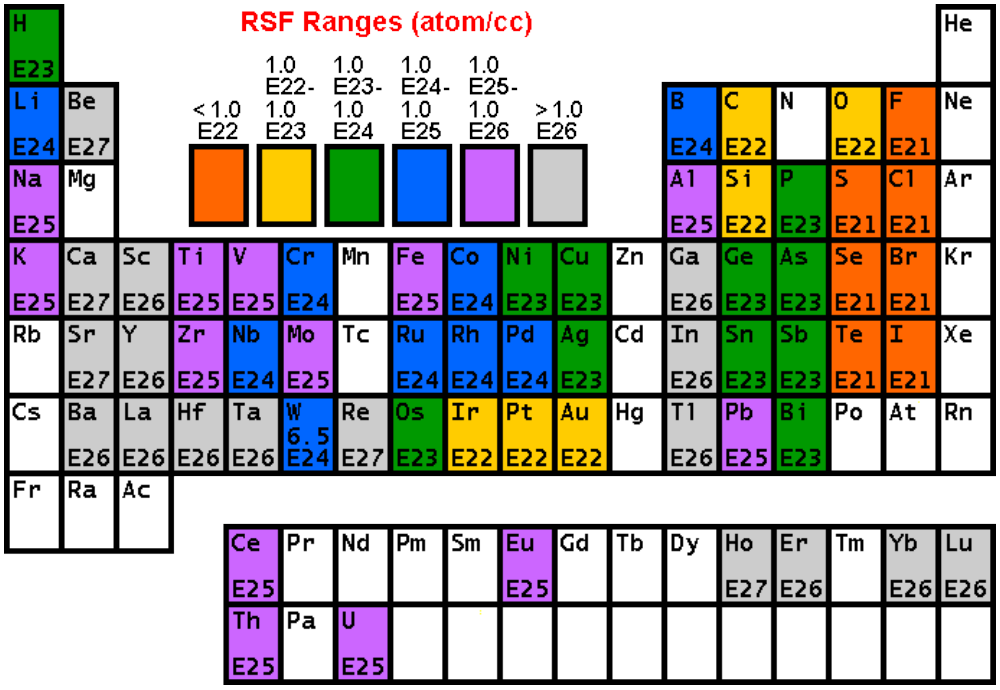


Figure 2.13: RSF values for positive ions under caesium primary ion bombardment, negative secondary ions on a silicon matrix. Reproduced with permission from (EAG Laboratories, 2017). Copyright © 2015-2021 Eurofins Scientific.

2.2.5.5 Artefacts

In common with all analytical techniques, SIMS analysis has many artefacts which need to be taken into consideration when interpreting the results. Some of the artefacts that can affect the secondary ion signals are the matrix effect, surface topography, preferential sputtering, crater edges, and re-deposition of sputtered materials. An understanding of the effects, influences and techniques developed to overcome such issues is important for obtaining meaningful analysis from each specific kind of sample.

The following sections consider a number of the most common and important artefacts relevant to this project.

2.2.5.5.1 Matrix effects

The secondary ion intensity and ion yield change not only with the concentration of the detected species, but also the chemical and electronic properties of the surrounding matrix (Wilson et al., 1989, Benninghoven et al., 1987). This phenomenon is called the matrix effect, and can lead to differences of several orders of magnitude in the detected ion signal from samples of similar chemical composition and must be carefully considered if the results are to be accurately interpreted. The whole field of quantification of SIMS data is dominated by the matrix effects. It is not possible to normalize the ion signals to a reference signal to correct the matrix effects as its influence on the ionization efficiency of each secondary ion will be different (Rudenauer, 1982) unless the reference has the same matrix as the sample. The matrix effect in metals under Cs^+ primary ion is weaker than when using the O^- primary ion due to the greater degree of oxidation of the metal surface induced by the O^- primary ions (Yu, 1982).

2.2.5.5.2 Surface topography

A flat sample is one of the primary requirements for SIMS analysis as topography can either enhance or supress secondary ion formation. There is also the contribution of primary beam damage, where rastering the primary beam over the sample surface can cause rippling, especially on the bottom of the crater (Laty et al., 1979). Figure 2.14 shows rippling as a function of sputtered depth with a 1 keV Cs^+ primary ion beam incident at 80°. The primary ion beam angle and its energy have both been found to have an effect on the surface roughening of the sample (van der Heide et al., 2003). To minimise roughening during analysis the sample can be bombarded obliquely and continually rotated during analysis (Konarski et al., 2003, Adams and Moens, 1987). This can be quite important for metal samples where different grains sputter at different rates.

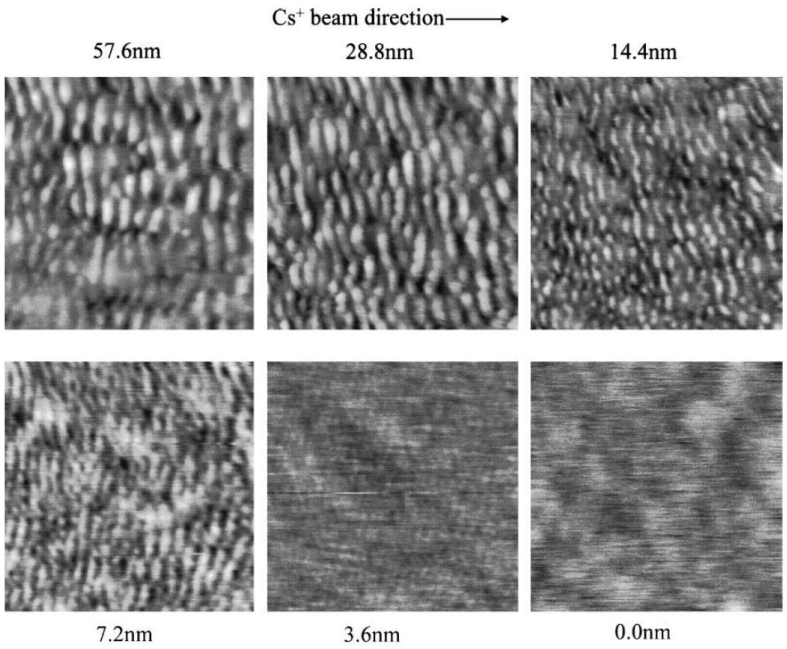


Figure 2.14: AFM scans of rippling on crater bottom of Si sample by ion sputtering. Reproduced with permission from (van der Heide et al., 2003). Copyright © 2003 Elsevier.

2.2.6 The CAMECA NanoSIMS 50

The NanoSIMS 50 is a specific type of dynamic SIMS instrument optimised for high lateral resolution imaging. It is the only dynamic SIMS instrument allowing simultaneously high lateral resolution (50 nm), high mass resolution ($m/\Delta m$ = 5000) and high sensitivity (ppb) (Slodzian et al., 1992).

The NanoSIMS has several important design characteristics (CAMECA, 2008):

1) Low current, highly focussed ion microprobe sources, for both O^- and Cs^+ ions, capable of beam diameters, and hence lateral resolutions, of 200 and 50 nm respectively. Recently, a new O^- source has been tested and able to achieve a similar lateral resolution as the Cs^+ source (CAMECA, 2017, Malherbe et al., 2016). The creation of primary ion sources will be described in section 3.7.1.

2) A co-axial probe-forming system which allows a shorter working distance and leads to a smaller spot size for a given current, a higher collection efficiency, and reduced broadening of the secondary beam favouring sensitivity at high mass resolution. However in the co-axial configuration, the constraint is that the primary and secondary ions must be of opposite polarity and equal energy.
3) A very high efficiency magnetic sector analyser that allows high mass resolution with a small spot size, (e.g. 80% transmission at 4500 $m/\Delta m$) whilst keeping analysis times short compared to a time-of-flight mass spectrometer.
4) Extremely high efficiency ion collection and detection optics in the five (seven in the latest instruments) independent detectors preserve elemental sensitivities similar to conventional dynamic SIMS even with a low current incident beam. The analyser sensitivity (or transmission) of the NanoSIMS is maintained at a very high level even when the mass resolution is increased. This is due to a very high normal extraction field allowing early secondary ion focussing, careful transport and rectangular shaping of the secondary beam that reduces aberrations, and the correction of the second order mass spectrometer optical aberrations.
5) Five (or seven) independent detectors allow five selected mass images to be recorded simultaneously originating from precisely the same sputtered volume.

The operating modes of the NanoSIMS are much the same as in conventional dynamic SIMS instruments, depth profiling, bulk analysis and chemical spectroscopy. In addition, the NanoSIMS is able to produce high resolution chemical images and three dimensional depth profiles. The schematic of the ion optics of the NanoSIMS 50 is shown in section 3.7. This is the instrument that has been used throughout this project.

2.2.6.1 Comparison of SIMS with other Techniques

The common methods that are usually used for surface analysis include AES (Briggs and Seah, 1983), EDS (Lyman et al., 1989), and x-ray photoelectron spectroscopy (XPS) (Briggs and Seah, 1983, Drummond et al., 1991), but none of these techniques have the unique combination of capabilities of SIMS to detect molecules as well as elements and isotopes, high sensitivity and high lateral resolution. EDX and AES are only able to detect elements, but not molecules and isotopes, and have relatively poor sensitivities. The NanoSIMS has a relatively small spot size (Stadermann et al., 1999) compared with other SIMS instruments and has the ability to detect much lower concentrations of selected analytes compared with techniques such as TEM and EDX or electron probe microanalysis (EPMA). In addition, the NanoSIMS has the ability to have simultaneous high lateral resolution and high sensitivity. Figure 2.15 compares the analytical spot size and detection limits of different analytical techniques. It is clear from the graph that the NanoSIMS has a combination of capabilities not achieved by any other technique.

Electron backscatter diffraction (EBSD) is a complementary technique to the NanoSIMS and is a powerful technique that generates electron diffraction patterns from the crystallographic alignment of grains within a material. These diffraction patterns can then be used to determine the orientation of individual grains, local sample texture and to show grain boundaries. EBSD mapping can be used in combination with other techniques to investigate grain boundary segregation to specific types of grain boundaries allowing the structural aspect of segregation to be studied. The combination of NanoSIMS and EBSD has not, however been widely reported (Karney et al., 2012, Lozano-Perez, 2008).

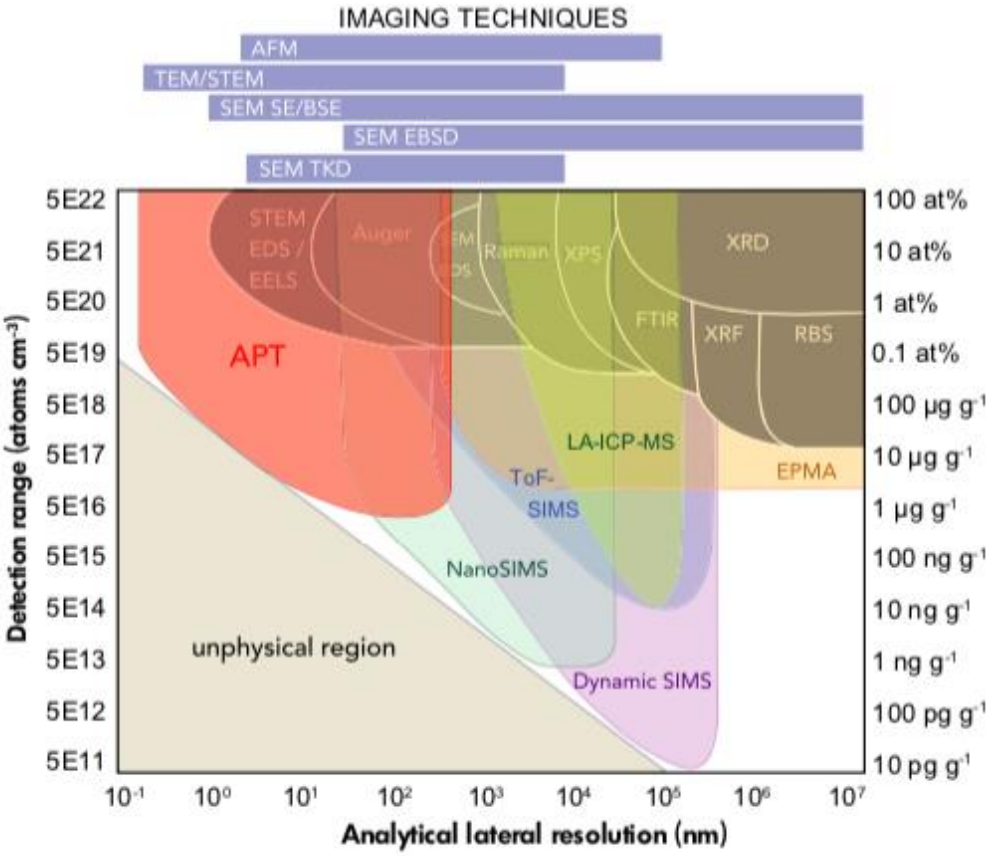


Figure 2.15: Comparison of different analytical techniques, analytical resolution versus detection limit. Reproduced with permission from (Reddy et al., 2020). Copyright © 2020 John Wiley and Sons.

2.3 Boron Hardenability Effect

A minute amount of boron (10 – 30 ppm) is commonly added to heat-treatable steels to give a positive effect on the hardenability at a minimum alloy cost (Kapadia, 1987). Boron in solution segregates to the prior austenite grain boundaries during austenizing which involves heating the steel to a high temperature, where it reduces the grain boundary energy and can decrease the nucleation rate of ferrite and bainite. This process will delay the austenite to ferrite or bainite phase transformation during cooling and contribute to the effect of boron on hardenability (Simcoe et al., 1955).

However, the effect of boron on hardenability can only take place when boron is present in solution. Unfortunately, the high affinity of boron for nitrogen leads to BN formation. BN is stable at high

temperature and remains undissolved at the normal austenizing temperature resulting in reduction in the boron hardenability effect. As a result, protection of the boron from reaction with nitrogen is the key to keep free boron available in solution in the steel. Strong nitride formers such as Ti and Al can be added to boron-treated steels to combine with any free nitrogen and thereby can suppress the formation of BN and enable boron to remain in solution (Shen and Hansen, 1997).

Heat treatment can change the boron hardenability effect by affecting the state and concentration of boron at austenite grain boundaries. The maximum hardenability will be achieved by careful choice of the optimum austenizing temperature, between 800°C and 1000°C depending on the chemical composition (Watanabe et al., 1983, Ueno and Itoh, 1988).

2.3.1 Grain Boundary Segregation

2.3.1.1 Equilibrium Segregation

Grain boundaries, phase boundaries, free surfaces and precipitate/matrix interfaces are loosely packed sites where solute atoms tend to migrate from bulk alloy to create a stable equilibrium condition also known as equilibrium segregation. This type of mechanism, which is driven by the minimization of the total Gibbs free energy of a system, only induces segregation to a few atomic layers at grain boundaries (Huang et al., 1997, McLean, 1957, Aust, 1974). This happens when impurities in a material diffuse at a high temperatures. The absorption of the impurity atoms at grain boundaries would decrease the interfacial free energy of the loosely packed sites (Karlsson and Norden, 1986).

An extensive review of models of equilibrium segregation is given by Lejcek in 2010 (Lejček, 2010). He explained the two main theories for the thermodynamics of grain boundary segregation, the Gibbs adsorption isotherm and Langmuir-McLean types of segregation isotherm (McLean, 1957, Lejček and Hofmann, 1995). Several other theories of equilibrium segregation have been proposed,

some applicable to binary systems (McLean, 1957, Seah and Hondros, 1973b) and some to more complex systems (Seah and Hondros, 1973b, Guttmann, 1975).

Figure 2.16 shows the solute enrichment factor, β, at grain boundaries in polycrystalline specimens as a function of the solubility of different impurity elements in the bulk. The data for a range of iron-, nickel- and copper-base binary alloys on the left column was originally plotted by (Seah and Hondros, 1973a). This figure was adapted by (Hofmann, 1990) and shows an additional column on the right hand side with systems where the solid solubility of the solute atoms is unknown. The solute enrichment factor, β is defined by as:

$$\boldsymbol{\beta} = \frac{\Delta \boldsymbol{N_2}}{\Delta \boldsymbol{N_2^0} \cdot \boldsymbol{X_2}} = -\frac{\mathbf{1}}{\Delta \boldsymbol{N_2^0}} \cdot \frac{\mathbf{1}}{\boldsymbol{kT}} \left(\frac{\boldsymbol{\partial \sigma}}{\boldsymbol{\partial X_2}} \right)_{\boldsymbol{T,P}} \tag{2.13}$$

where ΔN_2^0 is the boundary excess corresponding to a monolayer of solute at the interface, X_2 is the mole fraction of the dilute solute (segregant), σ is the grain boundary internal energy per unit area (of the grain boundary), k is the Boltzmann constant, T is the absolute temperature and $\partial\sigma/\partial X_2$ is evaluated at the dilute limit where $X_2 \rightarrow 0$.

Many studies on the relation of the grain boundary segregation to the grain boundary orientation have shown that segregation increases with misorientation angle (Thomas and Chalmers, 1955, Watanabe, 1985, Watanabe et al., 1980, Biscondi, 1982, Krakauer and Seidman, 1993). The solute segregation assessment has mostly been performed on samples with high angle grain boundaries rather than on low angle ones. However, scattered data are commonly acquired when the grain boundary concentrations are plotted against the total misorientation angle. These inconsistent results suggest that relationship between grain boundary structure and segregation is a complex one (Hofmann and Lejček, 1996).

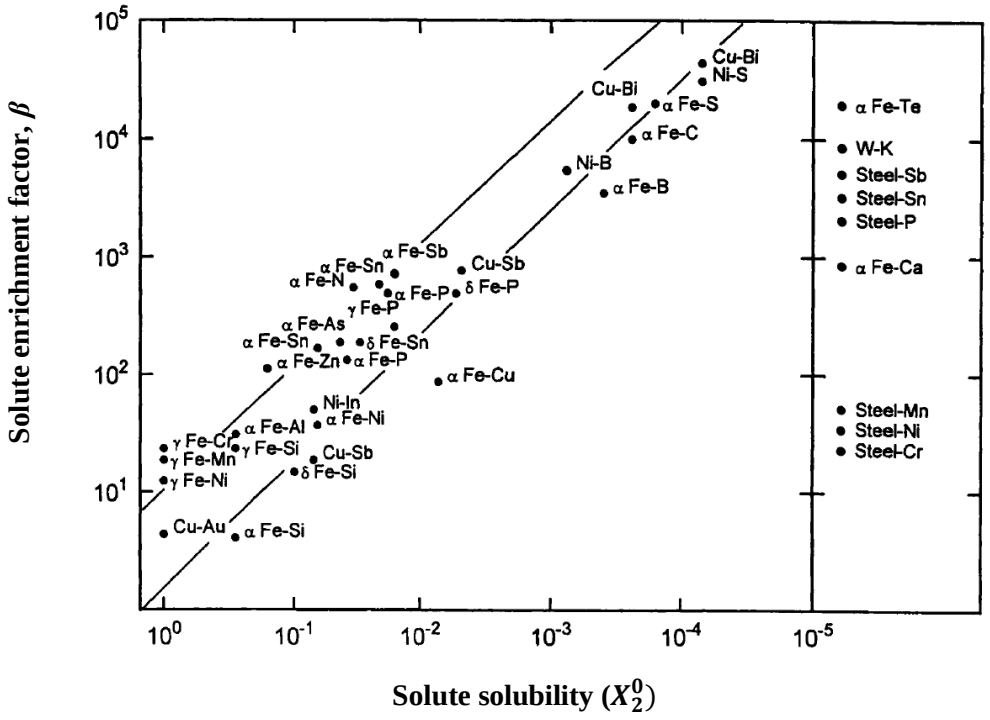


Figure 2.16: Collection of experimentally determined grain boundary segregation data showing the increase in solute enrichment factor, which is associated with a decrease in the solubility of the solute. The solute solubility of solutes in the systems given in the right part of the figure is unknown. The figure with data on the left column is republished with permission of The Royal Society (U.K.), from (Seah and Hondros, 1973a); permission conveyed through Copyright Clearance Center, Inc. The additional data on the right column is republished with permission of Taylor & Francis Group LLC – Books, from (Hofmann, 1990); permission conveyed through Copyright Clearance Center, Inc.

It is important to note that segregation happens preferably at boundaries with high energy instead of low ones (Joshi, 1975, Gleiter, 1970). Diminishing the excess free energy of the lattice defects at the boundary is what segregation relies on. Since the nature and structure of the grain boundaries will determine the boundary energy, this will also determine the grain boundary segregation level i.e high energies means high segregation (Gleiter and Chalmers, 1972).

Joshi declared that to observe a difference in segregation level at numerous boundaries, only two factors needs to be considered; grain boundary structure and energy (Joshi, 1975). Nevertheless, tests to relate grain boundary segregation directly to the structure as a function of misorientation angle between two nearby grains were not conducted. He also proposed that high angle boundaries would have a much better chance for segregation to occur, thermodynamically, since they store more energy

hence high level of energy equals high probability for segregation to occur. If a particular boundary is curved or facetted, a change of the segregation level can be seen locally at various boundary positions since the boundary plane affects the energy which in turn influence the segregation level.

2.3.1.2 Non-equilibrium Segregation

Most non-equilibrium segregation occurs during cooling from high temperatures (Karlsson and Nordén, 1988). It was first observed by Westbrook (Westbrook, 1964, Westbrook and Aust, 1963), who reported an increase in hardness measured at grain boundaries in quenched, dilute non-ferrous alloys and intermetallic compounds. The degree of segregation depends on factors such as heat treatment temperature, cooling rate, concentration of solute atoms and binding energy between solute atoms and vacancies (Karlsson et al., 1988).

The mechanism involved in this type of segregation relies on the formation of solute atom–vacancy complexes within the matrix, where the concentrations of these three species, solute atom (*I*), vacancy (*V*) and their recombined complex (*C*), are in dynamic equilibrium with each other (Faulkner, 1996, Tingdong, 2006):

$$\boldsymbol{I + V = C} \qquad \textbf{(2.14)}$$

Figure 2.17 (a) to (c) illustrates the interpretation of the thermally induced non-equilibrium segregation mechanism involving the formation of impurity-vacancy complexes within the matrix, where there is misfit between the impurity or solute atoms and matrix atoms. When a material has experienced rapid cooling from a high temperature during heat treatment, a supersaturation of vacancies will occur in the microstructure, and the grain boundaries will act as sinks for vacancies. During quenching, the vacancy concentration becomes lower in the grain boundaries but supersaturated in the grains. The concentration gradient allows the vacancies to diffuse towards the grain boundaries together with the impurity-vacancy complexes as shown in Figure 2.17 (a).

When the temperature increases, the diffusion of impurities and complexes is increased and this will lead to the accumulation of impurities within a few nanometres of the grain boundary as shown in Figure 2.17 (b). This process is not in equilibrium, and the segregation will reduce if the material is re-annealed with further increment of the temperature, to give enough energy for the impurity atoms to diffuse back down the concentration gradient that the non-equilibrium segregation has produced as shown in Figure 2.17 (c) (Faulkner, 1996, Zheng et al., 2012).

The back diffusion process occurs due to solute concentration at the grain boundary induced by diffusion of impurity-vacancy complexes is higher than equilibrium grain boundary concentration. The diffusion of impurity-vacancy complexes decreases with time but the back diffusion of solute atoms will increase with time. A critical time exists when the concentration of solute atoms reaches a maximum. The segregation process happens when the annealing time at a given temperature is shorter than the critical time, where the diffusion of impurity-vacancy complexes is the dominant process. On the other hand, de-segregation process will occur when the annealing time is longer than the critical time, where the back diffusion of solute atoms is the dominant process (Zheng et al., 2012).

The critical time, t_c, is defined by (Faulkner, 1981, Tingdong, 1987):

$$\boldsymbol{t_c = \frac{r^2 \ln(D_c/D)}{4\delta(D_c - D)}} \qquad \textbf{(2.15)}$$

Where r is the average grain radius, δ is a numerical factor, D_c and D is the diffusion coefficient of complexes and solute atoms respectively.

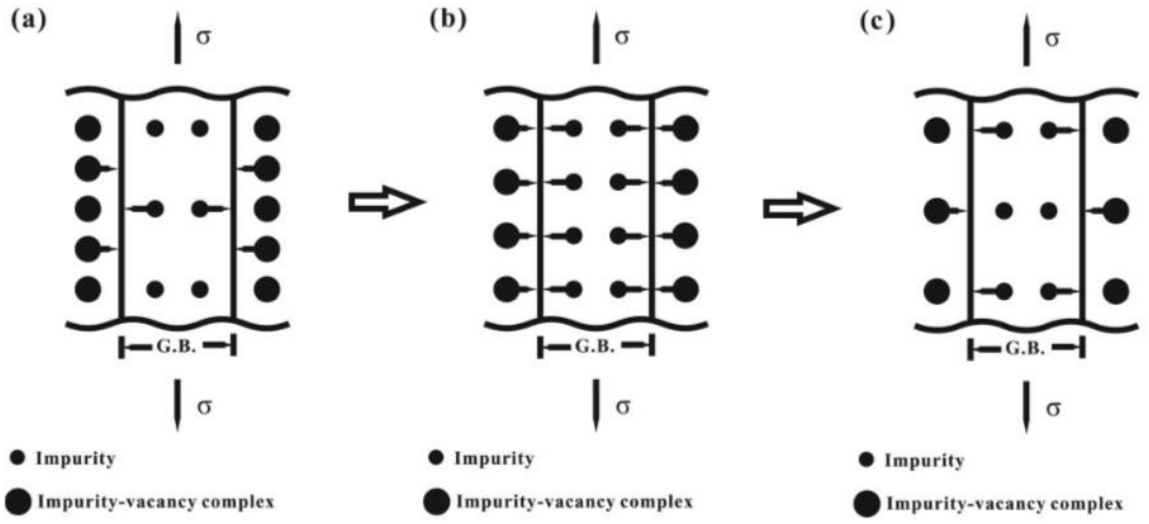


Figure 2.17: Schematic illustration of the thermally induced non-equilibrium grain boundary segregation. (a) During rapid cooling from high temperature: diffusion of impurity-vacancy complexes towards the grain boundary is dominant. (b) When the temperature increases: diffusion of complexes and impurities are accelerated and accumulation of the segregants are at maximum. (c) Further increment of the temperature: impurities back diffusion becomes dominant. Reproduced with permission from (Zheng et al., 2012). Copyright © 2012 Taylor & Francis.

Non-equilibrium segregation is very sensitive to the cooling rate as well as pre-deformation, and the degree of segregation can be much higher than equilibrium segregation (Lejček, 2010). Extensive studies on the kinetics of non-equilibrium segregation have been reported by Tingdong and Buyuan (Tingdong and Buyuan, 2004).

In 1972, Williams et al. (Williams, 1972, Williams et al., 1976) gave the first experimental results to confirm the existence of non-equilibrium grain boundary segregation of boron in steel. Segregation of boron to grain boundaries was noted when type-316 steel was solution treated at 1050°C and cooled in a stream of cold argon (~50°C/s). However, when the steel was water-quenched (~500°C/s), no segregation was observed. Therefore, this phenomenon is not equilibrium segregation, which is further confirmed by the fact that the higher the solution treatment temperatures, the greater the amount of boron segregated to grain boundaries after argon cooling.

Faulkner predicted that large grain size leads to more non-equilibrium segregation (Faulkner, 1981). If the concentration of quenched in vacancies is the same, the larger the grain size, the larger the flux

of C defects to each boundary. Coarser grains form fewer grain boundaries which then leads to an increased concentration of boron at grain boundaries for the same bulk boron content. Karlsson et al. (Karlsson et al., 1988, Karlsson, 1988) confirmed Faulkner's prediction for austenitic stainless steel. Figure 2.18 shows the boron ion micrographs of the same region obtained by SIMS and optical microscopy showing boron enrichment at boundaries and precipitates within grains. Certain twin grain boundaries were free of segregation, as circled in red. It has been pointed out by (Karlsson et al., 1988) that no segregation was found at special boundaries such as coherent twins but the majority of the grain boundaries showed the same intensity. In non-equilibrium segregation, the most important factor is the ability of the boundary to act as a vacancy sink.

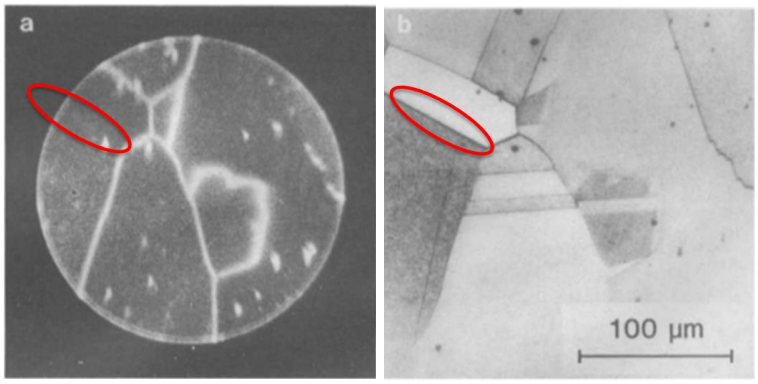


Figure 2.18: (a) SIMS image of $^{11}B^{16}O^-$ ions in steel cooled from 1250°C at 31°C/s, (b) Optical image taken after SIMS analysis. Red circle shows the twin grain boundary is free of segregation. Adapted with permission from (Karlsson et al., 1988). Copyright © 1988 Elsevier.

2.3.2 Quantification of Grain Boundary Segregation

In 1986, Hashimoto et al. (Hashimoto et al., 1987) used ion-implanted iron as standards to quantify trace boron in steels using SIMS (an IMF-3F CAMECA). The ion implantation technique was used because it can simply control the concentration of implanted elements and generate uniform dilute binary alloys. A large error of ±200% however was obtained in the calibration curve using the ion implantation standards ranging from per cent to parts per billion. The calibration curve of normalised boron intensity against the concentration in wt% obtained from SIMS depth profile is shown in Figure 2.19.

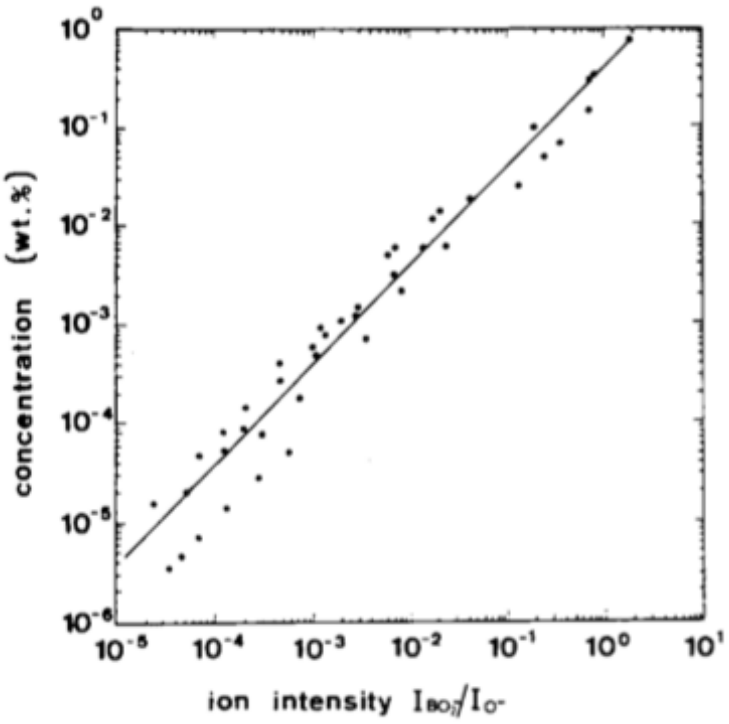


Figure 2.19: Calibration curve of boron obtained from the SIMS depth profile on boron implanted iron standards. Reproduced with permission from (Hashimoto et al., 1987). Copyright © 1987 Elsevier.

Quantitative analysis on equilibrium sulphur grain boundary segregation in nickel using the NanoSIMS has been demonstrated by Christien et al. (Christien et al., 2012). The sulphur grain boundary concentration decreases when the annealing temperature increases, following the thermodynamic models of equilibrium segregation, as shown in the NanoSIMS $^{32}S^-$ maps and sulphur concentration profiles in Figure 2.20.

Before an attempt to determine the S concentrations, depth profiles of nickel standards with sulphur concentrations (0.5, 38, 73 and 134 wt. ppm) were measured until steady state analytical conditions were reached, as shown in Figure 2.21. Accurate quantification can be achieved when this equilibrium is reached. Any analysis undertaken before this equilibrium region will not be quantitative and means that most static SIMS experiments can only be considered to be semi-quantitative.

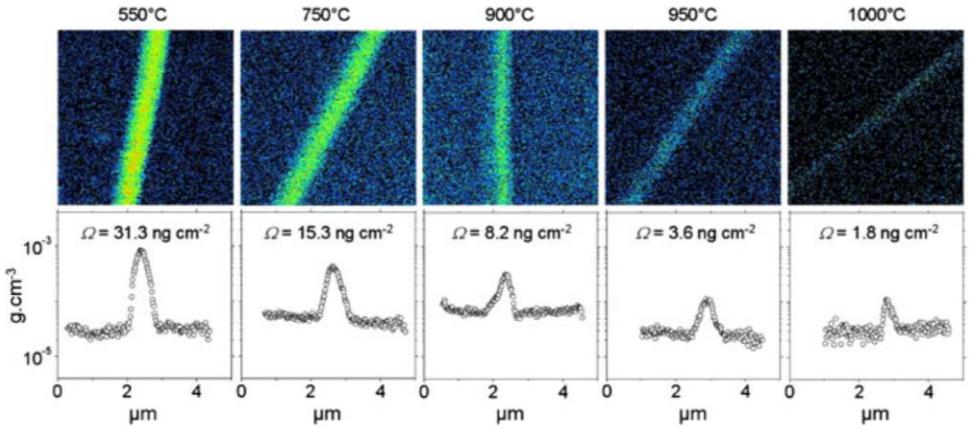


Figure 2.20: $^{32}S^-$ maps show the sulphur grain boundary equilibrium segregation on nickel and sulphur concentration profiles decrease with increasing annealing temperature from 550 to 1000°C. Ω is the grain boundary concentration in ng cm^{-2} (peak). Reproduced with permission from (Christien et al., 2012). Copyright © 2012 John Wiley and Sons.

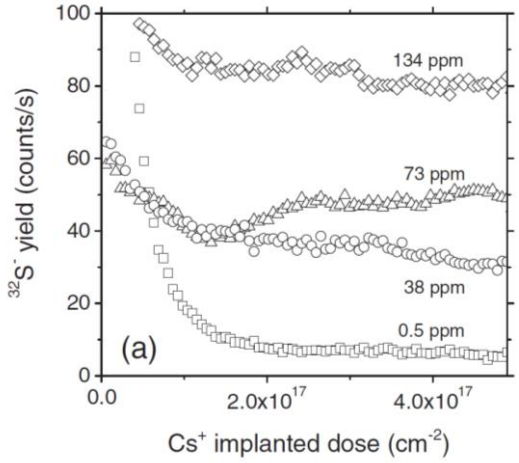


Figure 2.21: Sulphur NanoSIMS depth profiles on pure nickel standards with different bulk sulphur concentrations (0.5, 38, 73 and 134 wt ppm, respectively). Reproduced with permission from (Christien et al., 2012). Copyright © 2012 John Wiley and Sons.

Kim et al. (Kim et al., 2014a, Kim et al., 2014b) developed a new SIMS quantification technique using the CAMECA IMS 6F to understand the wear mechanism of friction stir welding (FSW) steels. To reduce the matrix effect in SIMS quantification, they used the ratio of cluster-polyatomic secondary ion species ($^{11}B^{16}O_2^-/^{56}Fe^{16}O^-$) to calibrate the secondary ion intensities of the B impurity in a steel matrix using four calibration standard reference materials.

More recently, Da Rosa et al. studied boron segregation in high-strength steels by quantifying both concentrations of boron atoms in solid solution in the grains and at the prior austenite grain boundaries using APT and NanoSIMS (Da Rosa et al., 2020). They used APT concentration measurements to calibrate the average NanoSIMS intensity in the grains. Da Rosa et al. pointed out that the RSF value for boron in the grain boundaries could be different from the grains due to the matrix effect on boron ionization, therefore the interfacial excess of solute should not be extracted from SIMS intensity profile across the grain boundary. However, taking this approach would lose the ability to analyse many more boundaries by SIMS than will ever be possible by APT, and also downplays the complexities involved in the very considerable calibration and estimation steps in extracting grain boundary segregation data from APT datasets.

2.3.3 Boron Grain Boundary Segregation Studies using SIMS or NanoSIMS

2.3.3.1 Steels

Table 2.2 summarises previously published studies of boron grain boundary segregation in a variety of steels using SIMS or NanoSIMS. In 1988, Karlsson et al. (1988) reported an extensive study on a large scale boron non-equilibrium segregation behaviour in austenitic stainless steels using a SIMS-IMS300. Kurban et al. (2006) studied the relationship between boron segregation and grain boundary character in Alloy 304 austenitic stainless steel using a SIMS-IMS 4F.

An early use of the NanoSIMS was by Lozano-Perez et al. (2008) where they studied trace elements segregation, including boron, in a stainless steel from a nuclear reactor. Two years later, Valle et al. (2011) used the NanoSIMS to study boron distribution and segregation at grain boundaries in high strength steels. They tried to identify B-based precipitates as borocarbides, boron nitrides or oxides by the overlays of the $^{11}B^-$, $^{11}B^{12}C^-$ and $^{11}B^{14}N^-$ maps. They interpreted the $^{11}B^{12}C^-$ signal as borocarbides and that precipitation was observed on the prior austenite grain boundaries in a Mo-free hot rolled sample. On the other hand, boron segregation was observed at prior austenite grain

boundaries in the Mo alloyed sample instead of B precipitation. No observations were reported to detect BN precipitates in these Ti-protected samples during hot rolling or after cooling, although BN precipitates were observed after welding in the weld area. However, questions remain unanswered on how does boron behaves with or without the addition of Ti in high strength steels during commercial industrial heat treatment (as-rolled, as-quenched, and quenched and tempered).

In the same year, Seol et al. (2011) reported a correlative study of boron segregation in a tempered HSLA steel containing 50 ppm boron using NanoSIMS, TEM and APT. Segregation of boron and borocarbides precipitates of approximately 2.5 μm in size were observed at the prior austenite grain boundaries. TEM confirmed the precipitates were $Fe_{23}(C,B)_6$, and APT revealed the boron concentration at the boundaries was approximately 1.7 ± 0.2 at.%. It is an advantage to use complementary techniques to obtain satisfactory results where one method alone usually does not provide enough information on the location or environment of the boron.

In the following year, Drillet et al. (2012) used NanoSIMS and TEM to study the evolution of boron and carbon at the austenite grain boundaries during hot rolling in high strength steels. This study also focused on the relationship of the boron precipitation and the final formability properties. Another observation was on the effect of tempering on the carbon in the martensite.

Another study of non-equilibrium boron segregation and boron precipitation behaviour in high strength steel which focused on the effects of cooling rate, austenitizing temperature and austenite deformation was done by Mun et al. (2012) using SIMS-IMS 6F. The effects of these variables were linked with the hardenability of the steel. Kang et al. (2014) used the same SIMS instrument to study the influence of boron on hot ductility of high Al, TWIP steels. They found that adding Ti to the steel can prevent BN and AlN precipitation and allows freedom of B to segregate at the grain boundaries, hence improve the ductility of the steel.

Table 2.2: Summary of boron grain boundary segregation studies using different type of SIMS or NanoSIMS in steels.

Materials	Instruments	Observation	Boron content	References
Low carbon boron steels	IMS 3F	Quantification of B by SIMS using ion implanted iron as standard.	10, 25, 40 ppm	(Hashimoto et al., 1987)
Austenitic stainless steel (AISI 316L)	IMS 300	Non-equilibrium B segregation study in austenitic stainless steel – large scale segregation behaviour.	1 – 40 ppm	(Karlsson et al., 1988)
Austenitic stainless steel (Alloy 304)	IMS 4F	Relationship between B segregation and grain boundary structure.	30 ppm	(Kurban et al., 2006)
Type 304 stainless steel (SUS304)	NanoSIMS 50	B segregation in stainless steel from nuclear reactor.	500 ppm	(Lozano-Perez et al., 2008)
HSLA steels	NanoSIMS 50	Correlative study of B segregation using NanoSIMS, APT and TEM.	50 ppm	(Seol et al., 2011)
High strength steels	NanoSIMS 50	Distribution of B in high strength steels.	20 – 40 ppm	(Valle et al., 2011)
High strength steels	NanoSIMS 50	Effect of B distribution during hot rolling.	20 ppm	(Drillet et al., 2012)
High strength steels	IMS 6F	Effects of cooling rate, austenitizing temperature and austenite deformation on the transformation behaviour of high strength steel.	20 ppm	(Mun et al., 2012)
TWIP steels	IMF 6F	Influence of B on hot ductility of high Al, TWIP steels.	17 – 26 ppm	(Kang et al., 2014)
FSW steels	IMF 6F	Quantification of B using SIMS.	1 – 110 ppm	(Kim et al., 2014a)
High strength steels	NanoSIMS 50	Correlative study of B segregation using NanoSIMS and APT	20 ppm	(Da Rosa et al., 2020)

There are three studies that have explored the quantification of boron in steels using SIMS or NanoSIMS. The first study of boron quantification in steels was done in 1987 by (Hashimoto et al., 1987) using ion implanted iron as a standard. Another attempt to quantify boron in steels was done in 2014 by (Kim et al., 2014a). Recently, Da Rosa et al. (Da Rosa et al., 2020) used the NanoSIMS and APT to quantify both boron in solution and at austenite grain boundaries. A review of quantification of grain boundary segregation using SIMS was presented in Section 2.3.2. The quantitative study of boron in high-strength steels using NanoSIMS from this thesis can be added to the list.

2.3.3.2 Nickel Based Superalloys

Addition of boron in small quantities can increase high temperature creep properties of polycrystalline superalloys due to its nature as grain boundary strengthener and preferentially residing at γ grain boundaries. A comprehensive review on the applications and metallurgy of Ni-

based superalloys, and the effect of boron and carbon as grain boundary strengthener will be discussed in Section 5.1.

Here, in Table 2.3 is a list of studies that have used SIMS or NanoSIMS to study the effect of boron in Ni-based superalloys. One of the earliest studies that used SIMS to study the effect of boron segregation in Ni-based superalloy (Inconel 718) was Huang et al. (1997). They relate the segregation effect with the microfisurring tendency in the heat affected zone (HAZ) and concluded that both equilibrium and non-equilibrium segregation occurred during heat treatment. On the other hand, Chen et al. (1998) concluded that the segregation of boron in the same type of alloy (Inconel 718) was mainly the non-equilibrium segregation. De-segregation of boron from grain boundaries was also observed at the beginning of the annealing process and promote the formation of borides due to resegregation and accumulation of complexes at grain boundaries.

Table 2.3: Summary of boron grain boundary segregation studies using different type of SIMS or NanoSIMS in Ni-based superalloys.

Materials	Instruments	Observation	Boron content	References
Ni-based superalloy – Inconel 718	IMS 4F	Effect of B segregation in alloy 718 on heat affected zones (HAZ) microfissuring	30 ppm	(Huang et al., 1997)
Ni-based superalloy – Inconel 718	IMS 4F	Non-equilibrium segregation of B	11, 43 ppm	(Chen et al., 1998)
Ni-based superalloy – Inconel 718	NanoSIMS 50	Segregation of B, P and C in Ni-based superalloy	110, 120 ppm	(Alam et al., 2012)
Ni-based superalloy – Alloy 263	NanoSIMS 50	Mechanism of serrated grain boundary formation	30 ppm	(Hong et al., 2012)

Alam et al. (2012) studied the segregation of boron, phosphorus and carbon in Ni-based superalloy (Inconel 718) using NanoSIMS and APT. The segregation behaviour of these elements was correlated with the weldability in the alloy, where they investigate the role of carbon to reduce the detrimental effect on weldability that is caused by boron and phosphorus. In the same year, Hong et al. (2012) used SEM, TEM and NanoSIMS to study the mechanism of serrated grain boundary formation in Ni-based alloy (Alloy 263).

2.4 Summary and Conclusions

The beginning of this review started with a brief introduction to the difficulties of detecting trace elements and impurity segregation in metals and the main techniques that have been used to study grain boundary segregation were discussed. This review has also covered the two key aspects related to the work presented in this thesis, a comprehensive discussion about secondary ion mass spectroscopy (SIMS) and boron hardenability effect and its relation to grain boundary segregation.

The purpose of this literature review has been to cover the most important research on boron grain boundary studies using SIMS and their limitations and provide new insights and answers to some scientific questions that have been outlined in section 1.2.

The capability of SIMS/NanoSIMS to investigate boron distribution in steels is outstanding. However, there are still some questions unanswered relating to the effect of boron on hardenability particularly the mechanisms that involve several stages of the steel manufacturing process i.e as-rolled, as-quenched, tempering and direct quenched. Further research is required to understand the protection of boron via Ti or Al and its effect on the hardenability of high strength steels. Some other questions that remain partly unanswered are how reheating time in the austenite region have an impact on the behaviour of boron in steels and what is the effect of Mo additions on boron distribution in steel.

All of the previous studies on Ni-based superalloys using SIMS have only observed boron segregation at grain boundaries. It is still not clear what the effect of boron as a grain boundary strengthener in Ni-based superalloys is due to boron segregated to the grain boundaries or alternatively as secondary phase particles such as M_3B_2 or M_5B_3. Thus, when designing new alloys, it is important to know the boron effect on the grain boundary character. A part of the work from this thesis using NanoSIMS to study boron at grain boundaries in a new polycrystalline superalloy is presented in Kontis et al. (2016) and will be reported in Chapter 5. The NanoSIMS is a complementary technique to SEM, APT and TEM used on the same alloys.

2.5 References

ADAMS, F. & MOENS, M. 1987. Recent developments in ion microscopy. *Spectrochimica Acta Part B: Atomic Spectroscopy,* 42**,** 1013-1025.

AKHURST, K. N., MCMAHON, C. J., BOATENG, A. & MACDONALD, D. D. 1980. Temper embrittlement and stress-corrosion cracking in steam-turbine rotor and disk steels. *Journal of Metals,* 32**,** 26-26.

ALAM, T., FELFER, P. J., CHATURVEDI, M., STEPHENSON, L. T., KILBURN, M. R. & CAIRNEY, J. M. 2012. Segregation of B, P, and C in the Ni-Based Superalloy, Inconel 718. *Metallurgical and Materials Transactions A,* 43**,** 2183-2191.

ALBER, U., MULLEJANS, H. & RUHLE, M. 1997. Improved quantification of grain boundary segregation by EDS in a dedicated STEM. *Ultramicroscopy,* 69**,** 105-116.

AUST, K. T. 1974. Selective segregation at grain boundaries. *Canadian Metallurgical Quarterly,* 13**,** 133-143.

BENNINGHOVEN, A. 1994. Surface analysis by Secondary Ion Mass Spectrometry (SIMS). *Surface Science,* 299-300**,** 246-260.

BENNINGHOVEN, A., RÜDENAUER, F. G. & WERNER, H. W. 1987 *Secondary ion mass spectrometry : basic concepts, instrumental aspects, applications, and trends,* New York, J. Wiley.

BISCONDI, M. 1982. Structure and mechanical-properties of grain-boundaries. *Journal De Physique,* 43**,** 293-310.

BOK SEOL, J., HO GU, G., SUK LIM, N., DAS, S. & GYUNG PARK, C. 2010. Atomic scale investigation on the distribution of boron in medium carbon steels by atom probe tomography and EELS. *Ultramicroscopy,* 110**,** 783-788.

BOXER, S. G., KRAFT, M. L. & WEBER, P. K. 2009. Advances in Imaging Secondary Ion Mass Spectrometry for Biological Samples. *Annual Review of Biophysics.*

BRIANT, C. L. & BANERJI, S. K. 1978. Intergranular failure in steel: the role of grain-boundary composition. *International Metals Reviews,* 23**,** 164-199199.

BRIGGS, D. & SEAH, M. P. 1983. *Practical surface analysis by Auger and X-ray photoelectron spectroscopy,* New York, John Wiley and Sons.

BRUEMMER, S. M., JONES, R. H., THOMAS, M. T. & BAER, D. R. 1980a. Fracture mode transition of iron in hydrogen as a function of grain-boundary sulfur. *Scripta Metallurgica,* 14**,** 137-141.

BRUEMMER, S. M., JONES, R. H., THOMAS, M. T. & BAER, D. R. 1980b. Sulfur induced fracture mode transition of nickel at cathodic potentials. *Scripta Metallurgica,* 14**,** 1233-1237.

CAMECA. 2008. *NanoSIMS 50/50L instrumentation booklet* [Online]. France. Available: http://www.cameca.com/literature/product-brochures.aspx [Accessed 30 September 2012].

CAMECA. 2017. *NanoSIMS 50L: NanoSIMS Instrumentation Booklet* [Online]. France. Available: https://www.cameca.com/products/sims/nanosims [Accessed 21 March 2021].

CAMERON, T. B. 1979. Methods of detecting boron in steel. *Journal of Metals,* 31**,** F31-F31.

CEREZO, A., GODFREY, T. J. & SMITH, G. D. W. 1988. Application of a position-sensitive detector to atom probe microanalysis. *Review of Scientific Instruments,* 59**,** 862-866.

CHEN, W., CHATURVEDI, M. C., RICHARDS, N. L. & MCMAHON, G. 1998. Grain boundary segregation of boron in INCONEL 718. *Metallurgical and Materials Transactions A,* 29**,** 1947-1954.

CHRISTIEN, F., BORJON-PIRON, Y., LE GALL, R. & SAILLET, S. 2010. Quantifying the effect of fracture surface topography on the scattering of grain boundary segregation measurement by Auger electron spectroscopy. *Materials Characterization,* 61**,** 73-84.

CHRISTIEN, F., DOWNING, C., MOORE, K. L. & GROVENOR, C. R. M. 2012. Quantification of grain boundary equilibrium segregation by NanoSIMS analysis of bulk samples. *Surface and Interface Analysis,* 44**,** 377-387.

CHRISTIEN, F., LE GALL, R. & SAINDRENAN, G. 2003. Synergetic effect of hardness and phosphorus grain-boundary segregation on the ductile-to-brittle transition temperature of 17-4 PH steel. *Metallurgical and Materials Transactions A: Physical Metallurgy and Materials Science,* 34 A**,** 2483-2491.

DA ROSA, G., MAUGIS, P., PORTAVOCE, A., DRILLET, J., VALLE, N., LENTZEN, E. & HOUMMADA, K. 2020. Grain-boundary segregation of boron in high-strength steel studied by nano-SIMS and atom probe tomography. *Acta Materialia,* 182**,** 226-234.

DANIEL, C., CHRISTIEN, F. & LE GALL, R. 2007. Intergranular fatigue cracking enhanced by impurity segregation. Vancouver.

DEMPSTER, A. J. 1918. A new Method of Positive Ray Analysis. *Physical Review,* 11**,** 316-325.

DOHERTY, J. E., GIAMEI, A. F. & KEAR, B. H. 1974. The importance of grain boundary morphology and cohesion on intergranular strength. *Canadian Metallurgical Quarterly,* 13**,** 229-236.

DOWSETT, M. G., ORMSBY, T. J., GARD, F. S., AL-HARTHI, S. H., GUZMAN, B., MCCONVILLE, C. F., NOAKES, T. C. Q. & BAILEY, P. 2003. Determination of the variation in sputter yield in the SIMS transient region using MEIS. *Applied Surface Science,* 203**,** 363-366.

DRILLET, J., VALLE, N. & IUNG, T. 2012. Nanometric Scale Investigation of Phase Transformations in Advanced Steels for Automotive Application. *Metallurgical and Materials Transactions A,* 43**,** 4947-4956.

DRUMMOND, I. W., OGDEN, L. P., STREET, F. J. & SURMAN, D. J. 1991. Methodology, performance, and application of an imaging x-ray photoelectron spectrometer. *Journal of Vacuum Science & Technology a-Vacuum Surfaces and Films,* 9**,** 1434-1440.

EAG LABORATORIES, E. 2017. *SIMS Tutorial: Theory: RSF Tables* [Online]. Eurofins Scientific. Available: https://www.eag.com/resources/tutorials/sims-tutorial-theory/ [Accessed 21 March 2021].

EGGELER, G. & DLOUHY, A. 2005. Boron segregation and creep in ultra-fine grained tempered martensite ferritic steels. *Zeitschrift Fur Metallkunde,* 96**,** 743-748.

FAULKNER, R. G. 1981. Non-equilibrium grain-boundary segregation in austenitic alloys. *Journal of Materials Science,* 16**,** 373-383.

FAULKNER, R. G. 1996. Segregation to boundaries and interfaces in solids. *International Materials Reviews,* 41**,** 198-208.

FUJIWARA, M., UCHIDA, H. & OHTA, S. 1994. Effect of boron and carbon on creep strength of cold-worked type 316 stainless-steel. *Journal of Materials Science Letters,* 13**,** 557-559.

GLEITER, H. 1970. The segregation of copper at high angle grain boundaries in lead. *Acta Metallurgica,* 18**,** 117-121.

GLEITER, H. & CHALMERS, B. 1972. High-angle grain-boundaries. *Progress in Materials Science,* 16**,** 1-&.

GUERQUIN-KERN, J. L., WU, T. D., QUINTANA, C. & CROISY, A. 2005. Progress in analytical imaging of the cell by dynamic secondary ion mass spectrometry (SIMS microscopy). *Biochimica Et Biophysica Acta-General Subjects,* 1724**,** 228-238.

GUTTMANN, M. 1975. Equilibrium segregation in a ternary solution - model for temper embrittlement. *Surface Science,* 53**,** 213-227.

HANNINEN, H. & MINNI, E. 1982. On grain-boundary segregation in austenitic stainless-steels. *Metallurgical Transactions a-Physical Metallurgy and Materials Science,* 13**,** 2281-2285.

HASHIMOTO, M., ISHIDA, Y., YAMAMOTO, R., DOYAMA, M. & FUJIWARA, T. 1984. Atomic and electronic-structures of a grain-boundary in iron with impurity segregation. *Surface Science,* 144**,** 182-195.

HASHIMOTO, S., DOI, S., TAKAHASHI, K., TERASAKA, M. & IWAKI, M. 1987. Quantitative analysis of boron in steel by secondary ion mass spectrometry using ion-implanted iron as standard. *Materials Science and Engineering,* 90**,** 119-125.

HASLBERGER, P., TURK, C., BABINSKY, K., CALISKANOGLU, D., CLEMENS, H. & PRIMIG, S. 2015. Boron Grain Boundary Segregation in a Heat Treatable Steel. *BHM Berg- und Hüttenmännische Monatshefte,* 160**,** 204-208.

HERBIG, M., RAABE, D., LI, Y. J., CHOI, P., ZAEFFERER, S. & GOTO, S. 2014. Atomic-Scale Quantification of Grain Boundary Segregation in Nanocrystalline Material. *Physical Review Letters,* 112**,** 126103.

HIPPSLEY, C. A., RAUH, H. & BULLOUGH, R. 1984. Stress-driven solute enrichment of crack-tips during low-ductility intergranular fracture of low-alloy steel. *Acta Metallurgica,* 32**,** 1381-1394.

HOEX, B. 2018. *Time of flight secondary ion mass spectroscopy (Tof-SIMS)* [Online]. Sydney: UNSW Sydney. Available: https://pv-manufacturing.org/metrology/time-of-flight-secondary-ion-mass-spectroscopy-tof-sims/ [Accessed March 21 2021].

HOFFMANN, E. D. & STROOBANT, V. 2007. *Mass spectrometry : principles and applications* Chichester, Wiley

HOFMANN, J. P., ROHNKE, M. & WECKHUYSEN, B. M. 2014. Recent advances in secondary ion mass spectrometry of solid acid catalysts: large zeolite crystals under bombardment. *Physical Chemistry Chemical Physics,* 16**,** 5465-5474.

HOFMANN, S. 1990. Segregation at grain boundaries. *In:* DOWBEN, P. A. & MILLER, A. (eds.) *Surface Segregation Phenomena.* Boca Raton, Florida: CRC Press.

HOFMANN, S. & LEJČEK, P. 1996. Solute segregation at grain boundaries. *Interface Science,* 3**,** 241-267.

HOFMANN, S., ZHOU, G., KOVAC, J., DREV, S., LIAN, S. Y., LIN, B., LIU, Y. & WANG, J. Y. 2019. Preferential sputtering effects in depth profiling of multilayers with SIMS, XPS and AES. *Applied Surface Science,* 483**,** 140-155.

HONG, H. U., KIM, I. S., CHOI, B. G., YOO, Y. S. & JO, C. Y. 2012. On the Mechanism of Serrated Grain Boundary Formation in Ni-Based Superalloys with Low γ′ Volume Fraction. *Superalloys 2012.*

HORREARD, F. 2000. Recent developments in SIMS instrumentation. *Elektronika,* 41**,** 7-1010.

HUANG, X., CHATURVEDI, M. C., RICHARDS, N. L. & JACKMAN, J. 1997. The effect of grain boundary segregation of boron in cast alloy 718 on HAZ microfissuring—A SIMS analysis. *Acta Materialia,* 45**,** 3095-3107.

ISHIKAWA, S., PFAENDTNER, J. A. & MCMAHON, C. J. 1999. The effect of boron on stress-relief cracking of alloy steels. *Materials Science and Engineering a-Structural Materials Properties Microstructure and Processing,* 272**,** 16-23.

JOSHI, A. 1975. Segregation at selective grain boundaries and its role in temper embrittlement of low alloy steels. *Scripta Metallurgica,* 9**,** 251-260.

KANG, S. E., BANERJEE, J. R., TULING, A. S. & MINTZ, B. 2014. Influence of B on hot ductility of high Al, TWIP steels. *Materials Science and Technology (United Kingdom),* 30**,** 486-494.

KAPADIA, B. M. 1987. Effect of boron additions on the toughness of heat-treated low-alloy steels. *Journal of Heat Treating,* 5**,** 41-53.

KARLSSON, L. 1988. Overview no. 63 Non-equilibrium grain boundary segregation of boron in austenitic stainless steel—III. Computer simulations. *Acta Metallurgica,* 36**,** 25-34.

KARLSSON, L. & NORDEN, H. 1986. Grain boundary segregation of boron. An experimental and theoretical study. *Le Journal de Physique Colloques,* 47**,** C7-257-C7-262.

KARLSSON, L. & NORDÉN, H. 1988. Overview no. 63 Non-equilibrium grain boundary segregation of boron in austenitic stainless steel-II. Fine scale segregation behaviour. *Acta Metallurgica,* 36**,** 13-24.

KARLSSON, L., NORDÉN, H. & ODELIUS, H. 1988. Overview no. 63 Non-equilibrium grain boundary segregation of boron in austenitic stainless steel—I. Large scale segregation behaviour. *Acta Metallurgica,* 36**,** 1-12.

KARNEY, G. B., BUTLER, P. G., SPELLER, S., SCOURSE, J. D., RICHARDSON, C. A., SCHROEDER, M., HUGHES, G. M., CZERNUSZKA, J. T. & GROVENOR, C. R. M. 2012. Characterizing the microstructure of Arctica islandica shells using NanoSIMS and EBSD. *Geochemistry Geophysics Geosystems,* 13.

KEAST, V. J. & WILLIAMS, D. B. 2001. Grain boundary chemistry. *Current Opinion in Solid State & Materials Science,* 5**,** 23-30.

KICMAN, A. T., PARKIN, M. C. & ILES, R. K. 2007. An introduction to mass spectrometry based proteomics—Detection and characterization of gonadotropins and related molecules. *Molecular and Cellular Endocrinology,* 260-262**,** 212-227.

KIM, J., LEE, S., KWUN, H., SHIN, K. & KANG, C. 2014a. Identifying of boron in FSW steel samples through SIMS technology. *Journal of Surface Analysis,* 20**,** 192-197.

KIM, J., LEE, S., KWUN, H., SHIN, K. & KANG, C. 2014b. SIMS evaluation of poly crystal boron nitride tool effect in thermo-mechanically affected zone of friction stir weld steels. *Metals and Materials International,* 20**,** 1067-1071.

KITA, N. T., USHIKUBO, T., FU, B. & VALLEY, J. W. 2009. High precision SIMS oxygen isotope analysis and the effect of sample topography. *Chemical Geology,* 264**,** 43-57.

KONARSKI, P., IWANEJKO, I. & MIERZEJEWSKA, A. 2003. SIMS depth profiling of working environment nanoparticles. *Applied Surface Science,* 203–204**,** 757-761.

KONTIS, P., ALABORT, E., BARBA, D., COLLINS, D. M., WILKINSON, A. J. & REED, R. C. 2017. On the role of boron on improving ductility in a new polycrystalline superalloy. *Acta Materialia,* 124**,** 489-500.

KONTIS, P., YUSOF, H. A. M., PEDRAZZINI, S., DANAIE, M., MOORE, K. L., BAGOT, P. A. J., MOODY, M. P., GROVENOR, C. R. M. & REED, R. C. 2016. On the effect of boron on grain boundary character in a new polycrystalline superalloy. *Acta Materialia,* 103**,** 688-699.

KRAHE, P. R. & GUTTMANN, M. 1974. Temper brittleness and grain boundary etching. *Metallography,* 7**,** 5-17.

KRAKAUER, B. W. & SEIDMAN, D. N. 1993. Absolute atomic-scale measurements of the gibbsian interfacial excess of solute at internal interfaces. *Physical Review B,* 48**,** 6724-6727.

KURBAN, M., ERB, U. & AUST, K. T. 2006. A grain boundary characterization study of boron segregation and carbide precipitation in alloy 304 austenitic stainless steel. *Scripta Materialia,* 54**,** 1053-1058.

LADNA, B. & BIRNBAUM, H. K. 1988. Surface and grain boundary segregation of sulfur and boron in nickel. *Acta Metallurgica,* 36**,** 745-755.

LAHA, K., KYONO, J. & SHINYA, N. 2012. Copper, Boron, and Cerium Additions in Type 347 Austenitic Steel to Improve Creep Rupture Strength. *Metallurgical and Materials Transactions a-Physical Metallurgy and Materials Science,* 43A**,** 1187-1197.

LARERE, A., GUTTMANN, M., DUMOULIN, P. & ROQUES-CARMES, C. 1982. Auger electron spectroscopy study of the kinetics of intergranular and surface segregations in nickel during annealing. *Acta Metallurgica,* 30**,** 685-693.

LATY, P., SEETHANEN, D. & DEGREVE, F. 1979. Microroughness induced on solids by ion-bombardment .1. Experimental results on sputtering of aluminum by A+(15 kev) - quantification of microroughness. *Surface Science,* 85**,** 353-364.

LEJČEK, P. 2010. Grain Boundary Segregation in Metals. Berlin, Heidelberg: Springer Berlin Heidelberg.

LEJCEK, P. & HOFMANN, S. 1994. Auger electron spectroscopy on both fracture surfaces of an (001)/(011) asymmetrical grain boundary. *Surface Science,* 307-309**,** 798-803.

LEJČEK, P. & HOFMANN, S. 1995. Thermodynamics and structural aspects of grain-boundary segregation. *Critical Reviews in Solid State and Materials Sciences,* 20**,** 1-85.

LI, C. & WILLIAMS, D. B. 2003. Application of automated crystallography for transmission electron microscopy in the study of grain-boundary segregation. *Micron,* 34**,** 199-209.

LI, T., WU, T.-D., MAZEAS, L., TOFFIN, L., GUERQUIN-KERN, J.-L., LEBLON, G. & BOUCHEZ, T. 2008. Simultaneous analysis of microbial identity and function using NanoSIMS. *Environmental Microbiology,* 10**,** 580-588.

LIEBL, H. 1975. Ion probe microanalysis. *Journal of Physics E: Scientific Instruments,* 8**,** 797-808.

LIU, C. M., NAGOYA, T., ABIKO, K. & KIMURA, H. 1992. Effect of boron on the grain boundary segregation of phosphorus and intergranular fracture in high-purity Fe-0.2 Pct P-B alloys. *Metallurgical Transactions A,* 23**,** 263-269.

LOZANO-PEREZ, S. 2008. Novel characterization of stress corrosion cracks. *In:* BAKER, R. T., MOBUS, G. & BROWN, P. D. (eds.) *Emag: Electron Microscopy and Analysis Group Conference 2007.*

LOZANO-PEREZ, S., SCHRODER, M., YAMADA, T., TERACHI, T., ENGLISH, C. A. & GROVENOR, C. R. M. 2008. Using NanoSIMS to map trace elements in stainless steels from nuclear reactors. *Applied Surface Science,* 255**,** 1541-1543.

LOZANO-PEREZ, S., YAMADA, T., TERACHI, T., SCHROEDER, M., ENGLISH, C. A., SMITH, G. D. W., GROVENOR, C. R. M. & EYRE, B. L. 2009. Multi-scale characterization of stress corrosion cracking of cold-worked stainless steels and the influence of Cr content. *Acta Materialia,* 57**,** 5361-5381.

LYMAN, C. E., WILLIAMS, D. B. & GOLDSTEIN, J. I. 1989. X-ray detectors and spectrometers. *Ultramicroscopy,* 28**,** 137-149.

MALHERBE, J., PENEN, F., ISAURE, M.-P., FRANK, J., HAUSE, G., DOBRITZSCH, D., GONTIER, E., HORRÉARD, F., HILLION, F. & SCHAUMLÖFFEL, D. 2016. A New Radio Frequency Plasma Oxygen Primary Ion Source on Nano Secondary Ion Mass Spectrometry for Improved Lateral Resolution and Detection of Electropositive Elements at Single Cell Level. *Analytical Chemistry,* 88**,** 7130-7136.

MCLEAN, D. 1957. *Grain boundaries in metals,* Oxford, Clarendon Press.

MCMAHON, C. J. & TRUAX, D. J. 1973. Mechanisms of stress-corrosion cracking of titanium-aluminum alloys in methanol-hcl solutions. *Corrosion,* 29**,** 47-55.

MCMAHON JR, C. J. 2003. Comment on "The role of non-equilibrium segregation in impurity segregation in steels". *Scripta Materialia,* 49**,** 1215-1217.

MEGA, T., SHIMOMURA, J.-I. & SETO, K. 1996. Grain Boundary Segregation of Phosphorus, Boron and Manganese in High Tensile Strength Steel Sheet. *Materials Transactions, JIM,* 37**,** 323-329.

MILLER, P. E. & DENTON, M. B. 1986. The quadrupole mass filter: Basic operating concepts. *Journal of Chemical Education,* 63**,** 617.

MOLOZNIK, K. L., BRIANT, C. L. & MCMAHON, C. J. 1979. Effect of grain-boundary impurities on the stress-corrosion cracking of a low-alloy steel. *Corrosion,* 35**,** 331-332.

MOORE, K. L. 2011. *High resolution secondary ion mass spectrometry analysis of trace elements in cereal grain and roots.* DPhil, University of Oxford.

MOORE, K. L., SCHRÖDER, M. & GROVENOR, C. R. M. 2012. Imaging Secondary Ion Mass Spectroscopy. *In:* TENDELOO, G. V., DYCK, D. V. & PENNYCOOK, S. J. (eds.) *Handbook of Nanoscopy.*

MOSTEFA, L. B., SAINDRENAN, G., BARBOUTH, N., BRASS, A. M. & CHENE, J. 1990. Intergranular segregation of sulfur in the Fe-Ni 36 alloys. *Scripta Metallurgica et Materialia,* 24**,** 773-777.

MULFORD, R. A., MCMAHON, C. J., POPE, D. P. & FENG, H. C. 1976. Temper embrittlement of Ni-Cr steels by phosphorus. *Metallurgical Transactions a-Physical Metallurgy and Materials Science,* 7**,** 1183-1195.

MULLER, D. A., SUBRAMANIAN, S., BATSON, P. E., SILCOX, J. & SASS, S. L. 1996. Structure, chemistry and bonding at grain boundaries in Ni3Al .1. The role of boron in ductilizing grain boundaries. *Acta Materialia,* 44**,** 1637-1645.

MUN, D. J., SHIN, E. J., CHOI, Y. W., LEE, J. S. & KOO, Y. M. 2012. Effects of cooling rate, austenitizing temperature and austenite deformation on the transformation behavior of high-strength boron steel. *Materials Science and Engineering a-Structural Materials Properties Microstructure and Processing,* 545**,** 214-224.

NAUDIN, C., FRUND, J. M. & PINEAU, A. 1999. Intergranular fracture stress and phosphorus grain boundary segregation of a Mn-Ni-Mo steel. *Scripta Materialia,* 40**,** 1013-1019.

O'CONNOR, D. J., SEXTON, B. A. & SMART, R. S. C. 1992. *Surface analysis methods in materials science,* Berlin, Springer-Verlag.

OEHLER, D. Z., ROBERT, F., MOSTEFAOUI, S., MEIBOM, A., SELO, M. & MCKAY, D. S. 2006. Chemical mapping of proterozoic organic matter at submicron spatial resolution. *Astrobiology,* 6**,** 838-850.

OEHLER, D. Z., ROBERT, F., WALTER, M. R., SUGITANI, K., MEIBOM, A., MOSTEFAOUI, S. & GIBSON, E. K. 2010. Diversity in the Archean Biosphere: New Insights from NanoSIMS. *Astrobiology,* 10**,** 413-424.

OGURA, T., MCMAHON, C. J., FENG, H. C. & VITEK, V. 1978. Structure-dependent intergranular segregation of phosphorus in austenite in a Ni-Cr steel. *Acta Metallurgica,* 26**,** 1317-1330.

OXFORD NANOSIMS, G. 2010. *NanoSIMS: The Instruments: Ion optical setup* [Online]. Oxford. Available: http://nanosims.materials.ox.ac.uk/nanosimshome/instrument.html [Accessed March 21 2021].

PHYTHIAN, W. J. & ENGLISH, C. A. 1993. Microstructural evolution in-reactor pressure-vessel steels. *Journal of Nuclear Materials,* 205**,** 162-177.

REDDY, S. M., SAXEY, D. W., RICKARD, W. D. A., FOUGEROUSE, D., MONTALVO, S. D., VERBERNE, R. & VAN RIESSEN, A. 2020. Atom Probe Tomography: Development and Application to the Geosciences. *Geostandards and Geoanalytical Research,* 44**,** 5-50.

RUDENAUER, F. G. 1982. Secondary ion mass spectrometry; future prospects. *International Journal of Mass Spectrometry and Ion Physics,* 45**,** 355-366.

SEAH, M. & HONDROS, E. Grain boundary segregation. Proceedings of the Royal Society of London A: Mathematical, Physical and Engineering Sciences, 1973a. The Royal Society, 191-212.

SEAH, M. P. & HONDROS, E. D. 1973b. Grain-boundary segregation. *Proceedings of the Royal Society of London Series a-Mathematical Physical and Engineering Sciences,* 335**,** 191-212.

SEOL, J.-B., LEE, B. H., CHOI, P., LEE, S. G. & PARK, C. G. 2013. Combined nano-SIMS/AFM/EBSD analysis and atom probe tomography, of carbon distribution in austenite/ε-martensite high-Mn steels. *Ultramicroscopy,* 132**,** 248-257.

SEOL, J. B., LIM, N. S., LEE, B. H., RENAUD, L. & PARK, C. G. 2011. Atom probe tomography and nano secondary ion mass spectroscopy investigation of the segregation of boron at austenite grain boundaries in 0.5 wt.% carbon steels. *Metals and Materials International,* 17**,** 413-416.

SHARMA, M., ORTLEPP, I. & BLECK, W. 2019. Boron in Heat-Treatable Steels: A Review. *Steel Research International,* 90.

SHEN, Y. & HANSEN, S. S. 1997. Effect of the Ti/N ratio on the hardenability and mechanical properties of a quenched-and-tempered C-Mn-B steel. *Metallurgical and Materials Transactions A,* 28**,** 2027-2035.

SHIN, J. & MCMAHON JR, C. J. 1984. Mechanisms of stress relief cracking in a ferritic steel. *Acta Metallurgica,* 32**,** 1535-1552.

SHIN, K. S. & MESHII, M. 1983a. Effect of sulfur segregation and hydrogen charging on intergranular fracture of iron. *Acta Metallurgica,* 31**,** 1559-1566.

SHIN, K. S. & MESHII, M. 1983b. Effects of sulfur and hydrogen on intergranular fracture of iron. *Journal of Metals,* 35**,** 91-91.

SHIN, K. S. & MESHII, M. 1983c. Intergranular fracture in iron due to the presence of sulfur segregation and permanent hydrogen damage. *Scripta Metallurgica,* 17**,** 1121-1124.

SIMCOE, C. R., ELSEA, A. R. & MANNING, G. K. 1955. Study of the Effect of Boron on The Decomposition of Austenite. *JOM,* 7**,** 193-200.

SLODZIAN, G., DAIGNE, B., GIRARD, F., BOUST, F. & HILLION, F. 1992. Scanning secondary ion analytical microscopy with parallel detection. *Biology of the Cell,* 74**,** 43-50.

SONG, X. L., YUAN, Z. X., JIA, J., LI, P. H., WANG, D. & FAN, L. X. 2011. Boron and Phosphorus Segregation Behavior at Grain Boundary in a Ti-If Steel after Annealing. *Advanced Materials Research,* 152-153**,** 320-325.

STADERMANN, F. J., WALKER, R. M. & ZINNER, E. 1999. Nanosims: The next generation ion probe for the microanalysis of extraterrestrial material. *Meteoritics & Planetary Science,* 34**,** A111-A112.

STARK, Y., FRÖMTER, R., STICKLER, D. & OEPEN, H. P. 2009. Sputter yields of single- and polycrystalline metals for application in focused ion beam technology. *Journal of Applied Physics,* 105**,** 013542.

SUGITANI, K., GREY, K., NAGAOKA, T. & MIMURA, K. 2009. Three-Dimensional Morphological and Textural Complexity of Archean Putative Microfossils from the Northeastern Pilbara Craton: Indications of Biogenicity of Large (> 15 mu m) Spheroidal and Spindle-Like Structures. *Astrobiology,* 9**,** 603-615.

SWINDEMAN, R. W., SIKKA, V. K. & KLUEH, R. L. 1983. Residual and trace-element effects on the high-temperature creep strength of austenitic stainless-steels. *Metallurgical Transactions a-Physical Metallurgy and Materials Science,* 14**,** 581-593.

TANZI, M. C., FARÈ, S. & CANDIANI, G. 2019. Chapter 7 - Techniques of Analysis. *In:* TANZI, M. C., FARÈ, S. & CANDIANI, G. (eds.) *Foundations of Biomaterials Engineering.* Academic Press.

TEHOVNIK, F., VODOPIVEC, F., CELIN, R., ARZENSEK, B. & GONTAREV, J. 2011. Effect of delta-ferrite, lead and sulphur on hot workability of austenitic stainless steels with solidification structure. *Materials Science and Technology,* 27**,** 774-782.

THOMAS, W. R. & CHALMERS, B. 1955. The segregation of impurities to grain boundaries. *Acta Metallurgica,* 3**,** 17-21.

THOMSON, J. J. 1910. LXXXIII. Rays of positive electricity. *The London, Edinburgh, and Dublin Philosophical Magazine and Journal of Science,* 20**,** 752-767.

TINGDONG, X. 1987. Non-equilibrium grain-boundary segregation kinetics. *Journal of Materials Science,* 22**,** 337-345.

TINGDONG, X. 2006. Critical time for Mg grain-boundary segregation in Ni-Cr-Co alloy. *Philosophical Magazine Letters,* 86**,** 501-510.

TINGDONG, X. & BUYUAN, C. 2004. Kinetics of non-equilibrium grain-boundary segregation. *Progress in Materials Science,* 49**,** 109-208.

TOMITA, M., KOIKE, M., AKUTSU, H., TAKENO, S., KAWAMURA, Y., SHIMIZU, Y., UEMATSU, M. & ITOH, K. M. 2012. Investigation of the factors determining the SIMS depth resolution in silicon-isotope multiple layers. *Journal of Vacuum Science & Technology B,* 30.

UENO, M. & ITOH, K. 1988. Optimum condition to obtain the maximum hardenability effect of boron. *Tetsu-To-Hagane/Journal of the Iron and Steel Institute of Japan,* 74**,** 910-917.

VALLE, N., DRILLET, J., PIC, A. & MIGEON, H. N. 2011. Nano-SIMS investigation of boron distribution in steels. *Surface and Interface Analysis,* 43**,** 573-575.

VAN DER HEIDE, P. 2014. *Secondary Ion Mass Spectrometry: An Introduction to Principles and Practices,* Wiley.

VAN DER HEIDE, P. A. W., LIM, M. S., PERRY, S. S. & BENNETT, J. 2003. A systematic study of the surface roughening and sputter rate variations occurring during SIMS ultrashallow depth profile analysis of Si with Cs+. *Nuclear Instruments and Methods in Physics Research Section B: Beam Interactions with Materials and Atoms,* 201**,** 413-425.

VICKERMAN, J. C. 2009. Molecular Surface Mass Spectrometry by SIMS. *In:* VICKERMAN, J. C. & GILMORE, I. S. (eds.) *Surface Analysis – The Principal Techniques.*

VICKERMAN, J. C., REED, N. & BROWN, A. 1989. Secondary Ion Mass Spectroscopy: Principles and Applications(Retroactive Coverage). *Oxford University Press, 1989***,** 341.

WAGNER, M. 2009. Single-Cell Ecophysiology of Microbes as Revealed by Raman Microspectroscopy or Secondary Ion Mass Spectrometry Imaging. *Annual Review of Microbiology.*

WATANABE, S., OHTANI, H. & KUNITAKE, T. 1983. The Influence of Hot Rolling and Heat Treatments on the Distribution of Boron in Steel. *Transactions of the Iron and Steel Institute of Japan,* 23**,** 31-37.

WATANABE, T. 1985. Structural effects on grain-boundary segregation, hardening and fracture. *Journal De Physique,* 46**,** 555-566.

WATANABE, T., KITAMURA, S. & KARASHIMA, S. 1980. Grain boundary hardening and segregation in alpha Iron-Tin alloy. *Acta Metallurgica,* 28**,** 455-463.

WESTBROOK, J. H. 1964. Segregation at grain boundaries. *International Materials Reviews,* 9**,** 415-471.

WESTBROOK, J. H. & AUST, K. T. 1963. Solute hardening at interfaces in high-purity lead .1. grain and twin boundaries. *Acta Metallurgica,* 11**,** 1151-&.

WILLIAMS, T. M. 1972. The segregation and effects of boron in an austenitic stainless steel. *Metal Science Journal,* 6**,** 68-9.

WILLIAMS, T. M., STONEHAM, A. M. & HARRIES, D. R. 1976. The segregation of boron to grain boundaries in solution-treated type 316 austenitic stainless steel. *Metal Science,* 10**,** 14-19.

WILSON, R. G., MAGEE, C. W. & STEVIE, F. A. 1989. *Secondary ion mass spectrometry : a practical handbook for depth profiling and bulk impurity analysis,* New York, Wiley.

WU, J., SONG, S. H., WENG, L. Q., XI, T. H. & YUAN, Z. X. 2008. An Auger electron spectroscopy study of phosphorus and molybdenum grain boundary segregation in a 2.25Cr1Mo steel. *Materials Characterization,* 59**,** 261-265.

YU, M. L. 1982. Matrix effects in the work-function dependence of negative-secondary-ion emission. *Physical Review B,* 26**,** 4731-4734.

ZHENG, L., SCHMITZ, G., MENG, Y., CHELLALI, R. & SCHLESIGER, R. 2012. Mechanism of Intermediate Temperature Embrittlement of Ni and Ni-based Superalloys. *Critical Reviews in Solid State and Materials Sciences,* 37**,** 181-214.

3 Experimental Techniques

3.1 Introduction

This chapter gives an overview of the sample preparation and experimental techniques and instruments used to carry out the work reported in this thesis. A variety of techniques have been used, such as optical microscopy, Secondary Electron Microscopy (SEM) and Electron Backscatter Diffraction (EBSD), and I have developed techniques to allow several of these to be applied to the same area of the samples. The main technique used was high-resolution Secondary Ion Mass Spectrometry (SIMS), more specifically the Cameca NanoSIMS 50, and this will therefore be described in more detail, especially with regard to general instrument alignment for the reliable analysis of metallic alloys. Detailed descriptions of the heat treatment processes of the different materials and sample-specific NanoSIMS alignment protocols will be presented in the following results chapters.

3.2 Sample Preparation

Most of the samples used in this thesis were supplied as large plates as shown in Figure 3.1 (a), which meant that they were too large to fit into the NanoSIMS holders. Samples were cut and clamped on precision vices prior detailed cutting using a BUEHLER IsoMet 5000 precision cutter to a size of 7.3 x 7.3 x 4 mm. The diamond blade selected was of a specific type, IsoCut CBN, and used for steel and nickel-based superalloy materials. The cutting process is presented in Figure 3.1 (b), (c) and (d).

The cross sections were then ground with silicon carbide paper up to 1200 grit and polished with diamond paste down to a particle size of 1 μm. Areas of interest were marked using microindentation so that exactly the same region of the sample could be analysed with optical, EBSD and NanoSIMS.

A typical NanoSIMS sample with dimensions 7.3 x 7.3 x 4 mm and alignment microindents is shown in Figure 3.2.

Steel samples were etched with 2% Nital (2 ml HNO_3 + 98 ml Ethyl alcohol) and the nickel-based superalloy samples were etched with Kalling's no. 2 (2 gram copper chloride + 50 ml HCl + 50 ml methanol) to reveal the microstructure for examination with optical microscopy or SEM. Before EBSD and NanoSIMS analysis, the samples were gently ground again with 4000 grade silicon carbide paper to remove the roughness caused by the etching process (without removing the microindents), and repolished with diamond paste down to a particle size of 1 μm. As a final step, the samples requiring EBSD analysis were polished with colloidal silica. The samples were loaded into a standard (biology) NanoSIMS holder as shown in Figure 3.3, which can hold 8 samples or standards for instrumental tuning.

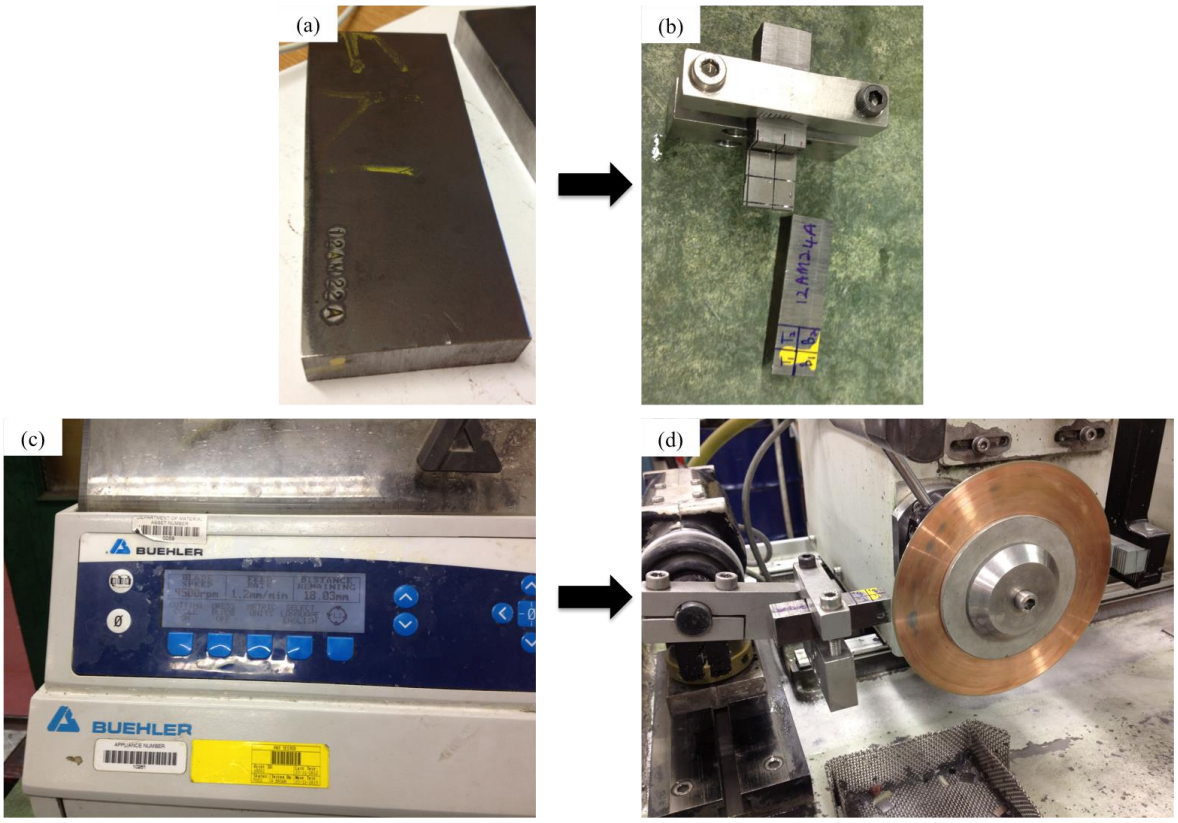


Figure 3.1: (a) A typical large sample bar received from my collaborators; (b) samples were clamped and cut on precision vices; (c) A BUEHLER IsoMet 5000 was set to cut a sample with the dimensions 7.3 x 7.3 x 4 cm; (d) the samples were cut using a IsoCut CBN diamond blade specifically selected for Fe and Ni-based superalloy materials.

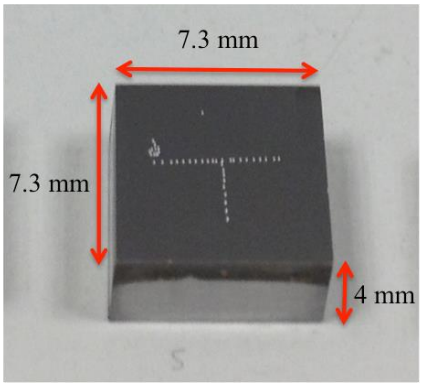


Figure 3.2: Typical NanoSIMS sample with dimensions allowing it to be loaded into the NanoSIMS holder. Microindents can be seen across the surface allowing for correlation between NanoSIMS, EBSD and optical microscopy.

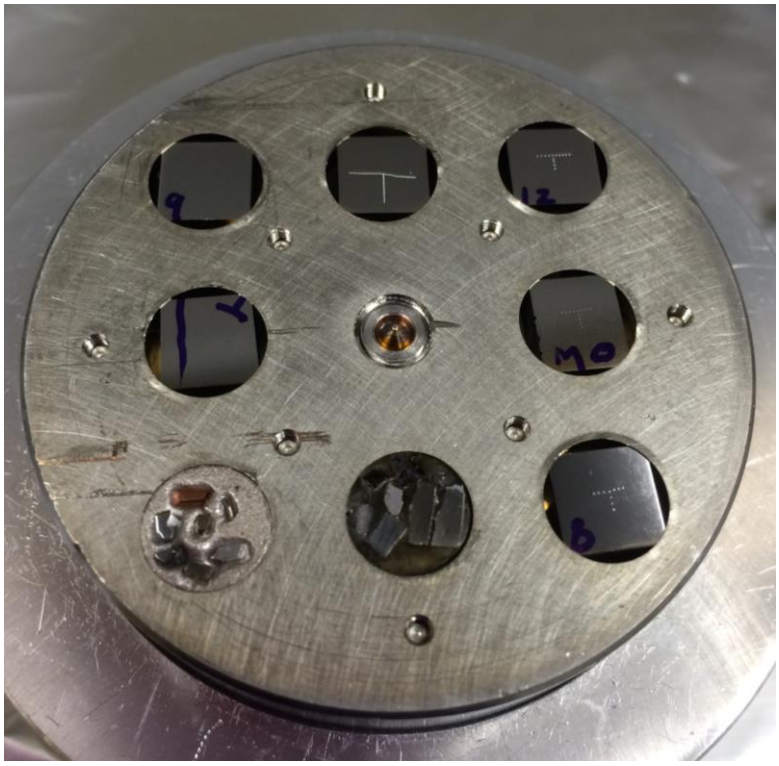


Figure 3.3: NanoSIMS (biology) sample holder with samples and standards loaded. Details of the standards used is presented in section 3.3.

3.3 Standards for NanoSIMS Analysis

As the bulk concentration of some elements in the alloys studied was very low it was necessary to load standards of pure material alongside the samples in order to ensure that the correct peak was chosen during NanoSIMS analysis. Several standards (B, BN, BNC, Fe, Al, Si, and GaP) were

mounted together by embedding them in resin in a 10 mm ring. Small pieces of each standard were placed into the ring, back filled with LR White resin and polymerised at 70°C. The standards were ground and polished to 1 μm diamond paste and coated with 5 nm platinum using a Cressington 208HR high-resolution sputter coater to avoid charging in the NanoSIMS. Standards made specifically for this experiment are shown in Figure 3.4 (a). The Cu, Co, Ni, Ti, Cr and Mo standards, shown in Figure 3.4 (b), were cut from metallurgically pure samples and mounted in Wood's metal.

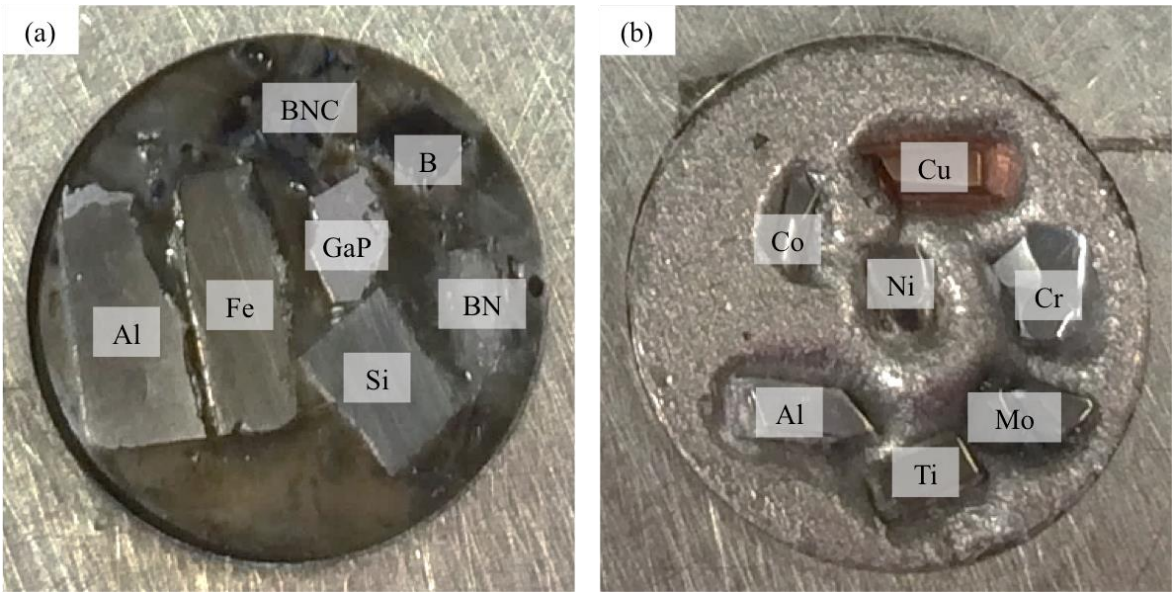


Figure 3.4: Standards used for NanoSIMS analysis

3.4 Light Microscopy

The optical microscope or light microscope uses visible light reflected from a sample surface and then magnified through a series of lenses to create images of the polished surface. It was used as the first technique to look at the microstructure of the steel and superalloy samples. A light microscope equipped with a digital camera (Axioskop 2 MAT fitted with Zeiss digital camera) was used to investigate the microstructure of the steels and map the samples after microindentation to find positions of interest on the samples and to allow easy correlation with EBSD and NanoSIMS. Figure 3.5 illustrates how this correlation across the three techniques was successfully achieved.

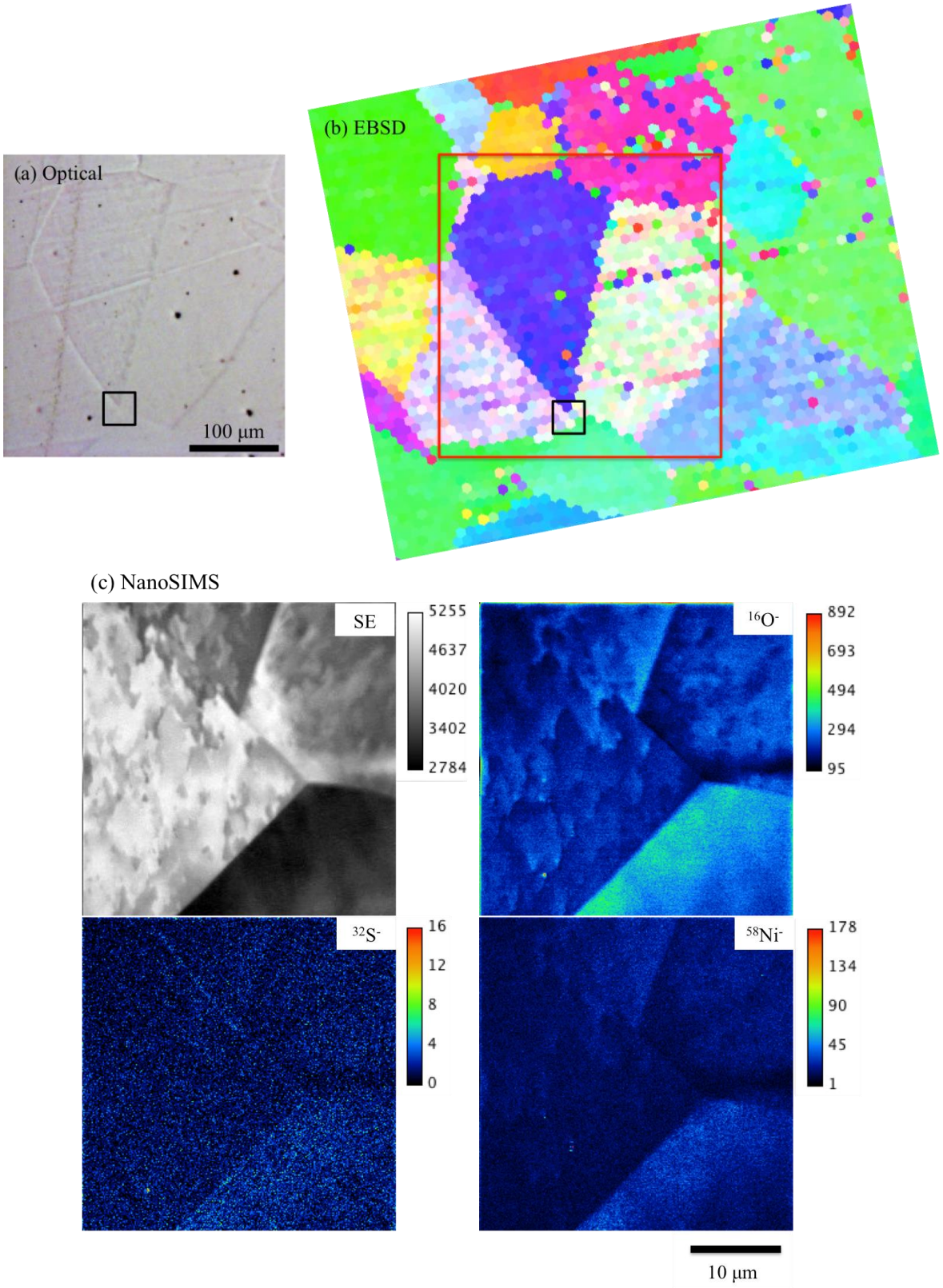


Figure 3.5: Example showing how the (a) optical image can be used to identify regions of interest and correlate with (b) EBSD and (c) NanoSIMS images. The large red box in (b) indicates the optical image area and the small black box in (a) and (b) indicates the NanoSIMS area.

3.5 Scanning Electron Microscopy (SEM)

Scanning electron microscopy (SEM) is a technique of choice that can quickly reveal information from material surfaces with minimal sample preparation required. Figure 3.6 shows the schematic diagram of basic components in an SEM and its working principle. A primary electron beam is created by the acceleration of electrons from the electron gun (electron source and accelerating anode) by an accelerating voltage usually between 1 and 30 kV in a low vacuum chamber (0.1 to 10^{-4} Pa). The electron beam is initially focussed by condenser lenses and then the objective lens and electromagnetic scanning coils allow the beam to be rastered precisely across the sample surface. The signals emitted from the sample were collected through a selection of detectors (secondary or back-scattered electrons or x-ray detector).

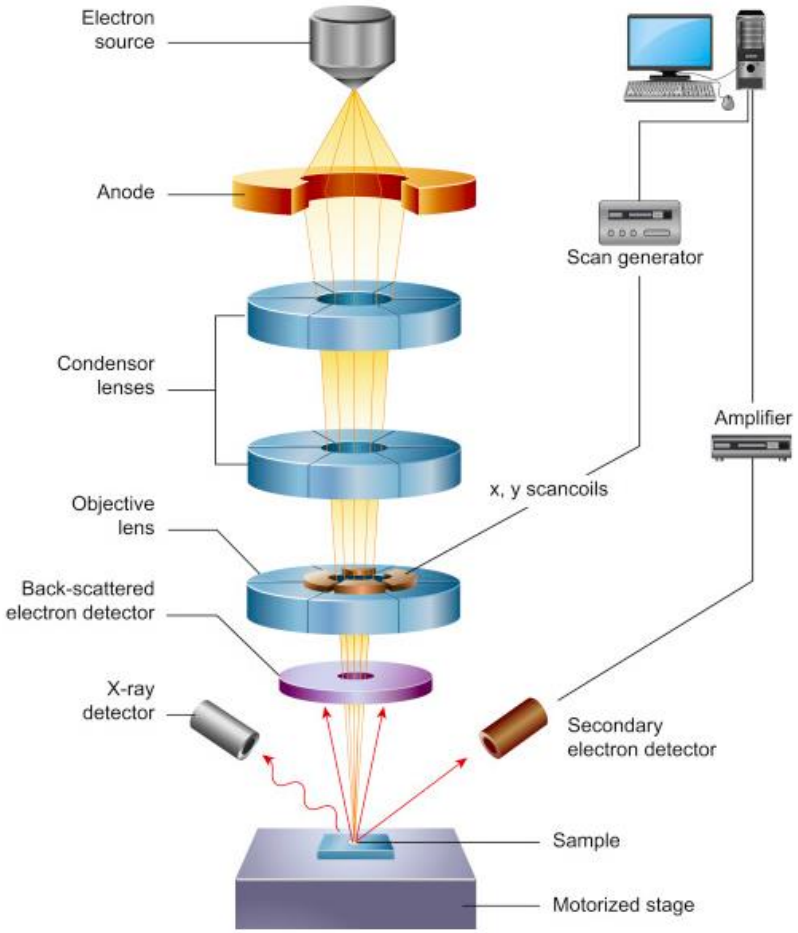


Figure 3.6: Schematic diagram of the core components in SEM microscope. Reproduced with permission from (Inkson, 2016). Copyright © 2016 Elsevier.

JEOL JSM-6300 and a JEOL JSM-840A scanning electron microscopes were used to image the topography and microstructure of the samples prior to NanoSIMS analysis. After NanoSIMS analysis, crystallographic sputtering was also examined using SEM. Preliminary experiments were performed on pure nickel samples with sulphur segregation at the grain boundaries. The samples were provided by Professor Frederic Christien, University of Nantes, France (Christien et al., 2012). Examples of crystallographic sputtering by an ion beam in pure nickel samples examined by SEM are shown in Figure 3.7. As can be seen in Figure 3.7 (a), crystallographic sputtering was only observed on one side of the grain boundary as this grain was at an orientation which allowed faster sputtering. However, the nickel sample in Figure 3.7 (b) did not show much crystallographic sputtering. SEM was also used to investigate the crater morphology and crater distribution on the samples as shown in Figure 3.8. Typical images were taken at 20 kV and at a variety of magnifications with a working distance of 15 mm.

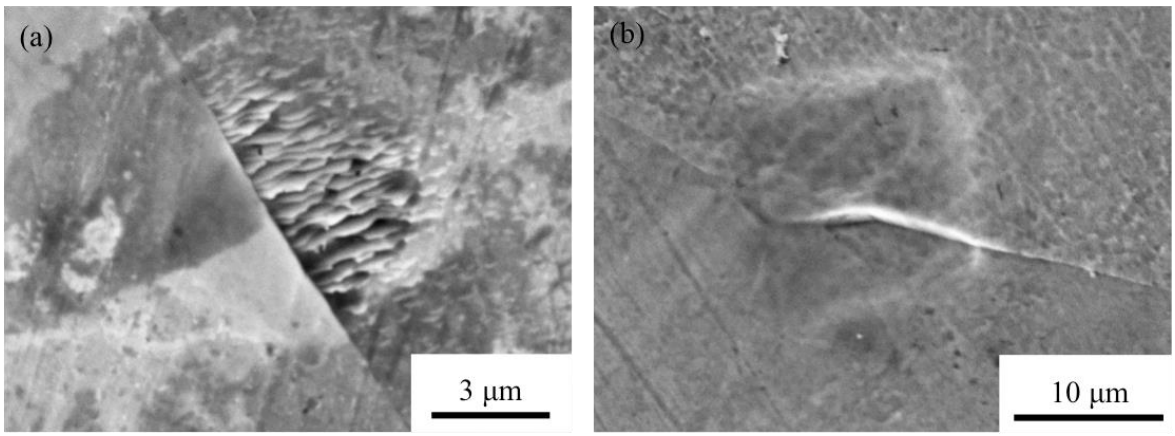


Figure 3.7: Example of crystallographic sputtering on pure nickel sample that occurs in some grains examined by SEM after NanoSIMS analysis.

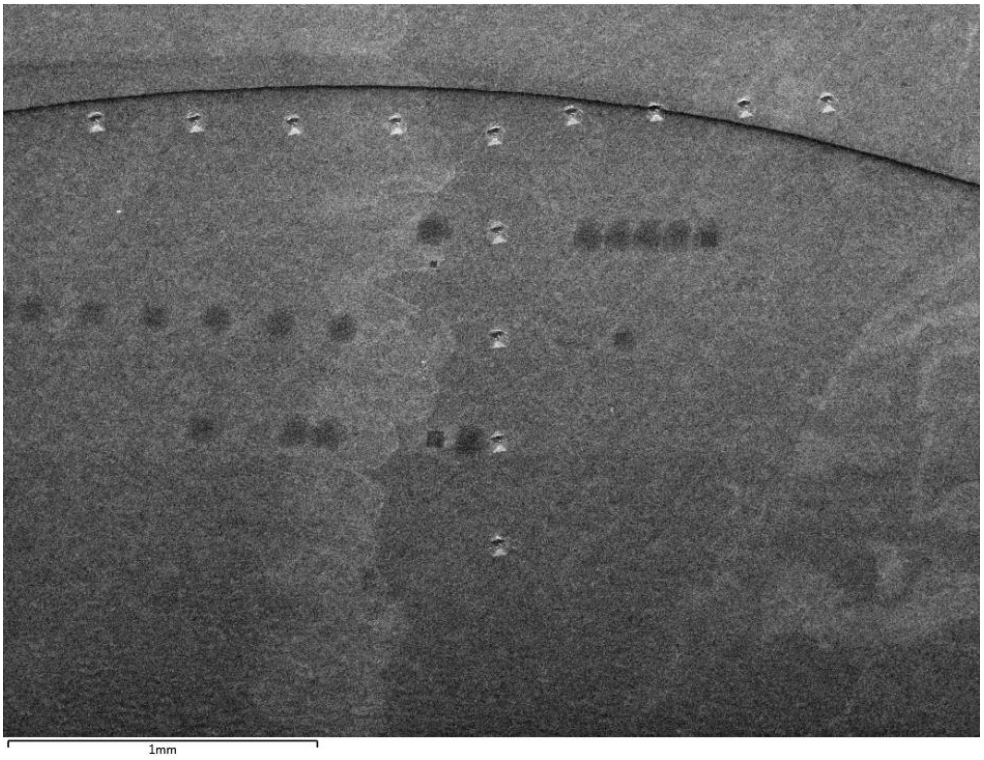


Figure 3.8: Low magnification (40x) SEM on steel sample showing NanoSIMS craters and microindents to help the correlation between NanoSIMS and other techniques.

3.6 Electron Backscatter Diffraction (EBSD)

By combining NanoSIMS and electron backscatter diffraction (EBSD), the chemistry and crystallography of the same grain boundary can be systematically analysed. Backscattered electrons are diffracted according to Bragg's Law and are normally absorbed into the bulk sample. If the sample is tilted to an angle of roughly 70°, then enough electrons escape from the surface and are directed towards a phosphor screen where a Kikuchi pattern is formed based on the crystallographic orientation of the diffracting planes. The electron beam is scanned across the sample, and Kikuchi patterns are measured for each pixel. The EBSD software controls the SEM and rasters the beam across the specimen on a user-specified pre-defined grid, pausing at each point only long enough to acquire the backscatter pattern, index the orientation, and record the x, y coordinates and the orientation vectors. EBSD patterns can be used to study the crystallographic orientation of the grains, grain boundary geometry and grain boundary character (Schwartz et al., 2009). In this work, EBSD was conducted on a JEOL JSM-6300 SEM equipped with Oxford Instruments Inca Crystal EBSD

system and a JEOL JSM-840A SEM with TSL OIM 4.0 EBSD system. As EBSD patterns are collected from a region within the top 50 nm of material, the top surface region must be free from both contamination and residual deformation from polishing, requiring a very high surface finish, this meant that EBSD analysis had to be conducted prior to NanoSIMS analysis which causes significant surface roughening.

Figure 3.9 shows the correlation between an EBSD map and NanoSIMS $^{11}B^{16}O_2^-$ map from the same area. It is easy to see that there are significant differences in the amount of boron segregated to the different grain boundaries. This observation may correlate with grain boundary misorientations, with certain misorientations being more favourable for boron segregation. However, it is difficult to make a direct correlation between EBSD maps and NanoSIMS image because the EBSD image shows the orientations of the transformed structure rather than the prior austenite structure, and for this reason combined NanoSIMS and EBSD experiments were not pursued further.

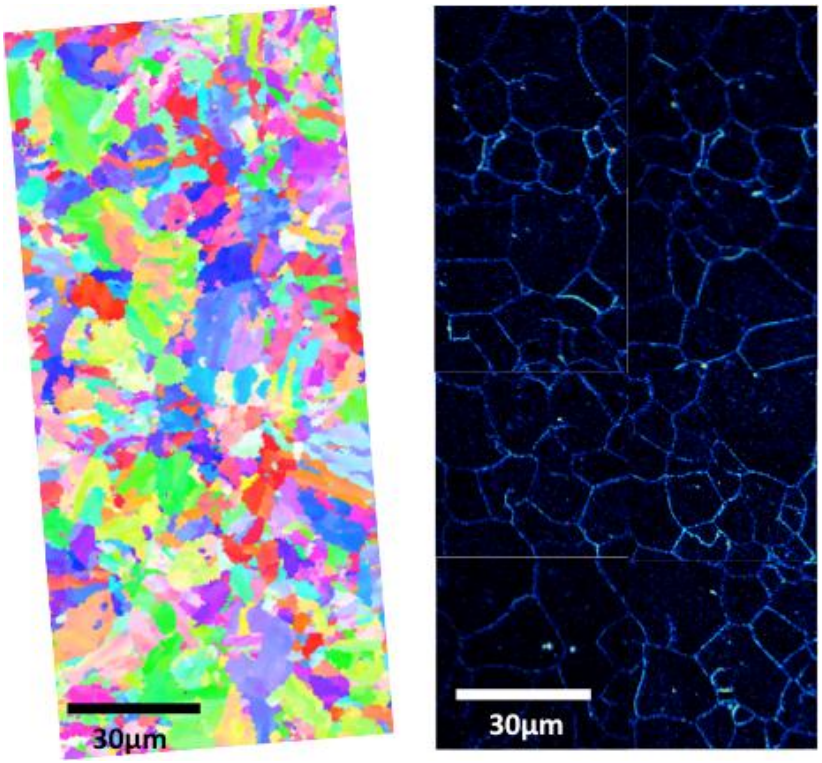


Figure 3.9: An example of the correlation between EBSD map and NanoSIMS $^{11}B^{16}O_2^-$ map of the same area

3.7 NanoSIMS Analysis

A CAMECA NanoSIMS 50 was used for high-resolution SIMS analysis to obtain chemical information from the sample surface. The operating modes of the NanoSIMS are much the same as in conventional dynamic SIMS instruments, depth profiling, bulk analysis and chemical spectroscopy. In addition, the NanoSIMS is able to produce high resolution chemical images and three-dimensional depth profiles. The fundamentals of SIMS analysis and a detailed description of the characteristics of the NanoSIMS instrument are given in the literature review, section 2.2. In this chapter, the creation of primary ion sources, practical aspects of the technique and tuning of the instrument will be described. Figure 3.10 shows the Oxford NanoSIMS situated in the Department of Materials with the key features labelled. Figure 3.11 shows the schematic of the ion optics of the NanoSIMS 50.

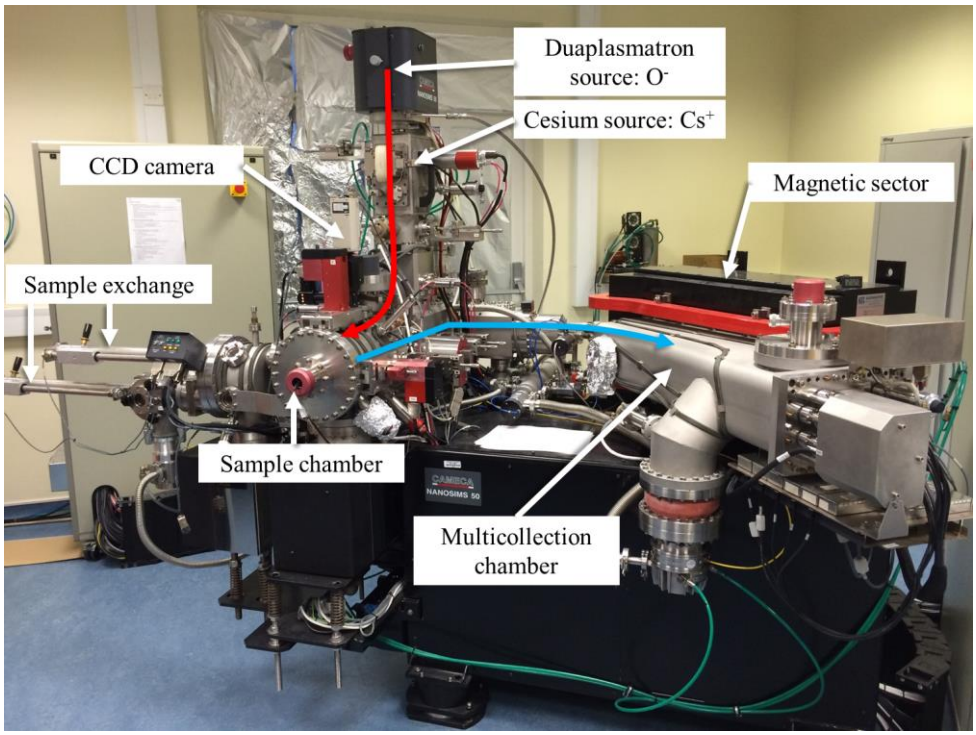


Figure 3.10: The Oxford CAMECA NanoSIMS 50 with the main components highlighted. The red arrow indicates the primary beam direction, the blue arrow indicates the secondary ion trajectory into the magnetic sector optics and multicollection chamber.

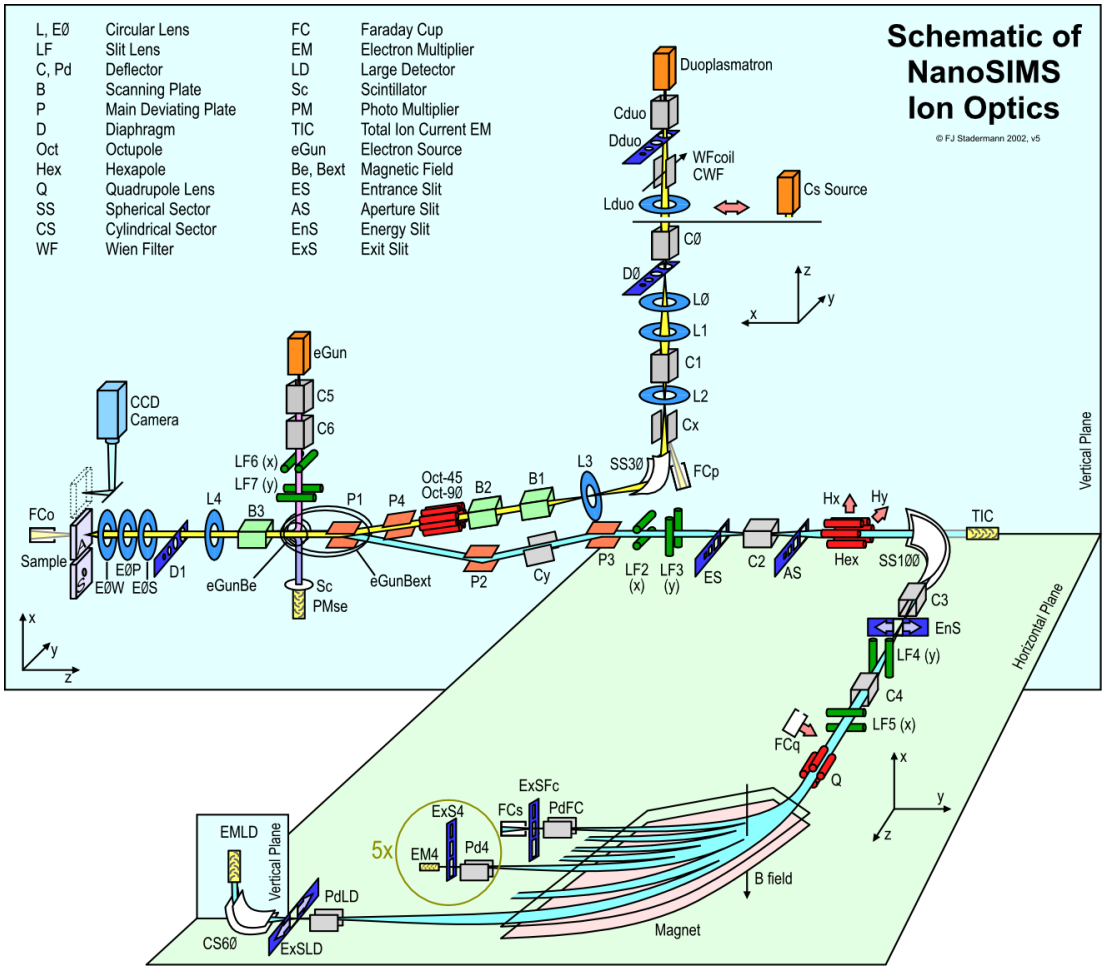


Figure 3.11: Schematic diagram of the NanoSIMS 50 showing the ion optics. Image courtesy of F. J. Stadermann from (Oxford NanoSIMS, 2010).

3.7.1 NanoSIMS Primary Ion Sources

The NanoSIMS instrument used in this study requires two ion sources to be able to detect elements across the periodic table because due to the co-axial optics it can only detect secondary ions with opposite polarity to the primary ions. The primary ion sources that are used in the NanoSIMS are a Cs^+ microbeam ion source that generates negative ions and an O^- duoplasmatron source that generates positive ions. All of the work presented in this study was undertaken using the Cs^+ source as the elements (and molecular ions) of interest, $^{12}C^-$, $^{11}B^{16}O_2^-$, $^{11}B^{12}C^-$, $^{11}B^{14}N^-$, and $^{52}Cr^{16}O^-$ have the highest secondary ion yield as negative ions. The smaller spot size of the Cs^+ source over the O^-

source also allowed for higher resolution mapping of boron and carbon distribution at the grain boundaries.

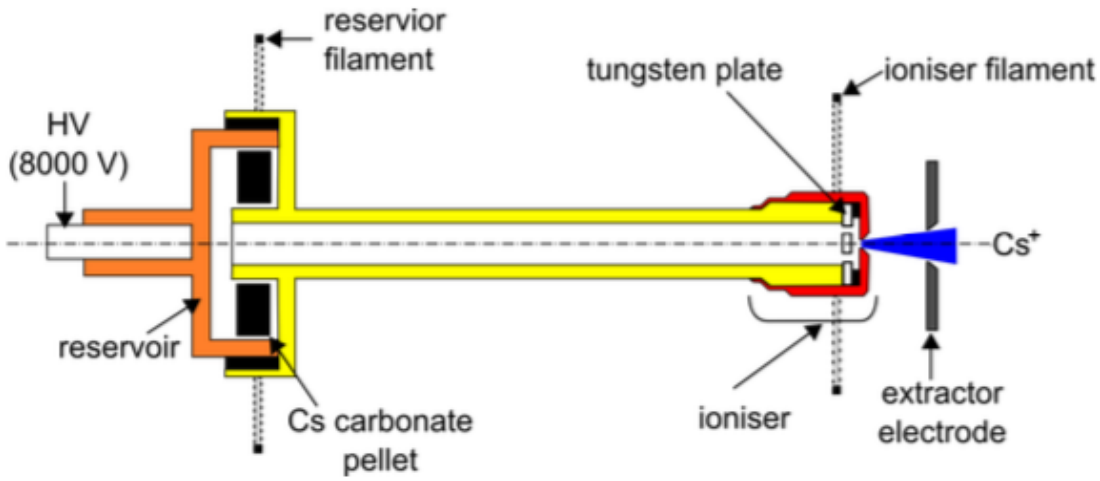


Figure 3.12: Schematic diagram of the CAMECA microbeam Cs source. Reproduced from (Moore, 2011), redrawn from (CAMECA, 2002).

Figure 3.12 shows a schematic diagram of the CAMECA microbeam Cs source that is used in the NanoSIMS. In the reservoir, a Cs carbonate (Cs_2CO_3) pellet is heated by a filament to 400°C to release the Cs vapour. When the tungsten plate, which is situated in the ioniser head, is heated up to 1100°C, the Cs vapor will be ionised by the tungsten plate into Cs^+ ions. The Cs^+ ions are then extracted and accelerated by the electric field generated by the extraction electrode that is placed in front of the ioniser. When using the Cs^+ primary ion source, the probe diameter can be focused down to 50 nm (CAMECA, 2002).

The duoplasmatron source in the NanoSIMS can produce both negative and positive ions (O^-, O_2^- or O_2^+). O^- is the most abundant species when in negative mode, while in positive mode O_2^+ is the most abundant. In NanoSIMS, only O^- ions are selected to detect the electropositive elements. The smallest beam diameter that can be achieved when using the O^- duoplasmatron source is between 200-300 nm.

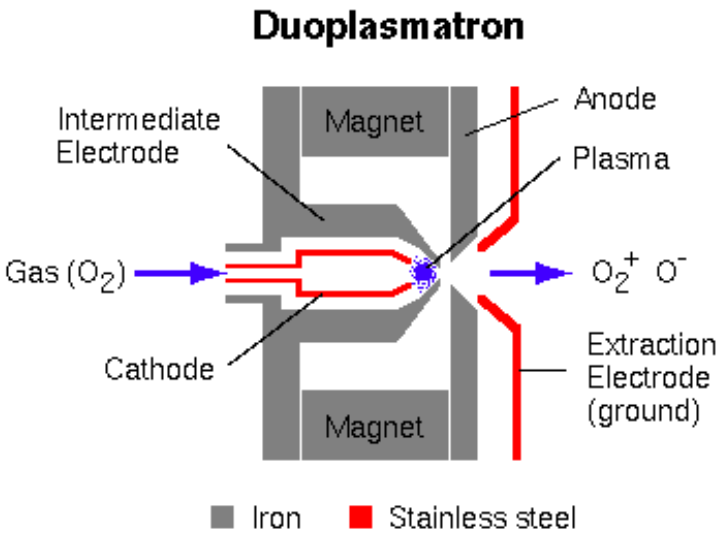


Figure 3.13: Schematic diagram of various components in a duaoplasmatron source. Reproduced with permission from (EAG Laboratories, 2017). Copyright © 2015-2021 Eurofins Scientific.

Figure 3.13 shows an illustration of a duoplasmatron source and its components. When oxygen gas (O_2) is introduced through a hollow cathode, a high density plasma is created and confined magnetically between the intermediate electrode and the anode close to the axis. Finally, the ions are extracted through a hole in the anode according to the polarity of the extraction potential. The O^- ions are achieved when the extraction electrode is set to a positive voltage and by decentralising the axis of discharge with the axis of the extraction hole. A Wien filter is necessary to select the primary ion species of interest from the duoplasmatron, i.e. O^- from O_2^-, O_3^- (CAMECA, 2002).

3.7.2 Tuning the Instrument

Periodically during the course of this work a full alignment of the secondary ion optics was necessary to maximise the mass resolving power and transmission of the instrument. A grid etched into silicon was used for this tuning to provide a stable source of ions and allow the focusing and astigmatism to be checked. Most lens settings stayed unaltered from the full tuning during each session of the experiment (usually lasting 1 week), but small changes several times each day were required to

maximise the signal intensity and improve the image quality.

At the beginning of every session the source was heated and allowed to stabilise. The primary ion beam current was then measured at different positions of the D1 aperture. Table 3.1 demonstrates the aperture position and size with the corresponding primary ion beam current and approximate beam size. After each new Cs source was installed, the Oxford NanoSIMS typically reached a primary beam current of 170 pA with D1=0, but the typical beam current for the majority of the experiments was 40 pA with D1=0. All results in this thesis were obtained with a primary ion beam current of >40 pA with D1=0. If the current was lower than this, too few secondary ions were emitted to allow meaningful analysis.

Table 3.1: The size of D1 aperture and corresponding primary ion beam current and beam size.

Aperture position	D1 diameter (µm)	Cs^+ current (pA)	Approximate beam size/resolution (nm)
D1=0	NA	40 – 170	NA
D1=1	750	4 – 17	120 – 300
D1=2	300	0.8 – 3.4	100 – 120
D1=3	250	0.4 – 1.7	50 – 100
D1=4	200	0.2 – 0.85	

When aligning the NanoSIMS, the first step was to set detector 5 to the highest mass of interest. This altered the magnetic field strength so the magnet needed to be left to stabilise for a few minutes after this change. The other four detectors were approximately set to the correct mass by physically moving the detectors along the exit plane of the magnetic sector.

As this research concerned the detection of elements with a low bulk concentration, ion signals for these elements from the samples were low. In order to avoid incorrect tuning by selecting an isobaric interference, standard samples were needed to accurately align the detectors. In order to do this, the beam was positioned onto the standard and a high mass resolution (HMR) scan was acquired. Typically, the highest signal from the standard was the signal of interest (contrary to what was occasionally observed on the sample). This was repeated until all the detectors were correctly positioned.

To find the areas of interest on the samples, the optical camera (CCD) attached to the NanoSIMS was used. To ensure optimum transmission of the ion signals, the CCD was also used to correctly set the Z height of the sample holder, when the sample was in focus on the CCD the Z height was correctly set. After selecting the region of interest, a high current mode (with D1=0) was used to clean the surface and implant Cs^+ for the amount of time calculated to give the dose required for steady state. The dose required for steady state is determined by depth profiling as indicated in Figure 3.14. It can be seen that $^{11}B^{16}O_2^-$ (purple line) has a higher yield compared to $^{11}B^{16}O^-$ (green line) which makes it the signal of choice to detect boron in this study. The primary ion dose is measured using the equation below:

$$\textbf{Dose} = \frac{\boldsymbol{Time} \times \boldsymbol{Current}}{\boldsymbol{Area} \times \boldsymbol{Charge}} \qquad \textbf{(3.1)}$$

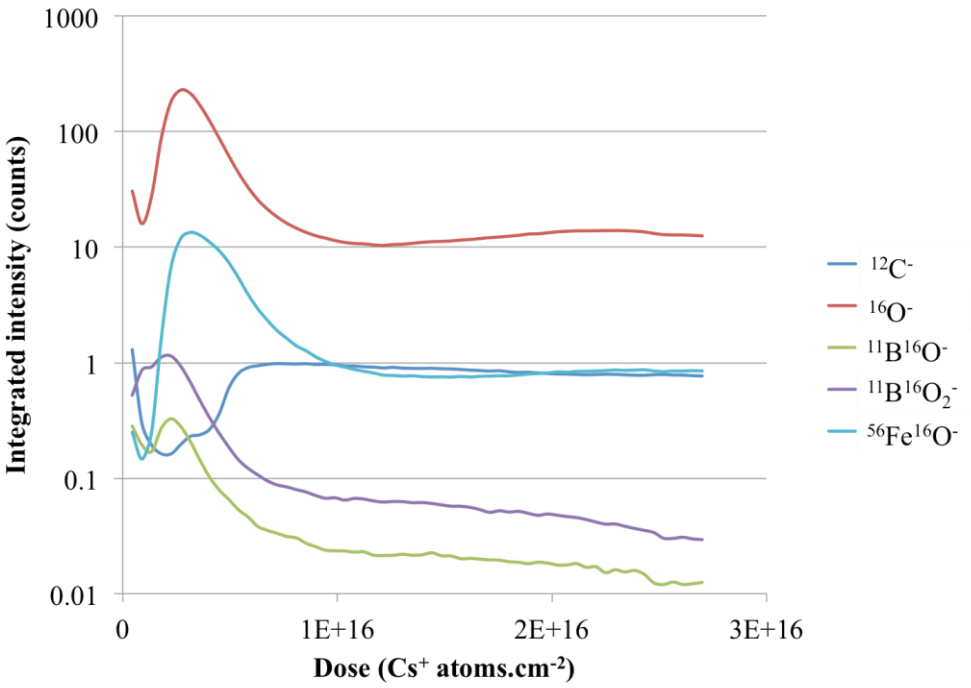


Figure 3.14: Typical depth profile on steel sample that required a dose of 1 x 10^{16} Cs^+ atoms.cm^{-2} for steady state.

For all samples, a large area (65 x 65 µm) was scanned with a high current beam to remove the oxide layer and implant Cs^+, and then analysis was carried out on a smaller region, typically 50 x 50 µm

with a lower current beam, to avoid any effects from the edge of the cleaned region. Figure 3.15 shows how the $^{11}B^{16}O_2^-$ signal evolves and the localisation of the boron is revealed as the oxide layer is removed. While the oxide is still present (T=0) it is not possible to see grain boundary segregation or precipitates. With further implantation, clear grain boundary localisation and precipitates are revealed as the residual oxygen implanted into the surface by the primary beam can contribute to the formation of molecular ions with B. After 20 minutes of cleaning most of the native oxide has been removed causing a reduction in the $^{11}B^{16}O_2^-$ signal (also observed in Figure 3.15) and a loss of the grain boundary features indicating there is an optimal implantation dose to obtain meaningful information from these samples, i.e. that there is a balance between cleaning the surface and removing so much of the surface that the $^{11}B^{16}O_2$ ions can no longer be formed.

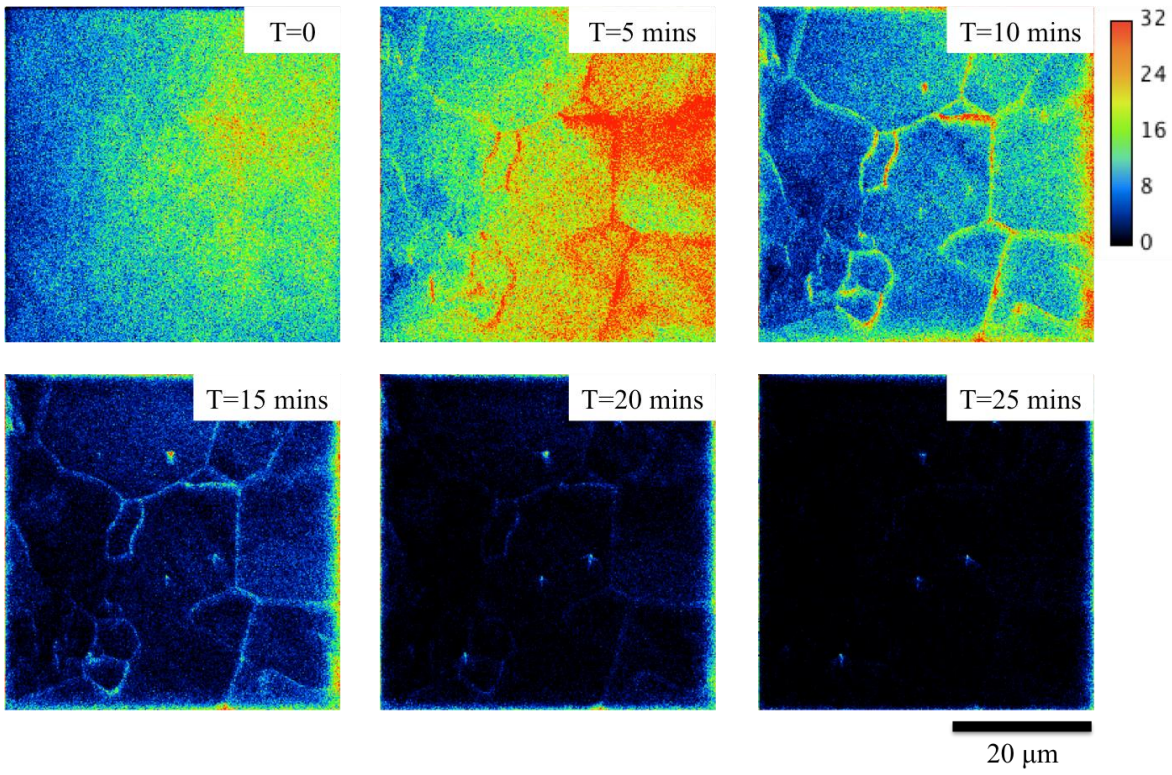


Figure 3.15: Effect of cleaning to remove surface oxide layer on the $^{11}B^{16}O_2^-$ signal as a function of sputter time with a beam current of 2.9 pA.

Obviously, not every sample behaves exactly the same way. It is noted that one of the steel samples (12AM22F) needed a much lower dose as compared to other samples as shown from Figure 3.16. The signals decreased significantly after cleaning with 1 x 10^{16} and 2 x 10^{16} Cs atoms/cm^2. The

normal dose of 2 x 10^{16} Cs atoms/cm^2 was too high as no localisation of boron could be observed and this is possibly because there is less native oxide on this sample. As a result, this sample required a much lower dose for effective cleaning, 9 x 10^{15} Cs atoms/cm^2 was sufficient to map clear boron distributions at the grain boundaries. Comparing $^{11}B^{16}O_2^-$ and $^{11}B^{16}O^-$ maps from this figure also showed higher intensity in $^{11}B^{16}O_2^-$ than $^{11}B^{16}O^-$. This observation is in agreement with the depth profile from Figure 3.14. The yield of different molecular ions depends on ionisation yield as some ions give more signal than others and also depends on the matrix surrounding the molecule of interest. The $^{11}B^{16}O_2^-$ on mass 43 is therefore used to form boron images in all future NanoSIMS analysis in this study and has also been the ion species of choice for many other studies (Hashimoto et al., 1987, Karlsson et al., 1988, Lozano-Perez et al., 2008, Kim et al., 2012, Yardley et al., 2013).

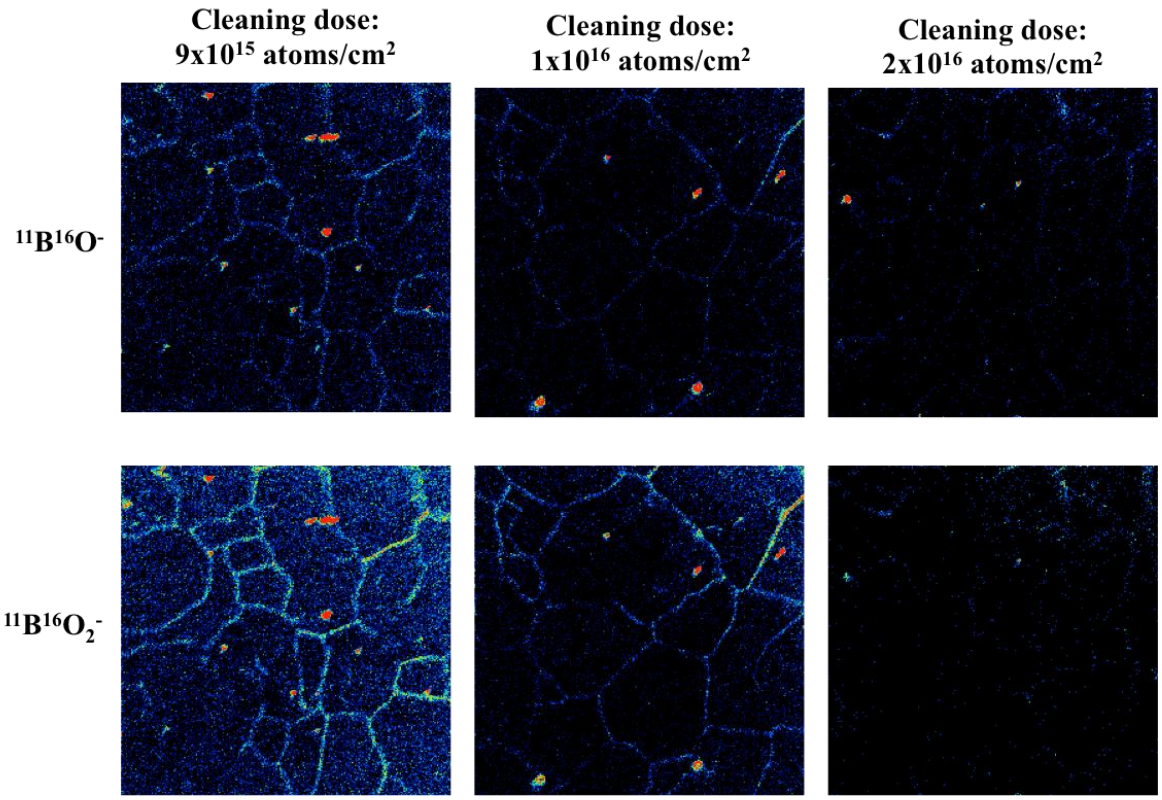


Figure 3.16: Comparison of $^{11}B^{16}O^-$ and $^{11}B^{16}O_2^-$ signals to identify the cleaning dose required on sample 12AM22F.

Higher magnification scans of particular features of interest were then taken within the implanted region to avoid the edges of previously sputtered SIMS craters, which gave strong topographical contrast. The position of the D1 aperture was selected depending on the experiment. Usually, for a new sample, D1 was initially set to position 2, then as selected features were imaged at higher resolution by using D1 aperture settings of position 3 or 4, and with longer image dwell times to achieve sufficient signal intensities. Before acquiring an image, further alignment on the sample was required to optimise the transmission. HMR scans were repeated on the sample to ensure the correct positioning of the detector, and SIB and C4x scans were performed to select the highest ion transmission efficiency, which changed for every sample. The NanoSIMS was set to acquire a 256 x 256 pixel image with a typical dwell time of 30 ms per pixel. Longer experiments were run overnight where a series of images were acquired sequentially from the same area, taking approximately 12 hours. A longer dwell time or high primary beam current is required to get enough counts to achieve reliable quantification and maximizing information from weak signals.

3.7.3 Resolving Mass Overlaps

In this study, cluster ions of trace elements, such as $^{11}B^{16}O_2^-$ from boron, were used for ion imaging due to their high detection sensitivity compared to the single atomic ions like $^{11}B^-$ (Hashimoto et al., 1987, Karlsson et al., 1988, Lozano-Perez et al., 2008, Kim et al., 2012, Yardley et al., 2013). It is well known that a native oxide can develop instantly after a fresh metal surface is exposed to air and in the case of steel samples can reach an eventual thickness of several nanometers at room temperature. This surface oxide layer allows the formation of the $^{11}B^{16}O_2^-$ peak even though oxygen may not be present in the feature of interest.

At mass 11 there are very few isobaric interferences, but at mass 43, the mass of $^{11}B^{16}O_2^-$, many ionic species can be detected. The three main interferences are $^{27}Al^{16}O^-$, $^{31}P^{12}C^-$ and $^{12}C_2{}^1H_3{}^{16}O^-$. Standard samples of polished Al and B sample were used to align the NanoSIMS detectors on the appropriate mass peaks of interest, i.e. $^{27}Al^{16}O^-$ and $^{11}B^{16}O_2^-$ to ensure the correct peak was chosen, as on all the

samples three peaks are normally observed. Inserting the entrance slit (ES), increases the mass resolution to assist with the accurate selection of the desired peak mass, but this process reduces the transmission of ions, thus reducing the measured counts, so after peak selection the ES slit was removed. The HMR data shown in Figure 3.17 gives three separate scans taken from steel reference sample 12AN15 (black dotted line) and the Al (red line) and B standards (blue line), and shows the separation of $^{27}Al^{16}O^-$, $^{11}B^{16}O_2^-$ and $^{12}C_2{}^1H_3{}^{16}O^-$ peaks at mass 43. These peaks, $^{27}Al^{16}O^-$ at 42.976 amu and $^{11}B^{16}O_2^-$ at 42.999 amu, only differ by 0.023 amu while $^{12}C_2{}^1H_3{}^{16}O^-$ at 43.018 amu differ by 0.019 amu with $^{11}B^{16}O_2^-$ and so can only be separated in a high-resolution mass spectrometer. However, $^{27}Al^{16}O^-$ (42.976 amu) and $^{31}P^{12}C^-$ (42.974 amu) overlap almost completely and cannot be resolved, so it is not possible to determine if the first peak on the steel sample HMR scan is $^{27}Al^{16}O^-$ or $^{31}P^{12}C^-$.

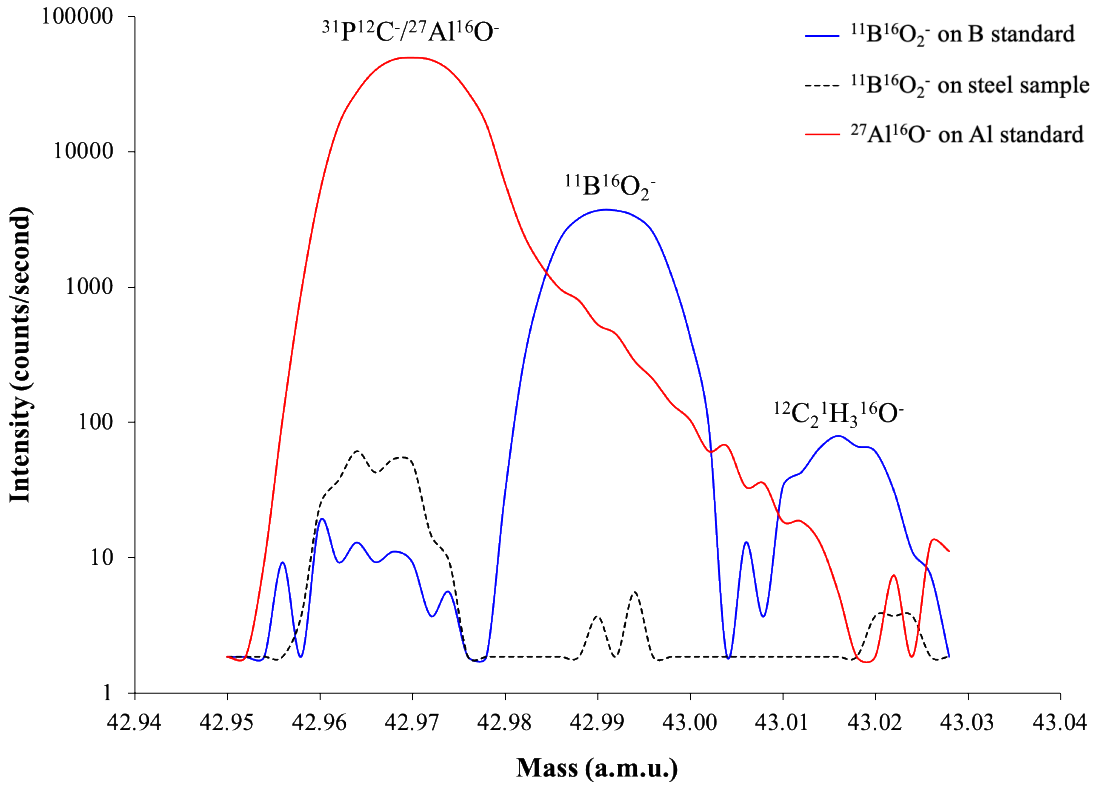


Figure 3.17: HMR scans at mass 43 from Al standard (red line), B standard (blue line) and steel reference sample 12AN15 (black dotted line).

3.7.4 Lateral Resolution

Estimation of the lateral resolution achieved in this high resolution analysis (mainly controlled by the incident beam size) can be measured from the distance between the 16% and 84% intensity levels of the maximum signal (Saka et al., 2014, Tom et al., 2012). Figure 3.18 shows a line scan performed across a boron rich particle on the grain boundary. The distance over which the $^{11}B^{16}O_2^-$ intensity changes from 84% to 16% of the maximum intensity reveals the estimated lateral resolution to be in the range of 90 - 110 nm using the smallest aperture D1=4 with FCo current measured as 0.74 pA.

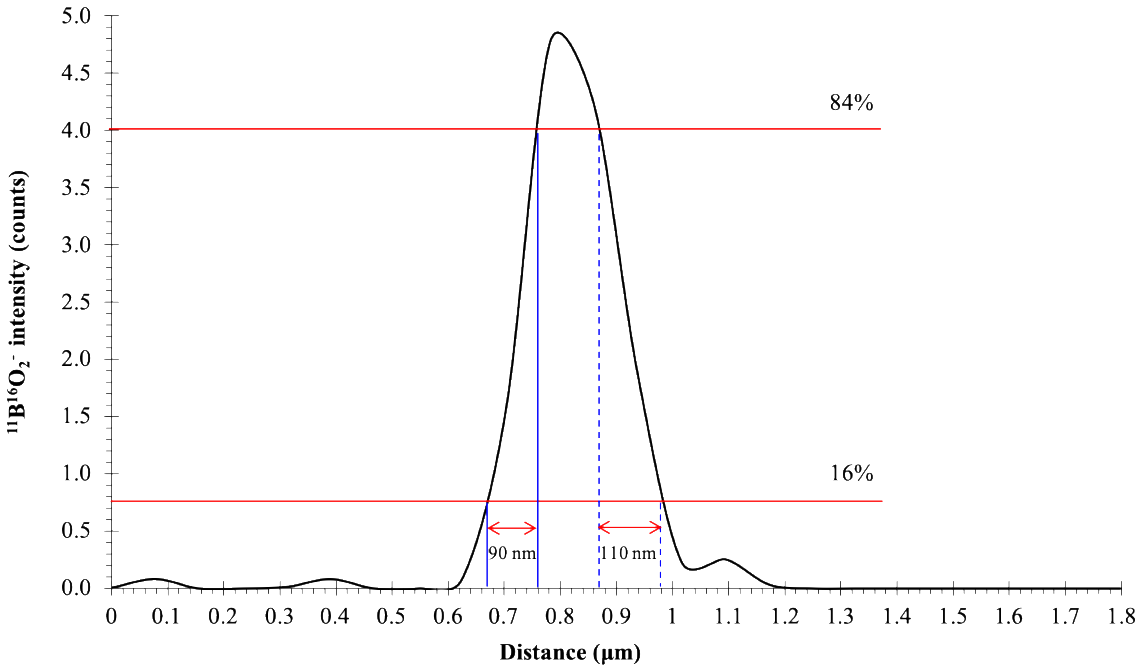


Figure 3.18: Resolution measurement: Estimated lateral resolution from the $^{11}B^{16}O_2^-$ signal of a boron rich particle scanned over a 20 x 20 µm area, 256 x 256 pixels. Using the 16% to 84% maximum signal criterion, the calculated lateral resolution is in the range of 90 to 110 nm.

3.7.5 Data Analysis and Presentation

ImageJ software (Abramoff et al., 2004, Schneider et al., 2012) with the OpenMIMS (Harvard) plugin was used to analyse all the NanoSIMS data. With ImageJ, data analysis such as line scans, particle counting, colour merging, drift correction of overnight scans and summation of images was

performed. NanoSIMS images are presented on a linear colour scale (unless otherwise stated) with black and blue indicating low counts and orange and red indicating high counts.

An attempt to use the ImageJ software to automatically count and measure the particle sizes in the quantification study of boron in particle sizes and size distributions was not successful due to the fact that the software will count any pixel with an elevated signal including artefacts created from edges and holes. Therefore, I decided to select the particles manually using a criterion that a minimum of five adjoining pixels had to have an elevated $^{11}B^{16}O_2^-$ content.

3.7.6 Quantification

In quantitative SIMS analysis, there exists some difficulty in calculating absolute atomic concentrations for all elements in the sample. It is mainly the extraction of total secondary ion currents stemming from not only single or cluster ions but also possible interferences with secondary ion peaks from other species of the different sample matrix. Hence, it is important to use high mass resolution to properly extract the secondary ion current for the measurement of trace boron concentrations from SIMS image data. Due to matrix effects and relative sensitivity factors (RSF), it is not possible to directly compare the counts from one ionic species with another just by looking at the images.

Quantification was only attempted for the steel samples. Boron ions were implanted into pure iron samples at the Surrey Ion Beam Centre to produce a set of standards. Boron was implanted into the iron at an accelerating voltage of 150 kV with doses of 1×10^{15}, 1×10^{16} and 5×10^{16} ions cm^{-2}. The concentration profile of boron in the iron surface was predicted using the Stopping and Range of Ions in Matter (SRIM) programme. The setup for SRIM is explained in section 4.5.1. A calibration curve for boron was obtained by taking depth profiles from each of these samples.

The quantitative analysis of boron in steels will be described in details in section 4.5. Three types of quantative analysis were performed using the NanoSIMS data which are the quantitative analysis of

total boron counts, quantification of grain boundary segregation and quantification of particle sizes and size distributions.

3.8 Correlation after NanoSIMS Analysis

The NanoSIMS depth profiling itself introduces artefacts that can complicate the analysis (e.g. mixing and redeposition). SIMS is based on the principle that charged atomic and molecular species are sputtered from the sample surface by ion bombardment. More specifically, the impact of the ions on the surface and their subsequent implantation causes an energy and momentum transfer to a limited area around the point of particle impact, resulting in a change in lattice structure and the sputtering of surface material (Benninghoven, 1975). It is the change in lattice structure (damage) that is the culprit in most SIMS induced artefacts. An understanding of the effects, influences and techniques developed to overcome such issues is important for obtaining meaningful analysis from each specific kind of sample.

NanoSIMS depth profiling imaging was acquired on a steel sample with a beam current 3 pA, 50 μm raster, counting time 5000 μs/px per slice and a total of 100 slices that required about 14 hours scan. Figure 3.19 shows a correlation between (a) NanoSIMS $^{11}B^{16}O_2^-$ map, (b) SEM image of the NanoSIMS crater, (c) overlapping image of NanoSIMS map and SEM image, (d) SE image from NanoSIMS and (e) MicroXAM image of the crater showing the topological information of the crater. The SEM image clearly shows there is variation in sputter rate due to the grain and martensite lath orientation. The grain boundary is more pronounced due to topography effects from differential sputtering between grains. MicroXAM image of the crater in Figure 3.19 (e) is enlarged in Figure 3.20 and the line scan profile is shown in Figure 3.21.

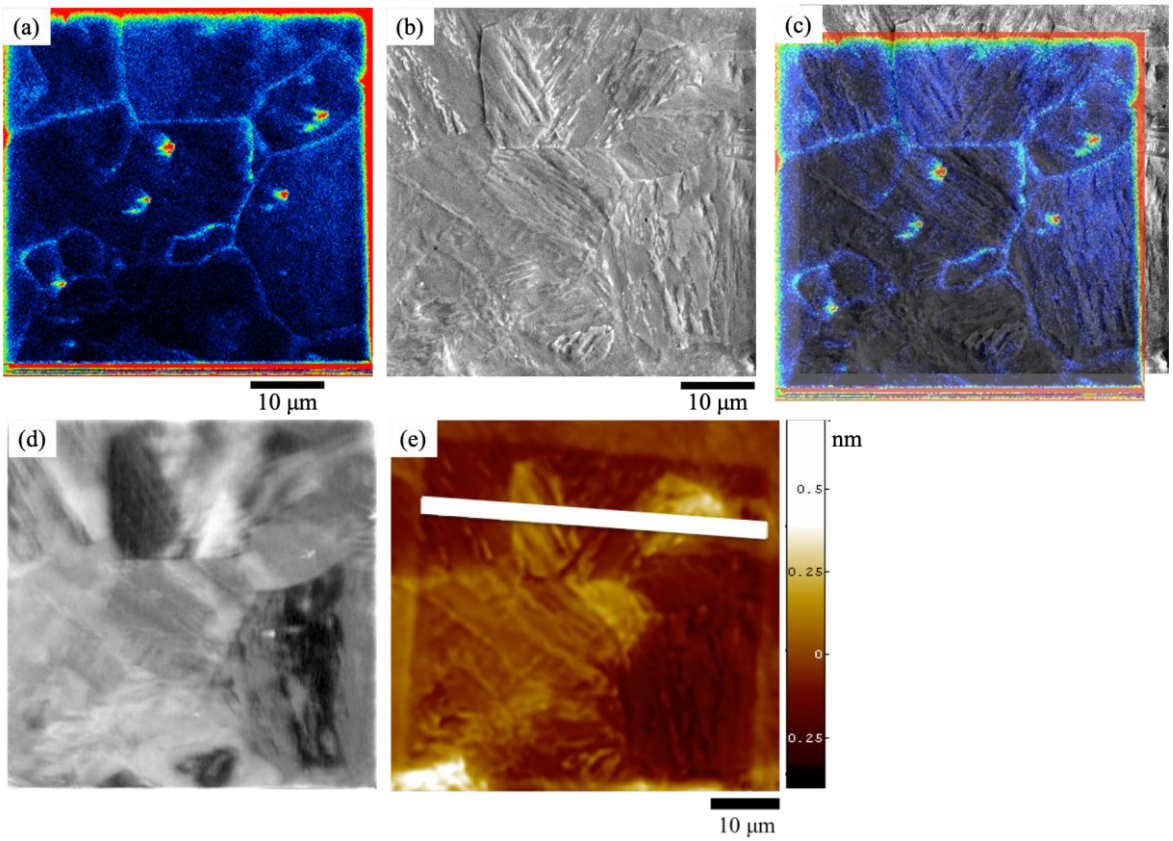


Figure 3.19: A compilation of images from the same area on the NanoSIMS crater. (a) NanoSIMS $^{11}B^{16}O_2^-$ map, (b) SEM image on the crater, (c) overlapping image of NanoSIMS $^{11}B^{16}O_2^-$ map and SEM image, (d) SE image from NanoSIMS and (e) MicroXAM image of the crater.

The MicroXAM is a high precision surface mapping microscope based on confocal optical microscope giving 2D profiles with a height resolution of a few nanometres. This instrument was used to analyse the surface morphology of the NanoSIMS crater. The average depth of the crater was about 400 nm, but the sputter rate varied between grains in the scanned area as shown in the line profile in Figure 3.21. Due to changes in the matrix surface composition, different sputter rates were observed, and this leads to a matrix effect that changes the ionization yield.

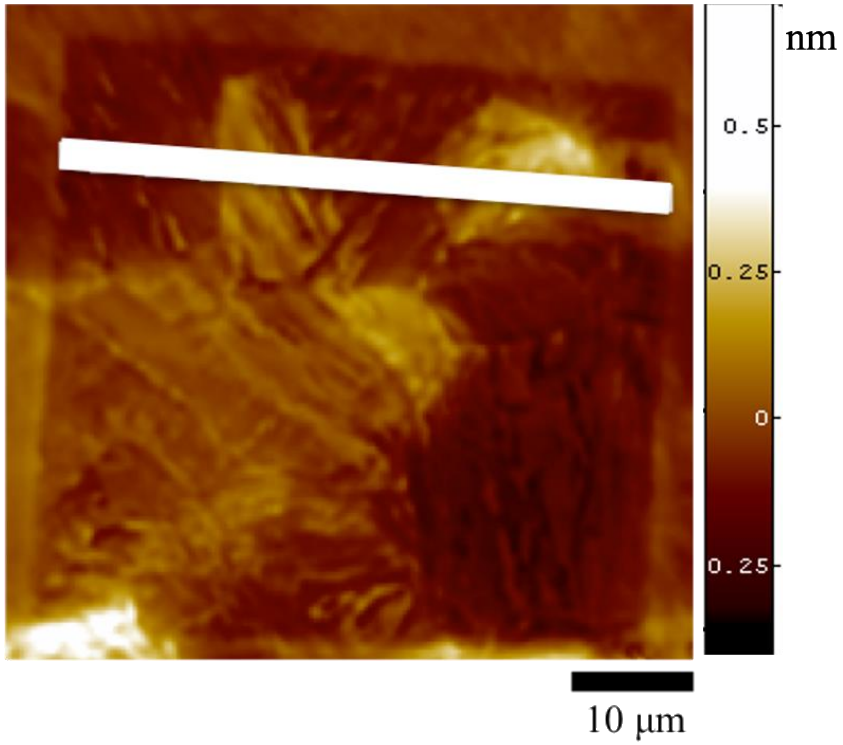


Figure 3.20: A line scan (white line) on MicroXAM image showing NanoSIMS crater on a steel sample.

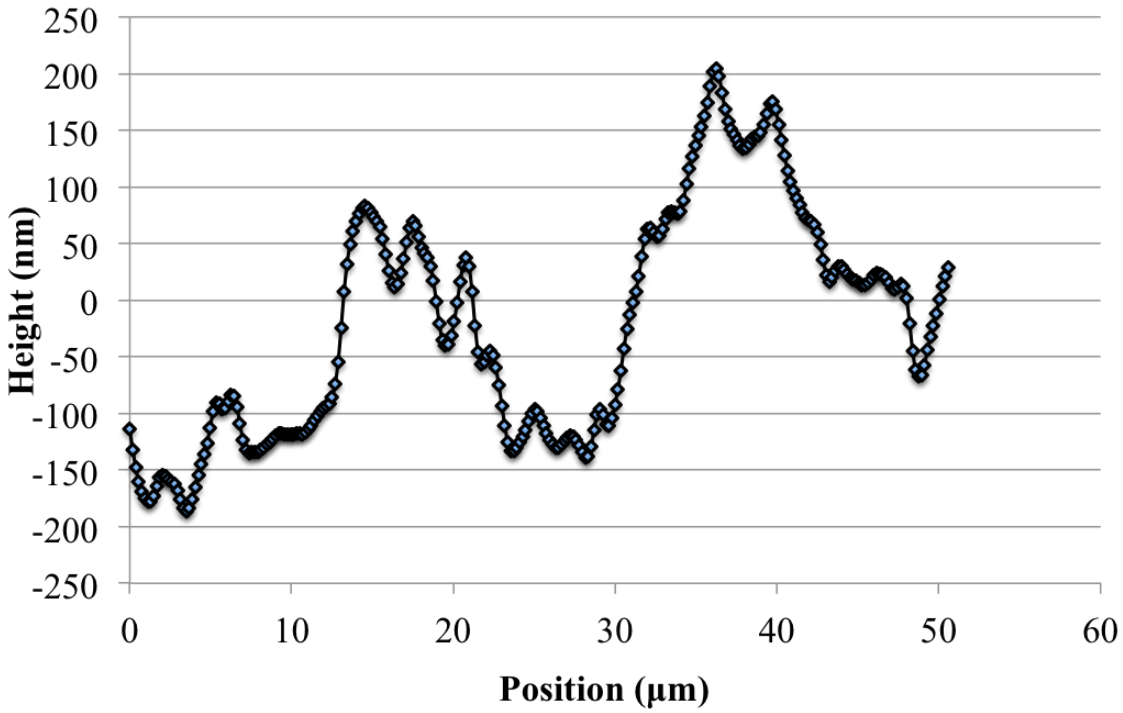


Figure 3.21: A plot of the variation of height across the NanoSIMS crater on steel sample as indicated by the white line in Figure 3.20.

3.9 References

ABRAMOFF, M., MAGALHAES, P. & RAM, S. 2004. Image Processing with ImageJ. *Biophotonics International,* 11**,** 36-42.

BENNINGHOVEN, A. 1975. Developments in secondary ion mass-spectroscopy and applications to surface studies. *Surface Science,* 53**,** 596-625.

CAMECA. 2002. *NanoSIMS 50 User's Guide: Primary column* [Online]. Available: https://nrims.harvard.edu/book/cameca-nanosims-50-primary-ion-optics-user-guide [Accessed 5 May 2021].

CHRISTIEN, F., DOWNING, C., MOORE, K. L. & GROVENOR, C. R. M. 2012. Quantification of grain boundary equilibrium segregation by NanoSIMS analysis of bulk samples. *Surface and Interface Analysis,* 44**,** 377-387.

EAG LABORATORIES, E. 2017. *SIMS Tutorial: Instrumentation: SIMS Primary Ion Sources* [Online]. Eurofins Scientific. Available: https://www.eag.com/resources/tutorials/sims-tutorial-instrumentation/ [Accessed 4 May 2021].

HASHIMOTO, S., DOI, S., TAKAHASHI, K., TERASAKA, M. & IWAKI, M. 1987. Quantitative analysis of boron in steel by secondary ion mass spectrometry using ion-implanted iron as standard. *Materials Science and Engineering,* 90**,** 119-125.

INKSON, B. J. 2016. 2 - Scanning electron microscopy (SEM) and transmission electron microscopy (TEM) for materials characterization. *In:* HÜBSCHEN, G., ALTPETER, I., TSCHUNCKY, R. & HERRMANN, H.-G. (eds.) *Materials Characterization Using Nondestructive Evaluation (NDE) Methods.* Woodhead Publishing.

KARLSSON, L., NORDÉN, H. & ODELIUS, H. 1988. Overview no. 63 Non-equilibrium grain boundary segregation of boron in austenitic stainless steel—I. Large scale segregation behaviour. *Acta Metallurgica,* 36**,** 1-12.

KIM, J., LEE, S., KWUN, H., KIM, J., SHIN, K. & LEE, J. 2012. A new method to determine trace boron concentration of iron and steel by SIMS direct ion image. *Metals and Materials International,* 18**,** 361-369.

LOZANO-PEREZ, S., SCHRODER, M., YAMADA, T., TERACHI, T., ENGLISH, C. A. & GROVENOR, C. R. M. 2008. Using NanoSIMS to map trace elements in stainless steels from nuclear reactors. *Applied Surface Science,* 255**,** 1541-1543.

MOORE, K. L. 2011. *High resolution secondary ion mass spectrometry analysis of trace elements in cereal grain and roots.* DPhil, University of Oxford.

OXFORD NANOSIMS, G. 2010. *NanoSIMS: The Instruments: Ion optical setup* [Online]. Oxford. Available: http://nanosims.materials.ox.ac.uk/nanosimshome/instrument.html [Accessed March 21 2021].

SAKA, S. K., VOGTS, A., KRÖHNERT, K., HILLION, F., RIZZOLI, S. O. & WESSELS, J. T. 2014. Correlated optical and isotopic nanoscopy. *Nature Communications,* 5**,** 3664.

SCHNEIDER, C. A., RASBAND, W. S. & ELICEIRI, K. W. 2012. NIH Image to ImageJ: 25 years of image analysis. *Nature Methods,* 9**,** 671-675.

SCHWARTZ, A. J., KUMAR, M., ADAMS, B. L. & FIELD, D. P. 2009. *Electron Backscatter Diffraction in Materials Science*, Springer US.

TOM, W., YVES, F., MATHIEU, G., URS, G., THILO, G., ERNST, M., URS, W., URS, M., AITZIBER HERRERO, O. & DANIEL, U. 2012. Design and performance of a combined secondary ion mass spectrometry-scanning probe microscopy instrument for high sensitivity and high-resolution elemental three-dimensional analysis. *Review of Scientific Instruments,* 83**,** 063702.

YARDLEY, S. S., MOORE, K. L., NI, N., WEI, J. F., LYON, S., PREUSS, M., LOZANO-PEREZ, S. & GROVENOR, C. R. M. 2013. An investigation of the oxidation behaviour of zirconium alloys using isotopic tracers and high resolution SIMS. *Journal of Nuclear Materials,* 443**,** 436-443.

4 Boron Segregation in Steel

4.1 Introduction

Boron is commonly added to high strength heat treatable steels in order to increase hardenability (Mun et al., 2012, Paju, 1992, Lin and Cheng, 1990). It readily segregates to grain boundaries where it either remains in solution or forms carbide / nitride precipitates thereby altering the character of the grain boundaries (Valle et al., 2011, Mun et al., 2012). The difficulty in detecting boron, and especially small amounts of boron, combined with a strong tendency for the formation of boron carbides (BC) and boron nitrides (BN), makes it difficult to clearly identify the mechanisms responsible for the beneficial effect of boron on hardenability.

Boron precipitation can occur during the cooling after casting (Jahazi and Jonas, 2002, Drillet et al., 2012, Tingdong et al., 1990). This step is well controlled in industry and the precipitation of boron nitride or boron oxide can be avoided by addition of elements such as titanium or aluminium, which trap both nitrogen and oxygen – this is called 'protection' (Paju, 1992, Lin and Cheng, 1990).

The hardenability enhancing effect of boron is thought to result from boron in solution segregating to austenite grain boundaries during rapid cooling (Tingdong et al., 1990, Jahazi and Jonas, 2002, Karlsson et al., 1988), and hence it is important to avoid the formation of boron-rich precipitates such as BN at earlier stages of processing. As has been described in previous chapters, high-resolution secondary ion mass spectrometry (NanoSIMS) is well-known for its high spatial resolution and sensitivity and is therefore ideally suited to the analysis of trace elements at grain boundaries – especially light elements which have proven to be an analytical challenge with other techniques such as atom probe tomography and TEM (Karlsson et al., 1988). The research reported in this chapter is a contribution to a systematic study of boron segregation effects on grain boundary properties as a way to understand the microstructural evolution of steels, and the effect that it has on the mechanical properties.

4.2 Materials and Methods

In total, 15 different steel samples were analysed, chosen to differ by one clear variable while keeping other processing parameters as similar as possible. A summary of the processing conditions for these samples is given in Table 4.1, and Table 4.2 shows the composition of the steels. All these samples were provided by Dr Matthew Green of Tata Steel, and formed part of the set of materials studied in the EU OPTIBOS project entitled 'New developments and optimisation of high strength boron treated steels through the application of advanced boron monitoring techniques' with partners in Germany, Belgium and Spain. The samples can be divided into four groups, with two comparisons at each of the three processing stages.

The first group contains two as-rolled samples, 12AM22 and 12AM23, which are aluminium (Al) protected and titanium (Ti) protected respectively. Additions of Al or Ti are the two primary methods used for B-protection in low carbon steels to maintain the desired boron hardenability effect as they are both strong nitride-formers. The most stable nitride is TiN followed by AlN and BN. The same two alloys have been reheated into the austenite region at 930°C for 30 minutes and water quenched to see if the boron is redistributed. These reheated samples are labelled as 12AM22AA and 12AM23AA. Finally, two quenched and tempered samples with the same composition are labelled as 12AM24 and 12AM25, Al-protected and Ti-protected respectively, to explore the effect of the tempering processes on microstructure and boron distribution.

Samples 12AM22F and 12AM22G are Al-protected steels with the same composition as 12AM22, but have different reheating times in the austenite region, 10 minutes and 180 minutes respectively.

The third group of samples have been reheated to 930°C and quenched, but have different aluminium and boron contents; 12AM15 (0.042 wt.% aluminium and 0.0030 wt.% boron) and 12AM16 (0.065 wt.% aluminium and 0.0025 wt.% boron). 12AM15D was given a different heat treatment, water quenched from 835°C directly after rolling without reheating but has the same composition as 12AM15. Both 12AM15 and 15D are therefore martensitic, and the interest is in whether the 930°C reheat stage redistributes the boron. However, a problem arose when sample 12AM15 was analysed

in the NanoSIMS because it was very magnetic. This causes serious analysis problems because both primary and secondary ions are deflected by the sample, and the data from this sample was discarded.

A final set of samples includes 13ZZ6ZBM which is an Al-protected steel containing 0.49 wt.% Mo, and 13ZZ9ZBM and 132212ZBM, which contain only 0.005 wt.% Mo and different concentrations of aluminium. All are water quenched from 930°C for 30 minutes and are fully martensitic. The aim with this set of samples is to study the effect of Mo on boron distribution.

Sample 12AN15 is an aluminium protected steel reference sample (with some Mo and Cr additions) that has been heat treated to 930°C for 15 minutes and water quenched. This is the sample on which much of the initial calibration for the NanoSIMS analysis reported in this chapter was carried out.

4.2.1 Full Manufacturing Sequence

The samples were extracted at four stages of the manufacturing process, as shown in Figure 4.1. Table 4.1 summarises the samples and experimental conditions.

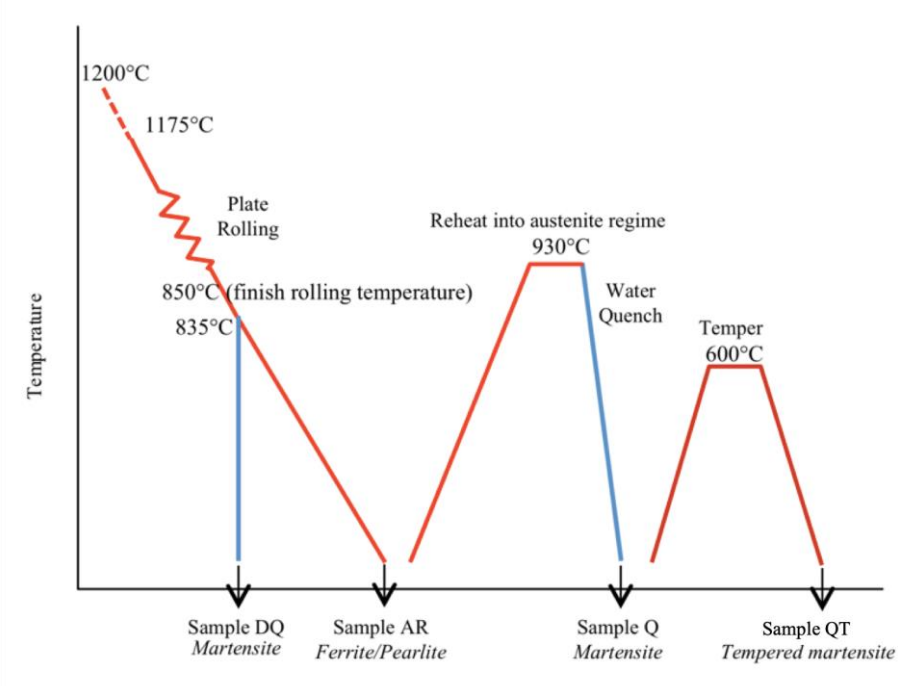


Figure 4.1: Heat treatment of the samples studied in this chapter: DQ, direct quenched; AR, as-rolled; Q, quenched; QT, quenched and tempered

Table 4.1: Summary of the sample processing conditions

Sample	Condition
12AN15 (Reference) Q	Reheated to 1200°C, hot rolled to 25mm plate, reheated 930°C for 15 minutes, water quenched
12AM22 (Al Protected) AR	Rolled, reheated to 1175°C, hot rolled to 15mm plate (finished rolling temperature-850°C), air cool
12AM23 (Ti Protected) AR	Rolled, reheated to 1175°C, hot rolled to 15mm plate (finished rolling temperature-850°C), air cool
12AM22AA (Al Protected) Q	Sample 12AM22 that has been reheated at 930°C for 30 minutes and water quenched
12AM23AA (Ti Protected) Q	Sample 12AM23 that has been reheated at 930°C for 30 minutes and water quenched
12AM22F Q	Sample 12AM22 that has been austenitised at 930°C for 10 minutes and water quenched
12AM22G Q	Sample 12AM22 that has been austenitised at 930°C for 180 minutes and water quenched
12AM24 (Al Protected) QT	Sample 12AM22 that has been reheated to 930°C for 30 minutes, water quenched, tempered at 600°C
12AM25 (Ti Protected) QT	Sample 12AM23 that has been reheated to 930°C for 30 minutes, water quenched, tempered at 600°C
12AM15 Q	Reheated to 1200°C, descaled, hot rolled to 20mm plate, air cool, reheated to 930°C, water quenched [plate centreline cooling rate (800-500°C) = 43°C/s
12AM16 Q	Reheated to 1200°C, descaled, hot rolled to 20mm plate, air cool, reheated to 930°C, water quenched [plate centreline cooling rate (800-500°C) = 43°C/s
12AM15D DQ	Reheated to 1200°C, descaled, hot rolled to 20mm plate, direct quenched from 835°C
13ZZ6ZBM (Mo alloyed) Q	30kg laboratory ingot rolled to 14mm plate reheated 930°C 30 minutes and water quenched
13ZZ9ZBM (Al protected good hardenability) Q	30kg laboratory ingot rolled to 14mm plate reheated 930°C 30 minutes and water quenched
13ZZ12ZBM (Al protected low hardenability) Q	30kg laboratory ingot rolled to 14mm plate reheated 930°C 30 minutes and water quenched

4.2.2 Materials Composition

The materials under investigation were all high-strength, low carbon steels. The chemical compositions of the steels are shown in Table 4.2, and the significant changes highlighted by coloured cells. The chemical data was provided by Tata Steel.

Table 4.2: Chemical compositions of the steels studied

Chemical composition in wt.%															
	C	Si	Mn	P	S	Cr	Mo	Ni	Cu	Al	N	Nb	V	Ti	B
12AN15 (Reference)	0.19	0.35	1.23	0.009	0.002	0.24	0.510	0.02	0.02	0.056	0.0042	0.031	0.027	0.0031	0.0024
12AM22 12AM24 (Al protected)	0.14	0.42	1.39	0.007	0.002	0.02	0.002	0.17	0.01	0.055	0.0040	0.031	0.059	0.0030	0.0023
12AM23 12AM25 (Ti Protected)	0.14	0.40	1.42	0.008	0.003	0.03	0.002	0.02	0.01	0.030	0.0050	0.032	0.062	0.0330	0.0020
12AM15 12AM15D	0.14	0.32	1.36	0.016	0.0016	<0.005	<0.005	<0.005	<0.005	0.042	0.0050	<0.001	<0.001	0.0014	0.0030
12AM16	0.16	0.33	1.39	0.011	0.0018	<0.005	<0.005	<0.005	<0.005	0.065	0.0050	<0.001	<0.001	0.0001	0.0025
13ZZ6ZBM (Mo alloyed)	0.15	0.33	1.39	0.011	0.0017	0.007	0.490	<0.005	<0.005	0.061	0.0035	<0.001	<0.001	0.0008	0.0025
13ZZ9ZBM	0.155	0.33	1.43	0.011	0.0018	<0.005	<0.005	<0.005	<0.005	0.077	0.0080	<0.001	<0.001	0.0009	0.0025
13ZZ12ZBM	0.155	0.32	1.38	0.009	0.0014	<0.005	<0.005	<0.005	<0.005	0.057	0.0060	<0.001	<0.001	0.0001	0.0025

4.3 Microstructure

For microstructural characterisation, the samples were prepared and polished as described in Chapter 3.2. Secondary electron microscopy (SEM) and optical microscopy were used to the image the microstructures, which depended upon the processing history and heat treatment conditions.

Figure 4.2 illustrates the iron-carbon phase diagram which shows the phase transformations that create the microstructures of low carbon steels above and below the eutectoid temperature (727°C) as a function of composition, C_0. When the alloy is cooling down from the dotted vertical line point *y* to *y'*, the microstructure changes from austenite (γ) at point *c* at about 875°C to γ and ferrite (α) at point *d* at about 775°C. Small α nuclei start to form along prior austenite grain boundaries and grow upon cooling to point *e*. This type of ferrite is called pro-eutectoid ferrite as it formed above the eutectoid temperature, and from an alloy below the eutectoid composition. When the temperature falls to point *f* below the eutectoid temperature, all of the γ phase enriched with carbon transforms into pearlite (α + Fe_3C) (Callister, 2001). The microstructure of pro-eutectoid ferrite and pearlite can be observed from the as-rolled samples in section 4.3.1.

In this study, when the steel samples are rapidly cooled (or water quenched) from the austenite region (930°C), a non-equilibrium single phase called martensite is formed by a diffusionless transformation from austenite. Carbon atoms are trapped in the octahedral sites of the body-centered cubic (BCC) structure because of rapid cooling leaving insufficient time for the carbon to form pearlite (α + Fe_3C). The BCC structure is elongated along one of its dimensions because the solubility of carbon in the structure is exceeded when martensite forms, hence the face-centered cubic (FCC) austenite experiences transformation into body-centered tetragonal (BCT) martensite (Callister, 2001, Krauss, 2015). The characteristic lamellar microstructure of martensite can be observed from the as-quenched samples in section 4.3.2.

Most as-quenched steels cannot be used directly for any applications due to martensite being hard and brittle, and internal stresses that are introduced during quenching may have a weakening effect. These internal stresses may be relieved by a heat treatment called tempering by heating the martensitic steel to temperature below the eutectoid (Callister, 2001). In this study, the steels were tempered at 600°C. When the steel is heated to a tempering temperature, the carbon atoms diffuse from the octahedral sites to form carbides. Therefore, by diffusional processes, the BCT martensite is replaced by the formation of tempered martensite, a mixture of ferrite and cementite (α + Fe_3C phases) or other carbide phases depending on the other solute elements (Krauss, 2015). This heat treatment improves the ductility and toughness of the steels. The microstructure of tempered martensite can be observed from the quenched and tempered samples in section 4.3.3.

In this section, the microstructures of steels after different heat treatment and processing histories have been discussed, and Figure 4.3 summarises the phase transformation from austenite (γ) to proeutectoid ferrite (α) and then to pearlite (α + Fe_3C), and to martensite (BCT phase) and tempered martensite (α + Fe_3C phases) resulting from slow cooling, rapid quenching and tempering respectively. The solid arrows represent transformations involving diffusion (slow cooling and tempering) while the dashed arrow represents a diffusionless transformation (rapidly quenched).

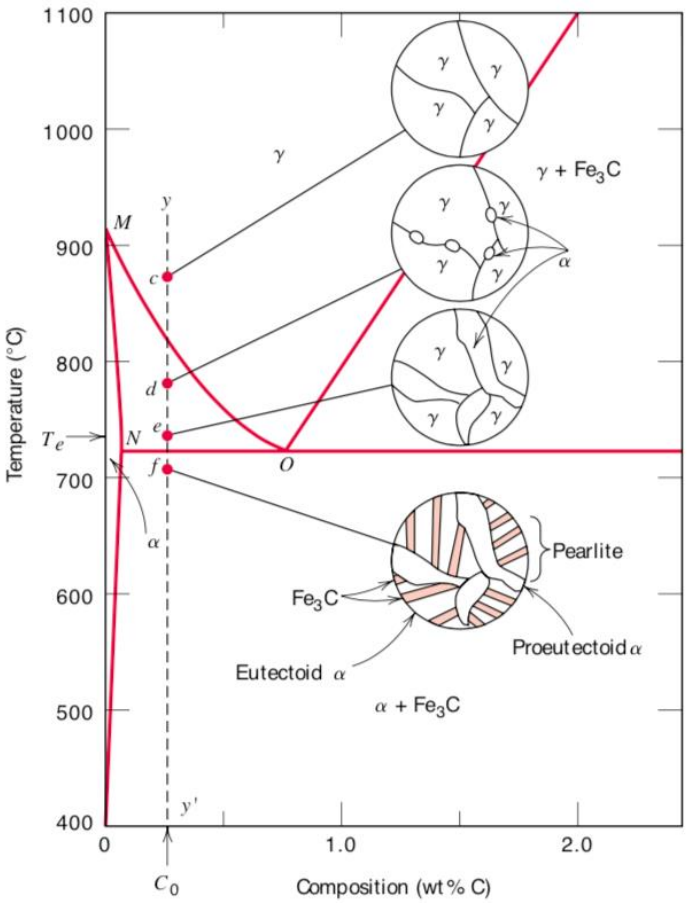


Figure 4.2: Iron-carbon phase diagram of steel showing the microstructures of the alloy at different temperatures (point *c*, *d*, *e* and *f*) at composition C_0 cooling from vertical line *y* to *y'*. Republished with permission of John Wiley & Sons – Books, from (Callister, 2001); permission conveyed through Copyright Clearance Center, Inc.

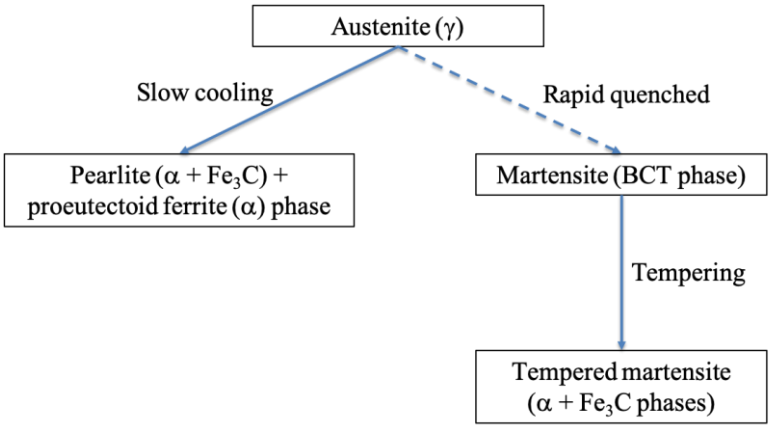


Figure 4.3: Phase transformation from austenite (γ) to pearlite (α + Fe_3C) and proeutectoid ferrite (α) during slow cooling or to martensite during rapid quenched. Martensite (BCT phase) is replaced by tempered martensite, a mixture of ferrite (α) and cementite (Fe_3C) during tempering heat treatment. Redrawn with permission of John Wiley & Sons – Books, from (Callister, 2001); permission conveyed through Copyright Clearance Center, Inc.

4.3.1 As-rolled Samples

Elongated grains were observed in the as-rolled samples due to the rolling process, and these samples contained a mixture of proeutectoid ferrite grains and pearlite. When the samples were air cooled, grains of ferrite start to form in the austenitic matrix and the remaining austenite becomes enriched in carbon and at the eutectoid temperature transforms into pearlite. The formation of microstructural banding consisting of alternating bands of proeutectoid ferrite and pearlite is a common phenomenon in hot rolled low alloy steels. Banding of ferrite/pearlite depends on microsegregation of alloying elements, cooling rates and austenite grain size (Offerman et al., 2002). The two-phase pearlite structure cannot be easily resolved by optical microscopy but can be resolved by secondary electron microscopy as shown in Figure 4.4 for sample 12AM22 (Al-protected) and Figure 4.5 for sample 12AM23 (Ti protected).

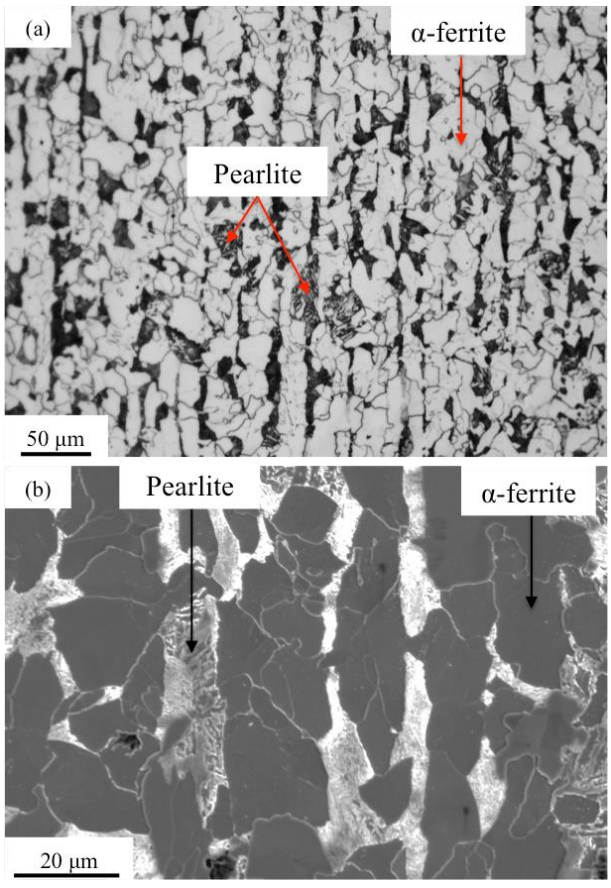


Figure 4.4: Microstructure of 12AM22 (Al-protected) as-rolled sample. (a) Optical microstructure of the steel showing dark bands of pearlite in a white α-ferrite matrix. (b) SEM micrograph showing a clearer view of the pearlite colonies and α-ferrite grains that appear darker in this image.

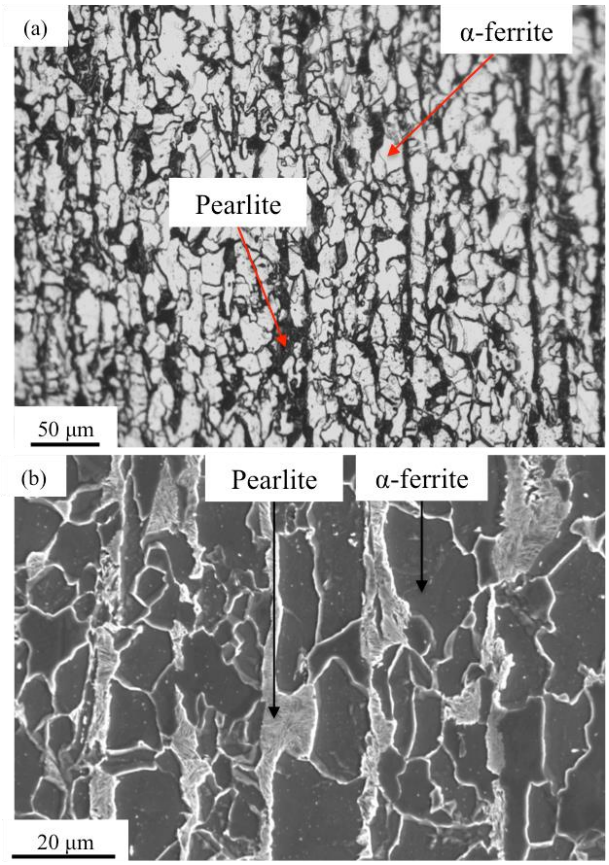


Figure 4.5: Microstructure of 12AM23 (Ti-protected) as-rolled sample. (a) Optical microstructure of the steel showing dark band pearlite in a white α-ferrite matrix. (b) SEM micrograph showing a clearer view of the pearlite colonies and α-ferrite grains.

4.3.2 As-quenched Samples

In the water quenched condition, a martensitic microstructure was developed in all the quenched samples, Figure 4.6 to Figure 4.9. The needle-shaped grains are the martensite phase, and the white regions are austenite that failed to transform during rapid quench, and is called retained austenite. The martensitic transformation is completely diffusionless so not even the interstitial carbon atoms will diffuse during the phase transformation. The transformation from austenite to martensite takes place by shear deformation, i.e., the cooperative movement of iron atoms (Bhadeshia and Honeycombe, 2006).

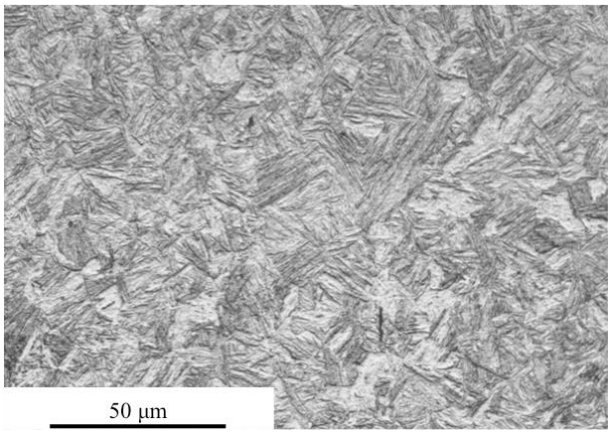


Figure 4.6: Needle shaped martensitic microstructure of the as-quenched 12AN15 reference sample acquired with optical microscope. This reference sample was reheated at 930°C for 15 minutes and water quenched.

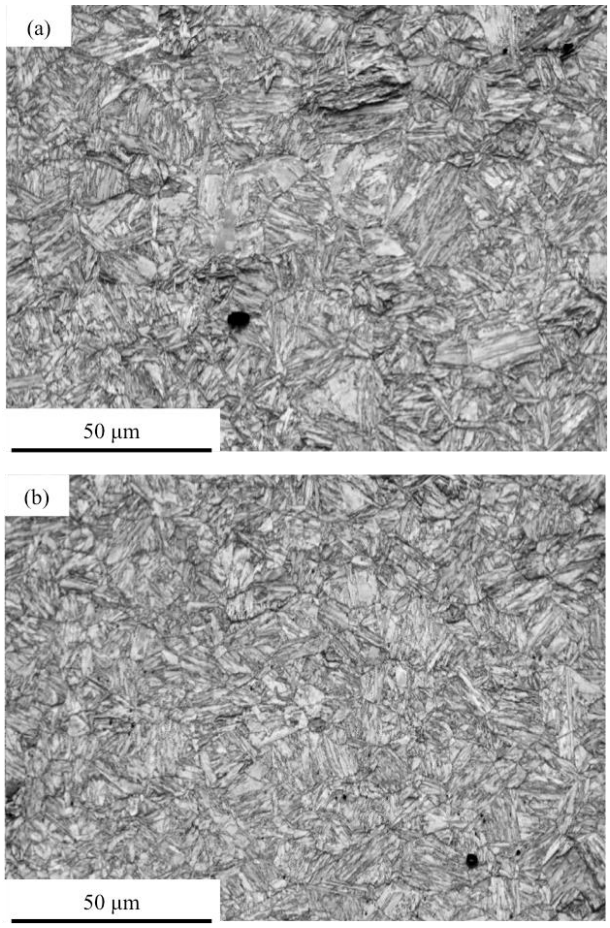


Figure 4.7: SEM images of the martensitic microstructure of as-quenched samples (a) aluminium protected 12AM22AA and (b) titanium protected 12AM23AA. Both samples clearly show bundles of parallel laths of martensite. These samples were reheated in the austenite regime at 930°C for 30 minutes and water quenched.

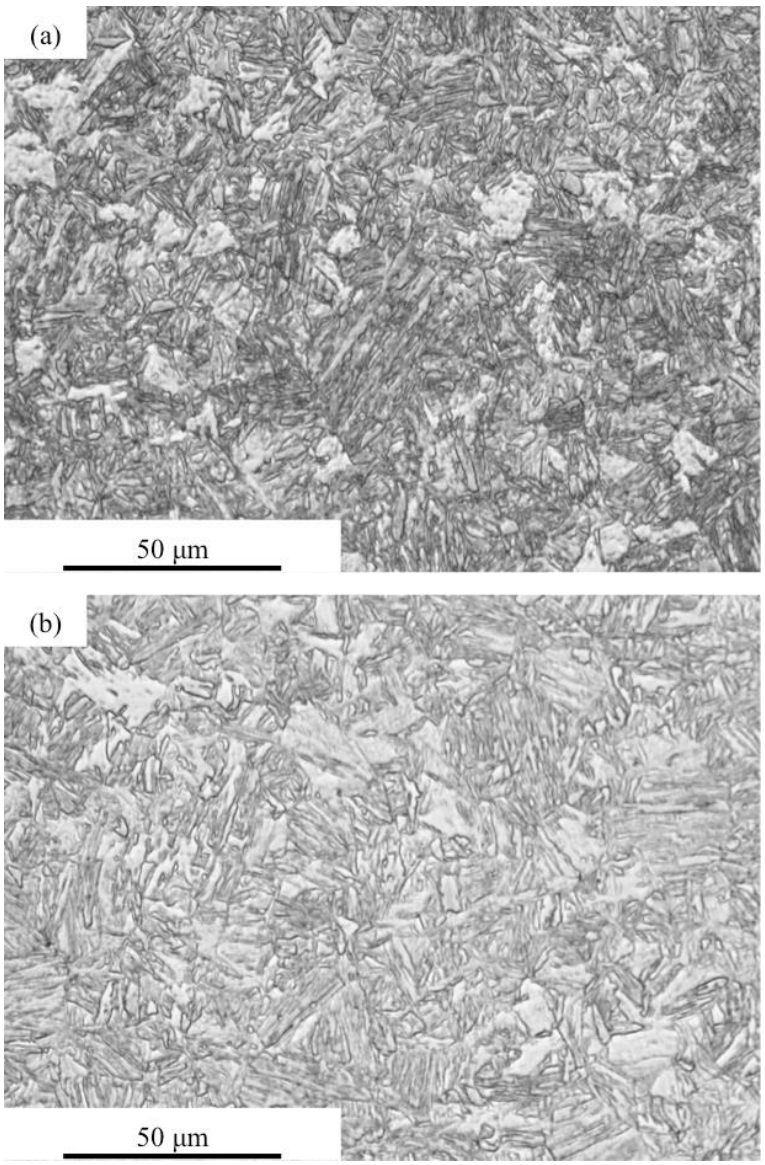


Figure 4.8: Optical microscope images of the martensitic microstructure of as-quenched samples (a) 12AM22F and (b) 12AM22G with reheating times in the austenite region (930°C) of 10 minutes and 180 minutes respectively. 12AM22F with the shorter reheating time shows finer lath martensite.

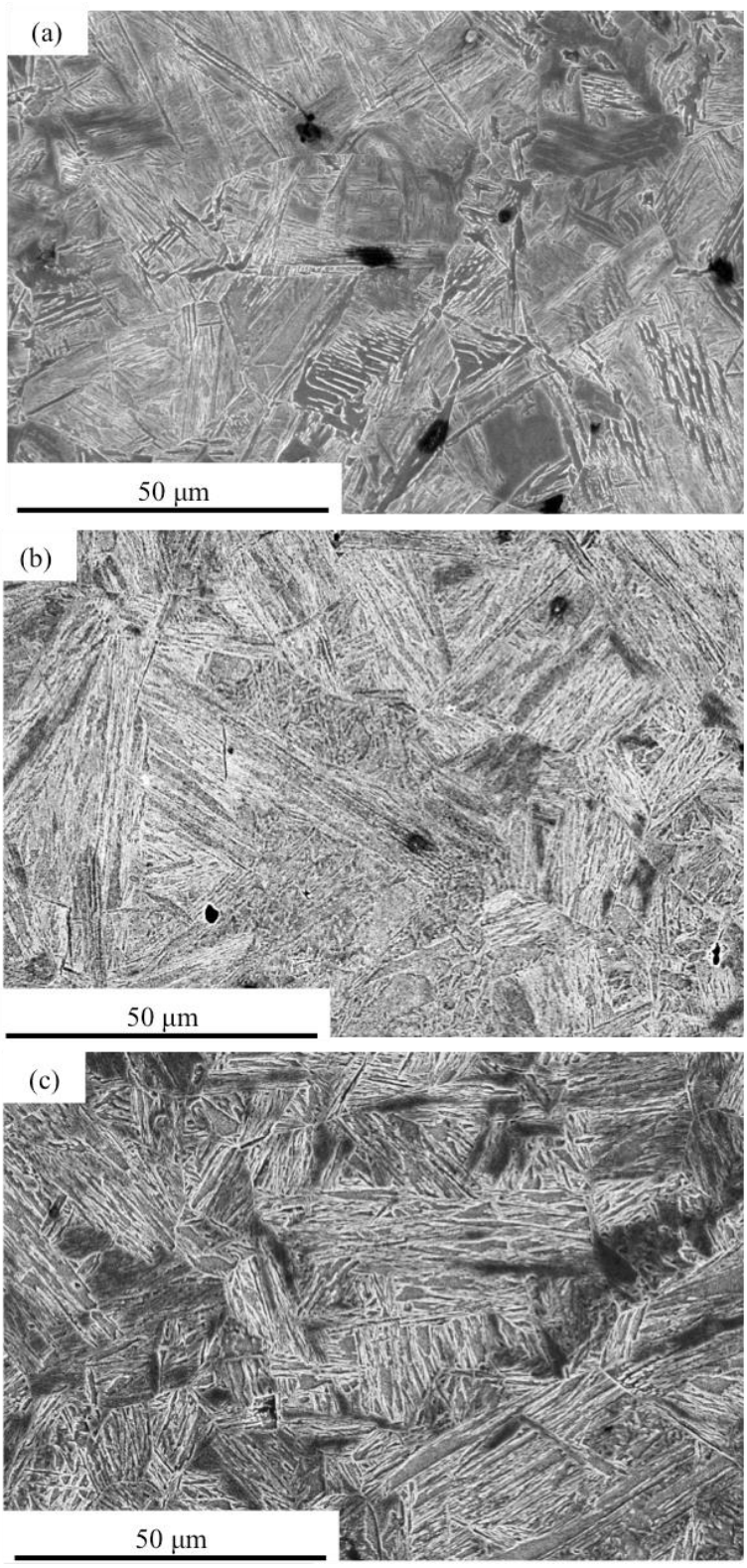


Figure 4.9: SEM images showing the martensitic microstructure of (a) sample 12AM15 and (c) 12AM16 water quenched from 930°C plate centreline cooling rate (800-500°C) = 43°C/s, and (b) direct quenched sample 12AM15D showing a very fine lath martensite when compared to the other samples.

4.3.3 Quenched and Tempered Samples

Quenching and then tempering are well-established means to give steels the best combination of strength and toughness due to the precipitation of a fine dispersion of alloy carbides during tempering (Krauss, 2015). The microstructures of the 12AM24 (Al-protected) and 12AM25 (Ti-protected) steels after this heat treatment are rather similar, typically exhibiting a tempered martensitic matrix with a fine dispersion of carbide precipitates along lath martensite boundaries and prior austenite grain boundaries. The microstructure of these steels is shown in Figure 4.10.

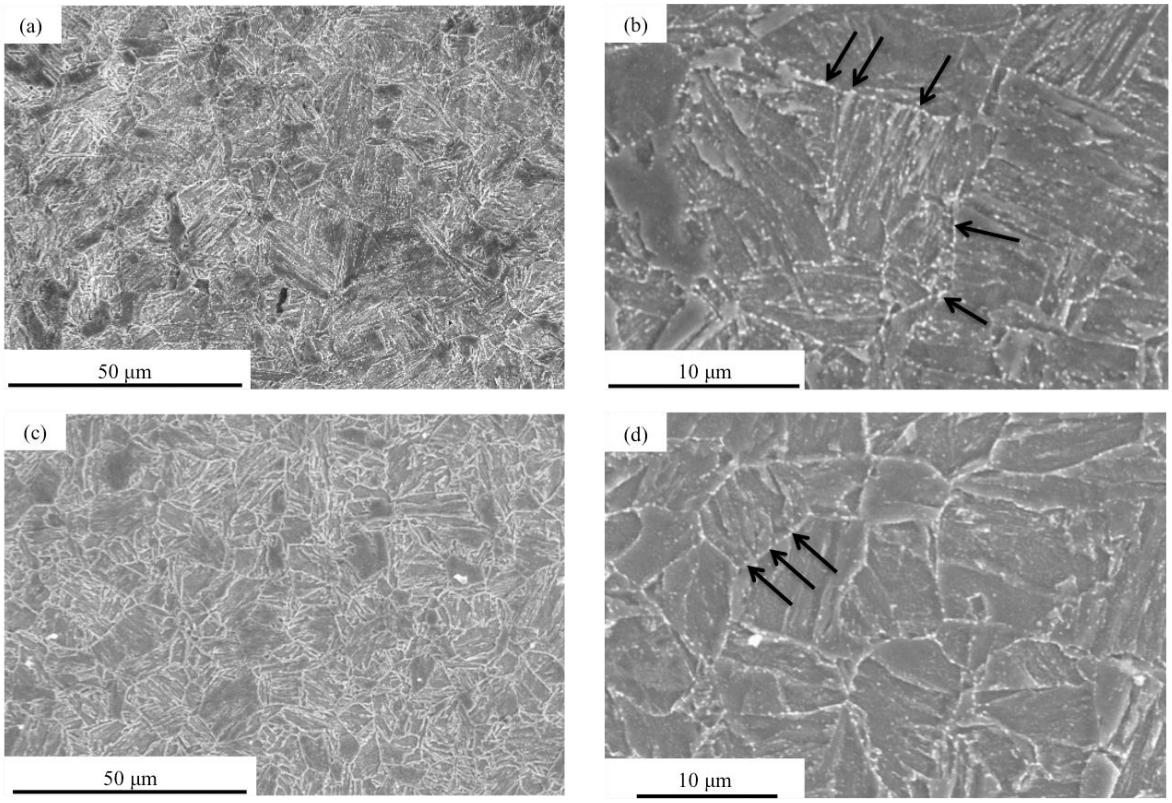


Figure 4.10: SEM images showing the tempered martensitic microstructure of sample (a) 12AM24 (Al-protected) and (c) 12AM25 (Ti-protected) at low magnification. Higher magnification SEM images focussing on the carbide precipitates (highlighted by arrows) along the grain boundaries on (b) 12AM24 (Al-protected) and (d) 12AM25 (Ti-protected).

4.4 Boron Distribution in Steels

The secondary ion images of the $^{11}B^{16}O_2^-$ signal for the aluminium and titanium protected steels subjected to the heat treatments described in section 4.2 are now discussed. Each material has been imaged with an area at least 150 μm^2 to give a more representative image of the distribution of impurity species in the samples, much larger than the average original austenitic grain size. The average grain size was calculated by dividing the number of intersections by the actual length line. The average grain size for the as-quenched reference sample 12AN15 was 10 μm. In order to be able to compare between results from the different steels, a fixed counting time for each image was chosen of 30,000 μs/px which took about 30 minutes for a 256 x 256 pixel image, and a large primary aperture (D1=2) with 300 μm diameter was chosen to give adequate lateral resolution without compromising on sensitivity. However, due to matrix effects and differences in the RSF values, it is difficult to compare the counts in one ion image with the counts of another. Several images with a 40 x 40 μm or 50 x 50 μm raster size were imaged and stitched together to give a map of the sample surface over 4 x 4 or 3 x 3 sets of images. Each of these composite images required two or three days of analysis. Each new image area was cleaned and implanted with Cs^+ as described in section 3.7.1.

4.4.1 Reference Sample 12AN15 – Al protected, as-quenched

Figure 4.11 shows a 4 x 4 set of $^{11}B^{16}O_2^-$ images over a 160 μm x 160 μm area. $^{11}B^{16}O_2^-$ images are scaled from 0 to 10 counts for clarity although there are pixels containing more counts than this. Images 1 to 8 were taken on day 1, and images 9 to 16 on day 2. There was clearly a problem in tuning for this initial experiment on this sample since there is a noticeable difference in the brightness and contrast of the images taken on the 2 days. Day 1 images appear to be much clearer than day 2 images. On day 2, some of the images (9, 10, 11, 13 and 16) show darker or almost no counts on the top half. This problem occurred because of misalignment of the secondary ion beam tuning probably due to magnet drift caused by changes in room temperature.

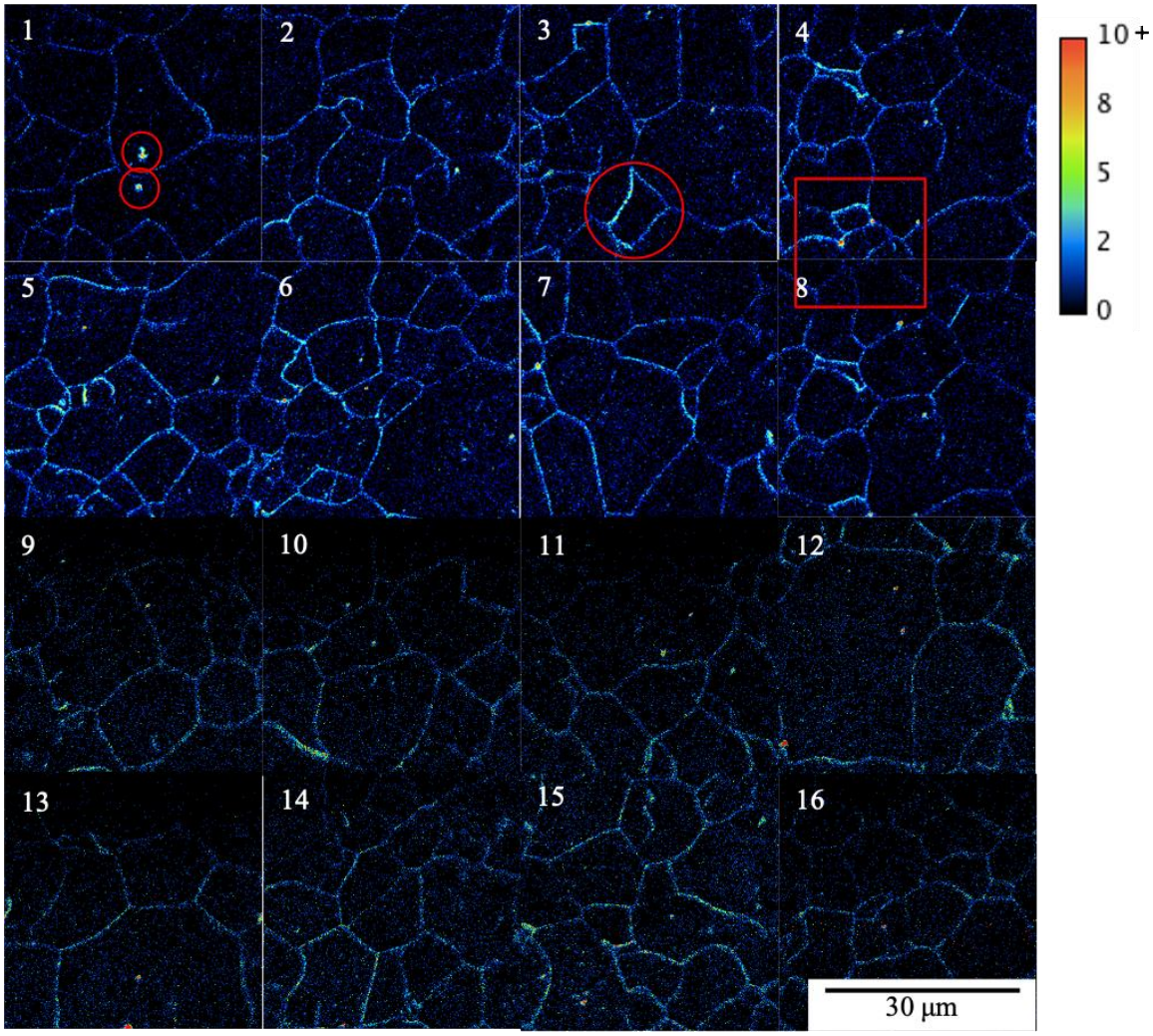


Figure 4.11: Ion micrographs showing the distribution of boron (mapped as $^{11}B^{16}O_2$) in sample 12AN15 (Reference sample: As-quenched). The red circles on image 1 indicate boron containing particles and the red circle on figure 3 indicates the location of subsequent line scans across the grain boundaries. The red square indicates the 20 µm x 20 µm area that was selected for high resolution imaging using D1=3 aperture.

From the data shown in Table 4.3, the current at the sample using D1=2 was measured in FCo as 1.2 pA on day 1 and 1.1 pA on day 2. However, the average total $^{11}B^{16}O_2^-$ counts on day 1 were approximately twice as high as on day 2 indicating it was a problem with the secondary alignment not the primary ion beam. In all the presentation of quantitative results below, the counts have been normalised by the beam current measured on the day of measurement so that every data set can be compared with other samples measured on different days. It is much harder to normalise for differences in secondary beam alignment since there is no obvious normalisation parameter measured apart from the total number of detected counts which may depend strongly on different

areas of the sample. Matrix effects can also lead to differences of several orders of magnitude in the detected ion signal and must be carefully considered if the results are to be accurately interpreted as discussed in Section 2.2.5.

Table 4.3: Total and normalised $^{11}B^{16}O_2$ counts on as-quenched reference sample 12AN15 relating to the images shown in Figure 4.11.

Image Number	Total $^{11}B^{16}O_2^-$ counts	Beam current on sample (pA)	Normalised $^{11}B^{16}O_2^-$ intensities: Total $^{11}B^{16}O_2^-$ counts/beam current, (counts/pA)
1	7973	1.2	6644
2	13290	1.2	11075
3	13599	1.2	11333
4	14271	1.1	12974
5	17248	1.2	14373
6	16469	1.2	13724
7	14265	1.2	11888
8	9903	1.2	8253
9	6678	1.1	6071
10	6236	1.1	5669
11	5676	1.1	5160
12	9694	1.1	8813
13	6116	1.1	5560
14	9602	1.1	8729
15	12674	1.1	11522
16	6561	1.1	5965

The $^{11}B^{16}O_2^-$ ion maps, as shown in Figure 4.11, reveal that the boron is primarily detected at the prior austenite grain boundaries rather than in the grain interior, with strong grain boundary segregation in this reference sample. Only a few small boron containing particles were observed in this sample as highlighted by red circles in image 1. Image 1 is enlarged in Figure 4.12 and two line scans were performed over the particles in the grains. These line scans are shown in Figure 4.13. The line scans were averaged over 10 pixels width to improve the counting statistics, and a step size of 0.16 μm was used along the arrow shown in the $^{11}B^{16}O_2^-$ image in Figure 4.12. The particle on line 1 is slightly bigger than the particle on line 2, thus the boron intensity on line 1 is almost twice that of the particle on line 2.

There are also significant differences in the amount of boron segregated at different grain boundaries, and this may correlate with grain boundary misorientations; certain misorientations being more favourable for boron segregation (Kurban et al., 2006). To give an overview of the different amount

of boron segregated to these grain boundaries, 3 line scans were performed over 3 different grain boundaries around the same grain in image 3. Image 3 is expanded and shown in Figure 4.14. The line scans are presented in Figure 4.15, indicating that the boron intensity on grain boundary 1 is approximately 2 times higher than on grain boundaries 2 and 3.

This measured boron distribution clearly shows that the retardation effect of boron on the austenite to ferrite transformation occurs due to segregation of boron to the prior austenite grain boundaries. This is clear when we compare the martensitic structure in Figure 4.6 with the segregation behaviour to the boundaries around much larger equiaxed grains. This segregation of boron is expected to occur when the sample was held at the austenizing temperature, 930°C for 15 minutes by equilibrium segregation (Tingdong et al., 1990) and through the non-equilibrium segregation mechanism during cooling from the austenizing temperature (Mun et al., 2012, Faulkner, 1981, Faulkner, 1996).

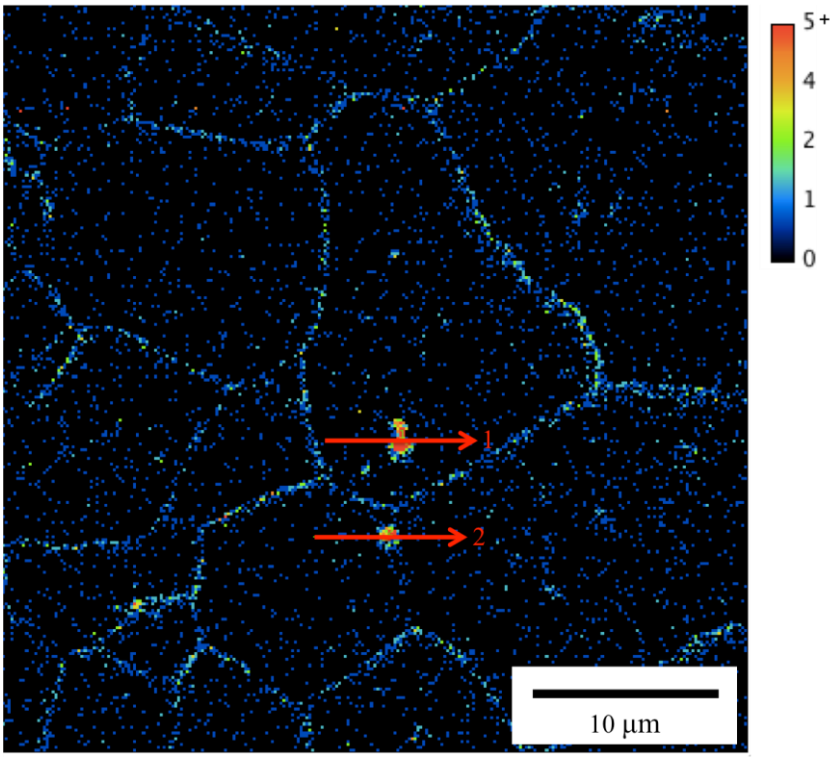


Figure 4.12: Enlargement of Image 1 as shown in Figure 4.11. Red arrows indicate the position and direction of the line scans across two boron rich particles in sample 12AN15.

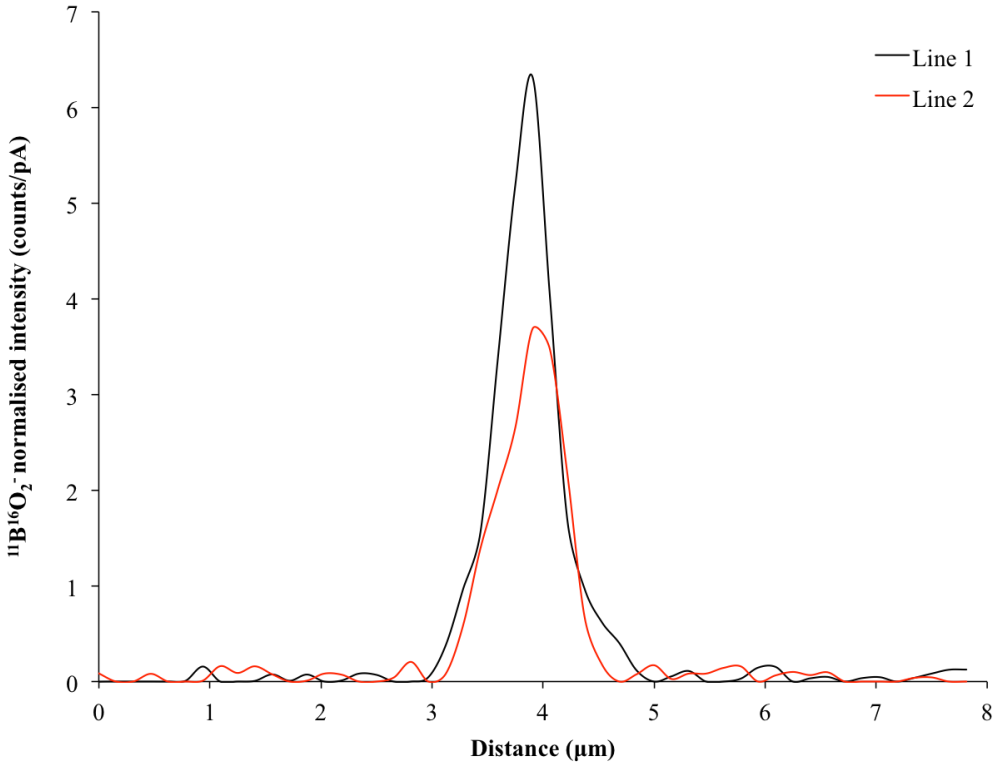


Figure 4.13: Line scans for $^{11}B^{16}O_2^-$ across the two boron rich particles as indicated by the red arrows marked 1 and 2 in Figure 4.12.

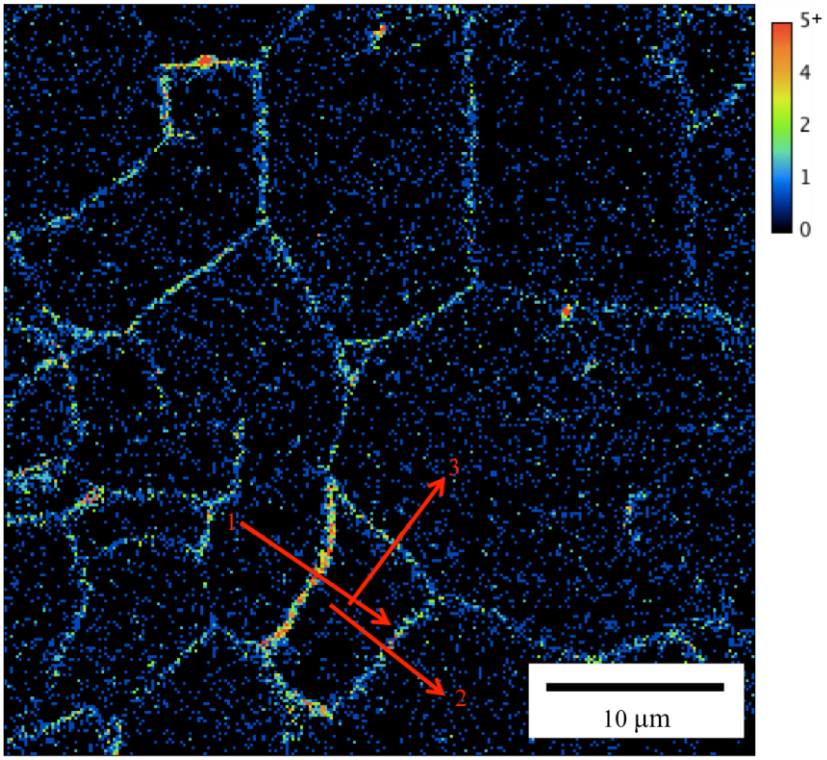


Figure 4.14: Enlargement of Image 3 as shown in Figure 4.11. Red arrows indicate the position and direction of the line scans across three grain boundaries with different boron segregation levels in sample 12AN15.

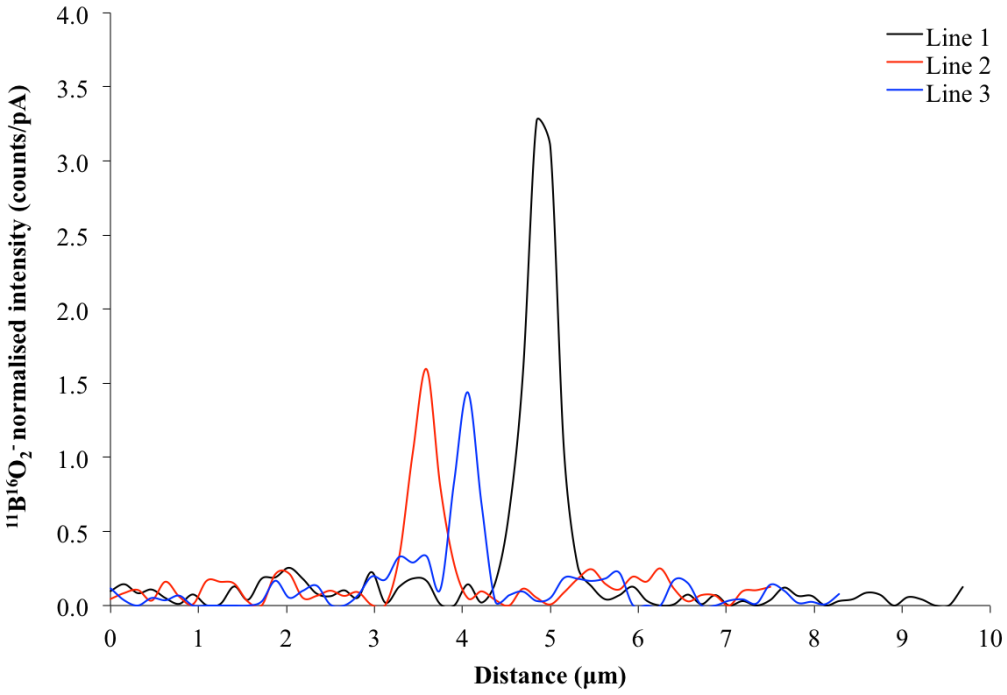


Figure 4.15: Line scans for $^{11}B^{16}O_2^-$ across three grain boundaries with different boron segregation levels on sample 12AN15 as indicated by the red arrows marked 1, 2 and 3 in Figure 4.14.

A 20 by 20 µm^2 area highlighted in the red square in Figure 4.11 was selected for high resolution imaging using a smaller aperture, D1=3. Longer counting times were required, due to the smaller aperture, to give a clear view of boron segregation at different prior austenite grain boundaries and possible boron containing precipitates in the sample. The dwell time was set to 60,000 µs/pixel per image and a total of 11 sequential images were summed. Summed images of the $^{12}C^-$, $^{11}B^{12}C^-$, $^{11}B^{14}N^-$ and $^{11}B^{16}O_2^-$ maps are shown in Figure 4.16. The martensitic microstructure of this quenched sample can be seen very clearly in the SE image and the $^{12}C^-$ map shows the inhomogeneous carbon distribution of the structure. The $^{11}B^{16}O_2^-$ map clearly shows the differences in the amount of boron segregated at different prior austenite grain boundaries. This higher resolution image also gives some evidence of intra-granular fine boron precipitates that can hardly be seen in Figure 4.11. Three large boron-rich particles were observed near the grain boundary as can be seen in the $^{11}B^{12}C^-$, $^{11}B^{14}N^-$ and

$^{11}B^{16}O_2^-$ maps. However, grain boundary segregation and some small boron precipitates do not appear in the $^{11}B^{14}N^-$ map.

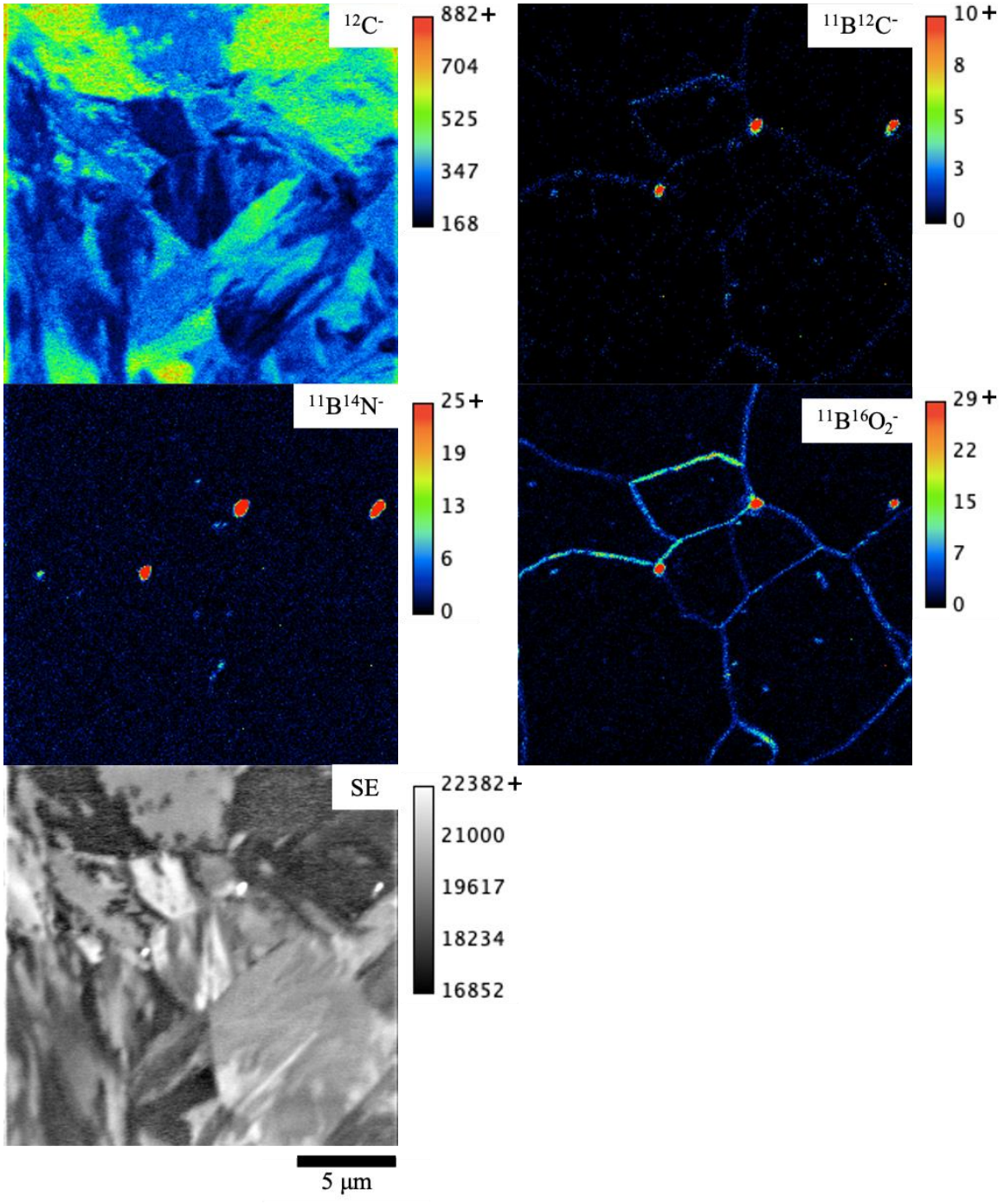


Figure 4.16: High resolution imaging using aperture D1=3 on selected area from Figure 4.11 of as-quenched reference sample 12AN15 showing the NanoSIMS maps of $^{12}C^-$, $^{11}B^{12}C^-$, $^{11}B^{14}N^-$, $^{11}B^{16}O_2^-$ and the secondary electron (SE) image. These images were summed from 11 sequential maps of 20 x 20 µm area with dwell time 60,000 µs/px/image.

4.4.2 Comparison of Al Protected Steels with Different Heat Treatments (12AM22, 12AM22AA, 12AM22F, 12AM22G and 12AM24)

4.4.2.1 Sample 12AM22 (as-rolled)

The process of hot deformation is suggested to increase the stability of boron segregating to austenite grain boundaries during cooling. By grain refinement, the grain boundary area will increase, and Mun et al. (2012) suggest that the effect of boron on hardenability in low carbon high strength steel could be maximized at small grain size. This directly conflicts with the previously referenced predictions of Faulkner (1981) that non-equilibrium segregation effects should be stronger at larger grain sizes. The significant increase of boron segregation at higher temperature i.e. 1200°C by non-equilibrium segregation and grain coarsening may lead to borocarbide precipitates that decrease the hardenability effect of boron in high strength steel (Mun et al., 2012).

Figure 4.17 shows a 4 x 4 set of $^{11}B^{16}O_2^-$ images over a 200 μm x 200 μm area. $^{11}B^{16}O_2^-$ images below are scaled from 0 to 10 counts for clarity although there are pixels containing more counts than this. It is clear that boron has started to precipitate during the hot rolling process as many large boron precipitates were observed in this sample. Much less segregation of boron along grain boundaries was observed in stark contrast to the 12AN15 as-quenched reference sample.

In image 14 of Figure 4.17, there is some indication of boron segregation at a grain boundary. Image 14 is enlarged in Figure 4.18 and a line scan performed over the grain boundary showing boron segregation and two line scans over boron containing particles. These line scans were averaged over 10 pixels width to improve the counting statistics and a step size of 0.2 μm, and are shown in Figure 4.19. The normalised $^{11}B^{16}O_2^-$ intensity on the grain boundary as indicated by line 1 is 1.3 counts/pA, which is 42 times lower than on the particle in line 2 and 7 times lower than on the smaller particle in line 3.

In image 13 in Figure 4.17, boron is also present in a stringer of large inclusions. The particles were very closely spaced and their size and shape indicated that the particles had been formed by the

break-up of a larger inclusion. It is likely that these lined up particles were formed along the rolling direction.

The total boron counts and the normalised intensities for the $^{11}B^{16}O_2^-$ maps shown in Figure 4.17 are summarised in Table 4.4. The sample beam current was measured in the FCo as 1.8 pA. The quantitative analysis of total boron counts for all the samples will be presented in section 4.5.2. The highest total boron counts are from image 13 which contains the lined up row of particles.

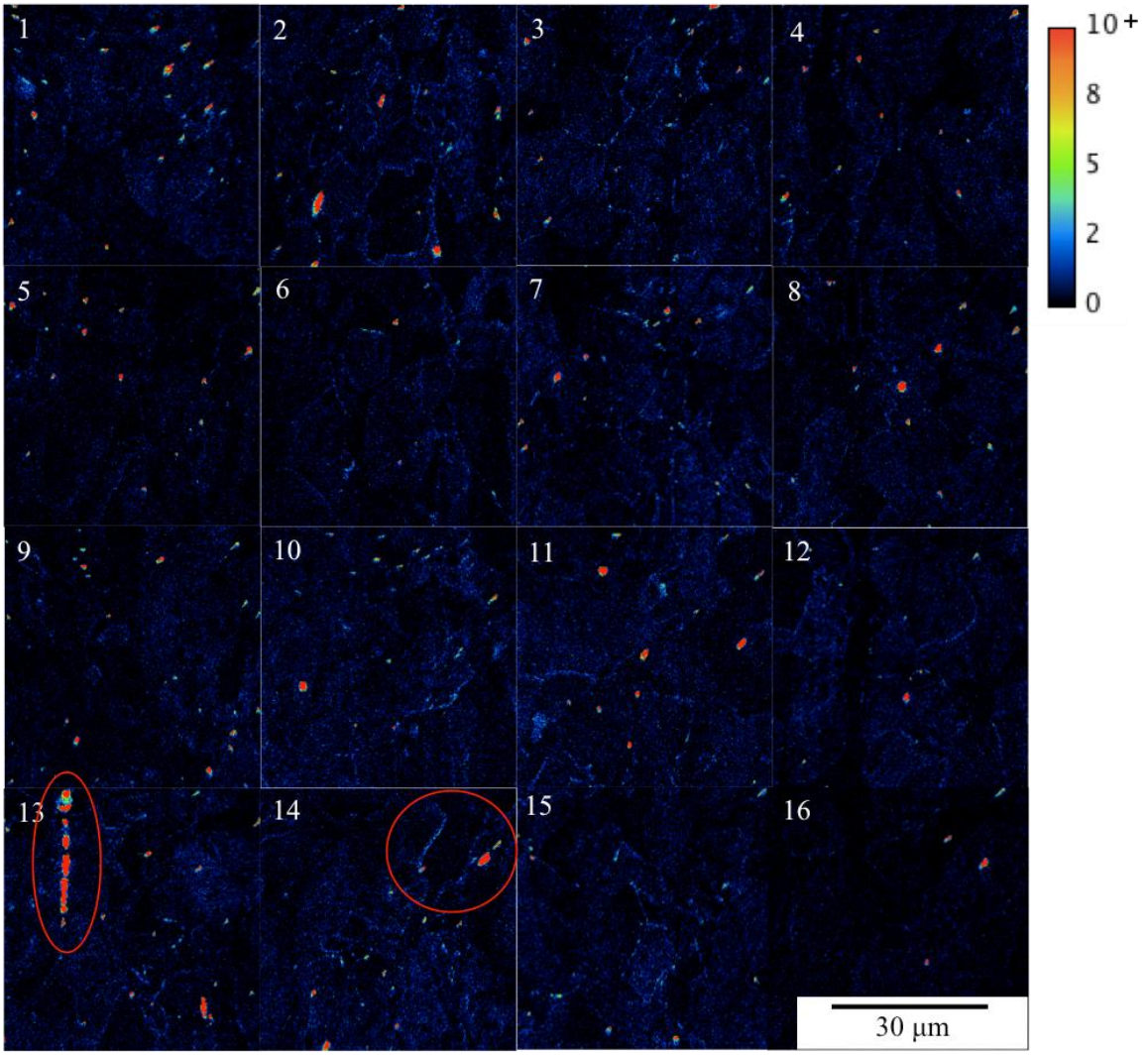


Figure 4.17: Ion micrographs showing the boron distribution, mapped as $^{11}B^{16}O_2$, in as-rolled, aluminium protected sample 12AM22. The red oval in image 13 shows the stringer produced during rolling process. The red circle in image 14 indicates the location of subsequent line scans on the grain boundaries and boron containing particles.

Table 4.4: Total and normalised $^{11}B^{16}O_2$ counts on as-rolled sample 12AM22 relating to the images shown in Figure 4.17.

Image Number	Total $^{11}B^{16}O_2^-$ counts	Beam current on sample (pA)	Normalised $^{11}B^{16}O_2^-$ intensities: Total $^{11}B^{16}O_2^-$ counts/beam current, (counts/pA)
1	31744	1.8	17636
2	40545	1.8	22525
3	32468	1.8	18038
4	26869	1.8	14927
5	22413	1.8	12452
6	21802	1.8	12112
7	34339	1.8	19077
8	31332	1.8	17407
9	26184	1.8	14547
10	34822	1.8	19346
11	41253	1.8	22918
12	26607	1.8	14782
13	67820	1.8	37678
14	40052	1.8	22251
15	30298	1.8	16832
16	16122	1.8	8957

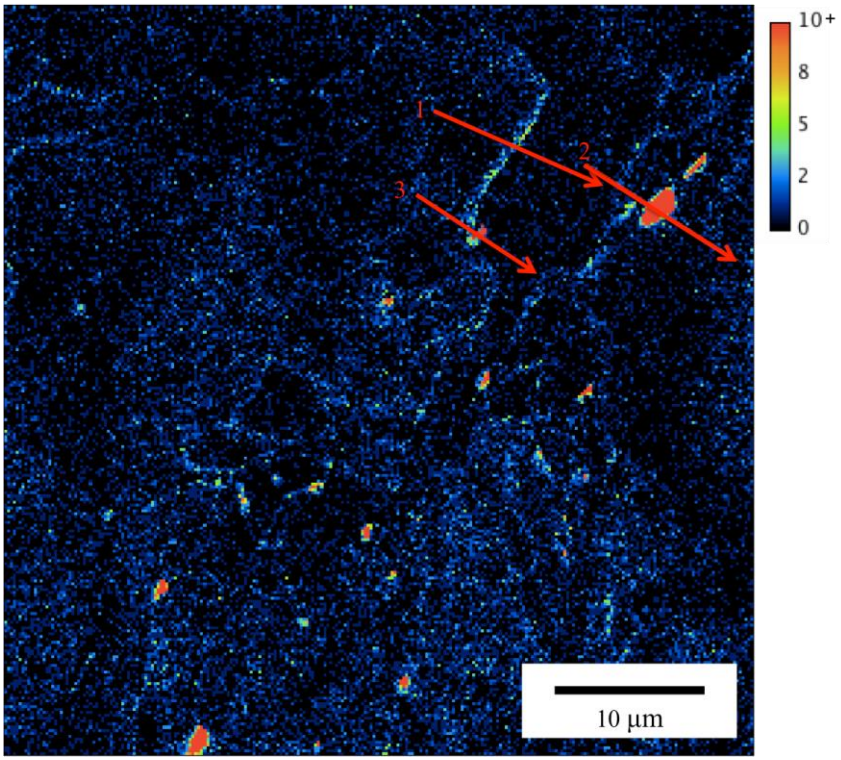


Figure 4.18: Location of the line scans across grain boundary segregation (line 1) and boron containing particles (line 2 and 3) on sample 12AM22.

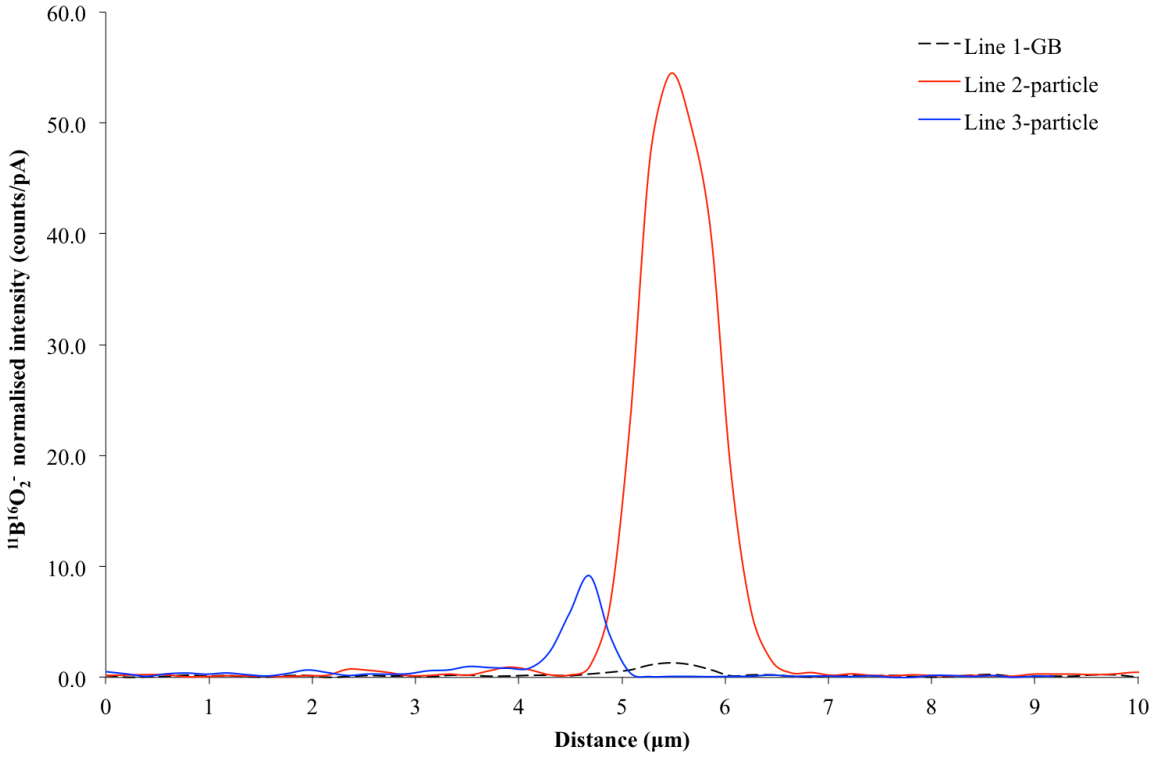


Figure 4.19: Line scans of $^{11}B^{16}O_2^-$ for the as-rolled sample 12AM22 across a grain boundary showing boron segregation (line 1) and two boron rich particles (lines 2 and 3) as indicated by the red arrows marked 1, 2 and 3 in Figure 4.18.

Figure 4.20 shows a typical data set from 12AM22 showing the five ion images simultaneously acquired from the NanoSIMS detectors. In order to improve the statistics, 25 sequential images were acquired on area 12 of Figure 4.17 adding an additional dose of 2.2 x 10^{16} Cs atoms/cm^2. The high intensity observed in the ^{12}C map indicates pearlitic regions and this can be related to the vertical band with the same microstructural features in the secondary electron image. The long acquisition time makes it much easier to see the higher $^{11}B^{16}O_2^-$ signal originating from the ferrite regions as mentioned previously. As observed in Figure 4.18, there is also some evidence of grain boundary segregation in this region as well as inter- and intra-granular boron rich precipitates.

The precipitates visible in the $^{11}B^{14}N^-$ map tend to be only the larger particles visible in the $^{11}B^{16}O_2^-$ image, and these also correlate well with bright particles observed in the SE image. With respect to the other particles that cannot be seen in the SE image, it is not possible to categorically define the type of particle since C or N could come from the matrix, surface contamination or adjacent carbide precipitates.

The $^{11}B^{12}C^-$ map appears to show grain boundary segregation around the pearlite grains. While this appears to correlate well with the $^{11}B^{16}O_2^-$ signal in these regions, the $^{11}B^{12}C^-$ signal does not show grain boundary segregation across the whole of the area, for example the long curved grain boundary in the top right of the image does not show any $^{11}B^{12}C^-$ segregation whereas it appears bright in the $^{11}B^{16}O_2^-$ image. There is an elevated signal of boron due to grain boundary segregation however the only region where there is also elevated carbon signal is at a pearlite/ferrite grain boundary. This would explain why no $^{11}B^{12}C^-$ grain boundary segregation is observed at ferrite grain boundaries as there simply is not enough carbon to generate the $^{11}B^{12}C^-$ ion.

Figure 4.21 shows the line profile across the area shown in Figure 4.20. It can be seen that the carbon signal is uniform across the ferrite grains. The absolute level of counts from each grain varies, presumably due to crystallographic effects. The carbon signal drops when in the boron rich precipitate. The line profiles across the precipitate show that this particular precipitate contains B, C and N. Although the $^{11}B^{14}N^-$ signal is higher than the $^{11}B^{12}C^-$ signal, due to matrix effects and differences in the RSF values it is difficult to be sure if there really is more nitrogen than carbon in this precipitate.

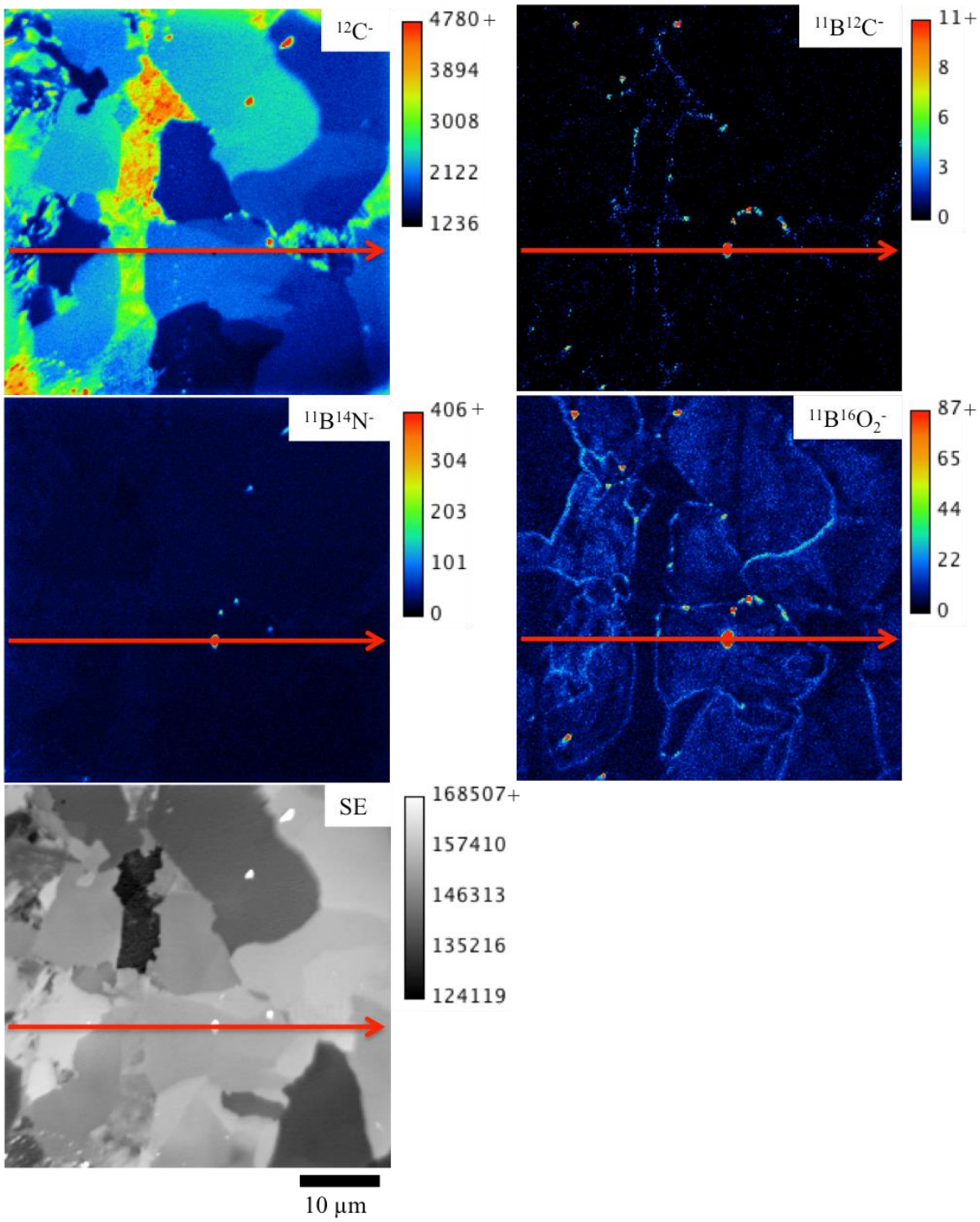


Figure 4.20: Location of the line scan on a selected area of sample 12AM22 from image 12 in Figure 4.17 showing the NanoSIMS maps of $^{12}C^-$, $^{11}B^{12}C^-$, $^{11}B^{14}N^-$, $^{11}B^{16}O_2^-$ and secondary electron (SE) image. These images were summed from 25 sequential maps to improve the counting statistics.

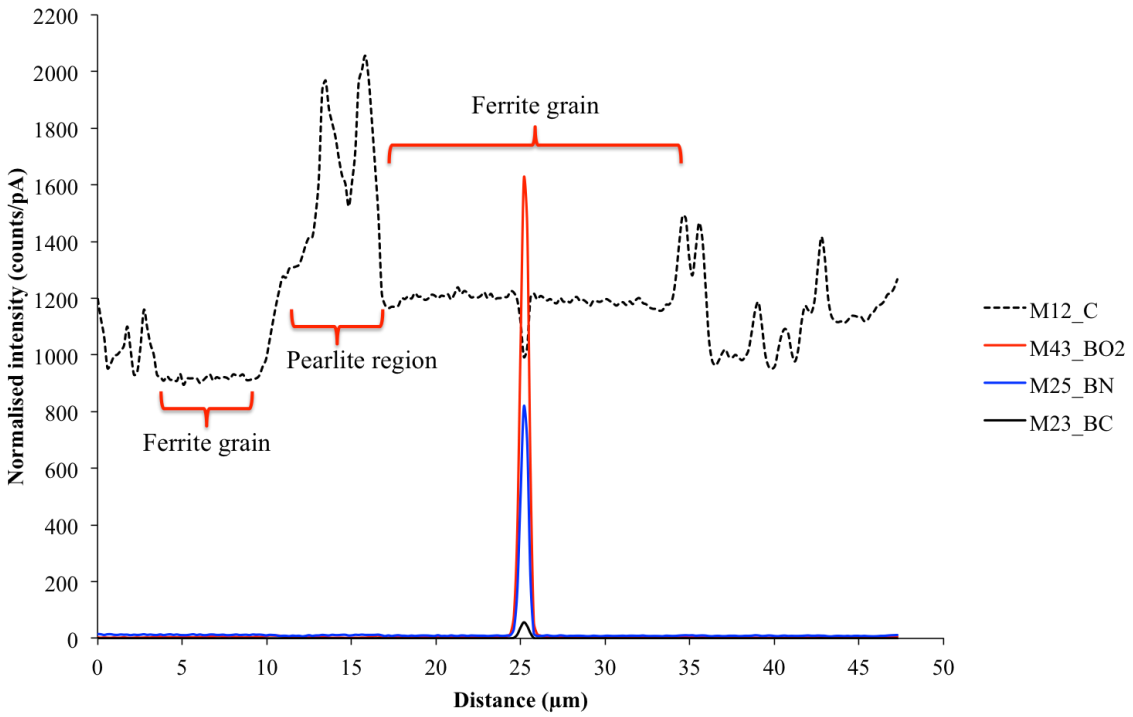


Figure 4.21: Line scans on sample 12AM22 as indicated by the red arrow in Figure 4.20 showing homogeneous carbon content in ferrite grains. The pearlite column shows high counts from carbon from the cementite plates. The location of a boron rich precipitate is also shown.

Small boron containing precipitates outline the shape of ferrite grains in the three boron signals, $^{11}B^{12}C^-$, $^{11}B^{14}N^-$ and $^{11}B^{16}O_2^-$ as can be seen in Figure 4.22. Four distinct particles were observed in the $^{11}B^{14}N^-$ map. One large particle was located within the grain while the other three particles were on the grain boundary. To distinguish between the boron precipitates, the $^{11}B^{12}C^-$ image was overlaid with the $^{11}B^{14}N^-$ image. The image shows $^{11}B^{12}C^-$ in red and $^{11}B^{14}N^-$ in blue. From the colour overlay image it can be seen that the three purple boron particles are a combination of $^{11}B^{12}C^-$ and $^{11}B^{14}N^-$ signal and perhaps can be identified as borocarbonitrides while others are boron carbides or boronitrides. To confirm the exact types of precipitates TEM analysis is required. A TEM study on almost the same composition of this sample shows large BN precipitates in the as-rolled condition but after reheating at 1150°C followed by fast cooling to room temperature the BN precipitates were reduced (Larrañaga-Otegui et al., 2016).

Some tiny precipitates were outlining the ferrite grain boundaries as observed in the $^{11}B^{12}C^-$ map. Co-diffusion of boron and carbon can lead to boron carbide precipitation which lowers the quantity of boron in solid solution and at the austenite grain boundaries and will reduce the hardenability of these steels (Hara et al., 2004). The $^{11}B^{12}C^-$ maps give a reliable indication of co-location of boron and carbon in these samples, and a way to differentiate boron carbides from other carbides such as Ti,NB(C,) or cementite (Drillet et al., 2012, Valle et al., 2011). The $^{11}B^{16}O_2^-$ signal shows both $^{11}B^{12}C^-$ and $^{11}B^{14}N^-$ particles as well as segregation of boron at the grain boundaries.

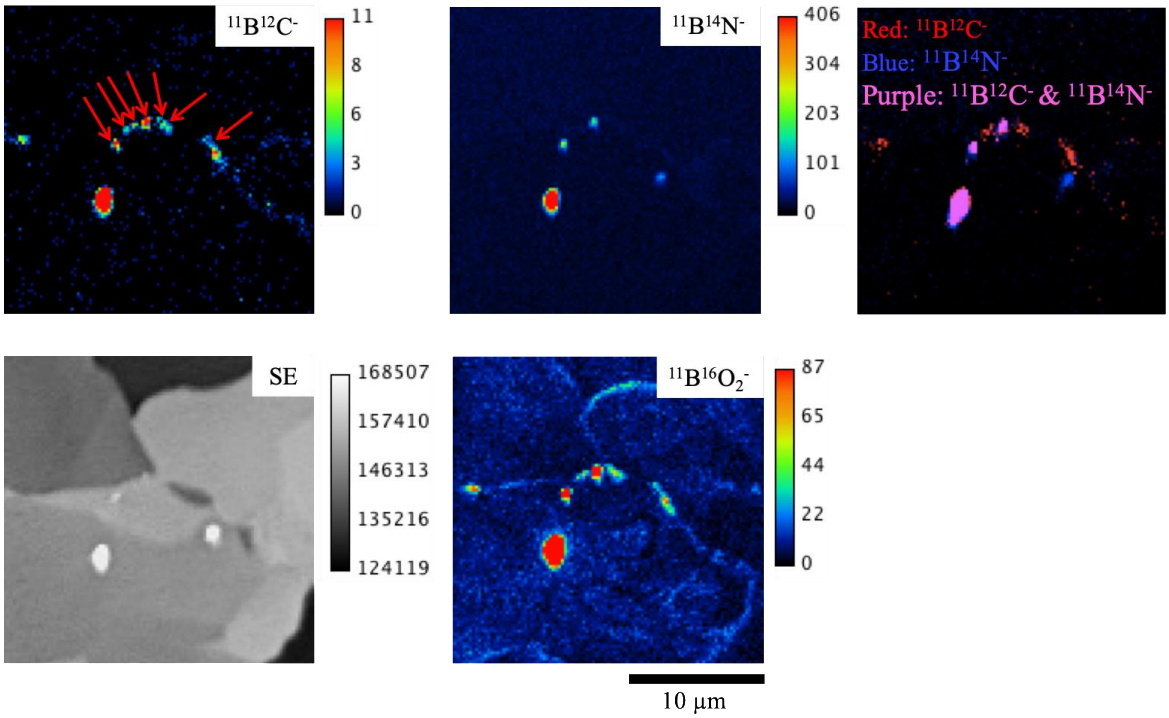


Figure 4.22: Comparison between boron particles ($^{11}B^{12}C^-$, $^{11}B^{14}N^-$, $^{11}B^{16}O_2^-$ and SE image) in sample 12AM22. Red arrow in the $^{11}B^{12}C^-$ map shows tiny precipitates outlining ferrite grain boundaries. Four distinct particles can be seen in the $^{11}B^{14}N^-$ map, one in the grain and the other three are on the grain boundaries. The $^{11}B^{16}O_2^-$ map shows both boron containing particles and boron segregation at the grain boundaries. The colour overlay image shows $^{11}B^{12}C^-$ in red, $^{11}B^{14}N^-$ in blue and combination of $^{11}B^{12}C^-$ and $^{11}B^{14}N^-$ in purple.

The carbon maps, an example of which is shown in Figure 4.23, can be used to locate precisely the position of pearlite ribbons. The carbon content in the primary ferrite grains is extremely uniform as can be seen from the line scan shown in Figure 4.24. The line scans were averaged over 10 pixels

width to improve the counting statistics and a step size of 0.2 µm was used along the red arrow shown in the $^{12}C^-$ and $^{11}B^{16}O_2^-$ image in Figure 4.23. Boron particles lie mostly on prior austenite grain boundaries along with grain boundary segregation of boron. The boron counts from pearlite are extremely low, about 2 counts/pA, whereas carbon counts in the pearlite region are very high, approximately 2000 counts/pA.

The pearlitic structure is developed due to carbon rejection into the remaining austenite during primary ferrite grain growth due to its low solubility in ferrite. Pearlite grows from carbon-enriched austenite and contains cementite, which has a much higher carbon content than ferrite. The boron signal is higher in ferrite grains compared to the pearlite. The pearlite regions gave, as expected, a higher carbon signal than the ferrite grains as can be seen in Figure 4.23 and Figure 4.24. Pearlite is formed during slow cooling through the eutectoid point in the Fe-C diagram. In this steel, at 0.14 wt.% carbon, the steel is categorised as hypoeutectoid, in which primary ferrite forms before the pearlite. The boron content in the primary ferrite formed at higher temperatures should, according the detail of the Fe-B binary phase diagram shown in Figure 4.25 contain about 0.008 wt% B while the ferrite formed by the pearlite reaction will contain much less B (approximately 0.001 wt%).

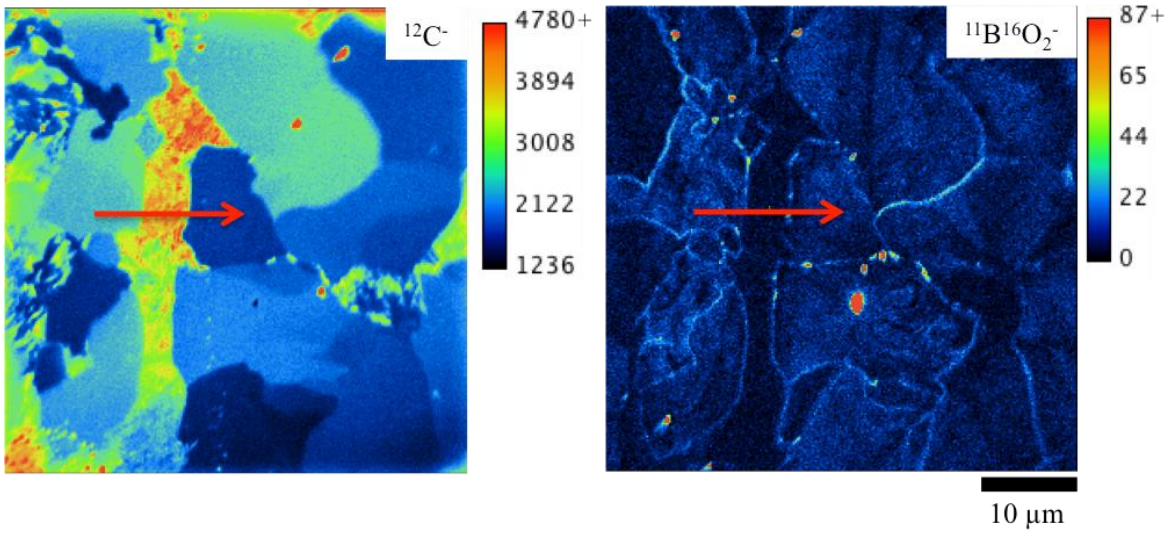


Figure 4.23: Comparison of carbon and boron map of sample 12AM22.

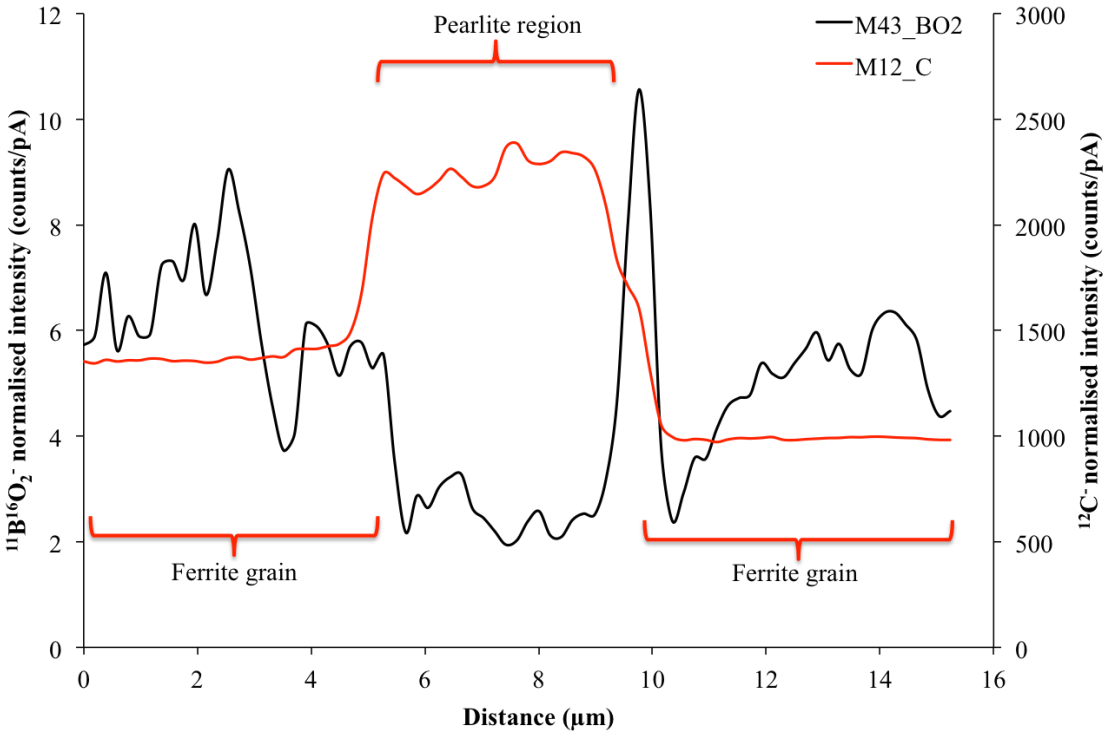


Figure 4.24: Line scans showing the comparison of carbon and boron in the pearlite and ferrite regions, where very high carbon counts were observed in the pearlite region but lower $^{11}B^{16}O_2^-$ counts.

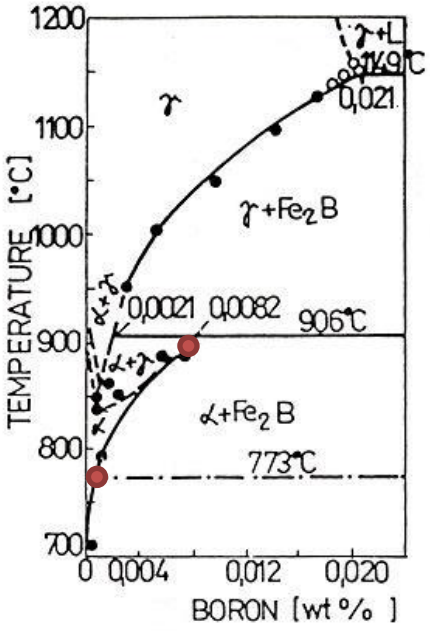


Figure 4.25: Fe-B binary alloy phase diagram at low boron concentrations (Metals, 2007). The estimated concentrations of B in ferrite formed at 900°C and by the pearlite reaction are marked by red circles.

4.4.2.2 Sample 12AM22AA (as-quenched: 30 minutes in the austenite region)

Figure 4.26 shows a 3 x 3 set of images over a 150 μm x 150 μm area of this sample. The $^{11}B^{16}O_2^-$ ion maps below are scaled from 0 to 5 counts to enhance the contrast of the images to show the appearance of boron segregation on the grain boundaries.

These images were acquired over two days. The intensity was normalised by the beam current measured on each day so that they can be compared with other samples measured on different days. All the images were taken on day 1 except images 1, 3 and 8, which were acquired on day 2. As shown in Table 4.5, the beam current at the sample was measured in FCo as 1.18 pA on day 1 and 1.07 pA on day 2 with D1=2.

Segregation of boron along prior austenite grain boundaries was observed in this sample. Only a few small boron containing particles were seen in images 1, 2, 3, 5 and 6 in Figure 4.26. The particles mostly appear within the grains with a few near the grain boundaries.

Image 3 is enlarged in Figure 4.27 and three line scans were performed over the grain boundaries and two line scans across boron containing particles. These line scans are shown in Figure 4.28. The line scans were averaged over 10 pixels width to improve the counting statistics with a step size of 0.2 μm along the arrow shown in the $^{11}B^{16}O_2^-$ image in Figure 4.27. The normalised $^{11}B^{16}O_2^-$ intensity at the grain boundaries is 1.2, 1.0 and 0.8 counts/pA for lines 1, 2 and 3 respectively. One large boron particle in the grain is seen on the left side of Figure 4.27 and line scan 4 shows the normalised intensity for the particle is 16 counts/pA, about 5 times higher than on the particle in line 5. In comparison with the particles in the reference as-quenched sample, 12AN15, the boron normalised intensity for the big particle on line 4 is almost 3 times higher than from the largest particle found in the reference sample. Detailed particle analysis will be discussed in Section 4.5.4.

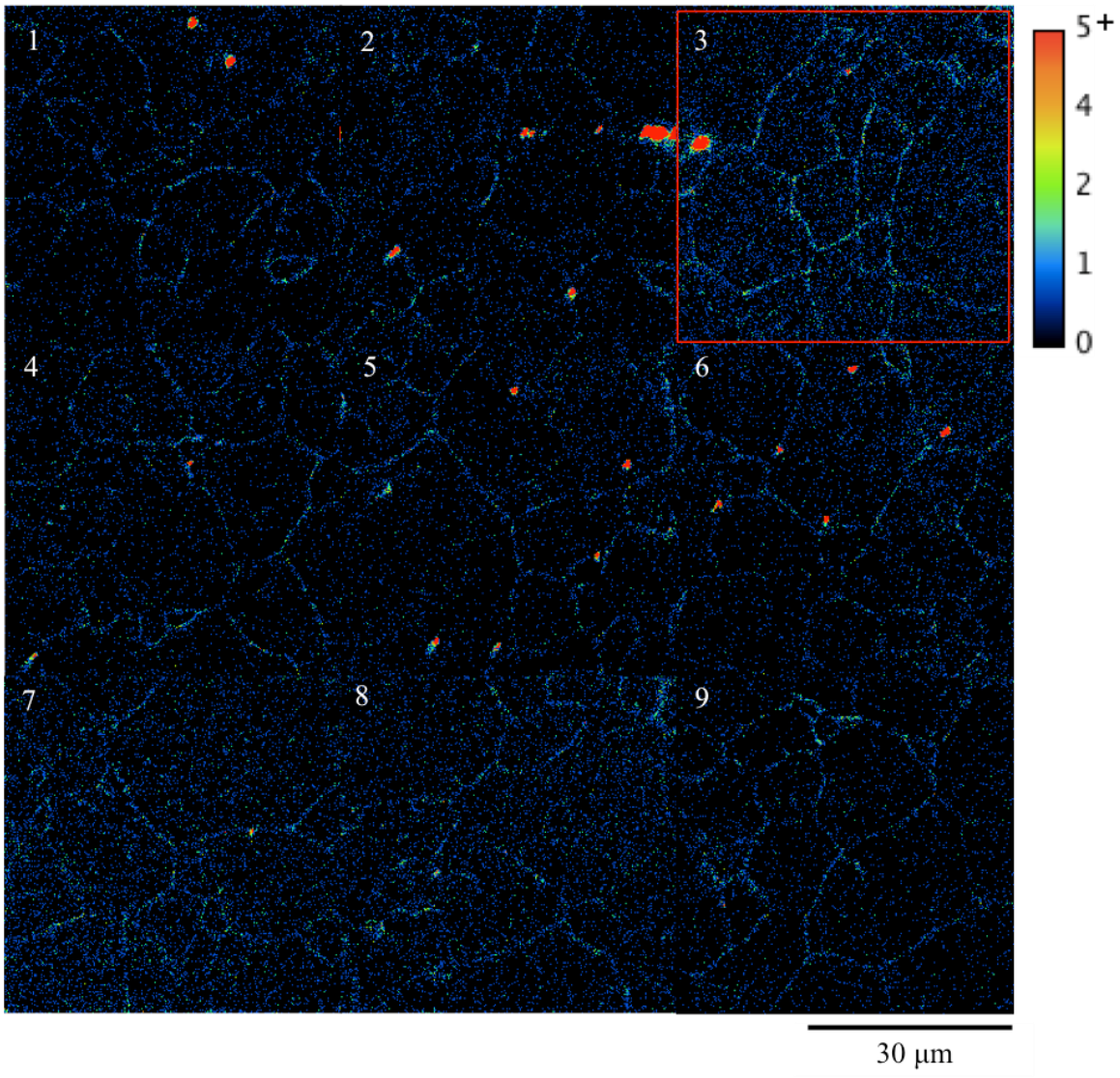


Figure 4.26: Ion micrographs showing the distribution of $^{11}B^{16}O_2$ in sample 12AM22AA (Al-protected, as-quenched). The red square in image 3 indicates the location of subsequent line scans on the grain boundaries and boron containing particles.

Table 4.5: Total $^{11}B^{16}O_2$ counts on as-quenched sample 12AM22AA relating to the images shown in Figure 4.26

Image Number	Total $^{11}B^{16}O_2^-$ counts	Beam current on sample (pA)	Normalised $^{11}B^{16}O_2^-$ intensities: Total $^{11}B^{16}O_2^-$ counts/beam current, (counts/pA)
1	3223	1.07	3012
2	8916	1.18	7556
3	12779	1.07	11943
4	4878	1.18	4134
5	4939	1.18	4186
6	5662	1.18	4798
7	8290	1.18	7025
8	7457	1.07	6969
9	4671	1.18	3958

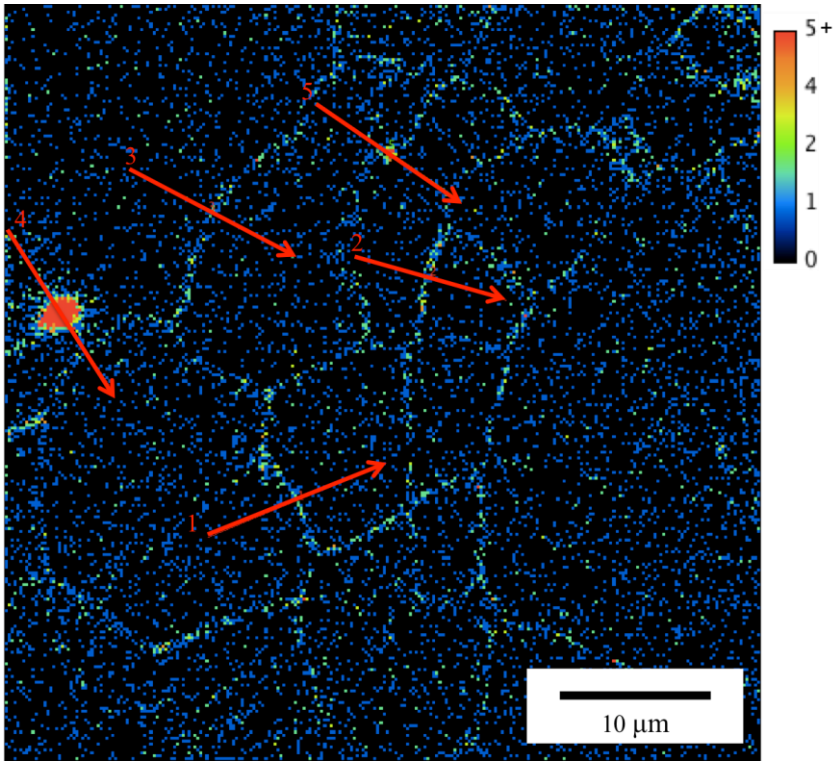


Figure 4.27: Line scans over grain boundaries (line 1, 2 and 3) and boron containing particles (line 4 and 5) in sample 12AM22AA in the area shown in image 3 in Figure 4.26.

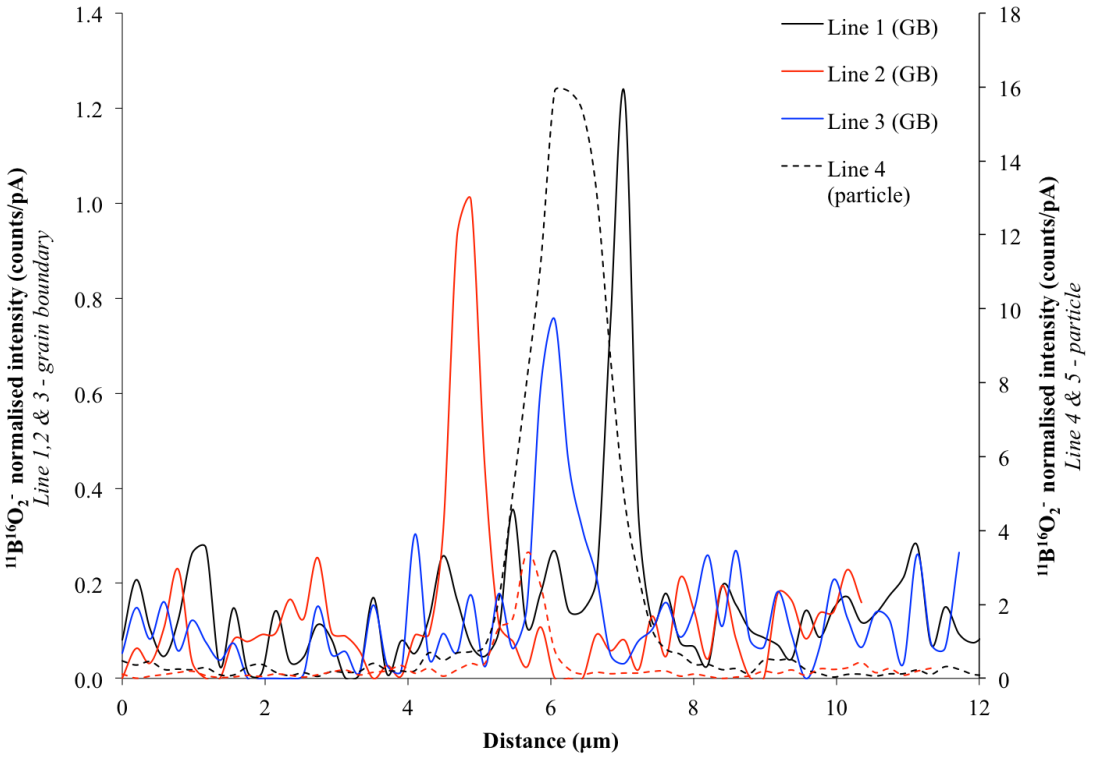


Figure 4.28: Line scans for $^{11}B^{16}O_2^-$ across grain boundaries for as-quenched sample 12AM22AA on line 1,2 and 3 and on the two boron rich particles on line 4 and 5 as indicated by the red arrow marked in Figure 4.27.

4.4.2.3 Sample 12AM22F (as-quenched: 10 minutes in the austenite region)

Figure 4.29 shows a 4 x 3 set of $^{11}B^{16}O_2^-$ images over a 200 μm x 150 μm area. The gap between each image is 50 μm. The $^{11}B^{16}O_2^-$ images below are scaled from 0 to 15 counts for clarity although there are pixels with higher counts than this. These images were acquired over two days. Again there was a problem in tuning for this experiment on this sample. Some of the images are darker in the bottom left of the scanned area. This problem likely occurred because of misalignment of the secondary ion beam tuning probably due to magnet drift caused by changes in the room temperature over the long duration of the experiment.

The $^{11}B^{16}O_2^-$ ion maps reveal that the boron is primarily located at the prior austenite grain boundaries rather than in the grain interior. Strong grain boundary segregation of boron was observed in this quenched sample. A few small boron containing particles were observed in this sample mostly in the grains but some were detected on the grain boundaries. Fewer particles were observed in this quenched sample compared to the as-rolled sample 12AM22.

The total boron counts and the normalised intensities for the $^{11}B^{16}O_2^-$ maps shown in Figure 4.29 are summarised in Table 4.6. The beam current at the sample was measured in FCo as 3.2 pA on the first day and 3.3 pA on the second day with D1=2.

The image 1 in Figure 4.29 is enlarged in Figure 4.30, and four line scans were performed over selected grain boundaries and three line scans were carried out over particles in the grains. These line scans are shown in Figure 4.31. The line scans were averaged over 10 pixels width to improve the counting statistics and a step size of 0.2 μm was used along the arrow shown in the $^{11}B^{16}O_2^-$ image in Figure 4.30. The normalised $^{11}B^{16}O_2^-$ intensities at the grain boundaries on line 1 to 4 range from 1 to 2 counts/pA. One large boron particle in the grain is seen on line 5 with a normalised intensity of about 10 counts/pA. These counts are about 7 times higher than those from the particle on line 7 and 1.5 times higher than from the particle on line 6.

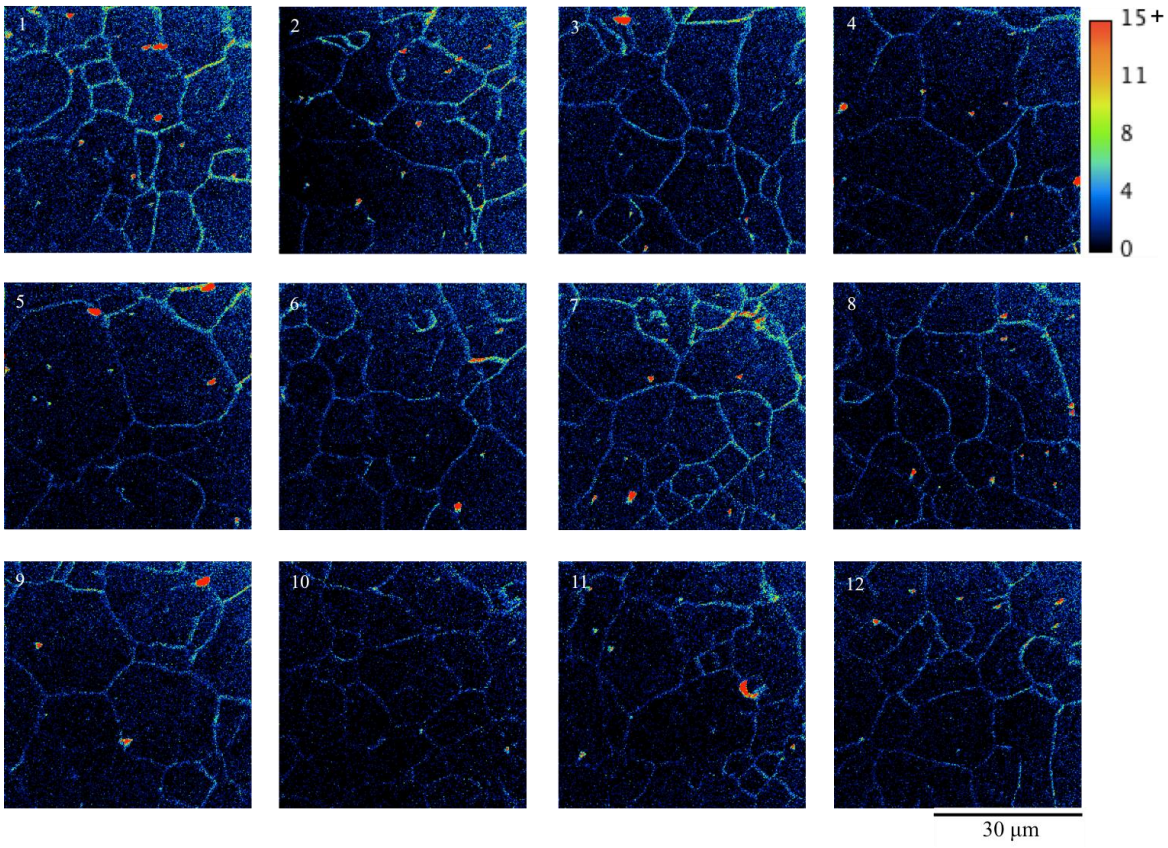


Figure 4.29: Ion micrographs showing the distribution of $^{11}B^{16}O_2$ in sample 12AM22F (Al-protected, as-quenched: 10 minutes in the austenite region). There is a 50 µm gap between each image.

Table 4.6: Total $^{11}B^{16}O_2$ counts on quenched sample 12AM22F relating to the images shown in Figure 4.29.

Image Number	Total $^{11}B^{16}O_2^-$ counts	Beam current on sample (pA)	Normalised $^{11}B^{16}O_2^-$ intensities: Total $^{11}B^{16}O_2^-$ counts/beam current, (counts/pA)
1	60812	3.2	18886
2	41098	3.2	12763
3	40514	3.2	12582
4	27994	3.2	8694
5	33590	3.2	10432
6	31226	3.2	9698
7	49489	3.2	15369
8	29595	3.2	9191
9	31265	3.2	9710
10	12561	3.3	3806
11	23300	3.3	7061
12	25121	3.3	7612

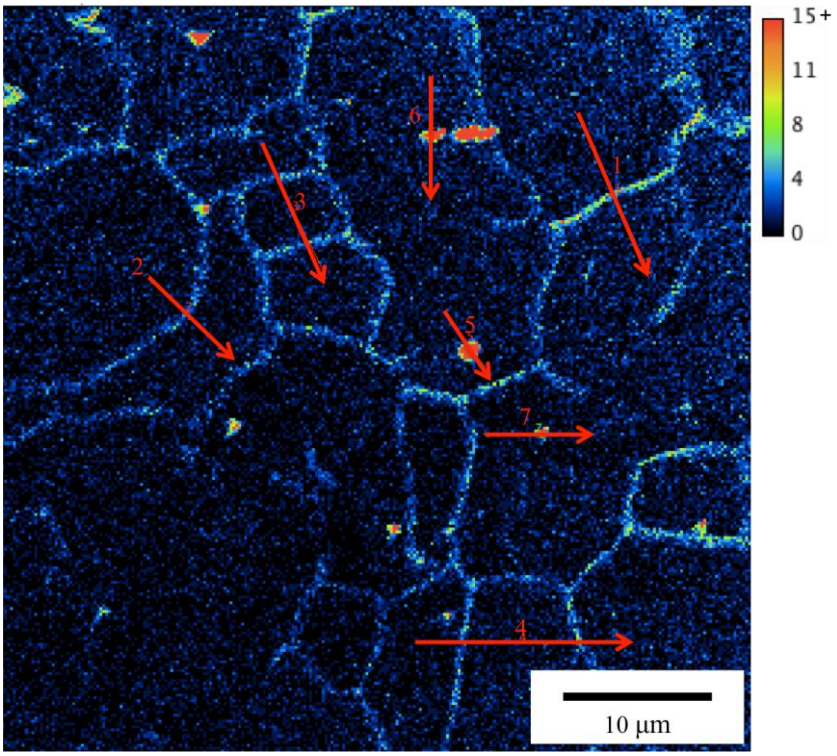


Figure 4.30: Location of the line scans across grain boundaries (line 1, 2, 3 and 4) and boron containing particles (line 5,6 and 7) on sample 12AM22F in the area shown in image 1 in Figure 4.29.

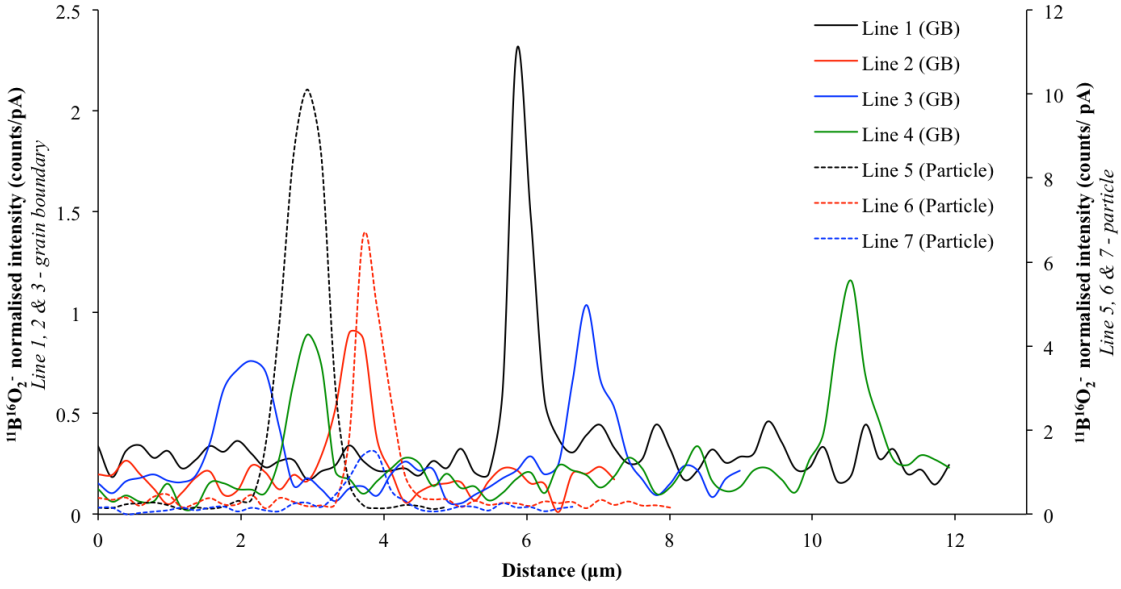


Figure 4.31: Line scans of $^{11}B^{16}O_2^-$ for the as-quenched sample 12AM22F across grain boundaries showing boron segregation (line 1, 2, 3 and 4) and three boron rich particles (lines 5, 6 and 7) as indicated by the red arrow marked in Figure 4.30.

4.4.2.4 Sample 12AM22G (as-quenched: 180 minutes in the austenite region)

Figure 4.32 shows a 3 x 3 set of images over a 150 μm x 150 μm area. The $^{11}B^{16}O_2^-$ ion maps below are scaled from 0 to 15 counts for clarity although there are pixels with higher counts than this. These images were acquired over two days. Strong grain boundary segregation of boron was observed in this quenched sample. Various sizes of boron containing particles were observed in this sample, mostly in the grains but some were detected on the grain boundaries. A few big particles can be seen in images 5 and 8. The longer time (180 minutes) at the austenitising temperature results in more grain boundary segregation and more particles in this sample compared to other two as-quenched samples 12AM22AA (30 minutes) and 12AM22F (10 minutes).

The total boron counts and the normalised intensities for the $^{11}B^{16}O_2^-$ maps shown in Figure 4.32 are summarised in Table 4.7. The beam current at the sample was measured in FCo as 3.00 pA on the first day and 3.23 pA on the second day with D1=2.

Image 9 in Figure 4.32 is enlarged in Figure 4.33, and three line scans were performed over grain boundaries and three line scans were carried out over selected particles in the grains. These line scans are shown in Figure 4.34. The line scans were averaged over 10 pixels width to improve the counting statistics and a step size of 0.2 μm was used along the arrow shown in the $^{11}B^{16}O_2^-$ image in Figure 4.33. The normalised $^{11}B^{16}O_2^-$ intensities at the grain boundaries on line 1 to 3 range from 1 to 1.5 counts/pA. Large boron particles on line 4 and 5 were found in the grain with normalised intensities of 13 and 14 counts/pA, respectively. The counts from these particles are about two times higher than from the particle on line 6.

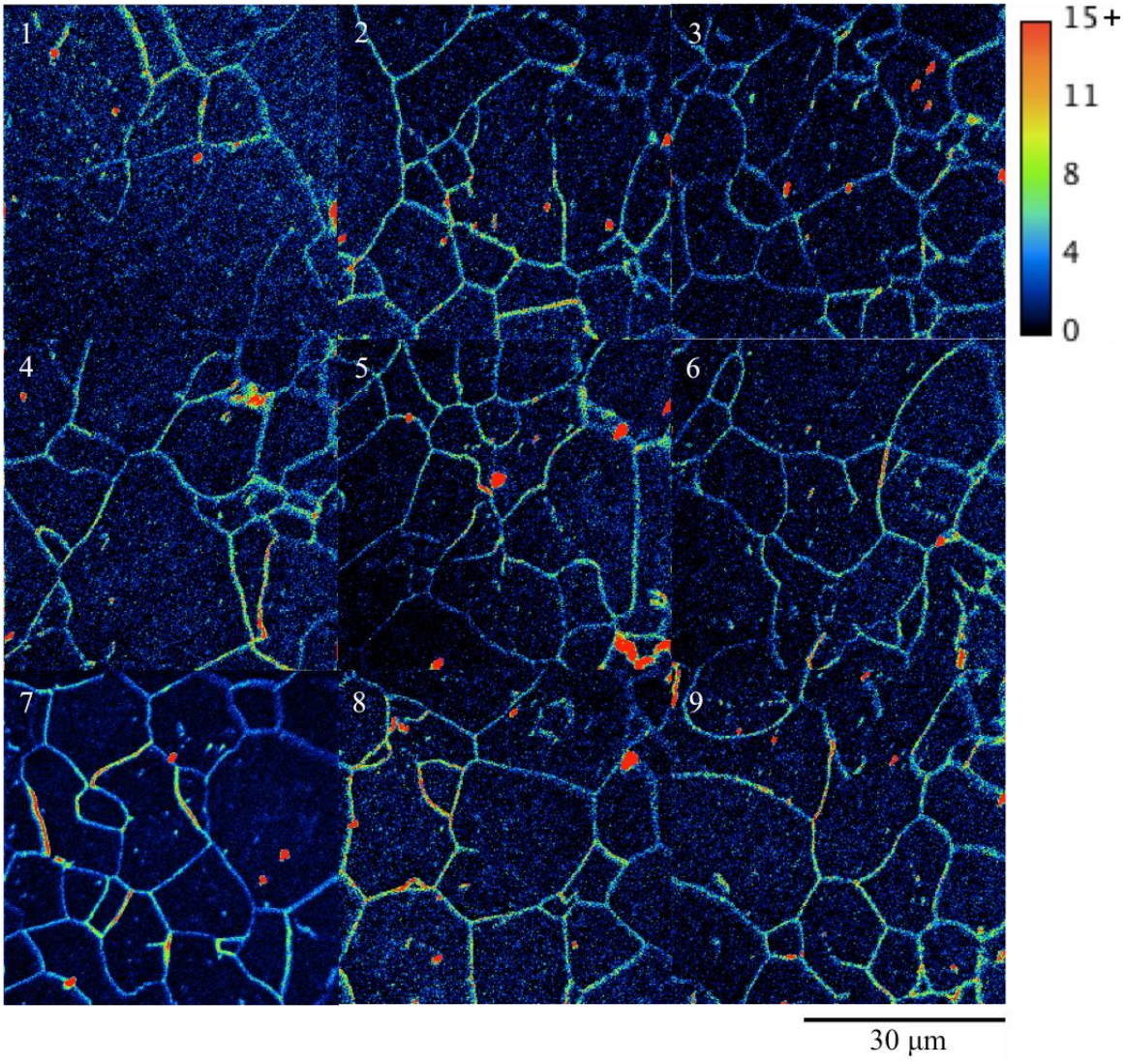


Figure 4.32: Ion micrographs showing the distribution of $^{11}B^{16}O_2$ in sample 12AM22G (Al-protected, as-quenched: 180 minutes at the austenitising temperature).

Table 4.7: Total $^{11}B^{16}O_2$ counts on quenched and tempered sample 12AM22G relating to the images shown in Figure 4.32.

Image Number	Total $^{11}B^{16}O_2^-$ counts	Beam current on sample (pA)	Normalised $^{11}B^{16}O_2^-$ intensities: Total $^{11}B^{16}O_2^-$ counts/beam current, (counts/pA)
1	36847	3.00	19938
2	33636	3.00	11212
3	33450	3.00	11150
4	74677	3.23	23120
5	100567	3.23	31135
6	46234	3.23	14314
7	153996	3.23	47677
8	60633	3.23	18772
9	90052	3.23	27880

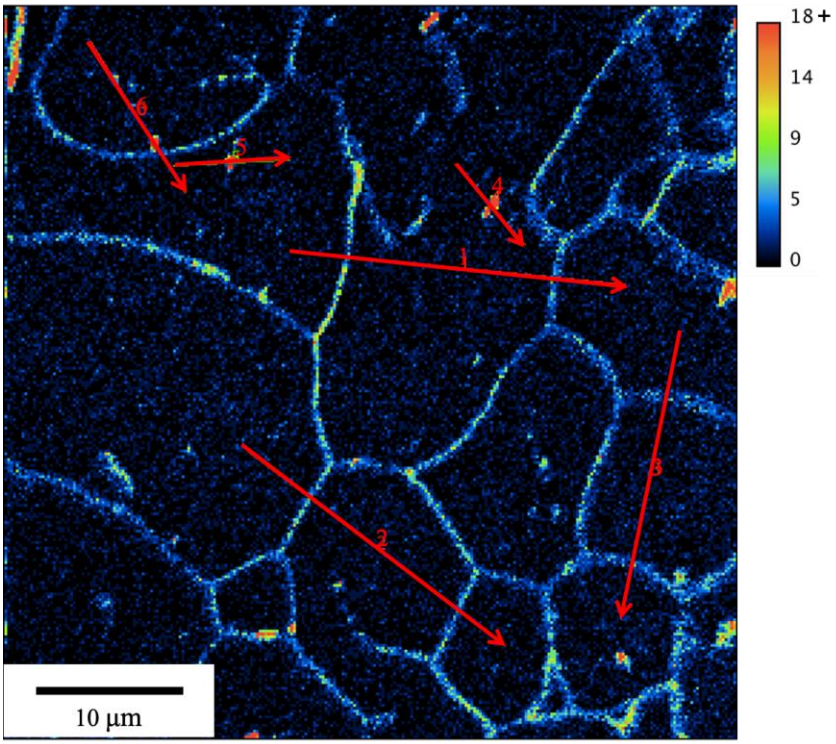


Figure 4.33: Location of the line scans across grain boundaries (line 1, 2, and 3) and boron containing particles (line 4, 5, and 6) on sample 12AM22G in the area shown in image 9 in Figure 4.32.

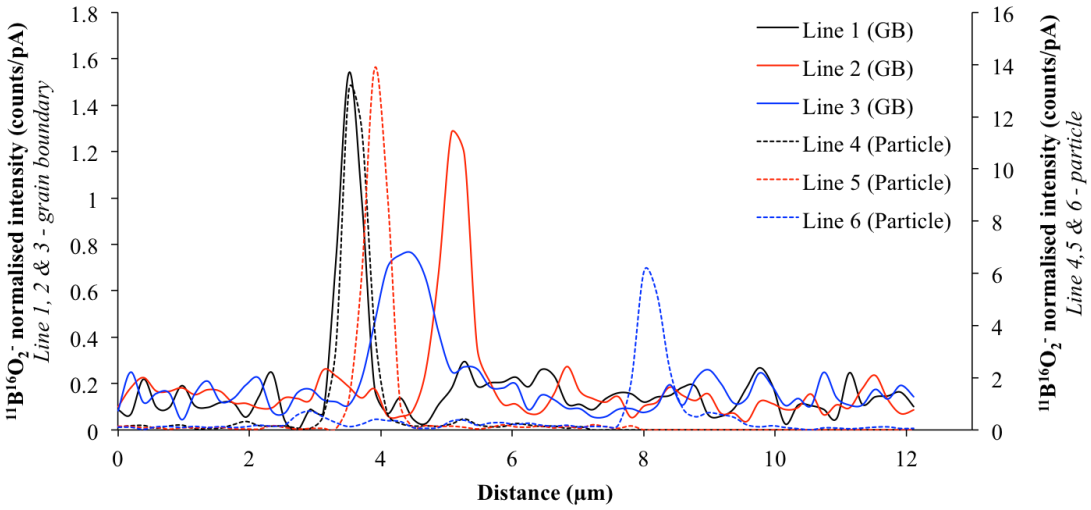


Figure 4.34: Line scans of $^{11}B^{16}O_2^-$ for the as-quenched sample 12AM22G across grain boundaries showing boron segregation (line 1, 2, and 3) and three boron rich particles (lines 4, 5, and 6) as indicated by the red arrow marked in Figure 4.33.

4.4.2.5 Sample 12AM24 (quenched and tempered) – first data acquisition

Martensite that is formed after quenching is so hard and brittle that it is necessary to modify its mechanical properties by a tempering process to achieve greater toughness and further improve ductility. This sample is aluminium protected, reheated to 930°C for 30 minutes, water quenched and finally tempered at 600°C.

Figure 4.35 shows a 4 x 4 montage of $^{11}B^{16}O_2^-$ NanoSIMS maps over an area of 200 μm x 200 μm on the first sample studied after the tempering treatment. The $^{11}B^{16}O_2^-$ ion maps below are scaled from 0 to 5 counts to enhance the contrast of the images to show the appearance of the boron segregation on the grain boundaries. Segregation at the prior austenite grain boundaries can just be seen, with small precipitates near the grain boundaries and a few quite large boron containing particles within the grains. It appears in this sample that these small boron precipitates were created during the tempering stage as they were not visible in the samples presented above.

Image 8 shows four big particles in the grains, which contribute to a large fraction of total boron counts in that area. The $^{11}B^{16}O_2^-$ normalised intensity in that area is nearly 6400 counts/pA, about 2 to 3 times higher than from areas without the big particles (2000-3000 counts/pA). Image 8 is enlarged in Figure 4.36 and four line scans were performed on the boron containing particles. These line scans are shown in Figure 4.37. The line scans were averaged over 10 pixels width to improve the counting statistics with a step size of 0.2 μm along the arrows. The normalised intensity for the largest particle in the area on line 1 was measured to be around 16 counts/pA. The intensities from the other particles on lines 2 to 4 were measured to be around 14 to 15 counts/pA. The particles in this sample seem to generate about 3 to 4 times more intensity in the $^{11}B^{16}O_2^-$ signal than particles in reference sample 12AN15, suggesting that they may have a different composition. Detailed particle analysis will be discussed in Section 4.5.4.

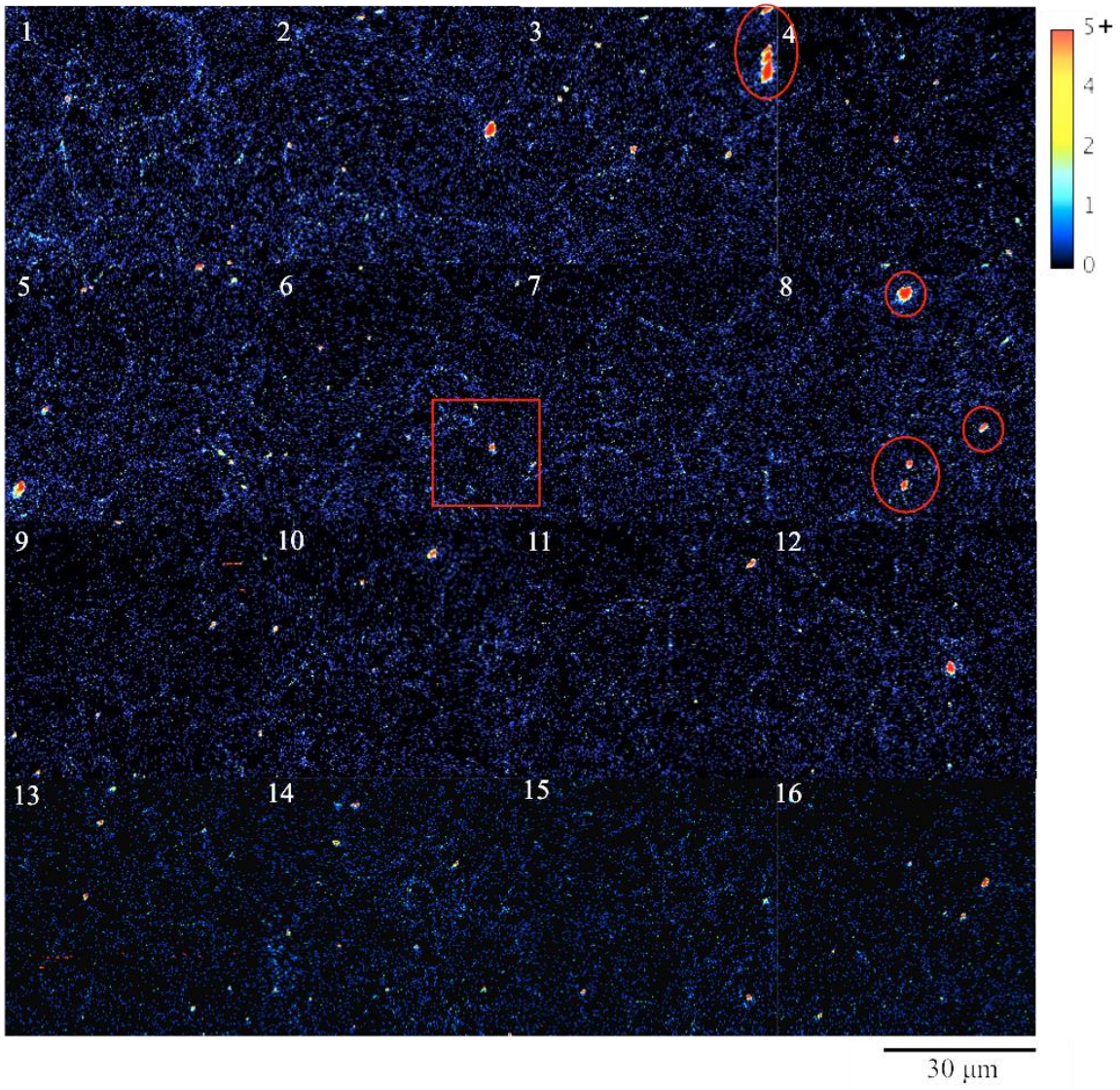


Figure 4.35: Ion micrographs showing the boron distribution of $^{11}B^{16}O_2$ in the quenched and tempered aluminium protected sample 12AM24. The red circle in image 3 shows the particle that was broken up during rolling process. Red circles in image 8 indicate the location of subsequent line scans on boron containing particles. The red square indicates the 20 µm area that was selected for high resolution imaging using the D1=3 aperture.

The total boron counts and the normalised intensities for the $^{11}B^{16}O_2^-$ maps shown in Figure 4.35 are summarised in Table 4.8. The beam current at the sample was measured in FCo as 1.8 pA on the first day and 1.7 pA on the second day.

Table 4.8: Total $^{11}B^{16}O_2$ counts on quenched and tempered sample 12AM24 relating to the images shown in Figure 4.35

Image Number	Total $^{11}B^{16}O_2^-$ counts	Beam current on sample (pA)	Normalised $^{11}B^{16}O_2^-$ intensities: Total $^{11}B^{16}O_2^-$ counts/beam current, (counts/pA)
1	8537	1.8	4743
2	9855	1.8	5475
3	12931	1.7	7606
4	4583	1.7	2696
5	9064	1.8	5036
6	6181	1.8	3434
7	5633	1.7	3314
8	10877	1.7	6398
9	4456	1.7	2621
10	5324	1.7	3132
11	4414	1.7	2596
12	6219	1.7	3658
13	3901	1.7	2295
14	5006	1.7	2945
15	3888	1.7	2287
16	3540	1.7	2082

Another area that has a large number of total boron counts is in image 3, with the $^{11}B^{16}O_2^-$ normalised intensity about 7600 counts/pA. The high counts in this area are mainly from the boron containing particles at the top right of this image. The particles were very closely spaced and their size and shape indicated that they had been formed by the break-up of a larger inclusion. These particles are likely formed during the rolling process as their direction is evidence for the rolling direction.

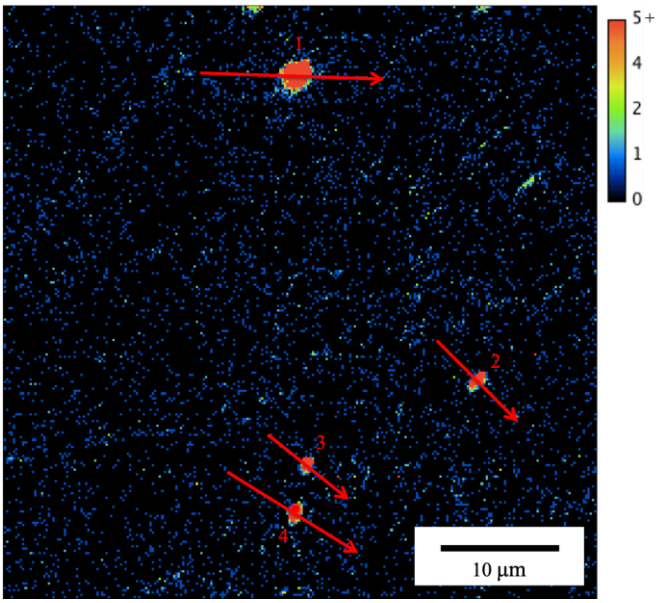


Figure 4.36: Red arrows indicate the position and direction of the line scans across four boron rich particles in sample 12AM24 relating to image 8 in Figure 4.35.

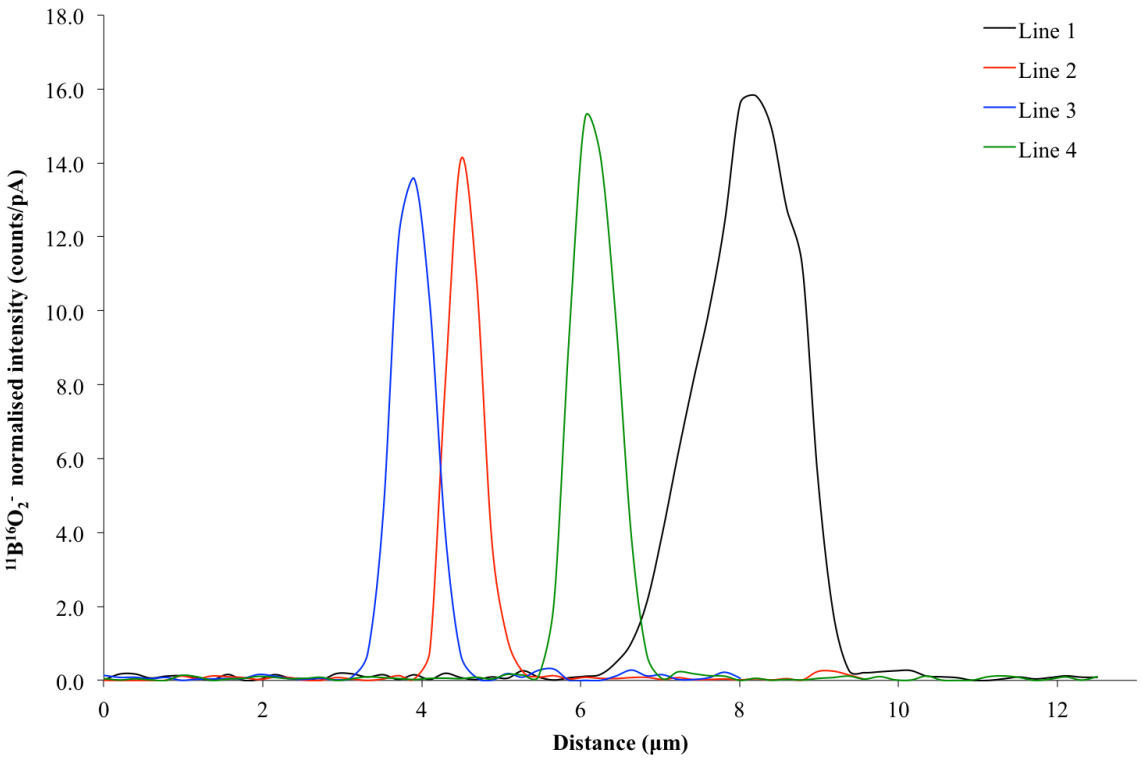


Figure 4.37: Line scans for $^{11}B^{16}O_2^-$ across four boron rich particles in sample 12AM24 as indicated by the red arrow marked 1, 2, 3 and 4 in Figure 4.36.

Segregation of boron at the prior austenite grain boundaries cannot be seen very clearly in this sample, as shown in the $^{11}B^{16}O_2^-$ maps in Figure 4.35. Longer counting times are needed to give a clear view of the boron segregation at the prior austenite grain boundaries and the fine scale precipitation. Image 5 in Figure 4.35 was the first image of a series of 28 scans acquired overnight with a dwell time of about 30 minutes per slice. Summed images of the $^{12}C^-$, $^{11}B^{16}O_2^-$, $^{11}B^{12}C^-$ and $^{11}B^{14}N^-$ maps are shown in Figure 4.38. The martensitic microstructure of the sample can be seen very clearly in the SE image, and the inhomogeneous distribution of carbon in the martensitic structure is shown in the $^{12}C^-$ map. There is what is assumed to be a large particle of contamination from sample preparation or dust on the surface that shows up on the right hand side of the SE image, and is also bright in the $^{12}C^-$ map. The $^{11}B^{16}O_2^-$, $^{11}B^{12}C^-$ and $^{11}B^{14}N^-$ images all show a similar, smaller particle distribution, so these can be confidently interpreted as B-rich precipitates.

Strong $^{11}B^{12}C^-$ signals are observed from some precipitates, however, there is lack of correlation with the $^{12}C^-$ signal. Most of the mass interferences at mass 23 are boron related but some of them do not

contain carbon such as $^{11}B_2{}^1H^-$ and $^{11}B^{10}B^1H_2^-$. This might explain why we do not see carbon in some of the precipitates. $^{11}B^{12}C^-$ signal can be used to interpret the boron precipitates but not all can be interpreted as carbides.

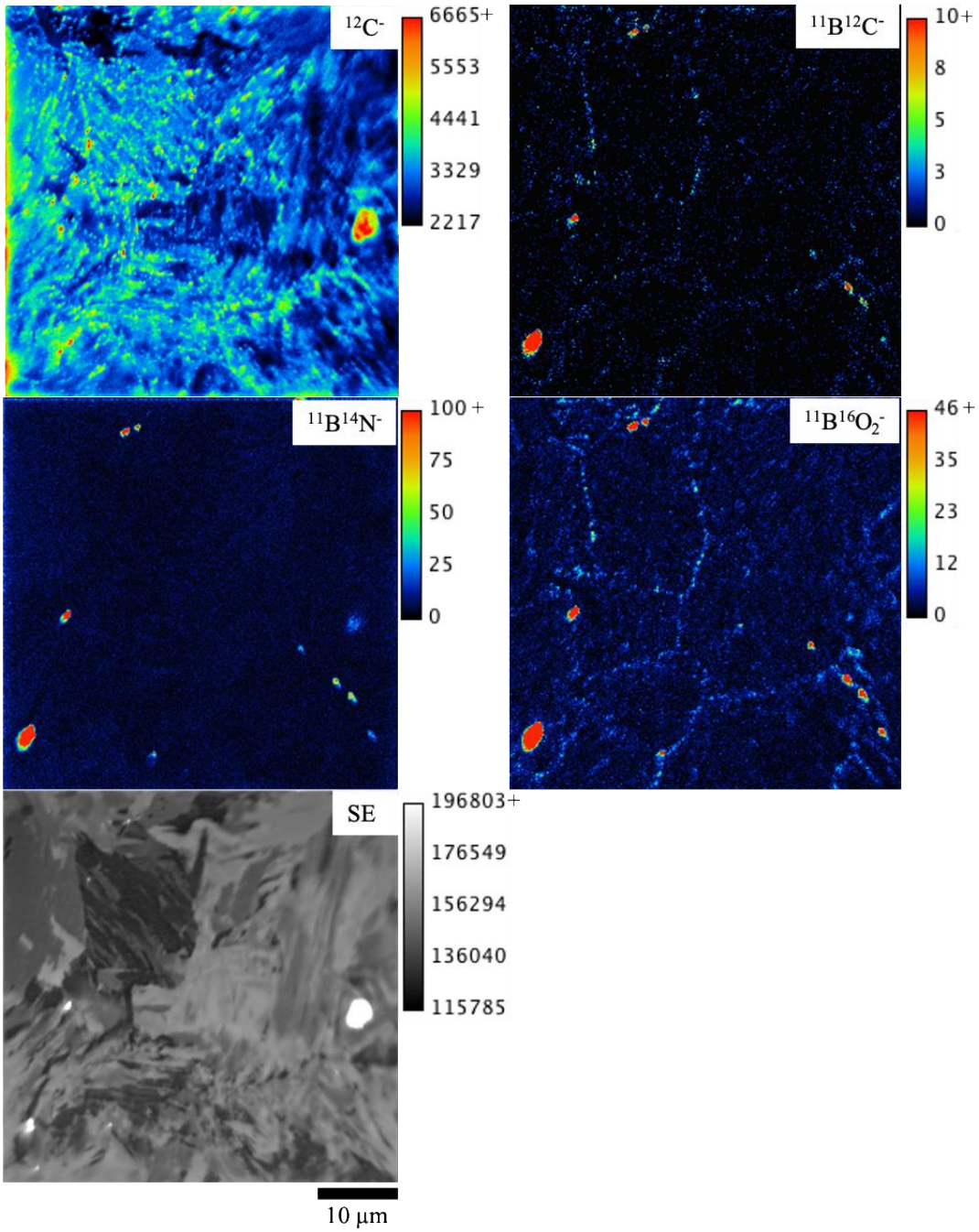


Figure 4.38: Selected area of sample 12AM24 from image 5 in Figure 4.35 showing the NanoSIMS maps of $^{12}C^-$, $^{11}B^{12}C^-$, $^{11}B^{14}N^-$, $^{11}B^{16}O_2^-$ and secondary electron (SE) image. These images were summed from 28 sequential maps.

Image 16 from Figure 4.35 was also scanned overnight for a longer duration to improve the counts. It was imaged for 27 slices with a dwell time of about 30 minutes per slice. Summed images of the $^{12}C^-$, $^{11}B^{16}O_2^-$, $^{11}B^{12}C^-$and $^{11}B^{14}N^-$ maps are shown in Figure 4.39.

From Figure 4.39, it is clear the particles that can be seen in the $^{11}B^{14}N^-$ map correlate well with the particles seen in $^{11}B^{16}O_2^-$ and $^{11}B^{12}C^-$ maps. Nevertheless, grain boundary segregation and some small precipitates on the grain boundaries do not show up in the $^{11}B^{14}N^-$ map. The distribution of carbon in the $^{12}C^-$ map shows the martensitic structure of the sample and small carbide precipitates on the grain boundaries. The carbide precipitates on the grain boundaries that can be seen in the $^{12}C^-$ map can be correlated to the $^{11}B^{16}O_2^-$ and $^{11}B^{12}C^-$ maps as indicated in the red circle.

The martensitic microstructure of the sample can again be seen very clearly from the SE image. Not all bright particles that can be seen in the SE image are boron rich, and they do not appear in the carbon map either. They might be another type of particle such as AlN or NbC, which have been detected in a few areas in this sample as shown in the SEM image in Figure 4.40 which was acquired by Tata Steel. Particle analysis on a series of similar images was undertaken on a FEI Quanta 600 FEG-SEM. EDX spot analysis along with morphological examination was used to identify the particle type and composition. Strong compositional contrast is produced using backscattered electrons and the particles of low atomic mass (e.g. BN) appear dark whereas those of higher mass (e.g. NbC) appear light.

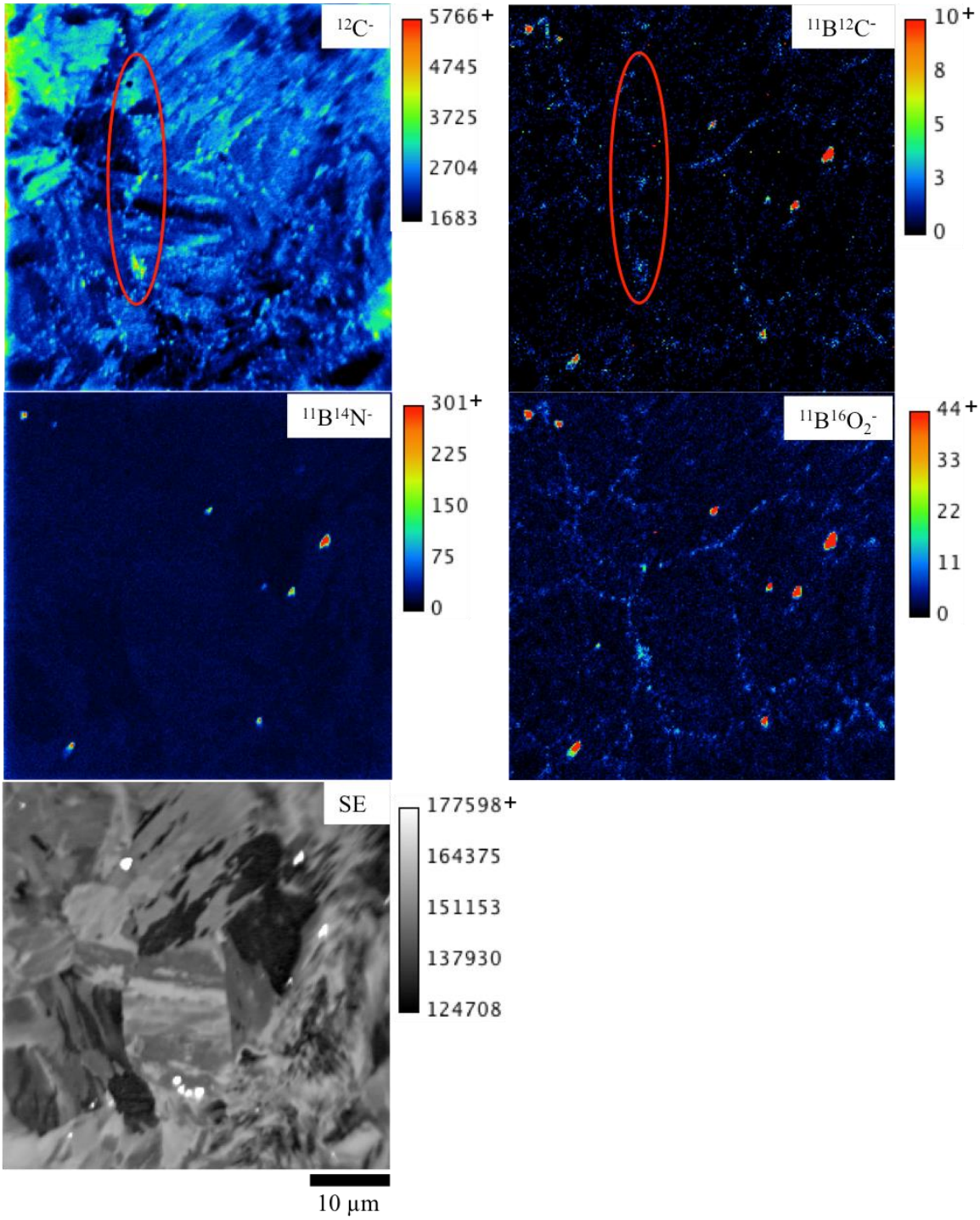


Figure 4.39: Selected area of sample 12AM24 from image 16 in Figure 4.35 showing the NanoSIMS maps of $^{12}C^-$, $^{11}B^{12}C^-$, $^{11}B^{14}N^-$, $^{11}B^{16}O_2^-$ and secondary electron (SE) image. These images were summed from 27 sequential maps. The red circle in $^{12}C^-$ and $^{11}B^{12}C^-$ maps indicate the small carbide precipitates outlining the grain boundaries.

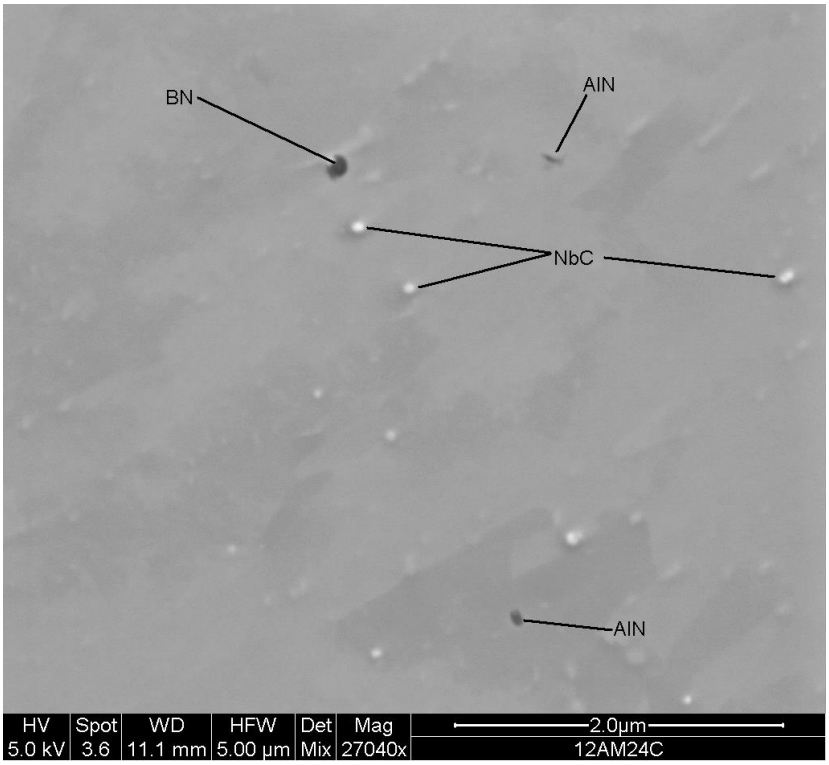


Figure 4.40: SEM backscattered electron image showing BN, AlN and NbC particles in sample 12AM24 (Image taken by Tata Steel).

A 20 by 20 μm^2 area highlighted in the red box in image 6 as shown in Figure 4.35, was selected for high resolution imaging using a smaller aperture, D1=3. The current on the sample was measured as 0.8 pA. The dwell time was set to 60,000 µs/pixel per image and a total of 19 sequential images were summed. Summed images of the $^{12}C^-$, $^{11}B^{16}O_2^-$, $^{11}B^{12}C^-$ and $^{11}B^{14}N^-$ maps are shown in Figure 4.41. Six particles with a strong $^{11}B^{14}N^-$ signal were detected in this area, with the largest particle also observed in the SE image, appearing very bright (but dark in the SEM image). Particles also can be seen in the $^{11}B^{12}C^-$ and $^{11}B^{16}O_2^-$ maps. Small boron containing precipitates were observed on the grain boundaries as seen in the $^{11}B^{12}C^-$ and $^{11}B^{16}O_2^-$ maps. There is some astigmatism in these NanoSIMS images, and it may be that the precipitates are actually more circular than they appear here. There does not appear to be grain boundary segregation in this sample in contrast to the clear segregation observed in 12AN15 and 12AM22AA, only small precipitates lying along the grain boundaries. The distribution of carbon in the $^{12}C^-$ map shows small carbide precipitates decorating the grain boundaries as well as in the grains themselves.

The total dose implanted in this area during this long acquisition was 9.3 x 10^{16} Cs atoms/cm^2 and the surface is also roughened due to the long scan with increasing dose. From the SEM image of the NanoSIMS crater, bottom right image of Figure 4.41, we can see that the crater is not perfectly square. This is probably due to primary beam misalignment in the NanoSIMS, this shape is commonly seen in NanoSIMS craters, and also due to image drift over the long acquisition caused by temperature changes in the NanoSIMS lab. Therefore, before analysis was undertaken on these results, the image stack was aligned to correct for drift using the ImageJ software. The SEM image also shows that different grains have been sputtered away at different rates due to different crystallographic orientations.

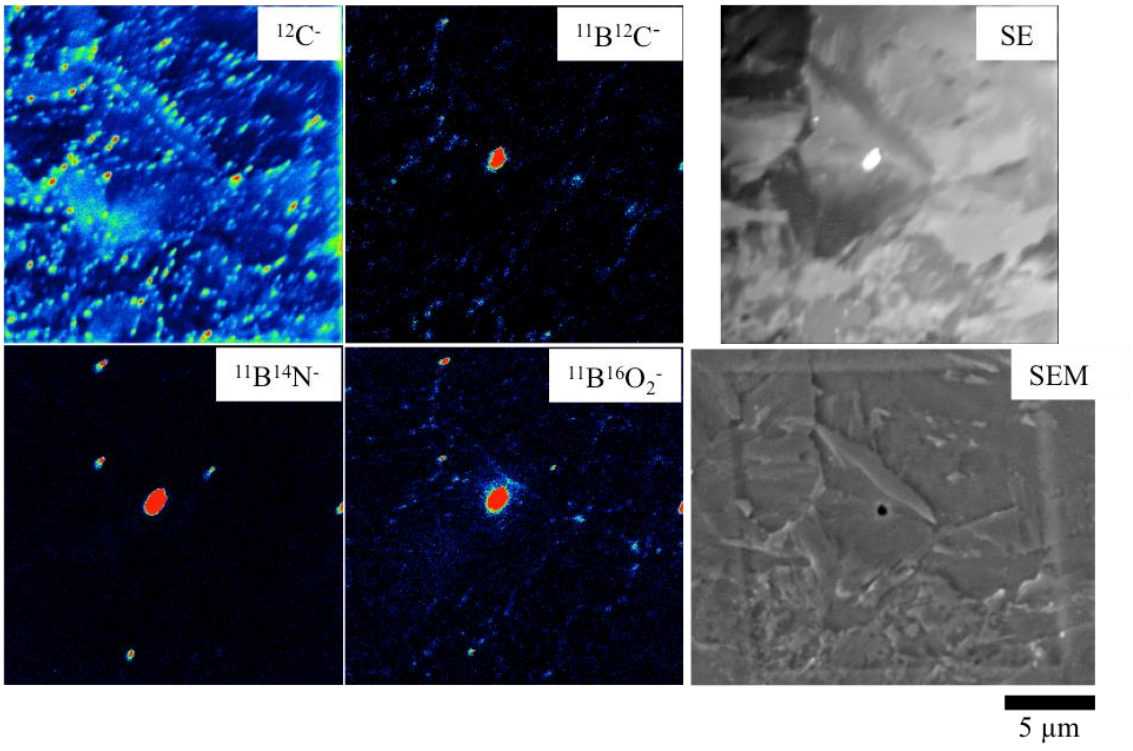


Figure 4.41: Sample 12AM24 from image 6 in Figure 4.35 at higher resolution using smaller aperture D1=3, raster size 20 µm, sum images of 19 slices, dwell time 60,000 µs/px. Bottom right: SEM image showing the morphology of the final NanoSIMS crater.

4.4.2.6 Sample 12AM24 (quenched and tempered) – second data acquisition

While undertaking subsequent data analysis to extract quantifiable information, it was noticed that the data for 12AM24 seemed to be an outlier by having low counts and does not show much information about the segregation at the prior austenite grain boundaries. Therefore, it was decided to repeat the analysis on this sample. Figure 4.42 shows a 4 x 4 montage of $^{11}B^{16}O_2^-$ NanoSIMS maps over an area of 200 μm x 200 μm of the same sample acquired from a new area to that analysed previously. The $^{11}B^{16}O_2^-$ ion maps below are scaled from 0 to 38 counts to enhance the contrast of the images to show the appearance of the boron segregation on the grain boundaries. The distribution of the boron is very similar to that observed in the previous analysis of this sample (Figure 4.35), however, the maps are now much clearer as the counts are improved probably as a result of improved alignment of the NanoSIMS to give a higher transmission of secondary ions. Segregation at the prior austenite grain boundaries can just be seen, with small precipitates near the grain boundaries and a few quite large boron containing particles within the grains. Again, it appears in this sample that the small boron-containing precipitates were created during the tempering stage as they were not visible in other samples.

The total boron counts and the normalised intensities for the $^{11}B^{16}O_2^-$ maps shown in Figure 4.42 are summarised in Table 4.9. The beam current at the sample was measured in FCo as 2.1 pA.

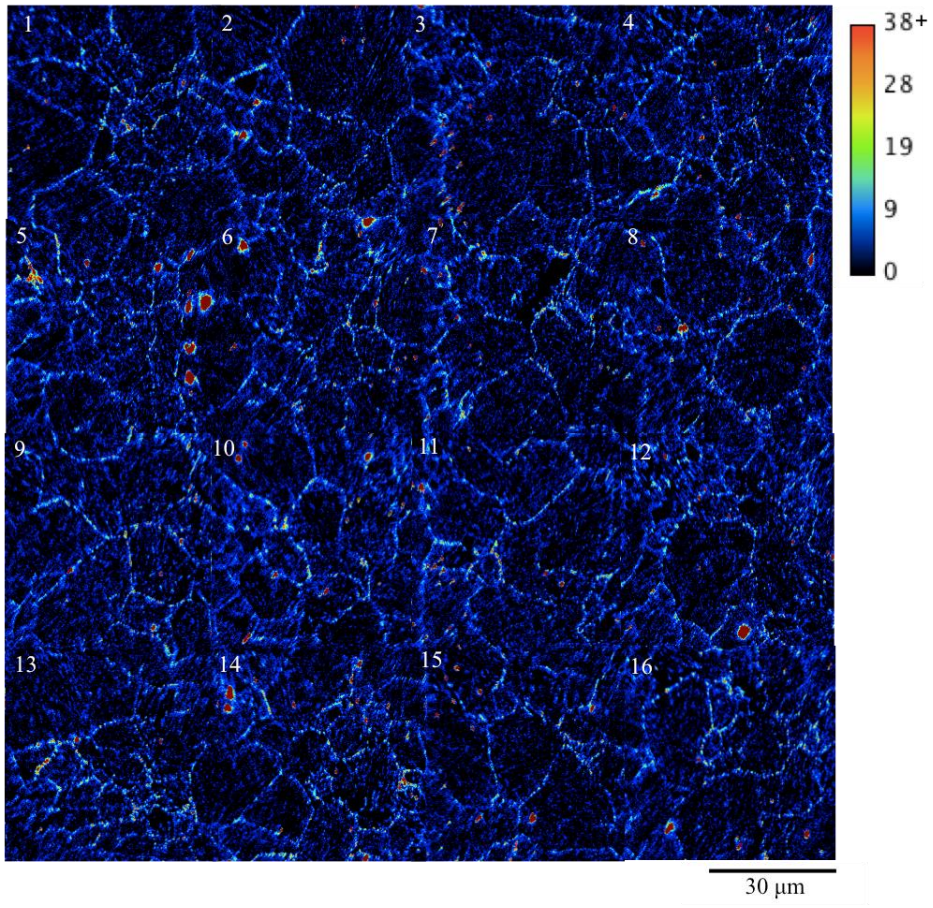


Figure 4.42: Ion micrographs showing the boron distribution of $^{11}B^{16}O_2$ in the quenched and tempered aluminium protected sample 12AM24.

Table 4.9: Total $^{11}B^{16}O_2$ counts on quenched and tempered sample 12AM24 relating to the images shown in Figure 4.42.

Image Number	Total $^{11}B^{16}O_2^-$ counts	Beam current on sample (pA)	Normalised $^{11}B^{16}O_2^-$ intensities: Total $^{11}B^{16}O_2^-$ counts/beam current, (counts/pA)
1	154909	2.1	73766
2	180934	2.1	86159
3	176305	2.1	83955
4	176440	2.1	84019
5	515253	2.1	87980
6	238297	2.1	77882
7	163552	2.1	113475
8	184759	2.1	245359
9	182901	2.1	87096
10	218810	2.1	104195
11	166271	2.1	79177
12	266342	2.1	126830
13	185659	2.1	95246
14	236808	2.1	86518
15	181687	2.1	112766
16	200017	2.1	88409

4.4.3 Comparison of Ti Protected Steels with Different Heat Treatments (12AM23, 12AM23AA and 12AM25)

The addition of titanium helps to avoid segregation of boron nitride at the grain boundaries. Free boron is now available to segregate at the grain boundaries and suppresses the nucleation of proeutectoid ferrite and improves the hardenability (Banerjee, 2017).

4.4.3.1 Sample 12AM23 (as-rolled)

Figure 4.43 shows a 4 x 4 set of $^{11}B^{16}O_2^-$ images over a 200 μm x 200 μm area from the first of the Ti-protected samples. $^{11}B^{16}O_2^-$ images below are scaled from 0 to 10 counts. It is clear that boron has started to precipitate out during the hot rolling process as many large boron precipitates were observed in this sample, many more than in the previously discussed samples. Surprisingly, given the assumed role of Ti as a strong nitride former that leads to the formation of more stable TiN instead of BN, this sample does not show very strong boron segregation to prior austenite grain boundaries, although the $^{11}B^{16}O_2^-$ map does show some segregation on most grain boundaries. More boron is distributed within the ferrite grains but not in the pearlite. As described previously, the pearlite regions show an elevated carbon signal as can be seen in Figure 4.46.

The total boron counts and the normalised intensities for the $^{11}B^{16}O_2^-$ maps shown in Figure 4.43 were summarised in Table 4.10. The sample beam current was measured in FCo as 1.42 pA, 1.38 pA and 1.33 pA on days 1, 2 and 3 respectively.

Image 11 is enlarged in Figure 4.44 and numerous large B-containing particles can be seen. One line scan was performed over a grain boundary and two line scans over boron containing particles. These line scans are shown in Figure 4.45. The line scans were averaged over 10 pixels width to improve the counting statistics with a step size of 0.2 μm along the arrow shown in the $^{11}B^{16}O_2^-$ image in Figure 4.44. The normalised $^{11}B^{16}O_2^-$ intensity on the grain boundary as indicated on line 1 is 1.2

counts/pA which is 60 times lower than on the particle on line 2 and 22 times lower than on the particle on line 3. The boron counts from the particles in this sample are at least 19 times higher than from the particles in reference sample 12AN15, and again this may suggest a higher boron concentration in these precipitates. Detailed particle analysis will be discussed in Section 4.5.4.

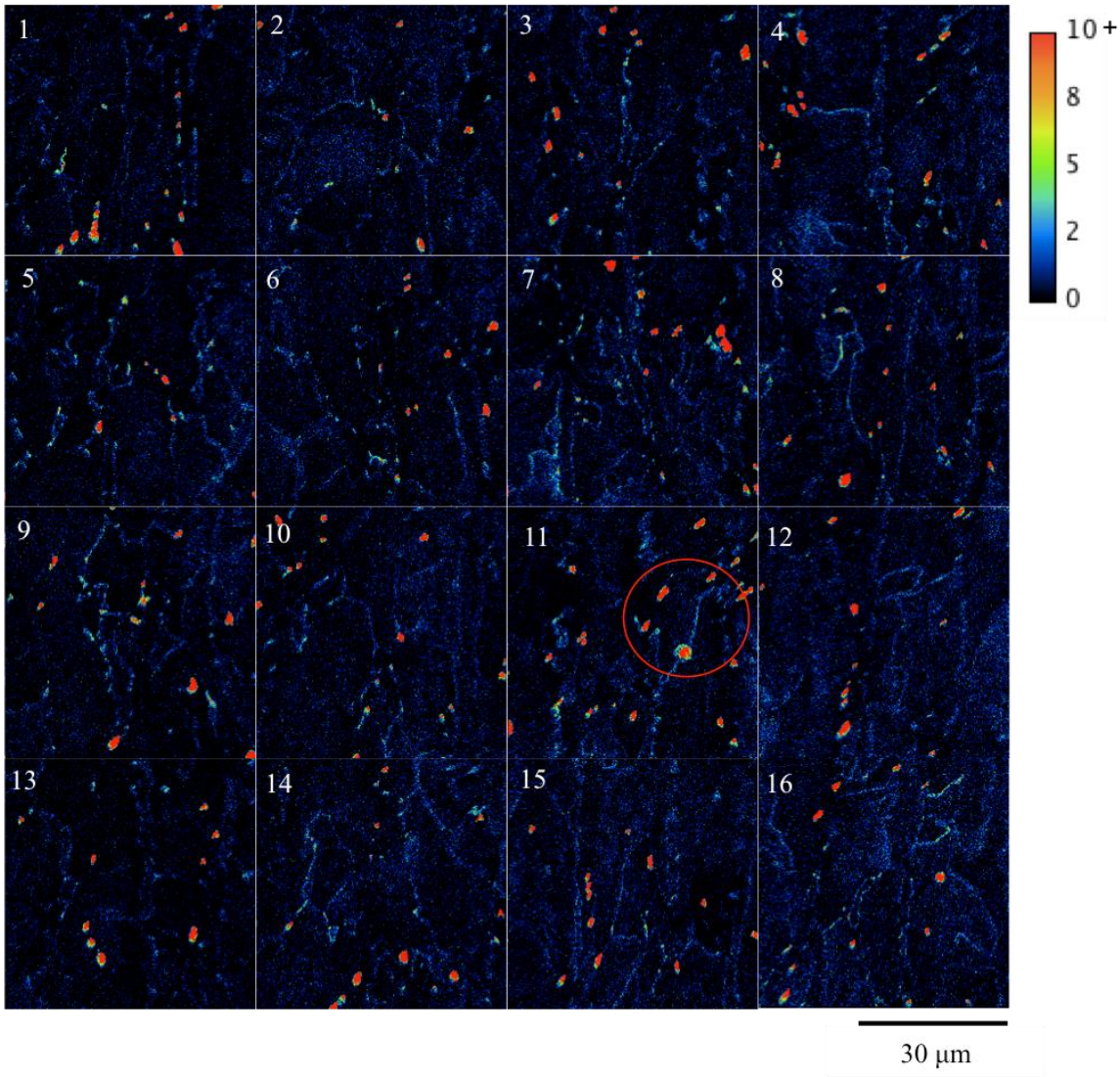


Figure 4.43: Ion micrographs showing the boron distribution of $^{11}B^{16}O_2$ in as-rolled, titanium protected sample 12AM23. Red circles in image 11 indicate the location of subsequent line scans on boron containing particles and on a grain boundary.

Table 4.10: Total $^{11}B^{16}O_2$ counts on as-rolled sample 12AM23 relating to the images shown in Figure 4.43.

Image Number	Total $^{11}B^{16}O_2^-$ counts	Beam current on sample (pA)	Normalised $^{11}B^{16}O_2^-$ intensities: Total $^{11}B^{16}O_2^-$ counts/beam current, (counts/pA)
1	27608	1.42	19442
2	21333	1.42	15023
3	28791	1.42	20275
4	35601	1.42	25071
5	20508	1.42	14442
6	22629	1.42	15936
7	47371	1.42	33360
8	34845	1.42	24539
9	31538	1.38	22854
10	26177	1.38	18969
11	38308	1.38	27759
12	16493	1.42	11615
13	19523	1.38	14147
14	30212	1.38	21893
15	32973	1.33	24792
16	19480	1.33	14647

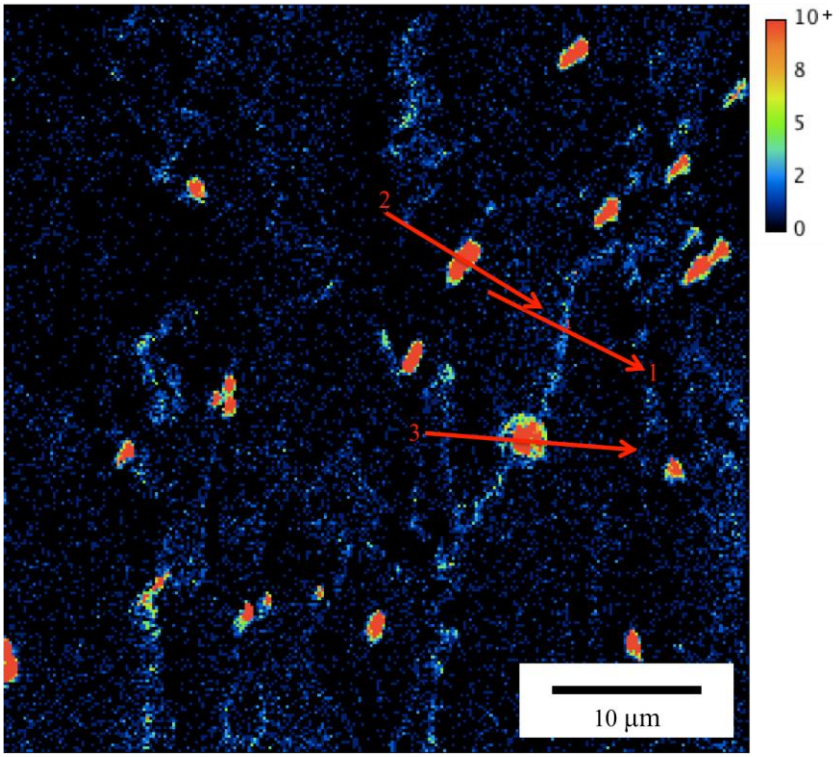


Figure 4.44: Line scans were performed on selected area of sample 12AM23 from image 11 in Figure 4.43. Line scans were taken over a grain boundary (line 1) and boron containing particles (line 2 and 3).

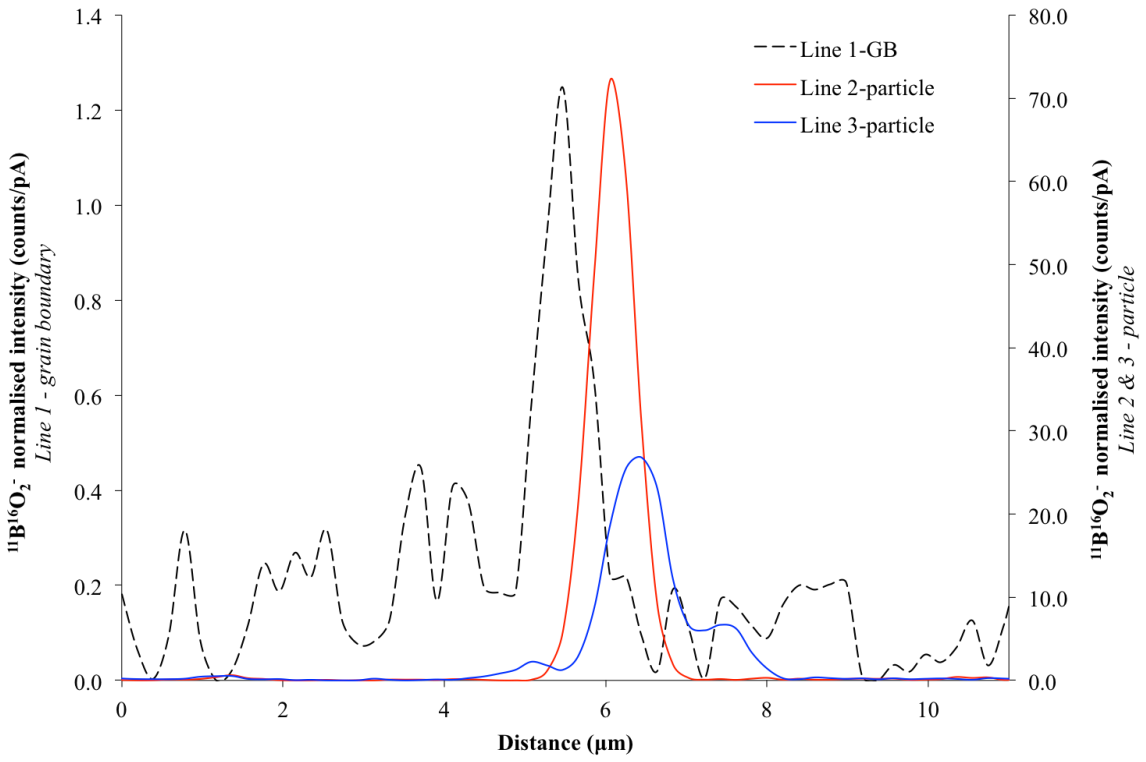


Figure 4.45: Line scans for $^{11}B^{16}O_2^-$ across a grain boundary for as-rolled sample 12AM23 on line 1 and two boron rich particles on line 2 and 3 as indicated by the red arrows marked 1, 2 and 3 in Figure 4.44.

Figure 4.46 shows a typical data set from 12AM23 showing five images simultaneously acquired from the NanoSIMS detectors for $^{12}C^-$, $^{11}B^{12}C^-$, $^{11}B^{14}N^-$, $^{11}B^{16}O_2^-$ and the secondary electron image. These images were summed from 27 sequential maps. The high carbon signal identifies the pearlite regions, which can easily be related with the small-grained microstructural features in the secondary electron image. A line scan was performed across ferrite grains, a pearlite region and two boron rich particles, and shown in Figure 4.47. It was averaged over 10 pixels width to improve the counting statistics with a 0.2 µm step size along the red arrow as shown in the NanoSIMS images in Figure 4.46. The normalised $^{11}B^{16}O_2^-$ intensity on the first boron containing particle is 20 counts/pA whereas on the second particle is two times higher than that.

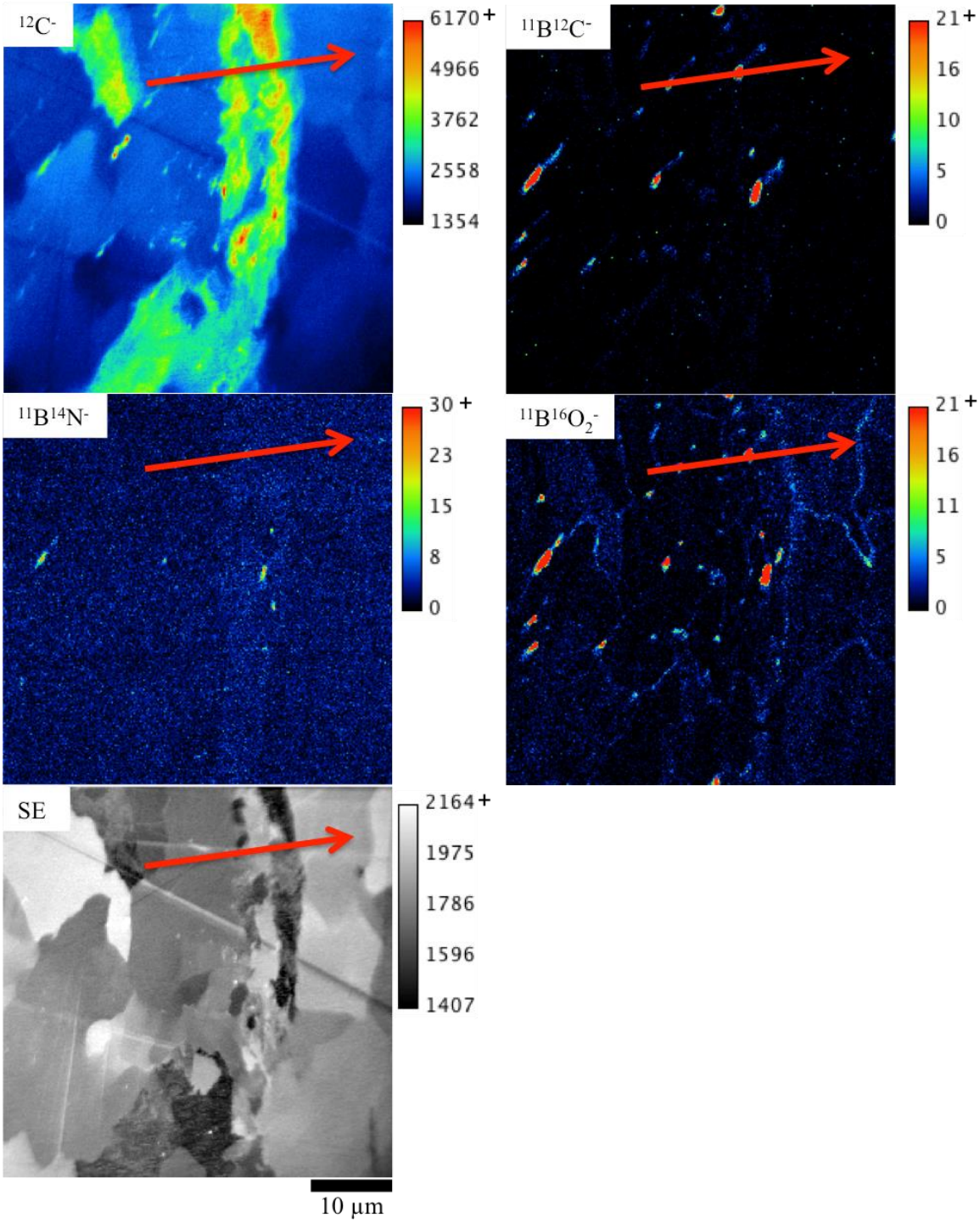


Figure 4.46: Selected area of as-rolled titanium protected sample 12AM23 showing the NanoSIMS maps of $^{12}C^-$, $^{11}B^{12}C^-$, $^{11}B^{14}N^-$, $^{11}B^{16}O_2^-$ and the secondary electron (SE) image. These images were summed from 27 sequential maps. The red arrow indicates the line scan performed across ferrite grains, a pearlite region and two boron rich particles.

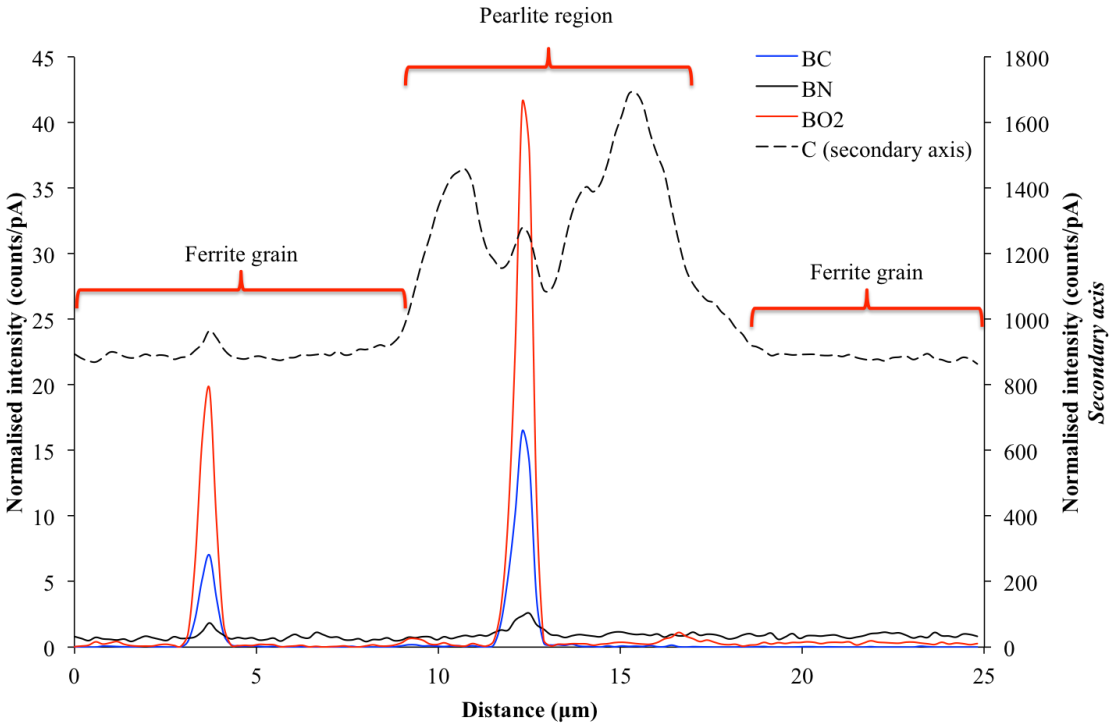


Figure 4.47: Line scans for $^{12}C^-$ (secondary axis), $^{11}B^{12}C^-$, $^{11}B^{14}N^-$, and $^{11}B^{16}O_2^-$ on as-rolled titanium sample 12AM23 as indicated by the red arrows in Figure 4.46 showing the homogeneous carbon content in the ferrite grains. The pearlite column shows high counts from carbon. The location of two boron rich precipitates is also shown.

The carbon maps, as shown in Figure 4.48, shows the position of pearlite region and ferrite grains. Line scan was used along the red arrow shown in the $^{12}C^-$ and $^{11}B^{16}O_2^-$ image. The carbon content in the primary ferrite grains is fairly uniform as can be seen from the line scan shown in Figure 4.49. Many boron particles were observed in the $^{11}B^{16}O_2^-$ image and some segregation at the grain boundaries. The boron counts from pearlite are extremely low, about 0.5 counts/pA, whereas carbon counts in the pearlite region are very high, nearly 3000 counts/pA. The boron signal is higher in ferrite grains compared to the pearlite. However, in this sample, the average boron counts in the ferrite grains are only two times higher than in the pearlite region as compared to Al-protected sample, 12AM22 which shows about 3 times higher.

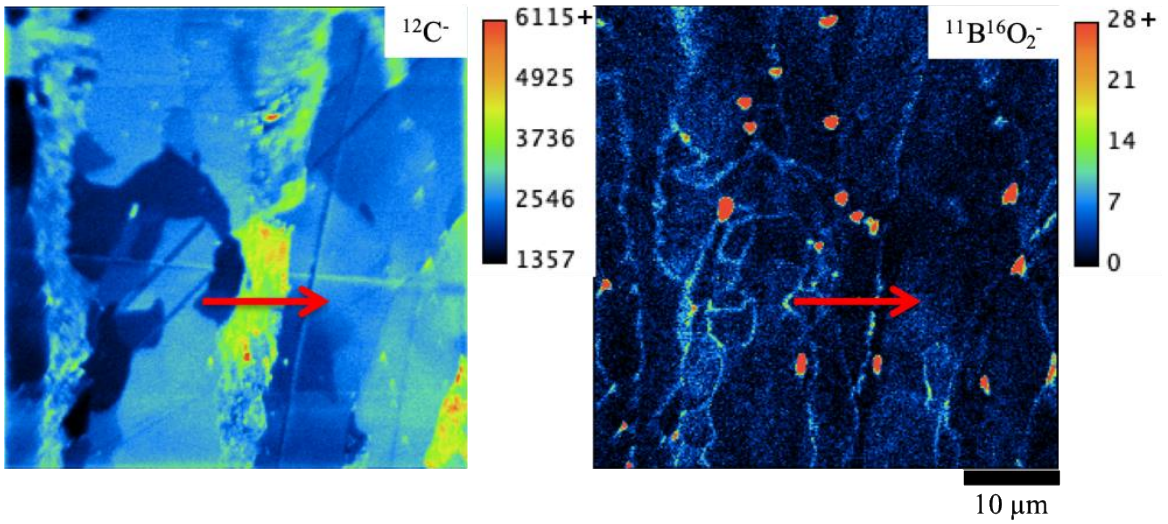


Figure 4.48: Comparison of carbon and boron map of sample 12AM23. The red arrow indicates the line scan performed across ferrite grains and a pearlite region.

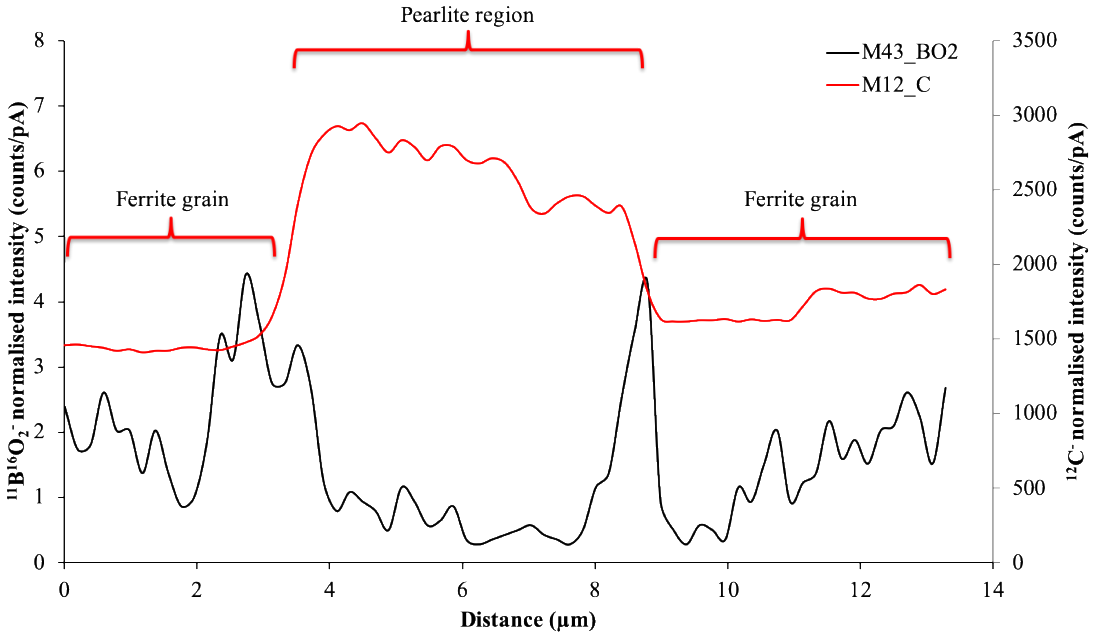


Figure 4.49: Line scans from sample 12AM23 showing the comparison of carbon and boron in the pearlite and ferrite regions, where higher carbon counts were observed in the pearlite region but lower $^{11}B^{16}O_2^-$ counts.

4.4.3.2 Sample 12AM23AA (as-quenched)

Figure 4.50 demonstrates a 3 x 3 set of $^{11}B^{16}O_2^-$ maps over a 150 μm x 150 μm area scaled from 0 to 5 counts to enhance the contrast of the images to show the appearance of the boron segregation on the grain boundaries. Segregation of boron along prior austenite grain boundaries was observed in this sample, with almost no sign of either large or small boron-containing particles. These images were acquired over a duration of three days. The intensity was normalised by the beam current measured on each day so that it can be compared with other samples and measurements on different days.

Table 4.11 displays the total $^{11}B^{16}O_2^-$ counts and its normalised intensities by beam current. The beam current at the sample was measured in FCo as 1.4 pA on day 1, 1.3 pA on day 2 and 1.1 pA on day 3.

Image 6 as shown in Figure 4.50 is enlarged in Figure 4.51 and three line scans were performed over grain boundaries and two line scans on boron containing particles. These line scans are shown in Figure 4.52. The line scans were averaged over 10 pixels width to improve the counting statistics and 0.2 μm steps along the red arrows shown in the $^{11}B^{16}O_2^-$ image in Figure 4.51. The normalised $^{11}B^{16}O_2^-$ intensities at the grain boundaries are 0.8, 1.1 and 0.9 counts/pA for lines 1, 2 and 3 respectively. The normalised intensity for the boron-containing particle on the grain boundary as shown on line scan 4 is 2.6 counts/pA, about 2 times higher than from the particles in the grain on line 5. In comparison with particles in the reference as-quenched sample 12AN15, the normalised intensity for the particle on line 4 is about 2 times lower than the largest particle found in the reference sample. Detailed particle analysis will be discussed in Section 4.5.4.

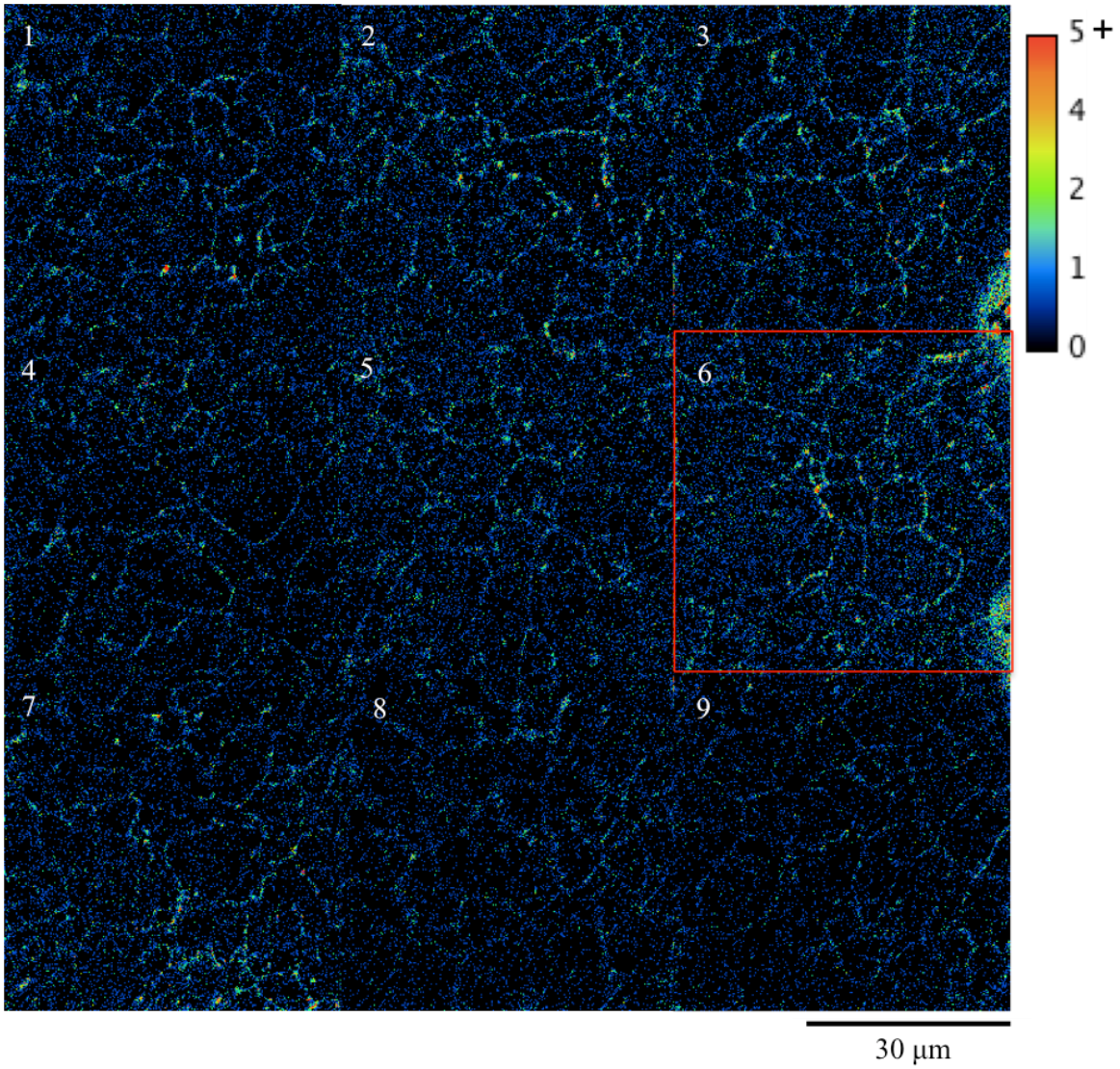


Figure 4.50: Ion micrographs showing the boron distribution of $^{11}B^{16}O_2$ in sample 12AM23AA (Ti-protected, as-quenched). The red square in image 6 indicates the location of subsequent line scans on the grain boundaries and boron containing particles.

Table 4.11: Total $^{11}B^{16}O_2$ counts on as-quenched sample 12AM23AA relating to the images shown in Figure 4.50.

Image Number	Total $^{11}B^{16}O_2^-$ counts	Beam current on sample (pA)	Normalised $^{11}B^{16}O_2^-$ intensities: Total $^{11}B^{16}O_2^-$ counts/beam current, (counts/pA)
1	11428	1.3	8791
2	13843	1.3	10648
3	15866	1.3	12205
4	8970	1.4	6407
5	11951	1.4	8536
6	18306	1.4	13076
7	11440	1.3	8800
8	7992	1.3	6148
9	7555	1.1	6038

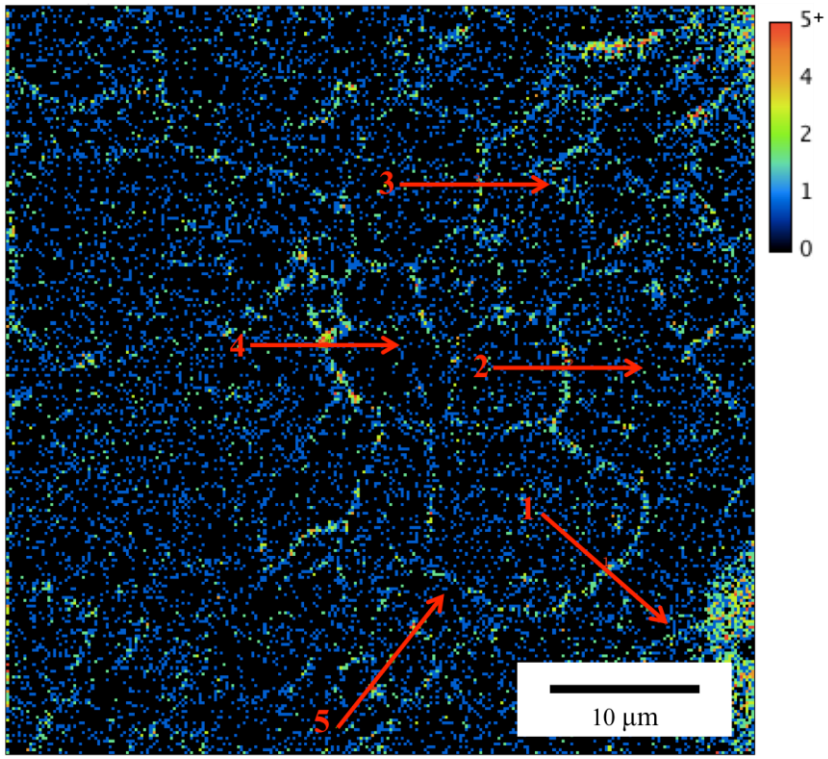


Figure 4.51: Line scans on grain boundaries (lines 1, 2 and 3) and boron containing particles (lines 4 and 5) from sample 12AM23AA.

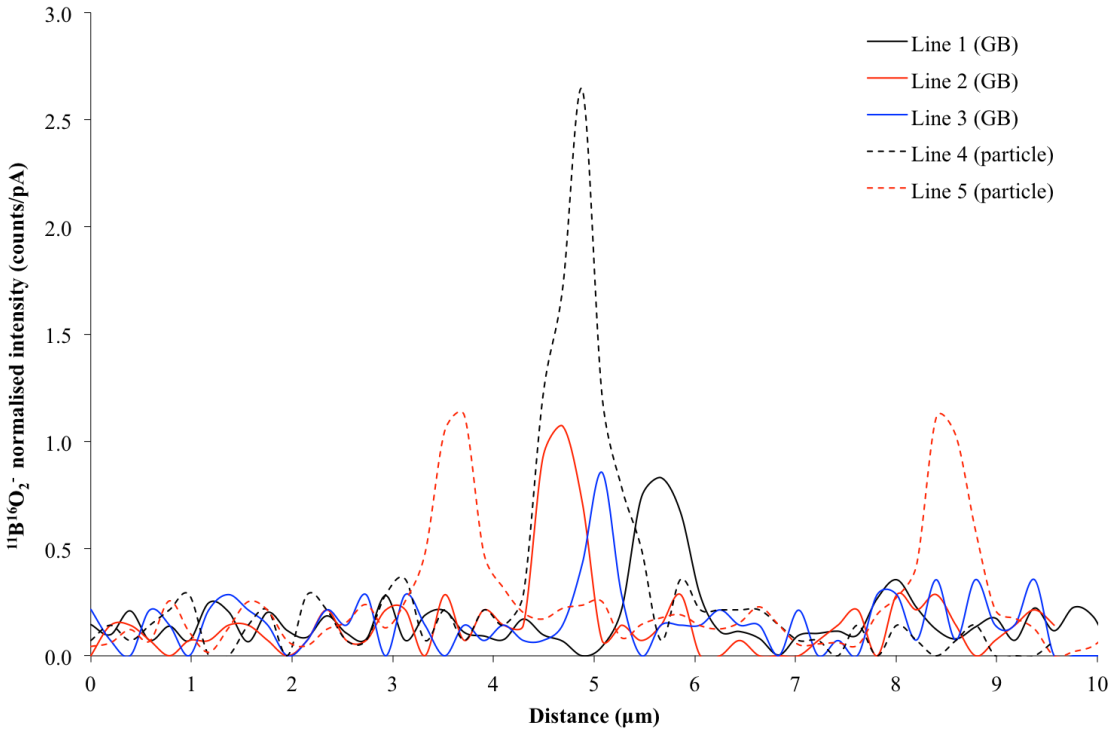


Figure 4.52: Line scans for $^{11}B^{16}O_2^-$ across grain boundaries for as-quenched sample 12AM23AA on lines 1,2 and 3 and on boron rich particles on lines 4 and 5 as indicated by the red arrows marked in Figure 4.52.

The smallest primary aperture (D1=4) was used to achieve a higher lateral resolution image from this sample to study small precipitates on the grain boundaries. Figure 4.53 shows the sum of 92 sequential images of 20 by 20 μm area. Each image was scanned with a dwell time of 10,000 μs/pixel for 256 by 256 pixels. The FCo current on the sample was measured as 0.74 pA. The analysis took nearly 17 hours with a total dose of $7x10^{16}$ Cs atoms per cm^2 implanted on the area. Three line scans were performed over grain boundaries and three line scans on boron containing particles, and shown in Figure 4.54. The line scans were averaged over 10 pixels width to improve the counting statistics with 0.08 μm steps along the arrows shown in the $^{11}B^{16}O_2^-$ image in Figure 4.53.

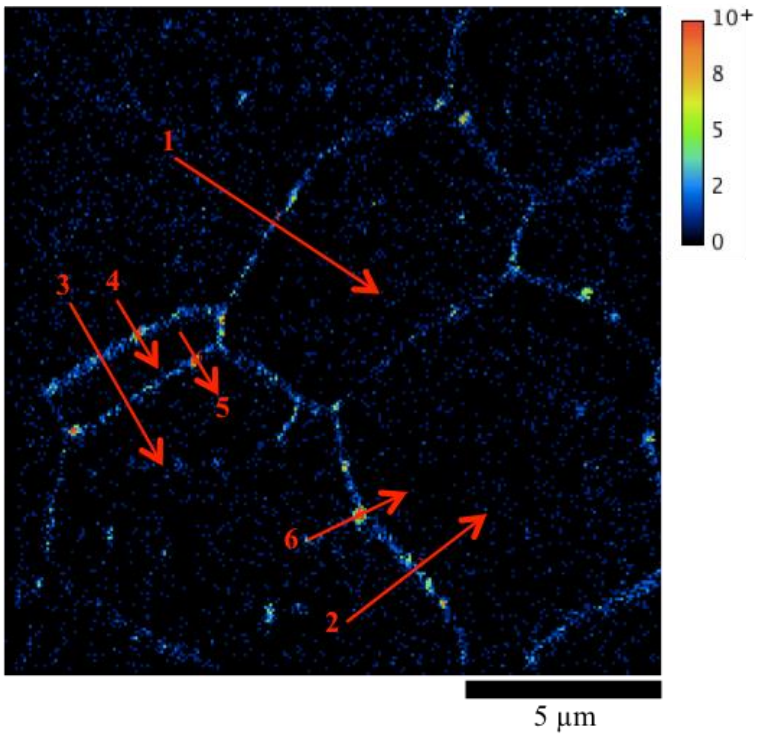


Figure 4.53: High resolution imaging using aperture D1=4 on sample 12AM23AA. This image was summed from 92 sequential maps of 20 x 20 μm area with dwell time 10,000 μs/px/image. Red arrows indicate the line scans performed over grain boundaries (lines 1, 2 and 3) and boron rich particles (lines 4, 5 and 6).

The normalised $^{11}B^{16}O_2^-$ intensities at the grain boundaries are 1.8 and 2.5 counts/pA for lines 1 and 2 respectively. Line scan 3 goes across two grain boundaries showing normalised $^{11}B^{16}O_2^-$ intensities

of 2.5 counts/pA from the first one and 1.3 counts/pA on the second. The normalised intensity for the boron containing particle on the grain boundary shown on line scan 4 is 5.7 counts/pA which is slightly lower than from the particle on the grain boundary on line 5. However, the particle on the grain boundary on line 6 shows nearly 2 times higher counts than either of the particles on lines 4 or 5.

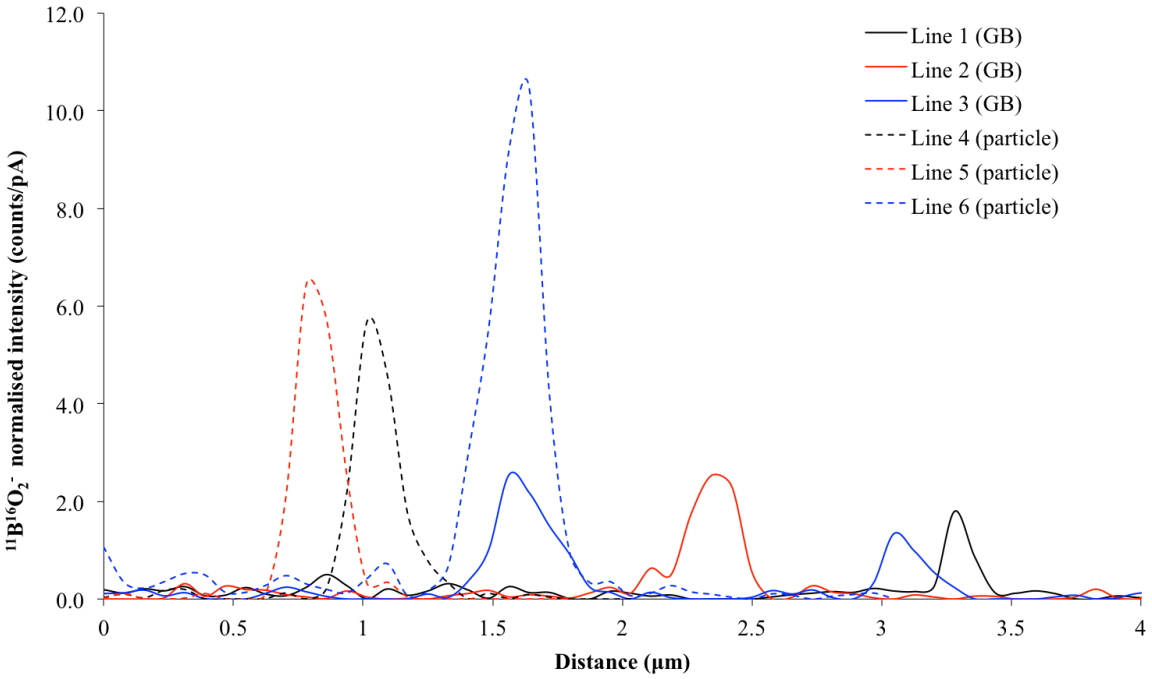


Figure 4.54: Line scans for $^{11}B^{16}O_2^-$ across grain boundaries for as-quenched sample 12AM23AA on lines 1, 2 and 3 and on boron rich particles on lines 4, 5 and 6 as indicated by the red arrows marked in Figure 4.53.

4.4.3.3 Sample 12AM25 (quenched and tempered)

Figure 4.55 shows a 4 x 4 montage of $^{11}B^{16}O_2^-$ NanoSIMS maps over an area of 200 µm x 200 µm. The $^{11}B^{16}O_2^-$ ion maps are scaled from 0 to 10 counts. Segregation at the prior austenite grain boundaries can be seen, with small precipitates near grain boundaries that appear to outline prior austenite grains. Very few coarse particles were observed in this sample compared to the as-rolled samples, with coarse particles appearing in the grains only in images 2, 6, 7 and 13. It seems that the small boron precipitates are formed during tempering, as already described for samples 12AM24 above. One very large particle was observed in image 5 resulting in high number of total boron

counts for that image, with an intensity of over 100,000 counts/pA, nearly a factor of 3 higher than the average number of total boron counts in the other images from this sample. Images 11, 13 and 14 show lower boron counts, around 20,000 counts/pA. Lower counts for those particular images might be caused by misalignment of the secondary ion beam tuning probably due to magnet drift caused by changes in room temperature. The boron counts in the grains do not look homogeneous as compared to the as-quenched sample, 12AM23AA, perhaps as a result of tiny precipitates in the grains. The total boron counts and the normalised intensities for the $^{11}B^{16}O_2^-$ maps shown in Figure 4.55 were summarised in Table 4.12. The beam current at the sample was measured in FCo as 1.5 pA on the first day, 1.45 pA on the second day and 1.27 pA on the third day.

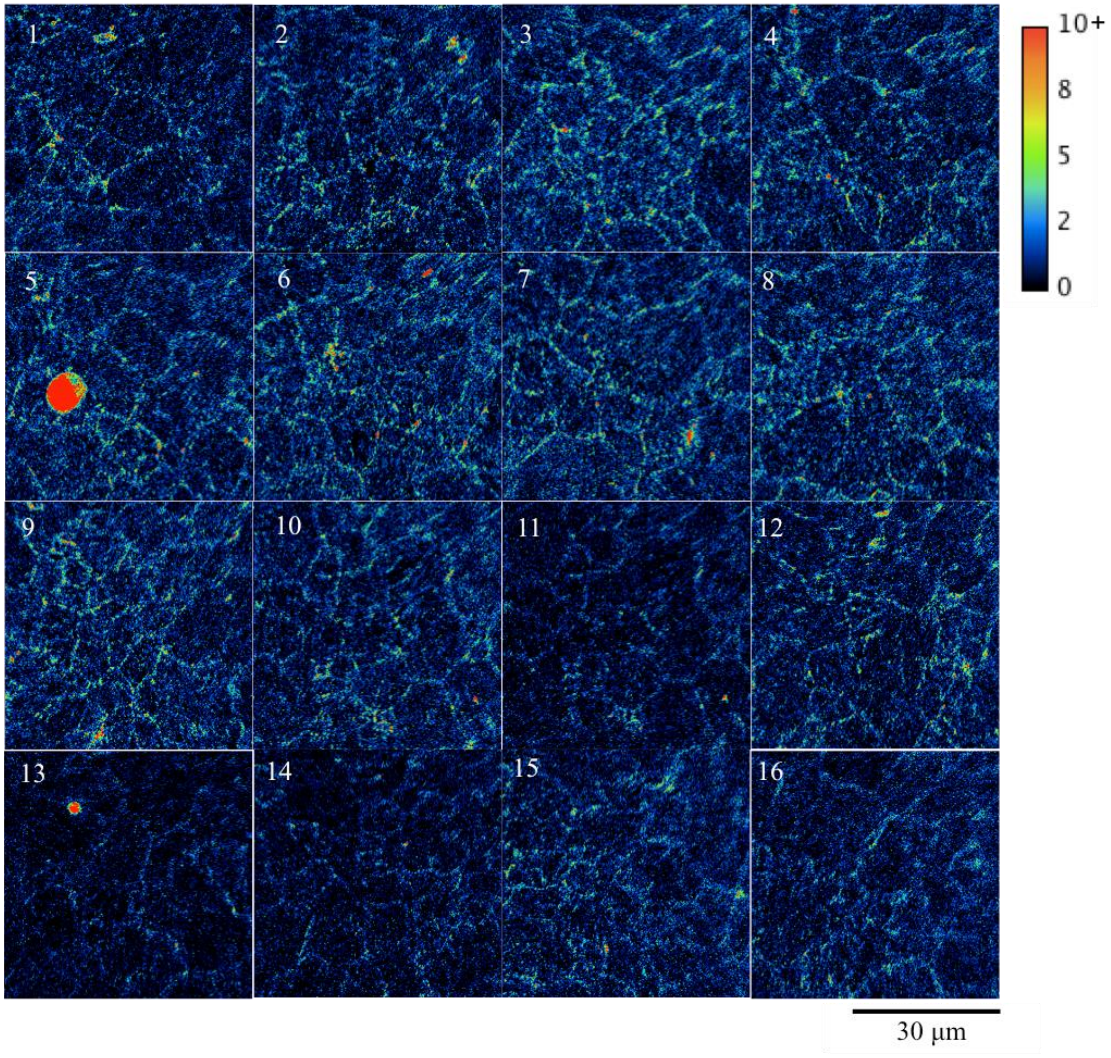


Figure 4.55: Ion micrographs showing the boron distribution of $^{11}B^{16}O_2$ in quenched and tempered titanium protected sample 12AM25.

Table 4.12: Total $^{11}B^{16}O_2^-$ counts on quenched and tempered sample 12AM25 relating to the images shown in Figure 4.55.

Image Number	Total $^{11}B^{16}O_2^-$ counts	Beam current on sample (pA)	Normalised $^{11}B^{16}O_2^-$ intensities: Total $^{11}B^{16}O_2^-$ counts/beam current, (counts/pA)
1	49467	1.5	32978
2	58432	1.5	38955
3	76990	1.45	53097
4	65770	1.45	45359
5	147472	1.45	101705
6	72185	1.45	49783
7	70318	1.45	48495
8	69518	1.45	47943
9	65622	1.45	45257
10	55399	1.45	38206
11	33988	1.45	23440
12	49111	1.45	33870
13	26882	1.27	21167
14	31035	1.27	24437
15	51458	1.27	40518
16	47546	1.27	37438

Image 2 in Figure 4.55 was scanned for longer to give more information on this sample by improving the counting statistics. 29 sequential images were acquired on image 2, adding an additional dose of 2.14 x 10^{16} Cs atoms/cm^2. Figure 4.56 shows the location of two line scans performed on image 2 showing the five images simultaneously acquired from the NanoSIMS detectors, for $^{12}C^-$, $^{11}B^{12}C^-$, $^{11}B^{14}N^-$, $^{11}B^{16}O_2^-$ and the secondary electron (SE) image.

The tempered martensitic structure of this sample can be seen very clearly in the SE image, and the inhomogeneous distribution of carbon in the martensitic structure is shown in the $^{12}C^-$ map. No coarse particles were found in the $^{11}B^{14}N^-$ map and only three coarse boron particles were observed near the top right in the $^{11}B^{16}O_2^-$ map, which correlate well with particles in $^{11}B^{12}C^-$ map. Line scan 1 was performed across two boron-containing particles and also transects a prior austenite grain boundary at the end, as shown in Figure 4.56. Both particles gave almost the same boron counts, with a normalised $^{11}B^{16}O_2^-$ intensity of about 36 counts/pA as indicated in line scan 1 shown in Figure 4.57. The normalised $^{11}B^{16}O_2^-$ intensity on the grain boundary is around 8 counts/pA.

Line scan 2 for this sample is shown in Figure 4.56, and was taken across several prior austenite grain boundaries and also crossed some small particles which are visible in the $^{11}B^{16}O_2^-$ map. A

magnified section of the $^{11}B^{16}O_2^-$ image is transposed onto the linescan to show the correlation between the grain boundary peaks and the smaller particles that were intersected. Three of the grain boundaries show approximately the same amount of normalised $^{11}B^{16}O_2^-$ counts of about 8 counts/pA. The last grain boundary with a boron-containing particle on it shows a spike with normalised $^{11}B^{16}O_2^-$ counts twice as high as from the other grain boundaries.

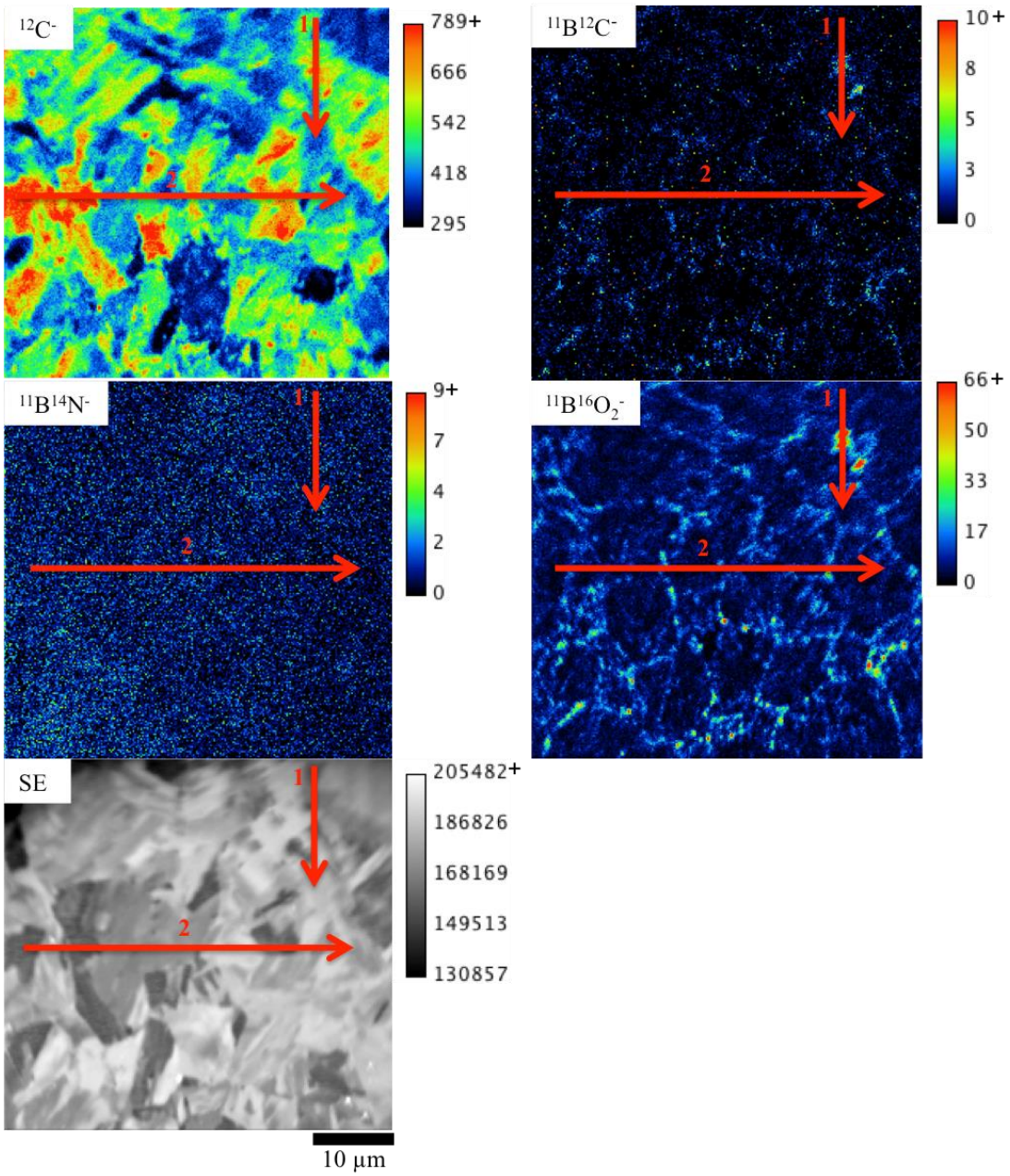


Figure 4.56: Line scans on selected area of sample 12AM25 from image 2 in Figure 4.55 showing the NanoSIMS maps of $^{12}C^-$, $^{11}B^{12}C^-$, $^{11}B^{14}N^-$, $^{11}B^{16}O_2^-$ and secondary electron (SE) image. These images were summed from 29 sequential maps to improve the counting statistics.

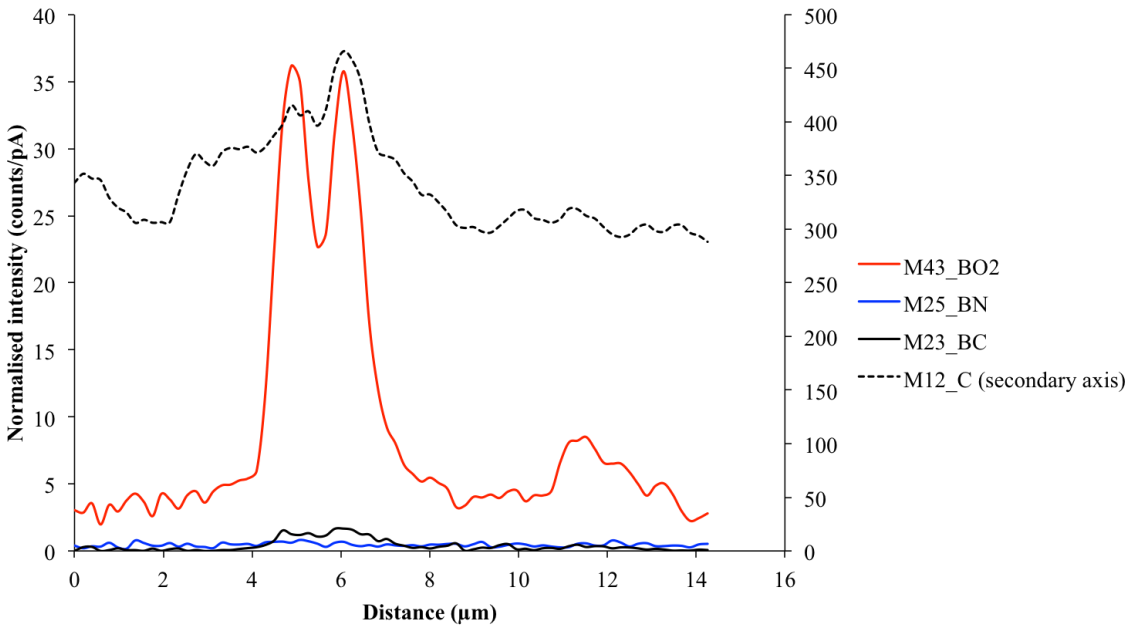


Figure 4.57: Line scans for $^{12}C^-$, $^{11}B^{12}C^-$, $^{11}B^{14}N^-$, $^{11}B^{16}O_2^-$ across grain boundaries and particles for as-rolled sample 12AM25 as indicated by red arrow no. 1 in Figure 4.56.

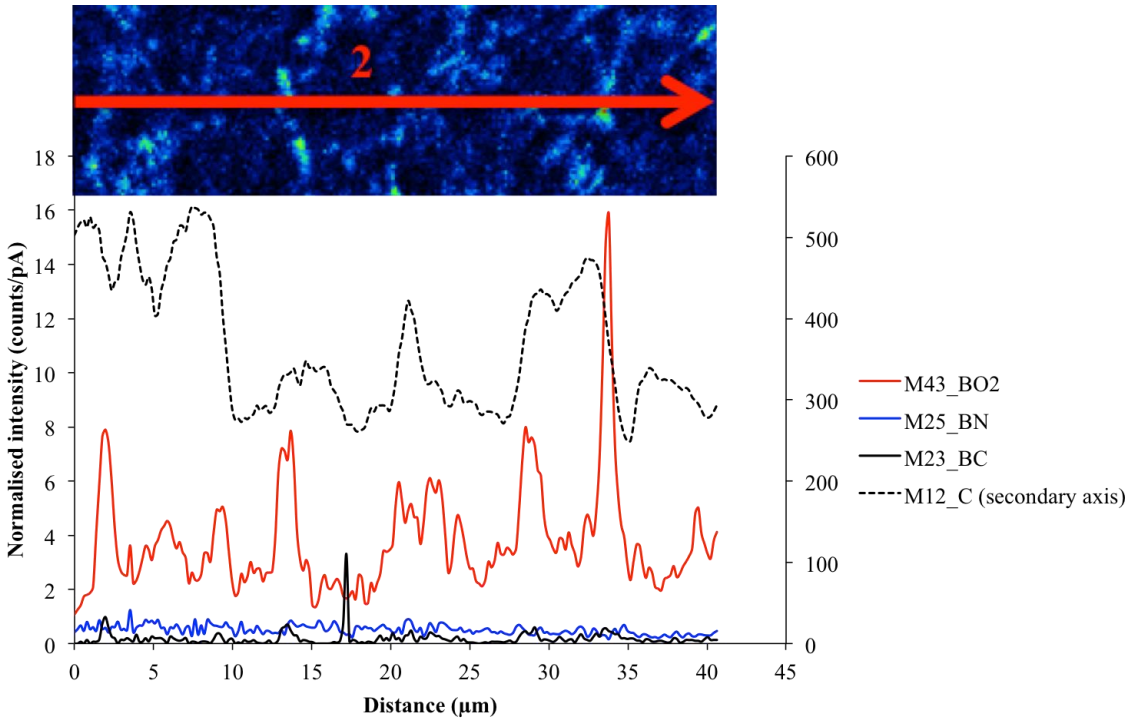


Figure 4.58: Line scans on sample 12AM25 as indicated by red arrow no. 2 in Figure 4.56 showing very variable counts of carbon (black dotted line) on the secondary axis.

4.4.4 Comparison of As-quenched (12AM16) and Direct Quenched (12AM15D) Samples

4.4.4.1 Sample 12AM16 (as-quenched)

Figure 4.59 shows a 4 x 3 set of $^{11}B^{16}O_2^-$ images over a 200 µm x 150 µm area. $^{11}B^{16}O_2^-$ images below are scaled from 0 to 5 counts for clarity although there are pixels with higher counts than this. Segregation of boron along prior austenite grain boundaries was observed in this sample and there are very few precipitates on the grain boundaries, which makes the grain boundaries in these $^{11}B^{16}O_2^-$ images seem much sharper and narrower than in other samples. These prior austenite grains are much larger compared with the previous groups of steels due to two factors; higher initial reheated temperature at 1200°C, and less deformation after hot rolling to 20 mm thickness as compared to other samples that have been rolled to 15 mm thickness. Table 4.13 shows the total boron counts and the normalised intensities by the beam current. The beam current at the sample was measured in FCo as 0.83 pA on day 1 and 0.36 pA on day 2.

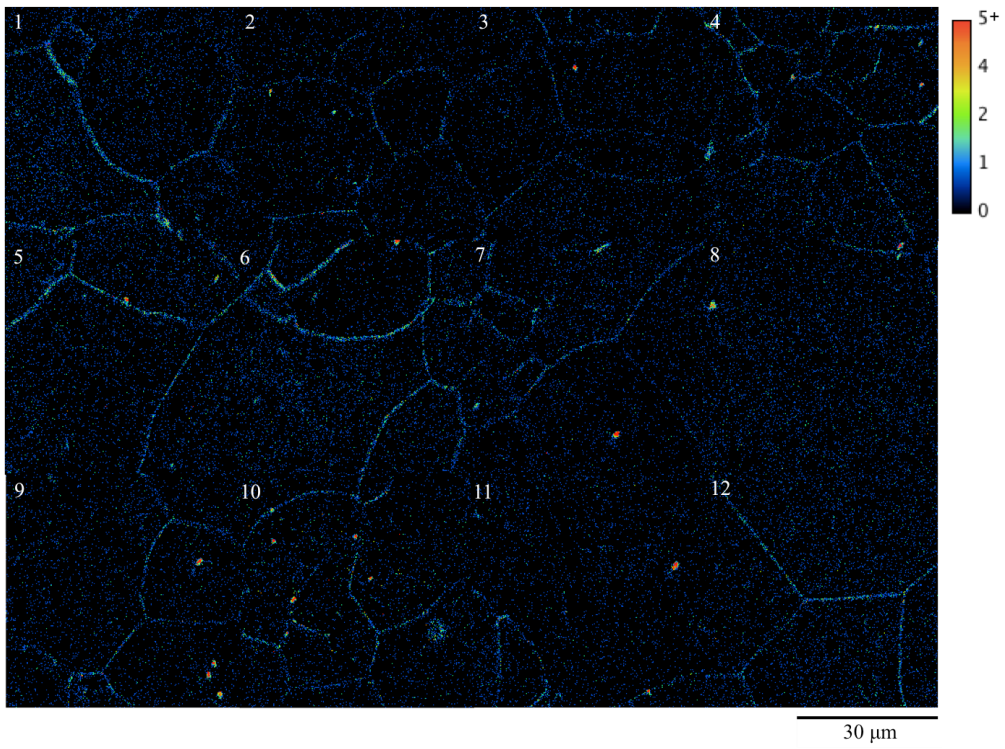


Figure 4.59: Ion micrographs showing the boron distribution, mapped as $^{11}B^{16}O_2$, in as-quenched, aluminium protected sample 12AM16.

Table 4.13: Total $^{11}B^{16}O_2$ counts on as-quenched sample 12AM16 relating to the images shown in Figure 4.59.

Image Number	Total $^{11}B^{16}O_2^-$ counts	Beam current on sample (pA)	Normalised $^{11}B^{16}O_2^-$ intensities: Total $^{11}B^{16}O_2^-$ counts/beam current, (counts/pA)
1	6394	0.83	7704
2	3367	0.83	4057
3	3382	0.36	9394
4	5160	0.36	14333
5	5564	0.36	15456
6	6478	0.36	17994
7	4809	0.36	13358
8	5007	0.36	13908
9	4652	0.36	12922
10	5136	0.36	14267
11	4033	0.36	11203
12	5596	0.36	15544

4.4.4.2 Sample 12AM15D (direct quenched)

Figure 4.60 shows a 4 x 3 set of $^{11}B^{16}O_2^-$ images over a 200 μm x 150 μm area. $^{11}B^{16}O_2^-$ images below are scaled from 0 to 10 counts for clarity although there are pixels with higher counts than this. Segregation of boron along prior austenite grain boundaries was observed in this sample, and only a few small boron-containing particles were seen in the maps. One large particle was observed in image 6. The prior austenite grains are larger than previous group of steels, but have a similar size to sample 12AM16 for the same reasons as mentioned in section 4.4.4.1. The level of segregation to grain boundaries in this direct quenched sample was considerably higher than observed in sample 12AM16 due to higher B content (30 ppm) as compared to 12AM15D (25 ppm). The total boron counts and the normalised intensities for the $^{11}B^{16}O_2^-$ maps shown in Figure 4.60 are summarised in Table 4.14. The beam current at the sample was measured in FCo as 0.72 pA on the first day, 1.04 pA on day 2 and 0.97 pA on the third day using aperture D1=2.

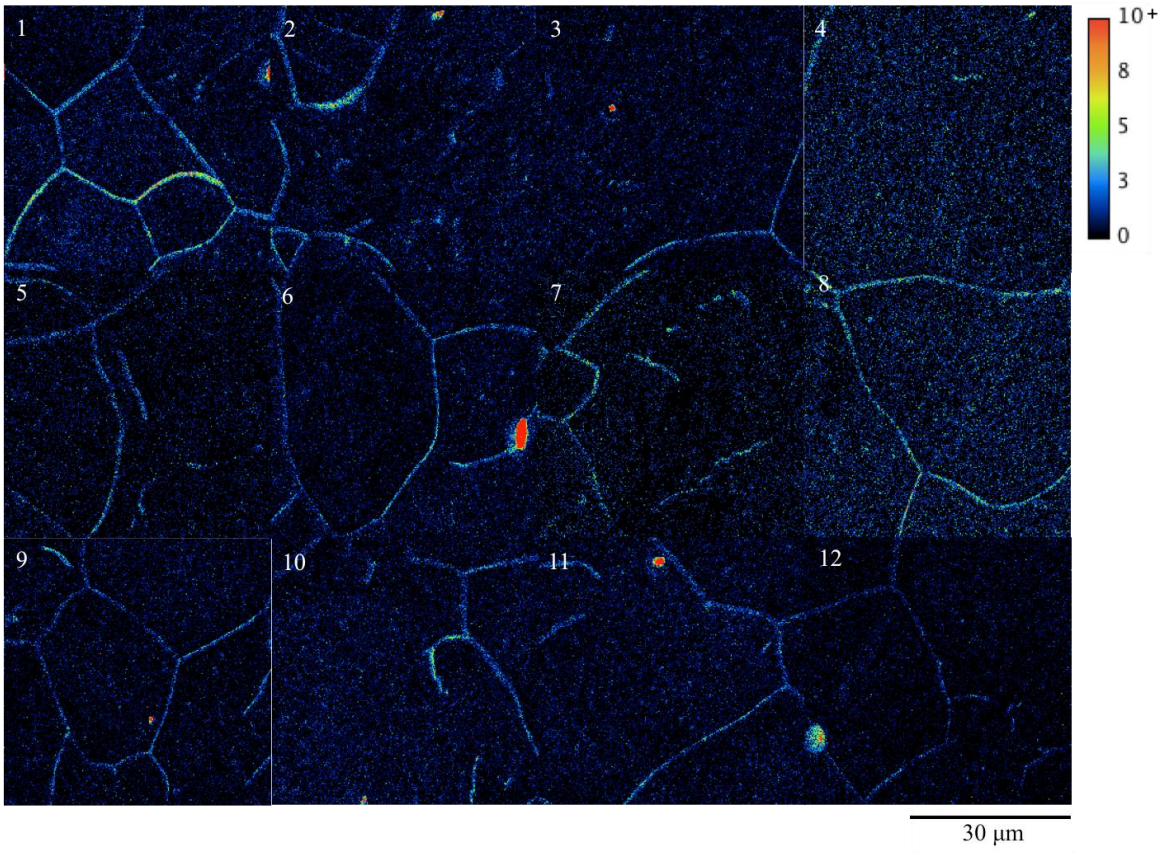


Figure 4.60: Ion micrographs showing the boron distribution of $^{11}B^{16}O_2$ in direct quenched sample 12AM15D.

Table 4.14: Total $^{11}B^{16}O_2$ counts on as-quenched sample 12AM15D relating to the images shown in Figure 4.60.

Image Number	Total $^{11}B^{16}O_2^-$ counts	Beam current on sample (pA)	Normalised $^{11}B^{16}O_2^-$ intensities: Total $^{11}B^{16}O_2^-$ counts/beam current, (counts/pA)
1	29304	0.72	40700
2	23409	0.72	32513
3	17752	0.72	24656
4	16018	0.72	22247
5	9980	1.04	9596
6	24574	1.04	23629
7	9417	1.04	9055
8	19067	0.72	26482
9	16422	1.04	15790
10	21859	0.97	22535
11	20648	0.97	21287
12	12305	0.97	12686

4.4.5 Comparison of Samples 13ZZ6ZBM, 13ZZ9ZBM and 13ZZ12ZBM

4.4.5.1 Sample 13ZZ6ZBM Mo alloyed

Effect of boron on the microstructure and properties of molybdenum-added steels has been investigated by several groups (Asahi, 2002, Hara et al., 2004, Han et al., 2008, Li et al., 2015). The addition of molybdenum retards the precipitation of $M_{23}(CB)_6$ and thus retains more boron in solution that can segregate to grain boundaries and contributes to hardenability (Asahi, 2002). Molybdenum strengthens the grain boundaries by lowering the activity of carbon in the ferrite which makes the material less susceptible to grain boundary precipitation (Banerjee, 2017).

Figure 4.61 shows four $^{11}B^{16}O_2^-$ images from the Mo alloyed (0.49 wt.% Mo) sample 13ZZ6ZBM. $^{11}B^{16}O_2^-$ images below are scaled from 0 to 10 counts for clarity although there are pixels with higher counts than this. Table 4.15, summarised the total $^{11}B^{16}O_2^-$ and its normalised intensity by beam current. The current at the sample was measured in FCo as 1.43 pA on day 1 and 1.8 pA on day 2 and 1.94 on day 3 using D1=2. Segregation at the prior austenite grain boundaries was observed in this sample with various sizes of boron containing particles. Big particles were spotted mostly in image 1 and image 4. Image 1 gives the highest normalised intensity, as there is a stringer of boron particles, and most of the boron counts are from these particles.

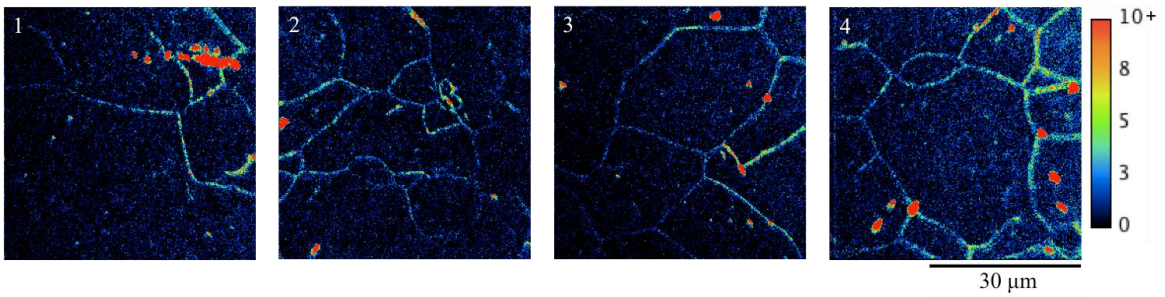


Figure 4.61: Ion micrographs showing the boron distribution, mapped as $^{11}B^{16}O_2$, in Mo alloyed (0.49 wt.% Mo) sample 13ZZ6ZBM.

Table 4.15: Total $^{11}B^{16}O_2$ counts on Mo alloyed sample 13ZZ6ZBM relating to the images shown in Figure 4.61

Image Number	Total $^{11}B^{16}O_2^-$ counts	Beam current on sample (pA)	Normalised $^{11}B^{16}O_2^-$ intensities: Total $^{11}B^{16}O_2^-$ counts/beam current, (counts/pA)
1	92729	1.43	64845
2	36146	1.43	25277
3	20220	1.80	11233
4	25736	1.94	13266

4.4.5.2 Sample 13ZZ9ZBM (Al protected – good hardenability)

Figure 4.62 shows three $^{11}B^{16}O_2^-$ images of an aluminium protected (0.077 wt.% Al) sample 13ZZ9ZBM. $^{11}B^{16}O_2^-$ images below are scaled from 0 to 10 counts for clarity although there are pixels with higher counts than this. The summarised data for the total $^{11}B^{16}O_2^-$ and its normalised intensity by beam current is shown in Table 4.16. The current at the sample was measured in FCo as 1.74 pA using the aperture D1=2. The $^{11}B^{16}O_2^-$ ion maps, as shown in Figure 4.62, reveal that the boron is primarily detected at the prior austenite grain boundaries rather than in the grain interior in this quenched Al protected sample. A few big boron-containing particles were observed mostly in image 1 and 2.

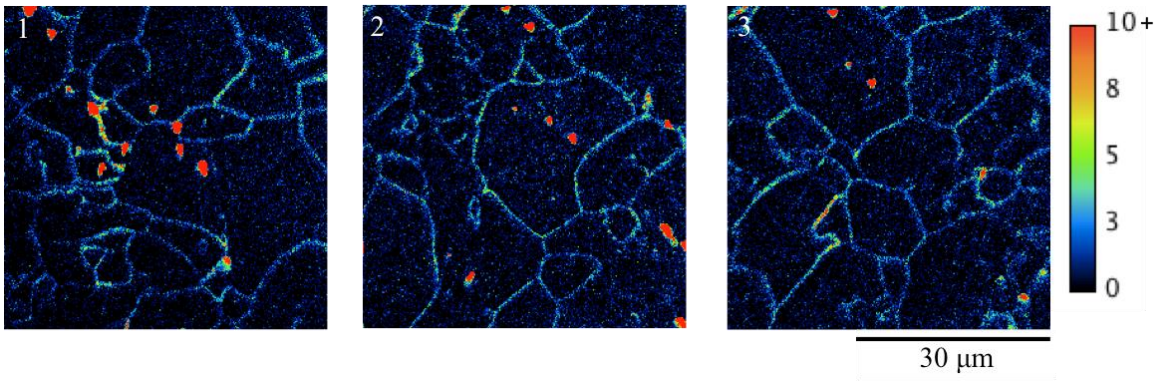


Figure 4.62: Ion micrographs showing the boron distribution, mapped as $^{11}B^{16}O_2$, in Al-protected (0.077 wt.% Al) sample 13ZZ9ZBM.

Table 4.16: Total $^{11}B^{16}O_2$ counts on Al-protected sample 13ZZ9ZBM relating to the images shown in Figure 4.62.

Image Number	Total $^{11}B^{16}O_2^-$ counts	Beam current on sample (pA)	Normalised $^{11}B^{16}O_2^-$ intensities: Total $^{11}B^{16}O_2^-$ counts/beam current, (counts/pA)
1	37243	1.74	21404
2	25782	1.74	14817
3	24058	1.74	13826

4.4.5.3 Sample 13ZZ12ZBM (Al protected – low hardenability)

Figure 4.63 shows three $^{11}B^{16}O_2^-$ images of aluminium protected (0.057 wt.% Al) sample 13ZZ12ZBM. $^{11}B^{16}O_2^-$ images below are scaled from 0 to 10 counts for clarity although there are pixels with higher counts than this. The summarised data from these three images is tabulated in Table 4.17, showing the total $^{11}B^{16}O_2^-$ counts and its normalised intensity. The current at the sample was measured in FCo as 1.51 pA on day 1 and 1.80 pA on day 2 using D1=2. The $^{11}B^{16}O_2^-$ images illustrate the segregation of boron at the prior austenite grain boundaries with various sizes of particles decorated in the grains and a few on the grain boundaries. Several big particles were seen in image 1 and one large elongated particle was found in image 2, which is the highest total boron counts compared to other images.

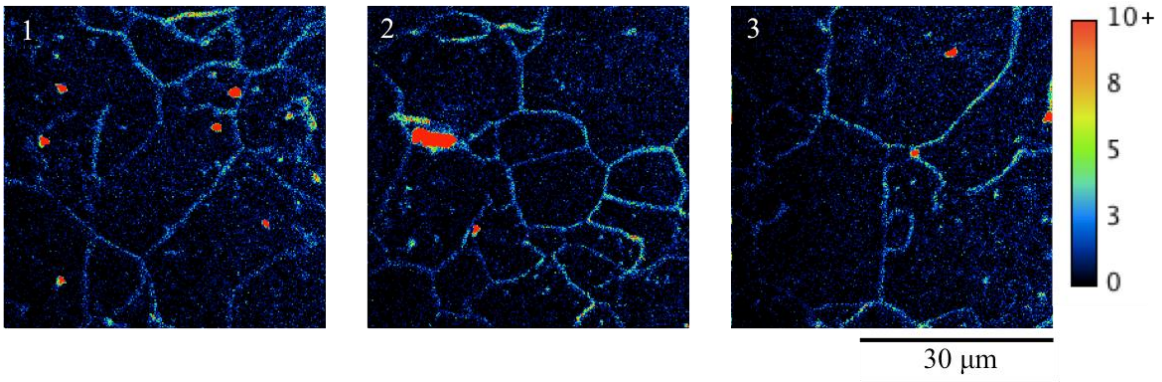


Figure 4.63: Ion micrographs showing the boron distribution, mapped as $^{11}B^{16}O_2$, in Al-protected (0.057 wt.% Al) sample 13ZZ12ZBM.

Table 4.17: Total $^{11}B^{16}O_2$ counts on Al-protected sample 13ZZ12ZBM relating to the images shown in Figure 4.63.

Image Number	Total $^{11}B^{16}O_2^-$ counts	Beam current on sample (pA)	Normalised $^{11}B^{16}O_2^-$ intensities: Total $^{11}B^{16}O_2^-$ counts/beam current, (counts/pA)
1	24498	1.51	16224
2	46892	1.51	31054
3	18314	1.80	10174

4.4.6 Discussion and Summary of Boron Distributions

Figure 4.64 shows the percentage of the total boron counts (%) measured from particles, grain boundaries and matrix in all the 15 steel samples studied in this chapter. It is divided into three groups of heat treatments; as-rolled (light grey), quenched (medium grey), and quenched and tempered (dark grey).

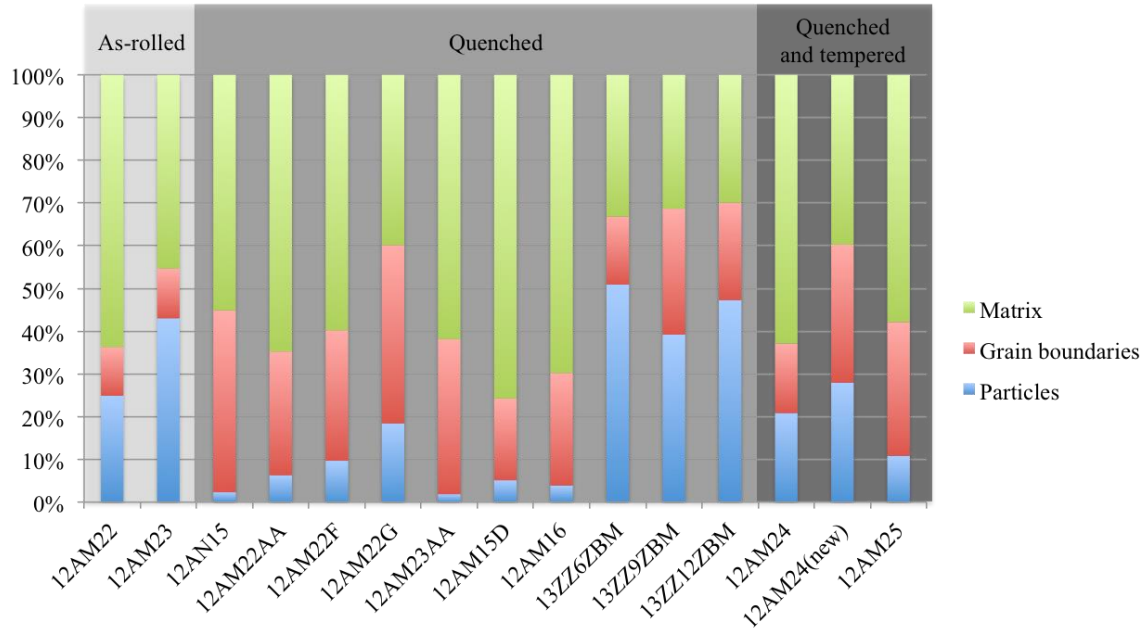


Figure 4.64: Fraction of boron counts in matrix, grain boundaries and particles (in percentages) grouped by their heat treatments.

Both as-rolled samples, aluminium protected 12AM22 and titanium protected 12AM23, show high percentages of the total detected boron in particles rather than segregated to the grain boundaries. 25% of boron was found in the particles in the aluminium protected sample 12AM22, only 11% in the grain boundaries, and the remaining 64% remains in the matrix. The as-rolled titanium protected

sample 12AM23 shows a very high proportion of boron in the particles, 43%, and only 12% of the boron was found in the grain boundaries, with the remaining 45% in the matrix.

All the as-quenched samples except 13ZZ6ZBM, 13ZZ9ZBM and 13ZZ12ZBM samples show similar boron distributions. More boron was found in the grain boundaries and less boron in particles. Reference sample 12AN15 shows the highest percentage (43%) of boron segregated to the grain boundaries and the lowest percentage (2%) of boron in particles, with the remaining 55% in the matrix. The aluminium protected as-quenched sample 12AM22AA shows 29% of boron in the grain boundaries and 6% in the particles, with the balance of 65% in the matrix. 36% of the boron was detected in the grain boundaries of the titanium protected as-quenched sample 12AM23AA. This sample also shows the lowest percentage of boron in the particles (2%), the same as in the reference sample 12AN15, and the remaining 61% in the matrix.

Sample 12AM22F which has been treated for 10 minutes at the austenizing temperature does not show much difference to the as-quenched sample 12AM22AA which has been treated for 30 minutes at the austenizing temperature. The percentage of boron at the grain boundaries in both samples is about 30%. The percentage of boron in particles in 12AM22F is slightly higher (10%) compared to 12AM22AA (6%). Sample 12AM22G which has been treated for 180 minutes at the austenizing temperature has the highest percentage (42%) of boron at the grain boundaries compared to 12AM22AA and 12AM22F, and the percentage of boron in particles in 12AM22G is also the highest (18%). This means that the percentage of the boron in the matrix for this sample was the lowest (40%) compared to the other two comparable samples.

Both samples 12AM15D and 12AM16 have much larger prior austenite grain size compared with other steels studied here due to the high normalizing temperature (1200°C). Less grain boundary segregation was observed in 12AM15D than 15AM16, with 19% and 26% of the boron in grain boundaries, respectively. Only 5% and 4% of the boron was found in particles in samples 12AM15D and 12AM16. That means that more boron was found in the matrix, 76% in 12AM15D and 70% in 12AM16 rather than in the grain boundaries and particles. This is expected because the standard

isotherm analysis of McLean and others predicts that the amount of equilibrium segregation will be lower at higher temperatures, and the much higher solubility of boron in austenite at 1200°C (Figure 4.25) may suppress the formation borocarbides and nitrides. Very similar behaviour in terms of boron segregation at the grain boundaries in the direct quenched and the conventional as-quenched steels has been observed. The direct quenched sample also shows strong boron segregation at the grain boundaries and less boron in particles. Therefore, the direct quenched method can be an alternative to reduce costs and increase overall efficiency in the steel making industry.

In sample 13ZZ6ZBM, 0.49 wt% of molybdenum was added to the steel to enhance the hardenability effect of the boron. Sample 13ZZ9ZBM has a higher hardness compared to sample 13ZZ12ZBM due to higher contents of alloying elements (Si, Mn, Al, and Ti) that give strength and hardness to the steel. All these three samples show boron segregation at the grain boundaries, with some big (2 to 3 μm) boron containing particles. A high percentage of the boron was detected in particles compared to the grain boundaries, 51% in 13ZZ6ZBM, 39% in 13ZZ9ZBM and 47% in 13ZZ12ZBM. 16%, 29% and 23% of boron was segregated at the grain boundaries in 13ZZ6ZBM, 13ZZ9ZBM and 13ZZ12ZBM, respectively. These steels show the lowest amount of boron in the matrix, about 30%.

After quenching and tempering, the amount of boron in the grain boundaries in the aluminium protected sample 12AM24 slightly reduced to 16% (first data acquisition) and slightly increased to 32% (second data acquisition) as compared to the initial percentage 29% in as-quenched sample 12AM22AA. The amount of boron in grain boundaries in the titanium protected sample 12AM25 slightly reduced to 31%. After the tempering process, small precipitates were observed in both samples resulting in the percentage of boron in the particles increasing to 21% (first data), 28% (second data) and 11% in sample 12AM24 and 12AM25, respectively. 63% (first data) and 40% (second data) of boron was in the matrix of sample 12AM24 and 58% in the matrix of 12AM25.

Figure 4.65 shows the fractions of total normalised boron counts in the matrix, grain boundaries and particles normalised by total dose implanted, and grouped by heat treatment. The aluminium

protected samples as-rolled 12AM22 and quenched and tempered 12AM24 (first data acquisition) were analysed in the NanoSIMS in the same week in March 2013, and with the same tuning of the machine (and the same bulk boron content of 23 ppm). They would be expected give almost the same total number of boron counts, but the total boron counts from 12AM22 are much higher than from 12AM24. The titanium protected sample as-rolled 12AM23 and quenched and tempered 12AM25 were analysed in the NanoSIMS in the same week in July 2013, with the same tuning and experimental setup. Surprisingly, even though the samples have the same boron content (20 ppm), sample 12AM25 shows a much higher total number of boron counts compared to sample 12AM23.

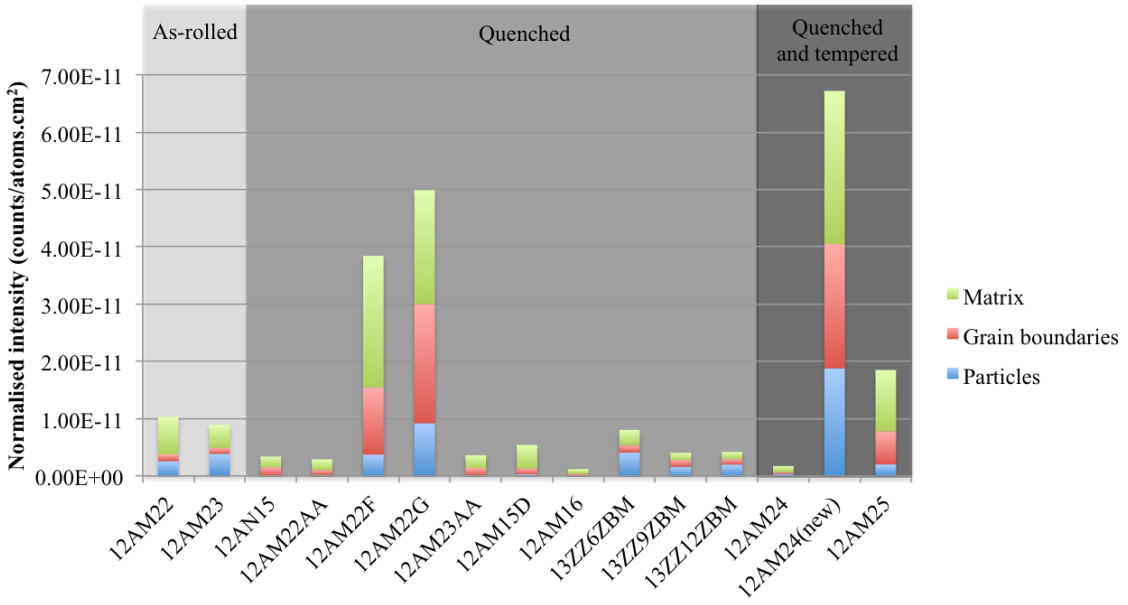


Figure 4.65: Fraction of boron counts in matrix, grain boundaries and particles normalised by total dose implanted grouped by heat treatments.

There are several possible reasons for these surprising results, some to do with the samples and others related to the NanoSIMS technique itself. It is possible that the samples themselves are not uniform in composition, and although reasonably large areas have been mapped on each steel this may not have captured the average composition of the material. This is a problem with all high-resolution techniques in that it is hard to know if the areas analysed are truly representative of the bulk material.

Figure 4.67 and Figure 4.68 summarise the fractions of the total detected boron counts in particles, grain boundaries and matrix in the aluminium protected quenched and tempered sample 12AM24 for 16 separate regions, 50 μm square, that have been analysed over two days. The aim of this analysis is to show how changes in local microstructure over hundreds of μm can change the quantitative data extracted. A comparison of the measured distribution of boron in the 9 top right images, the 9 bottom left images and all 16 images is shown in Figure 4.66. The top right 9 images give more total boron counts compared to the 9 bottom left images, and also have more counts in the particles (25%) compared to the 9 bottom left images (12%). The percentage of boron counts in the grain boundaries does not vary very much, 15% in the top right images and 17% in the bottom left images. The remaining boron fraction was in the matrix was 59% in the top right images and 70% in the bottom left images. This finding shows how a small number of big particles in the imaged area will affect the distribution of counts to the different microstructural features, and how an inhomogeneous microstructure can distort the quantitative data extracted using high spatial resolution techniques. This problem must be considered when looking at the data extracted on the other samples in this study and could explain the differences in the data noted above.

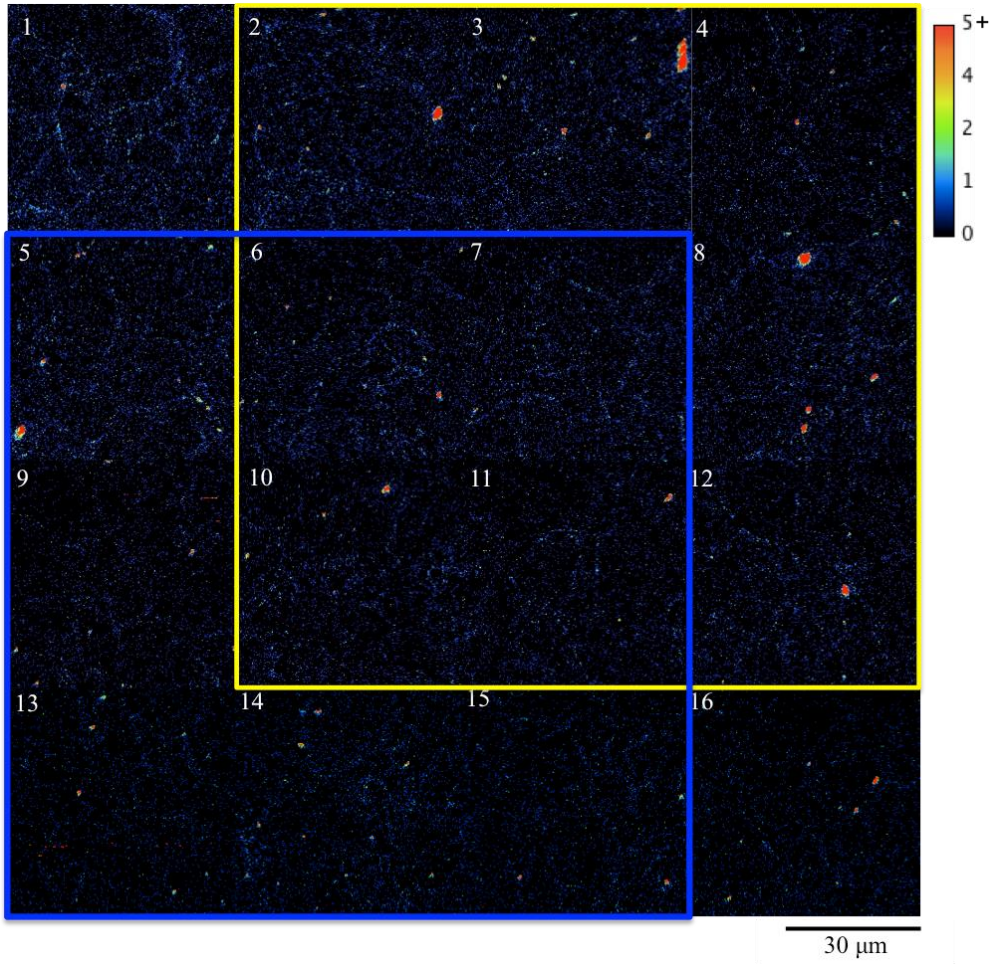


Figure 4.66: Ion micrographs showing the boron distribution of $^{11}B^{16}O_2$ in the quenched and tempered aluminium protected sample 12AM24. The 9 top right images are in the yellow square and the 9 bottom left images are in the blue square.

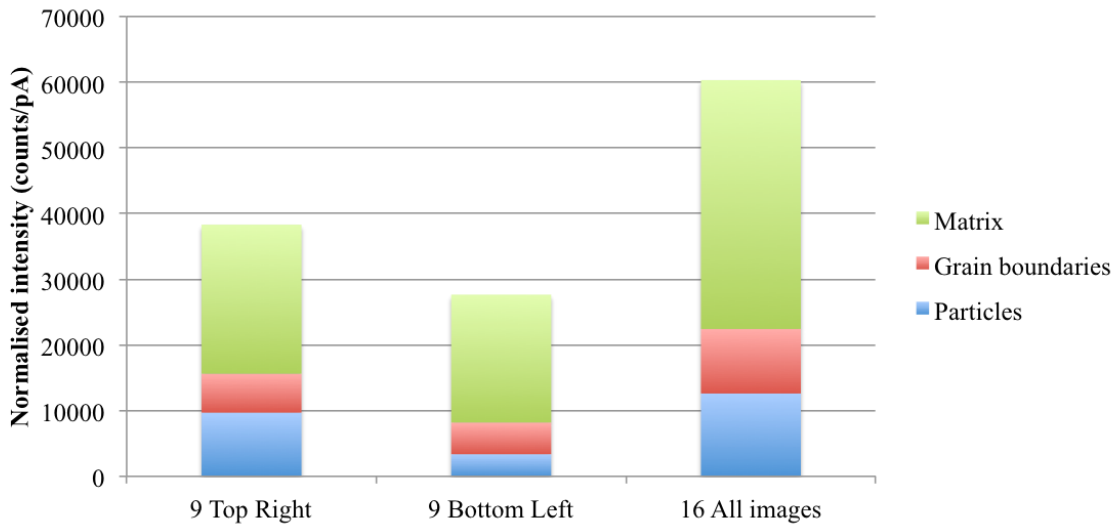


Figure 4.67: Fraction of boron counts in different sets of images (as shown in Figure 4.66) from sample 12AM24 (normalised with beam current)

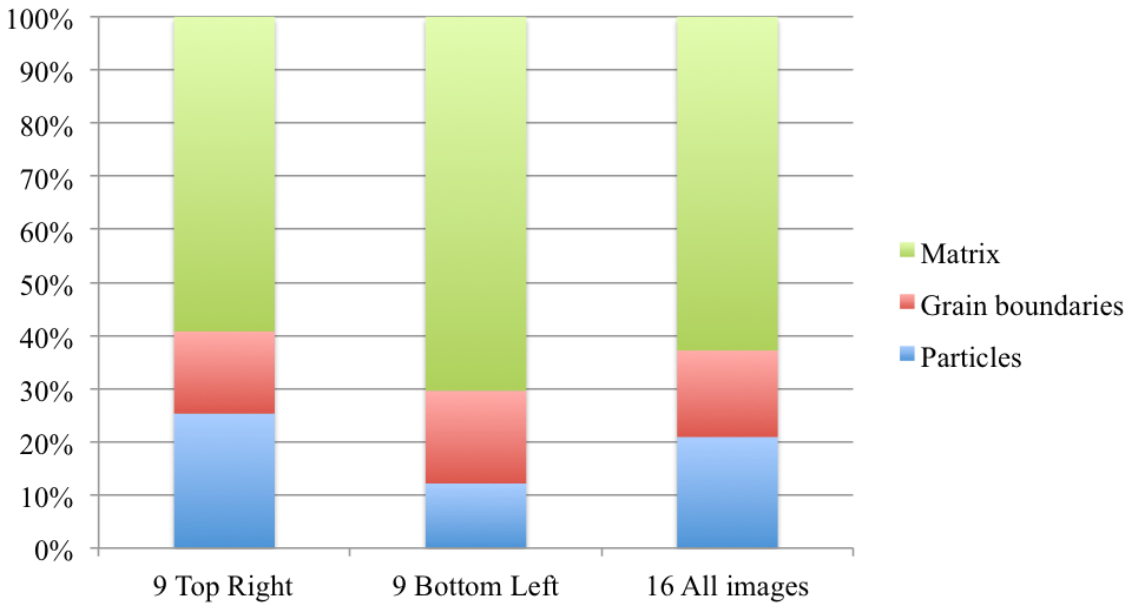


Figure 4.68: Fraction of boron counts in different sets of images (as shown in Figure 4.66) from sample 12AM24 (in percentages)

Matrix effects also complicate the use of all SIMS techniques when analysing metallurgical samples. Apparent differences in matrix composition may result from local variations in ionization yield from different materials (ferrite – both primary and in pearlite which have different compositions as discussed above – and cementite) and variable sputter rates as a function of the orientation of

crystalline materials. However, the data presented on the relative percentages of boron detected in grain boundaries, particles and the grain interiors (matrix) from the NanoSIMS maps will be rather independent of the total yield of boron counts, and can still give a reliable indication of how the characteristic distribution of boron varies in these steels after different heat treatments. Some alloys clearly contain only a small volume fraction of boron-containing particles, and these tend to show strong grain boundary segregation (although it is not evident whether this is a result of equilibrium or non-equilibrium processes). Other samples show a large number of particles and much less grain boundary segregation. The average B content in the pro-eutectoid ferrite is clearly higher than in the pearlite, consistent with the solubility of B at different temperatures predicted by the phase diagram.

4.5 Quantitative Analysis of Boron in Steels

4.5.1 Ion-implanted Standard Samples

This section describes an attempt to quantify the grain boundary segregation of boron described above using specially prepared samples with B implanted into pure iron. In order to predict the concentration profile of B in the iron surface, Stopping and Range of Ions in Matter (SRIM) calculations were performed in the SRIM 2013 version with the 2008 stopping power version using the Transport of Ions in Matter (TRIM) program. The TRIM calculations were made with Kinchin-Pease model using the 'Detailed Calculation with full Damage Cascades' and basic plots using 'Ion Distribution with Recoils projected on Y-Plane'. A total of 10,000 boron ions with 150 keV energy were simulated in iron. The screen shot of the TRIM setup window is presented in Figure 4.69 and the output of Ion Range Distribution is shown in Figure 4.70. The boron concentration in atoms/cm^3 was calculated from the TDATA.txt output by multiplying the boron ion distribution (atoms/cm^3) / (atoms/cm^2) by the ion dose (ions/cm^2).

Two NanoSIMS depth profiles were acquired on each of the three samples with boron implanted into pure iron at doses of 1 x 10^{15}, 1 x 10^{16} and 5 x 10^{16} B ions cm^{-2}, and are shown in Figure 4.72 where the $^{11}B^{16}O_2^-$ ion intensity is shown as a function of increasing Cs^+ implanted dose. The

distribution curves of boron are approximately Gaussian in shape as we would expect from implanted samples.

In order to turn $^{11}B^{16}O_2^-$ counts into a concentration, it is necessary to know the boron content in these samples at the peak of this implantation profile. This calibration can then be used to calculate local boron concentrations from NanoSIMS maps. The peak values on the SRIM profiles in Figure 4.71 can be used to generate 3 points on a plot of $^{11}B^{16}O_2^-$ counts against real boron concentration. To try and account for instrumental parameter variations, two sets of calibration data were collected on the three boron implanted samples, and the average data is plotted in Figure 4.73. The boron concentration was found to be proportional to $^{11}B^{16}O_2^-$ ion intensity and gives us confidence that it can be used to quantify boron concentrations in different regions of the microstructures shown above, including segregation at grain boundaries.

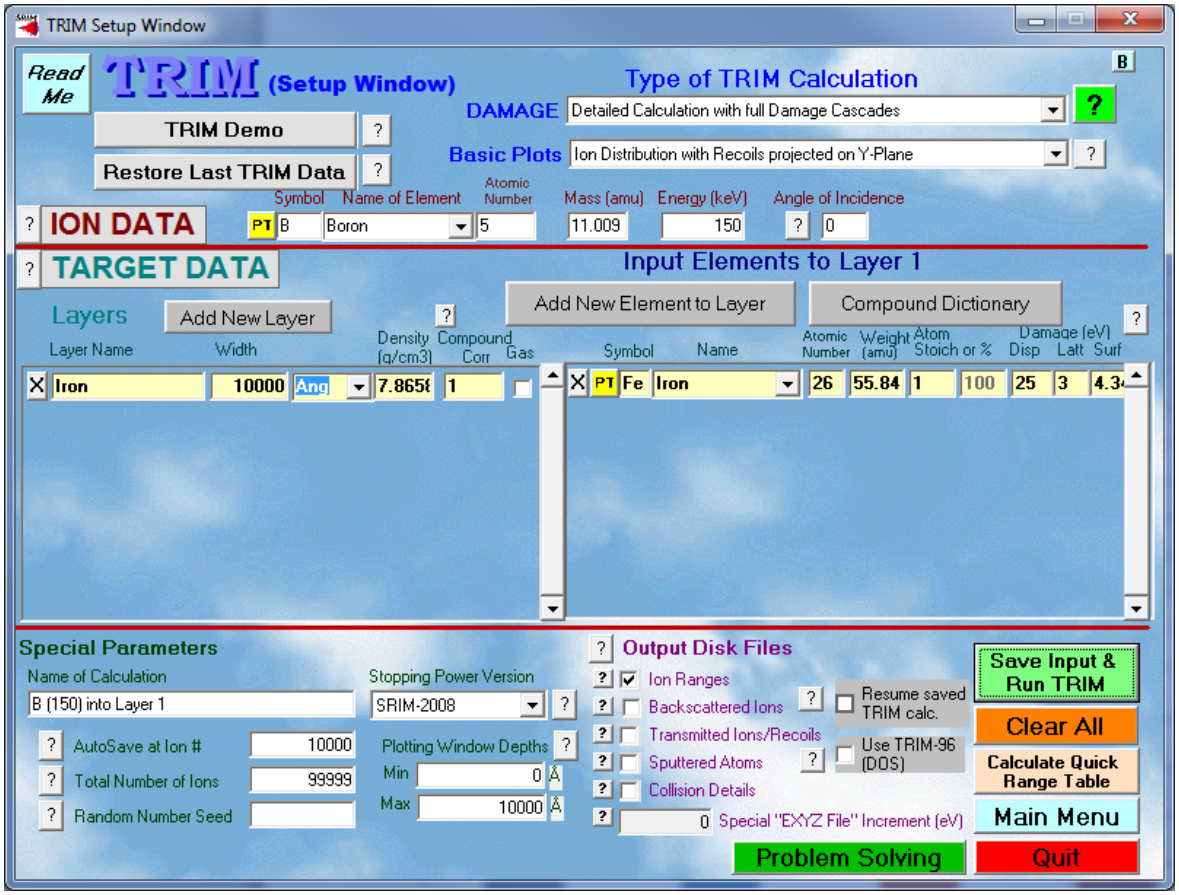


Figure 4.69: Screen shot of TRIM setup window using SRIM 2013 version with the 2008 stopping power version. 10,000 boron ions were simulated with 150 keV energy in iron.

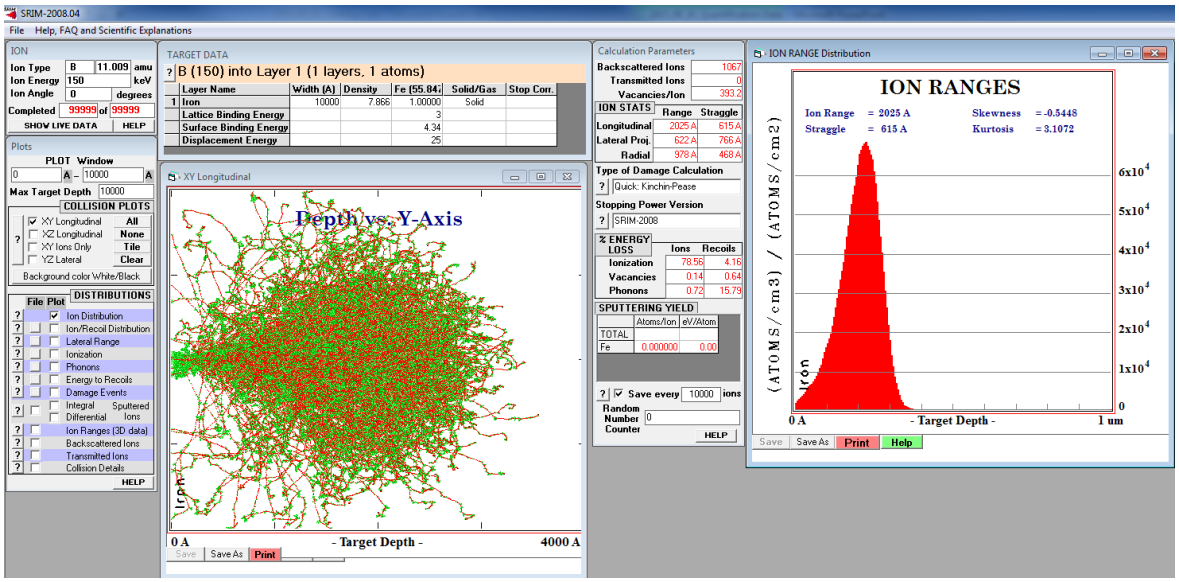


Figure 4.70: Screen shot of SRIM output of Ion Range Distribution.

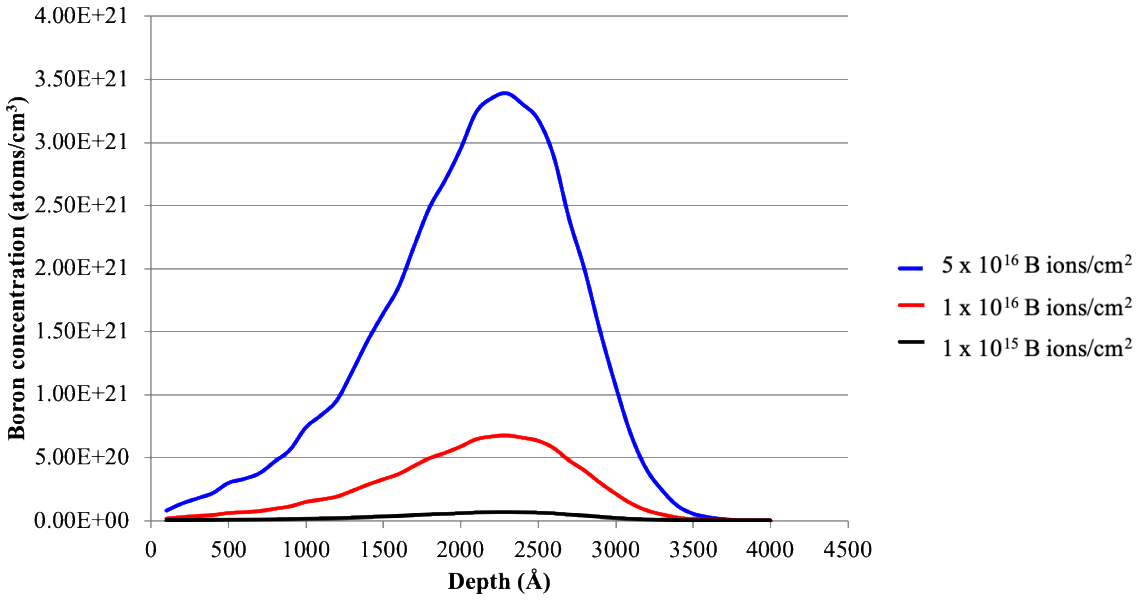


Figure 4.71: SRIM profiles for boron ion distributions predicted for the three samples implanted at doses of 1 x 10^{15}, 1 x 10^{16} and 5 x 10^{16} B ions cm^{-2} into pure iron at 150 keV.

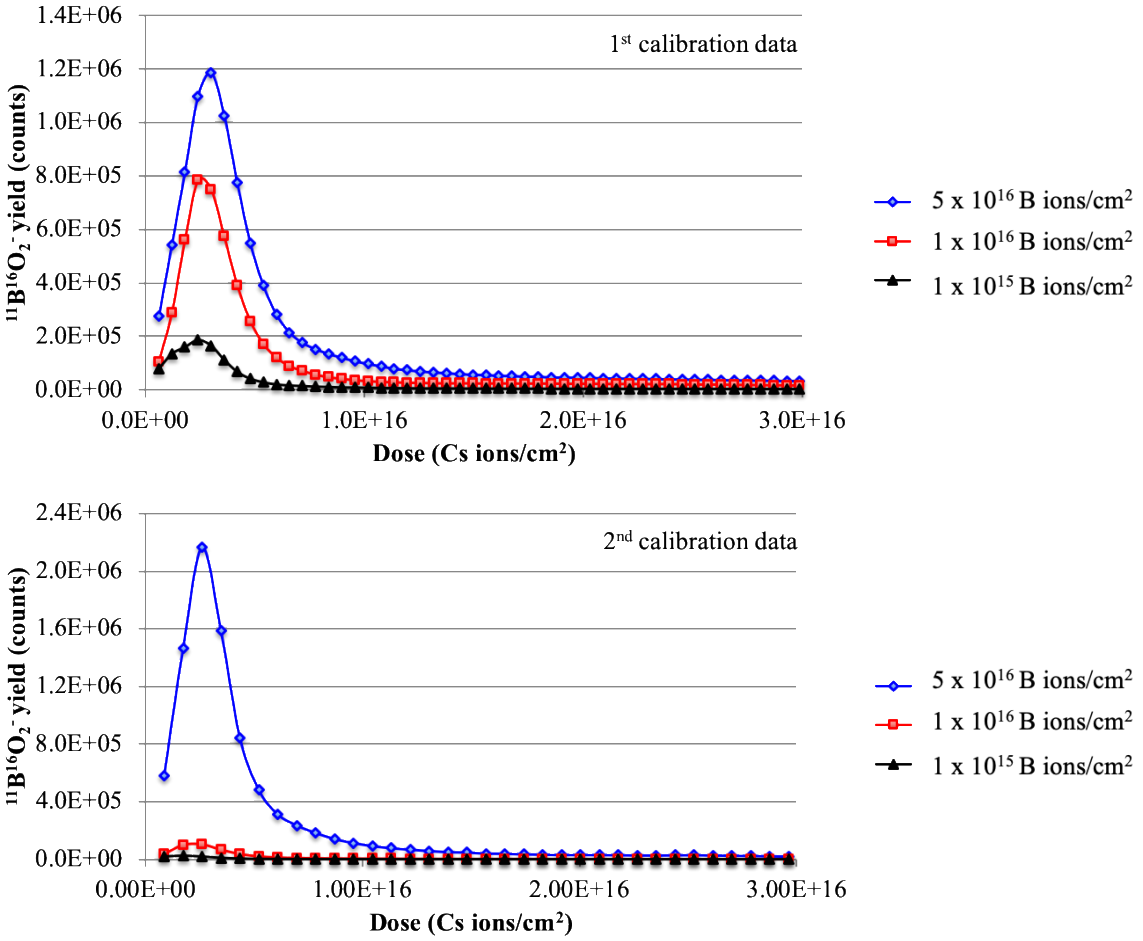


Figure 4.72: Two sets of NanoSIMS depth profiles of boron ions implanted into iron at doses of 1 x 10^{15}, 1 x 10^{16} and 5 x 10^{16} B ions cm^{-2} using the $^{11}B^{16}O_2$ signal

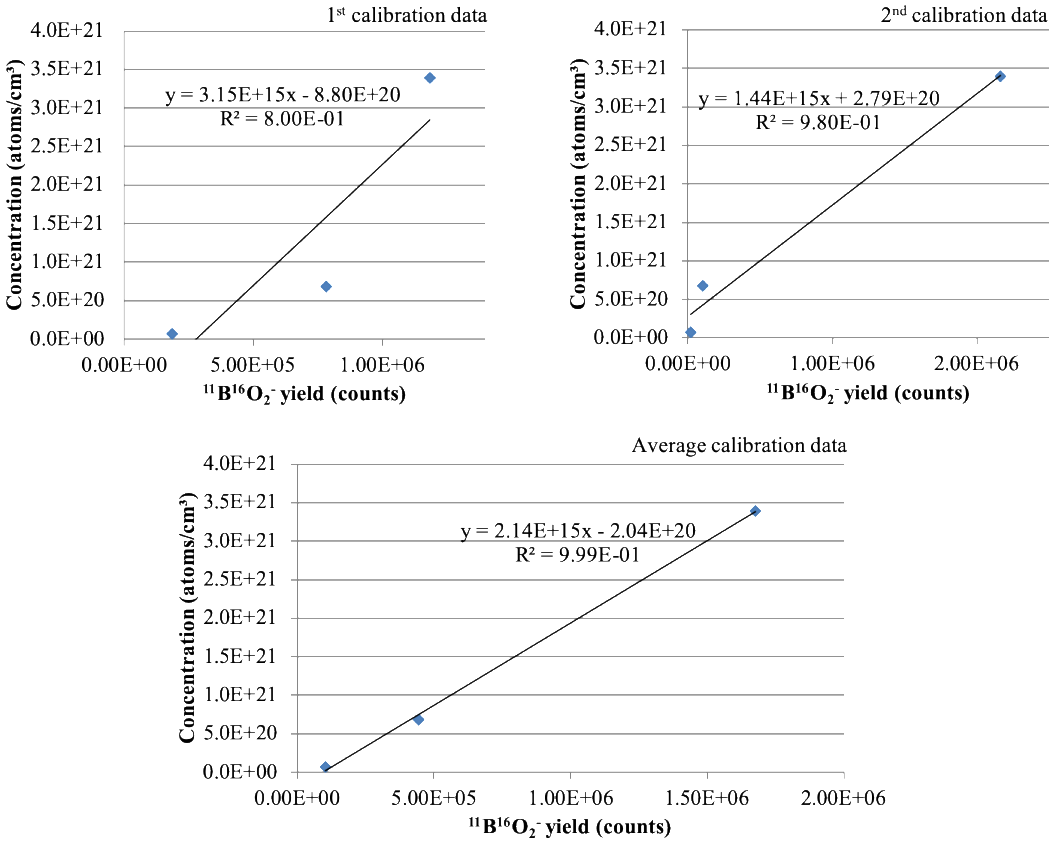


Figure 4.73: Relationship between $^{11}B^{16}O_2^-$ yield and boron concentration for boron ions implanted into iron standards at doses of 1 x 10^{15}, 1 x 10^{16} and 5 x 10^{16} B ions cm^{-2} for the first and second sets of calibration data, and the average of these two sets of data. The $^{11}B^{16}O_2^-$ yield for each sample was taken from the peak of the depth profile from Figure 4.72, and boron concentration on each standard was from the peak of the SRIM profile in Figure 4.71.

4.5.2 Quantitative Analysis of Total Boron Counts

Before conclusions can be drawn from quantitative analysis of boron in steel, we need to check that the analysis conditions are sufficiently well controlled. In order to make all the data comparable, the total boron signals from each sample were normalised by the dose implanted, which depends on the analysis time, beam current and area scanned. Figure 4.74 shows the total normalised boron intensity against the known bulk alloy boron content in all the steel samples analysed, and Figure 4.75 shows the same graph with addition of the three boron ion implanted standard samples. Circles indicate as-rolled samples (AR), squares indicate quenched samples (Q), triangles indicate quenched and tempered samples, and diamonds indicate direct quenched samples. The difference between the maximum and minimum of the total normalised boron intensities for all the samples is almost two

orders of magnitude, although the actual bulk boron concentrations in these materials are very similar, Table 4.2.

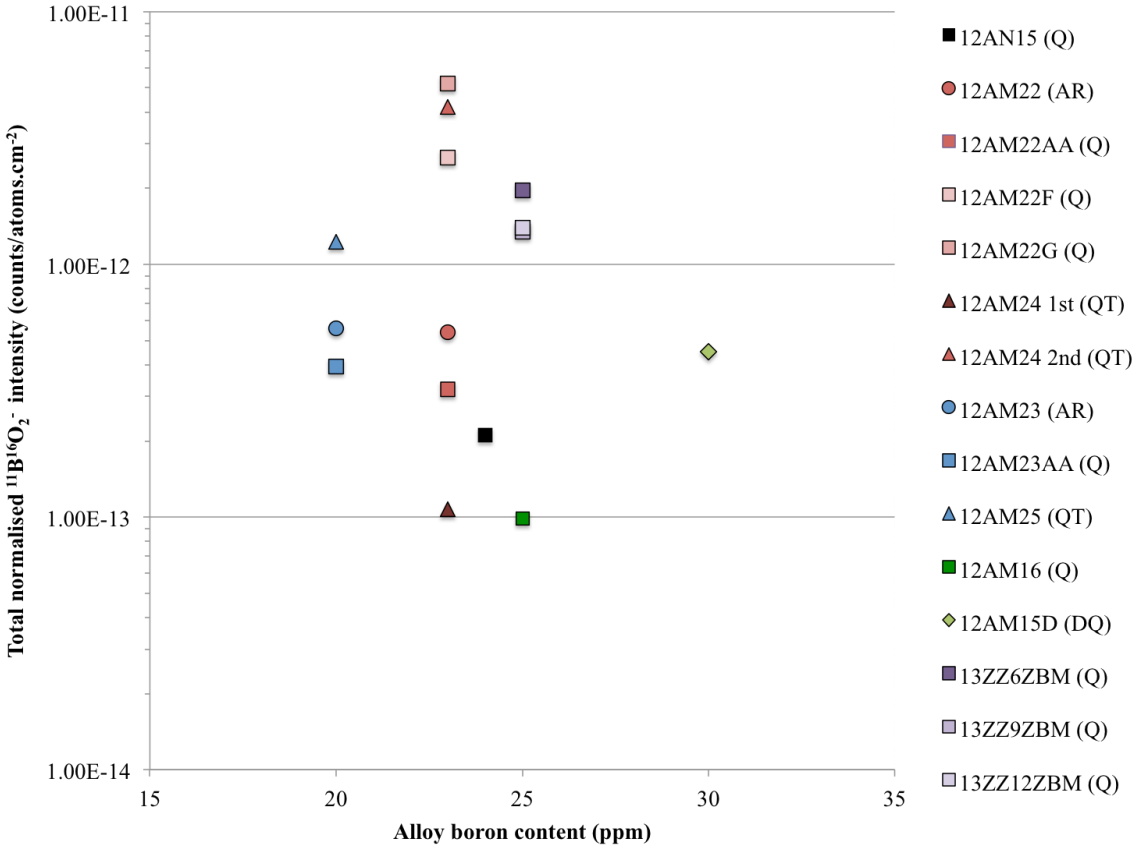


Figure 4.74: Total $^{11}B^{16}O_2^-$ intensity normalised by Cs^+ dose implanted against alloy boron content in ppm for all the steel samples. Circles (●) represent as-rolled (AR) samples, squares (■) indicate quenched (Q) samples, triangles (▲) indicate quenched and tempered (QT) samples and diamonds (◆) represent direct quenched (DQ) sample.

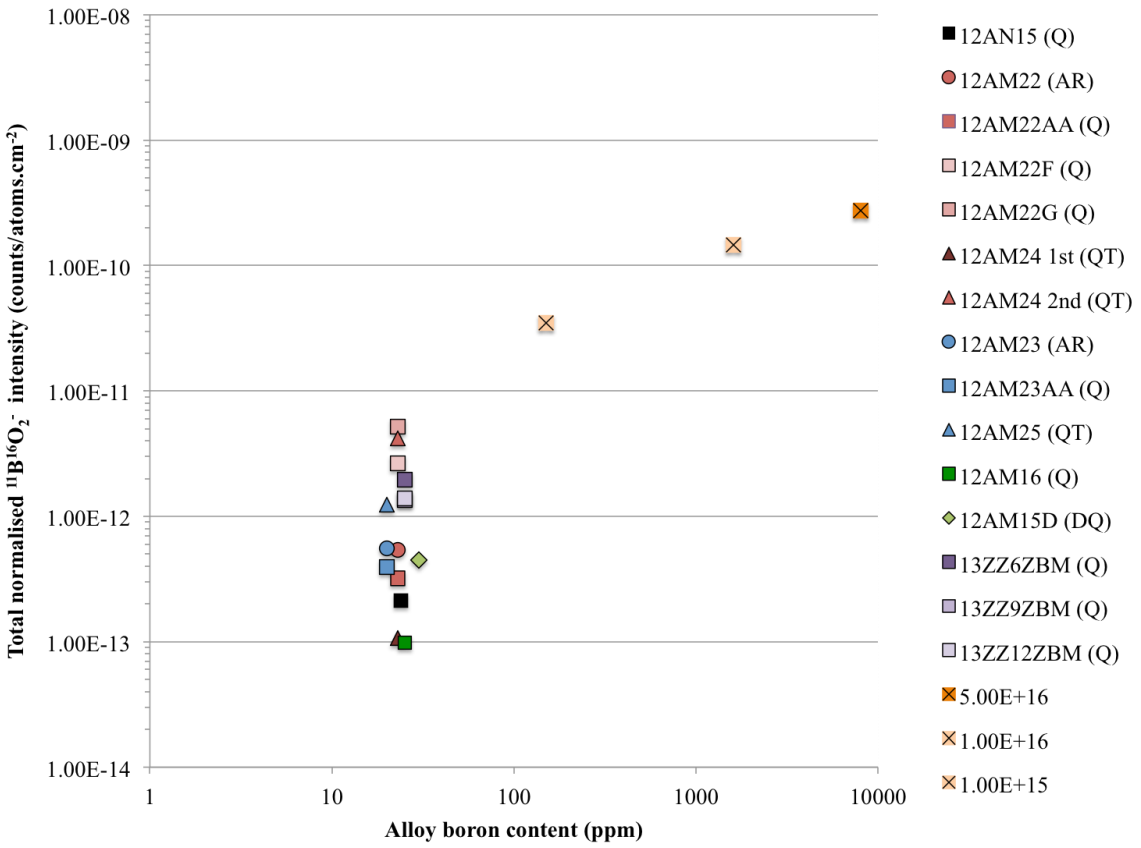


Figure 4.75: Total $^{11}B^{16}O_2^-$ intensity normalised by Cs^+ dose implanted against alloy boron content in ppm for all steel samples and three boron ion implantation standards (1 x 10^{15}, 1 x 10^{16} and 5 x 10^{16} B ions cm^{-2}). Circles (●) represent as-rolled (AR) samples, squares (■) indicate quenched (Q) samples, triangles (▲) indicate quenched and tempered (QT) samples and diamonds (◆) represent direct quenched (DQ) sample.

The spread in the boron counts measured from the steel samples reduces to around one order of magnitude when the boron intensities were normalised by the carbon intensity as shown in Figure 4.76. The reason for trying this normalisation process is that the carbon content is also rather constant in all the samples, and so normalising by carbon counts should compensate for variations in experimental conditions like precise alignment and tuning of the secondary ion column. However, the data from the ion implantation standards do not lie on a straight line after normalised with carbon, which suggests that at least some of the carbon signal arises from surface contamination which can be very different on samples prepared at different times. There are no significant changes of the spread of total boron intensities after normalisation with the oxygen signal as can be seen in Figure 4.77 and so this normalisation method was not continued.

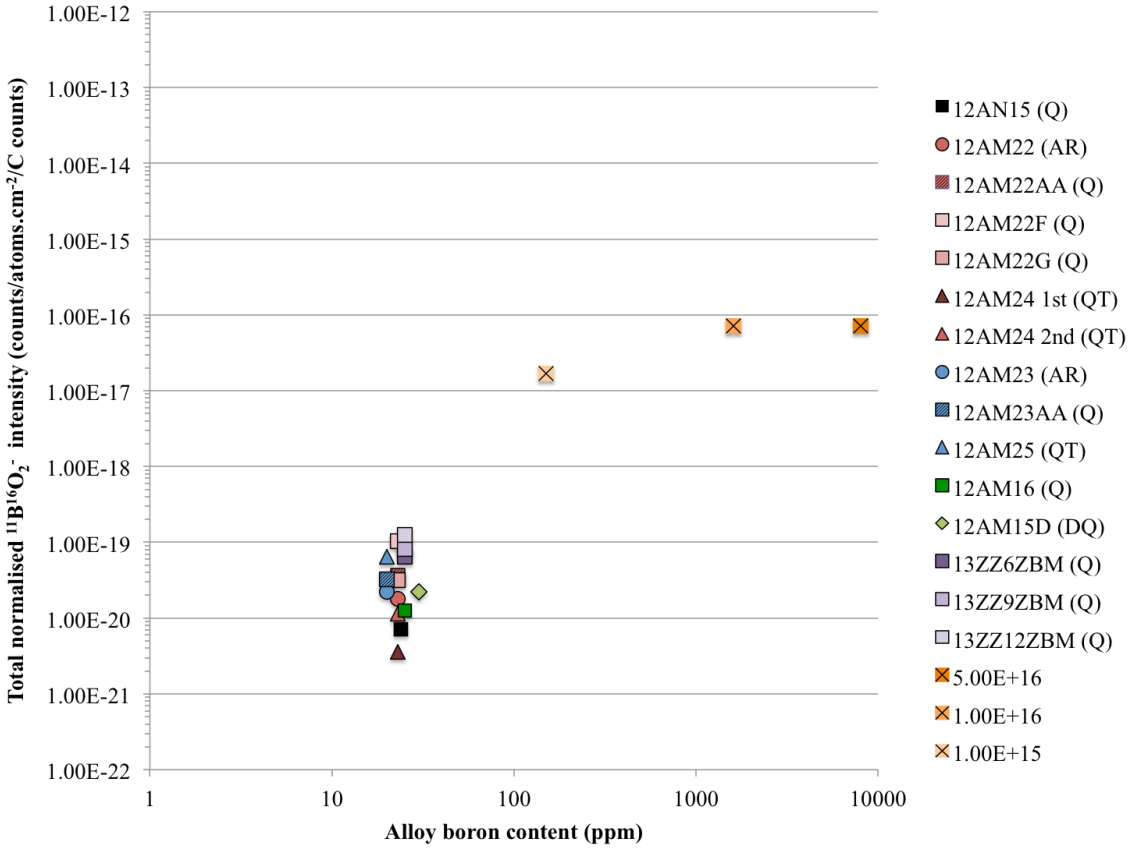


Figure 4.76: Total $^{11}B^{16}O_2^-$ intensity normalised by Cs^+ dose implanted and carbon counts against alloy boron content in ppm for all steel samples and three boron ion implantation standards (1 x 10^{15}, 1 x 10^{16} and 5 x 10^{16} B ions cm^{-2}). Circles (●) represent as-rolled (AR) samples, squares (■) indicate quenched (Q) samples, triangles (▲) indicate quenched and tempered (QT) samples and diamonds (◆) represent direct quenched (DQ) sample.

Total boron counts vary by more than factor of 10 even though rather large areas are analysed and instrumental conditions are kept as constant as possible. This means that calibrating boron counts against implanted standards may not be the best way to compare samples analysed many months apart. So, a method based on the internal standard offered by the concentration of boron in the grains on either side of a grain boundary was tried instead.

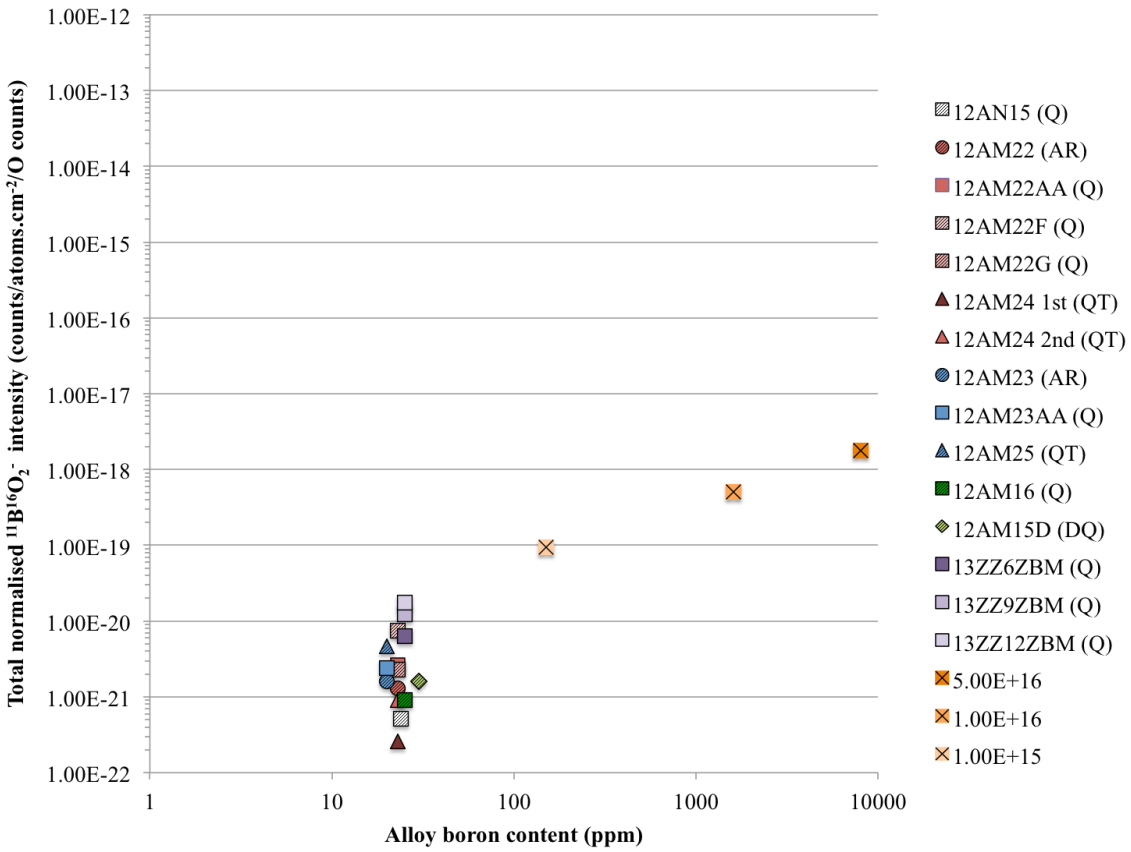


Figure 4.77: Total $^{11}B^{16}O_2^-$ intensity normalised by Cs^+ dose implanted and oxygen counts against alloy boron content in ppm for all steel samples and three boron ion implantation standards (1 x 10^{15}, 1 x 10^{16} and 5 x 10^{16} B ions cm^{-2}). Circles (●) represent as-rolled (AR) samples, squares (■) indicate quenched (Q) samples, triangles (▲) indicate quenched and tempered (QT) samples and diamonds (◆) represent direct quenched (DQ) sample.

4.5.3 Quantification of Grain Boundary Concentration

Figure 4.78 shows an example of a $^{11}B^{16}O_2^-$ map acquired from a region containing several prior austenite grain boundaries in the molybdenum alloyed steel sample 13ZZ6ZBM. Line scans were performed on ten different grain boundaries. The line scans were averaged over 10 pixels width to improve counting statistics and a step size of 0.2 μm. The line scans can be converted into concentration profile by converting each pixel from $^{11}B^{16}O_2^-$ yield, *Y* (counts), to a boron concentration, *C*, expressed in atoms.cm^{-3} using the first equation from (Christien et al., 2012):

$$C = \frac{Y}{Y_{Std}} C_{Std} \qquad (4.1)$$

Where C_{Std} is the known boron concentration of the boron implanted standard material in atoms.cm^{-3} and Y_{Std} is the counts of the $^{11}B^{16}O_2^-$ yield measured on implanted standard material using the same aperture configuration as on the sample (D1=2, 300 µm diameter). Therefore, $\frac{C_{Std}}{Y_{Std}}$ is the average gradient (2.14 x 10^{15}) from the calibration curve from Figure 4.73.

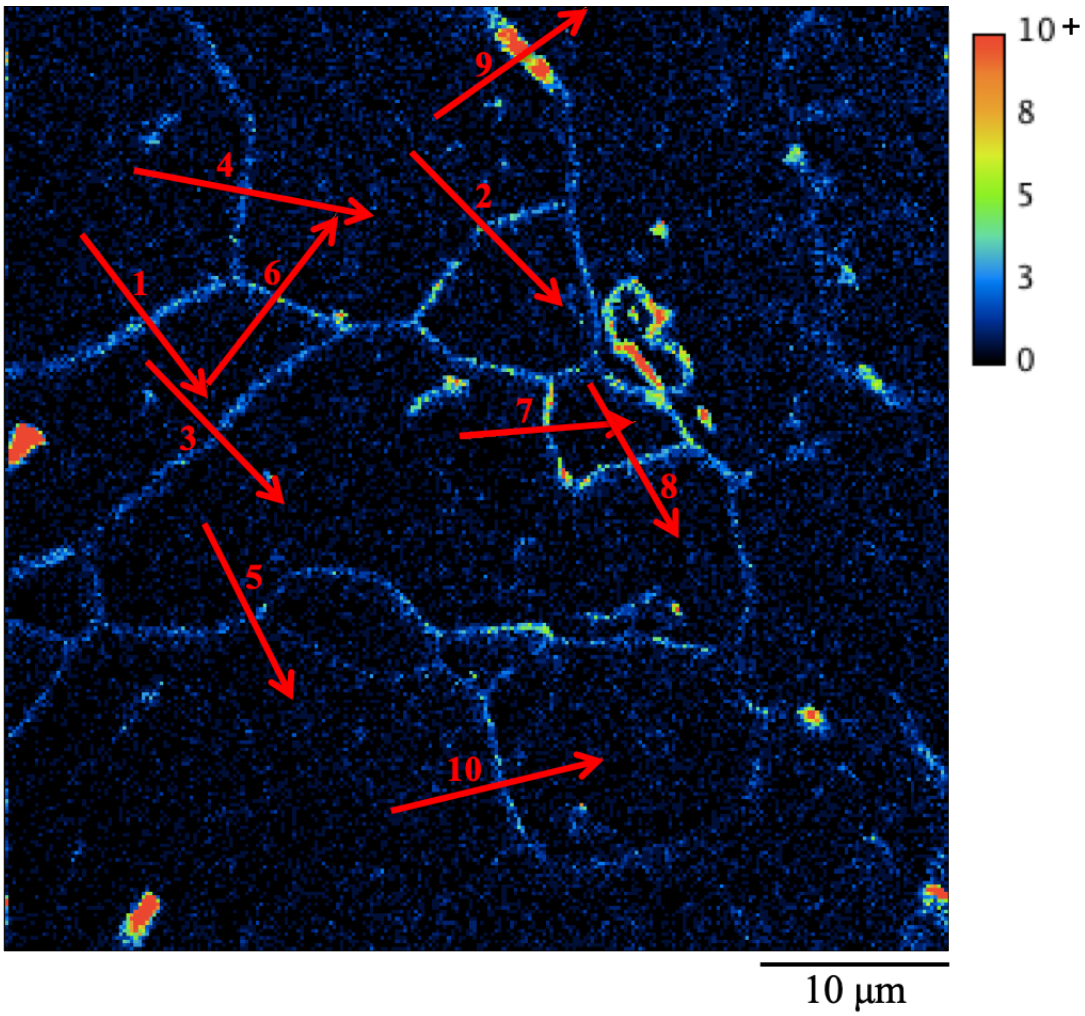


Figure 4.78: Ten line scans across grain boundaries in the molybdenum alloyed steel sample 13ZZ6ZBM

Boron concentration profiles for line 1 and line 9 are presented in Figure 4.79 as examples. Line 9 hits boride precipitates along the grain boundary, and so cannot be used to show segregation to the boundary plane and indicates that care is required when electing line profiles.

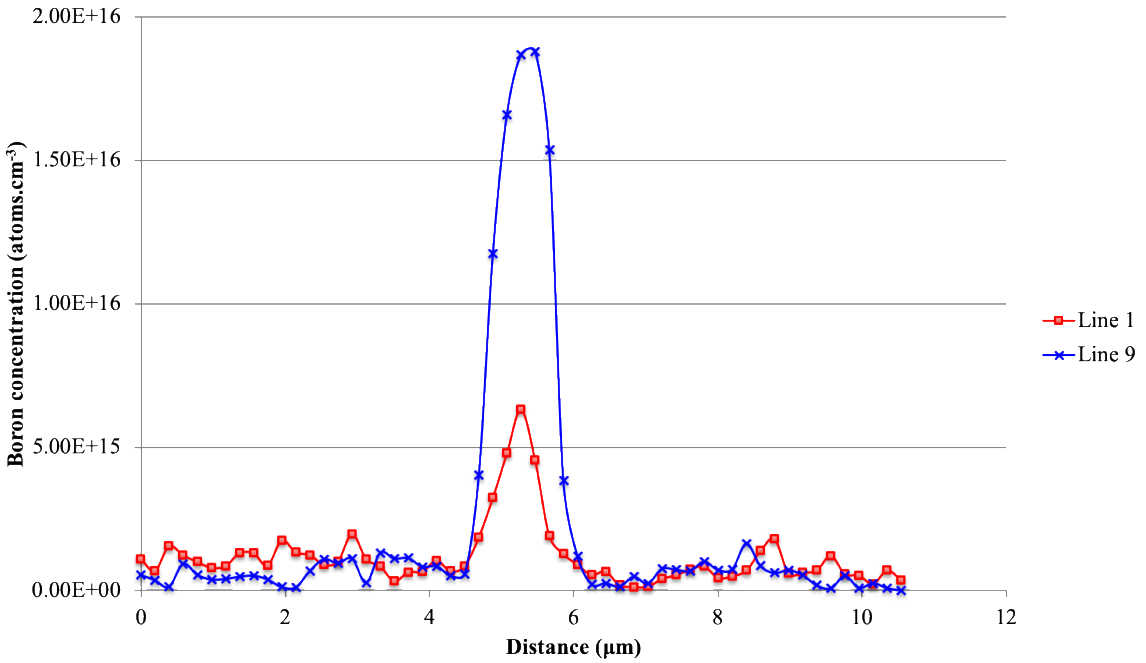


Figure 4.79: Boron concentration profile from line 1 (red) and line 9 (blue) on sample 13ZZ6ZBM as indicated in Figure 4.78. Line 9 crosses over precipitates and cannot therefore be used for quantification of grain boundary segregation.

The boron grain boundary concentration can be determined from the peak area measured on the concentration profile. From the concentration profile, it can be observed that the background level is not zero and it corresponds to the boron contents in the grains.

To calculate the concentration, first the trapezium rule is used to estimate the area under the curve from the concentration profile which is given by integration between the distance (µm) X_0 to X_n and $^{11}B^{16}O_2^-$ yield (counts) Y_0 to Y_n as illustrated in Figure 4.80. This rule is applied by splitting the area under curve into a number of trapeziums each of which has the length or step size, h.

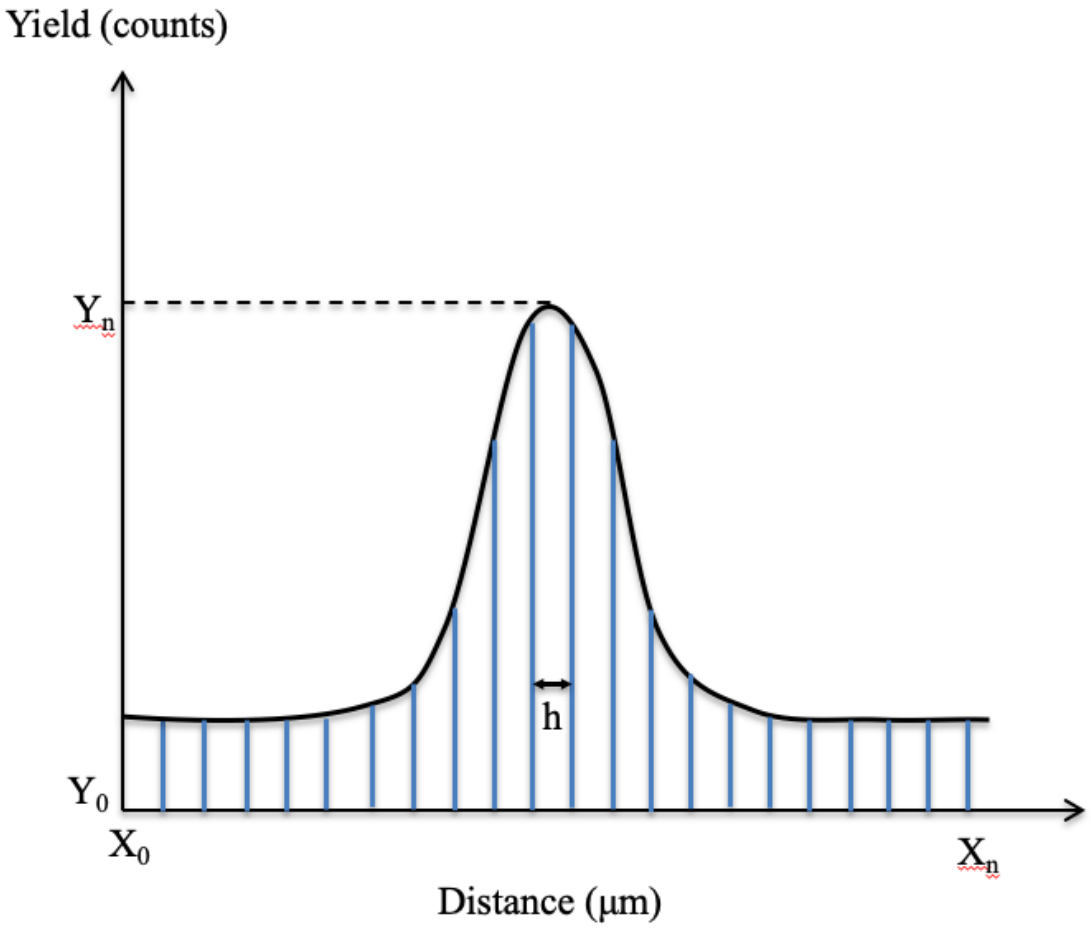


Figure 4.80: Sketch of a typical line scan extracted from a NanoSIMS image across a grain boundary. An estimate of the area under the curve is calculated using the trapezium rule from the distance (µm) X_0 to X_n and $^{11}B^{16}O_2^-$ yield (counts) Y_0 to Y_n. The area under the curve is divided into a smaller number of trapeziums which have the length h.

The area under the curve is given by integration as defined by:

$$\int_{X_0}^{X_n} \boldsymbol{f(X)dx} = \frac{\boldsymbol{1}}{\boldsymbol{2}}\boldsymbol{h}[(\boldsymbol{Y_o} + \boldsymbol{Y_n}) + \boldsymbol{2}(\boldsymbol{Y_1} + \boldsymbol{Y_2} + \cdots + \boldsymbol{Y_{n-1}})] \qquad \textbf{(4.2)}$$

where $Y_0 = f(X_0)$ and $Y_1 = f(X_1)$ etc.

When the interval is divided into smaller intervals, h is given by $\frac{(X_n - X_0)}{n}$.

Therefore, the trapezium rule is applied for each smaller area under the curve using the basic equation of a trapezium:

$$\textbf{Area} = \left(\frac{Y_1+Y_2}{2}\right)(X_1 - X_0) \qquad (4.3)$$

For all of the results presented below, the calculation of boron segregation was carried out in Excel.

Figure 4.81 illustrates the total area, A_{Total} (counts.µm) contributions to two different regions; first the background or bulk area, A_{Bulk} and second the grain boundary area, A_{GB}:

$$A_{Total} = A_{Bulk} + A_{GB} \qquad (4.4)$$

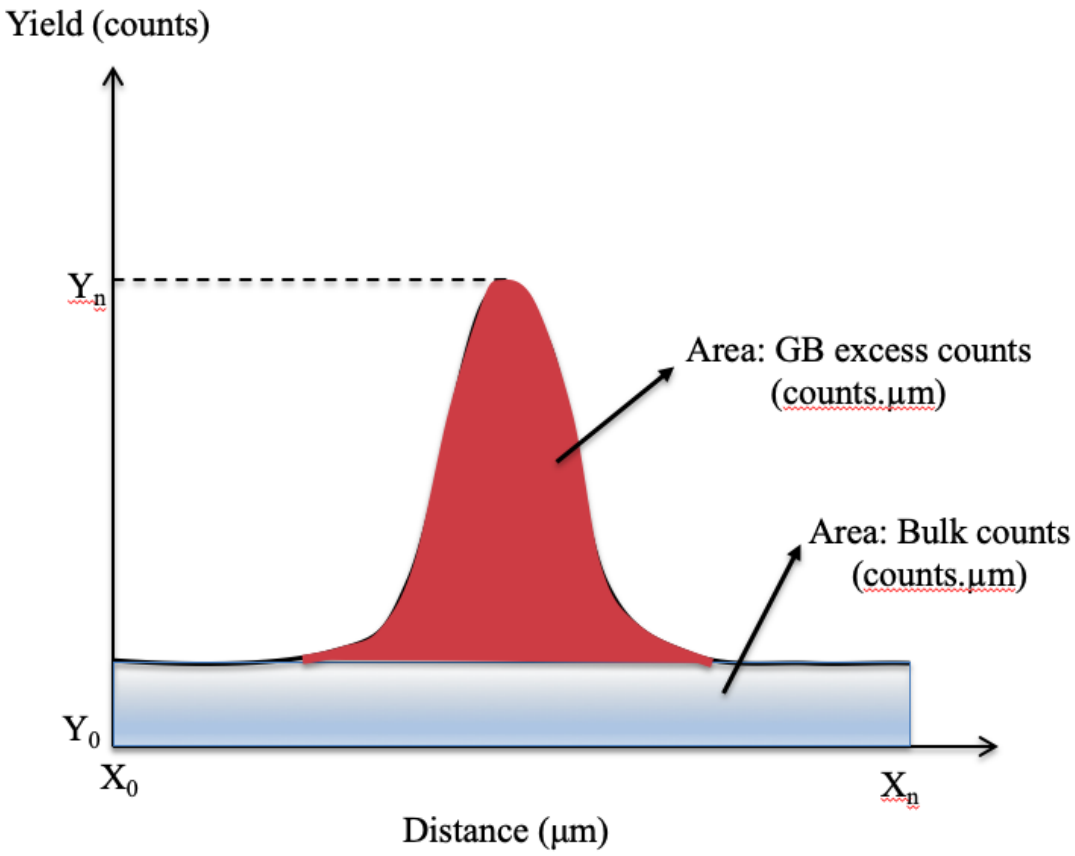


Figure 4.81: The total area (A_{Total}) contributions to background or bulk area (A_{Bulk}) and grain boundary area (A_{GB}).

The peak width observed in the line scans or the concentration profile is not the real grain boundary width but the broadening effect introduced by the width of the primary beam at high current (1 to 2 pA) which was required to achieve good counting statistics. The peak width from the line scans is approximately 1000 nm at half maximum which is 1000 times larger than the grain boundary width, taken to be 1 nm. Therefore, to find the real grain boundary concentration, C_{GB}, the peak area in counts.µm needs to be converted to excess counts per 1 nm grain boundary width by multiplying by 1000. Figure 4.82 illustrates the peak width at half maximum is about 1000 times larger than the 1 nm real grain boundary width.

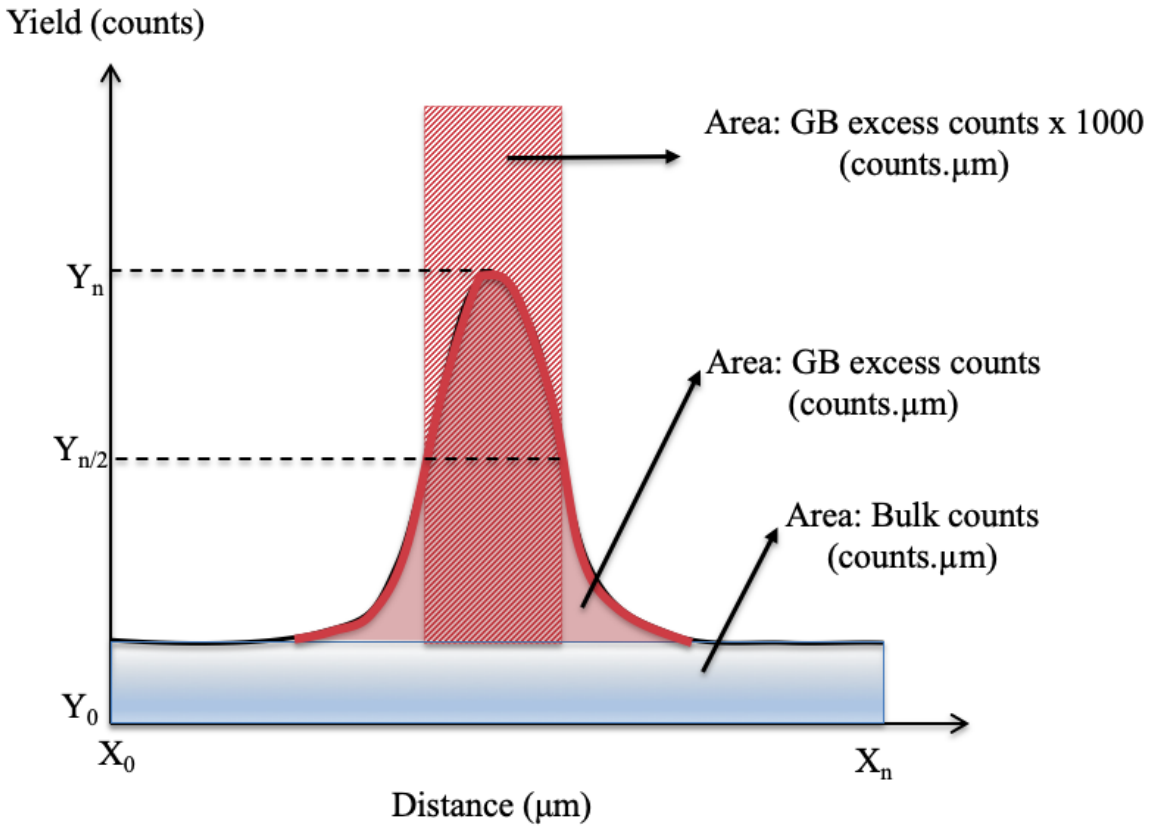


Figure 4.82: The peak width at half maximum is about 1000 times larger than the 1 nm real grain boundary width. C_{GB} is determined from the excess counts per 1 nm grain boundary width.

Therefore, the boron grain boundary concentration, C_{GB} in atoms.cm^{-2} can be determined from the peak area measured on the line scan using the proportional equation below:

$$C_{GB} = A_{GB} \times \frac{C_{Std}}{Y_{Std}} \quad (4.5)$$

where A_{GB} is the peak area in counts.cm, C_{Std} is the known concentration of boron implanted standard in atoms.cm^{-3} and Y_{Std} is the $^{11}B^{16}O_2^-$ yield in counts measured on the implanted standard material. Therefore, $\frac{C_{Std}}{Y_{Std}}$ is taken from the average gradient (2.14 x 10^{15}) taken from the calibration curve shown in Figure 4.73.

A summary of the quantification of boron segregation to all the grain boundaries shown in Figure 4.78 is given in Table 4.18. The average boron concentration at the 9 grain boundaries that do not have obvious precipitates is 1.6 atoms.nm^{-2}. The apparent boron concentration on grain boundary 9 is about 11 atoms.nm^{-2} because the small precipitates contain many more B atoms. Using the ferrite unit cell dimensions of 0.287 nm and the fact that there are 2 atoms per unit cell in the bcc ferrite structure, the number of Fe atoms per nm^{-3} is approximately 82, so the NanoSIMS results suggest that grain boundaries 1-8 and 10 each contain a few percent of boron atoms.

The grain boundary segregation data from the Mo sample 13ZZ6BM is the same order of magnitude as the data from APT analysis (Li et al., 2015) of a similar Mo steel sample, which have boron excess values of 5.27 atoms.nm^{-2}.

Table 4.18: Example of grain boundary quantification analysis on molybdenum alloyed steel 13ZZ6ZBM

Grain boundary	Peak Area (counts.cm)	Grain boundary boron concentration (atoms.nm^{-2})
1	0.11	2.4
2	0.06	1.3
3	0.11	2.3
4	0.05	1.2
5	0.06	1.2
6	0.09	2.0
7	0.05	1.1
8	0.08	1.6
9	0.52	11.2
10	0.06	1.3

Figure 4.83 shows the average boron concentration in atoms.nm^{-2} for grain boundaries in samples 12AM22, 12AM23, 12AN15, 12AM22AA, 12AM23AA, 13ZZ6ZBM, 13ZZ9ZBM, 13ZZ12ZBM, 12AM24 (first), 12AM24 (second) and 12AM25. The average boron concentration was measured on at least 10 grain boundaries per sample. Based on the results shown in Figure 4.83, the 12AM24 (first) appears to be anomalous as it is lower than all the other samples (as previously indicated) and repeating this experiment was clearly necessary. Both as-rolled samples, aluminium protected 12AM22 and titanium protected 12AM23, have a similar average boron concentration of 0.6 atoms.nm^{-2}. All the as-quenched samples show a higher amount of boron concentration in the grain boundary, as compared to the as-rolled samples, ranging from 0.7 to 1.6 atoms.nm^{-2}. The highest average boron concentration is 5.1 atoms.nm^{-2} in the second sample of quenched and tempered aluminium protected sample 12AM24, followed by 2.8 atoms.nm^{-2} in the quenched and tempered titanium protected sample 12AM25. The reason for higher concentrations in the quenched and tempered samples is that the tempering heat treatment brings out precipitates on the grain boundaries with possible precipitation in the matrix. These small precipitates cannot be resolved in the NanoSIMS and hence line profiles will inadvertently cross over them.

The second way to estimate grain boundary concentration, C_{GB} in boron wt. fraction was using the modified equation from equation 4.1:

$$C_{GB} = \frac{A_{GB}}{A_{Bulk}} \times 0.00008\ B\ wt.fraction \qquad (4.6)$$

Therefore, the boron grain boundary concentration, C_{GB} in boron wt. fraction can be determined from the peak area measured on the line scan. The peak area in A_{GB} in counts.µm is converted to excess counts per grain boundary width which is taken to be 1 nm. A_{Bulk} is the average background counts which is assumed to arise from the solid solution limit of 900°C which is 0.008 wt.% B taken from the Fe-B binary phase diagram (Metals, 2007).

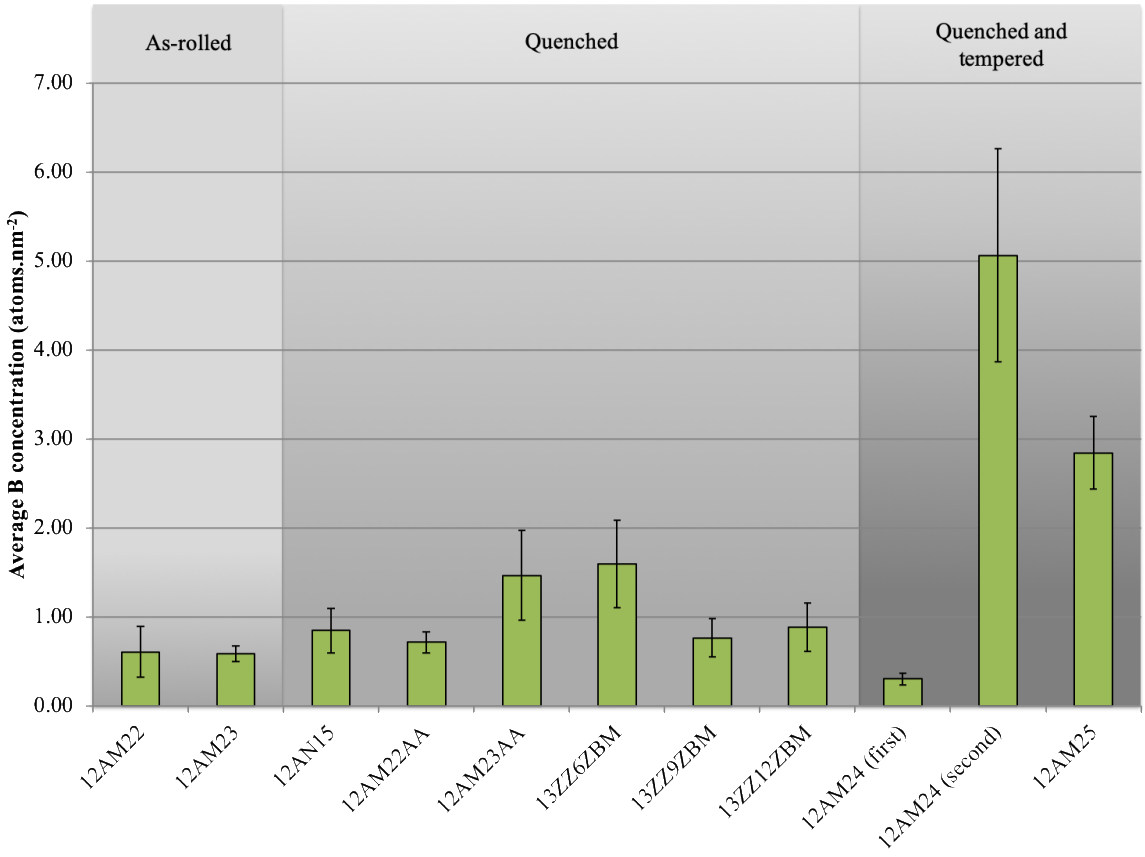


Figure 4.83: Average B concentrations at grain boundaries in atoms.nm^{-2} for as-rolled samples (Al-protected sample 12AM22 and Ti-protected sample 12AM23), quenched samples (reference sample 12AN15, Al-protected sample 12AM22AA, Ti-protected sample 12AM23AA, Mo-alloyed 13ZZ6ZBM, Al-protected with high hardness 13ZZ9ZBM, and Al-protected with low hardness 13ZZ12ZBM), and quenched and tempered samples (Al-protected sample 12AM24 and Ti-protected sample 12AM25). Note that 12AM24 (first) appears to be anomalous based on these results hence the need to repeat this analysis.

An example of the calculation to determine the fraction of segregated boron in the boundary volume, is illustrated by a line scan from the Mo sample 13ZZ6ZBM in Figure 4.84. The average area of background counts, A_{Bulk} in this sample is 3.4 counts.µm. The peak area, A_{GB} in counts.µm is converted to excess counts per grain boundary width which is taken to be 1 nm. The fraction of boron in the boundary volume at this grain boundary is 0.02 wt. fraction which is equivalent to the sum of excess counts per grain boundary width over the average area of background counts (3.4 counts.µm) and 0.008 wt.% boron content.

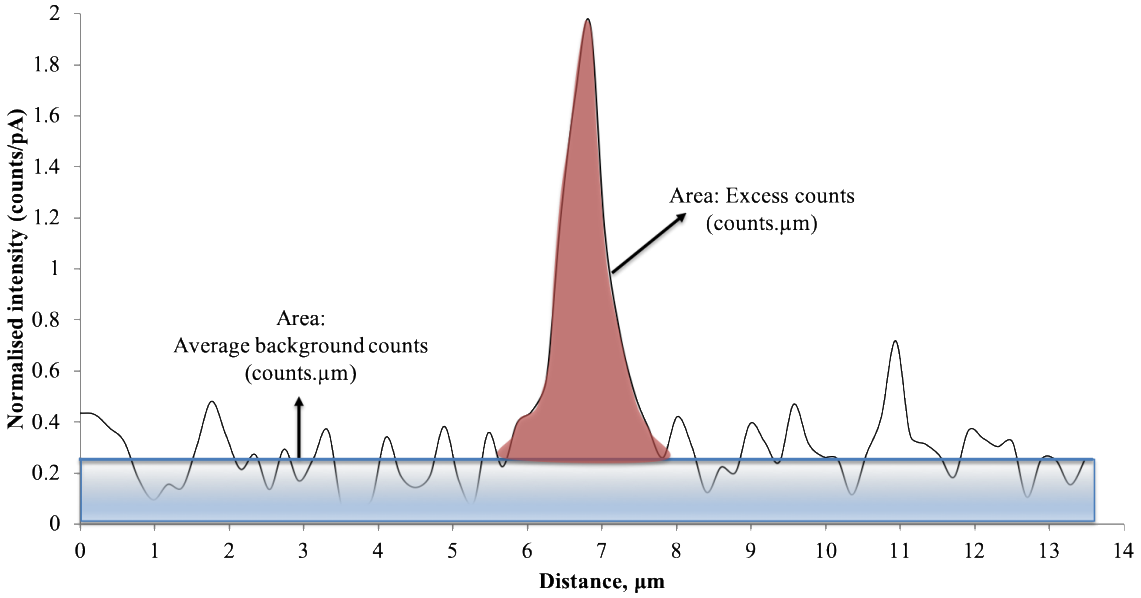


Figure 4.84: Line scan on grain boundary 4 in Mo sample 13ZZ6ZBM showing the average background counts and the area of the peak equivalent to B excess counts in counts.µm.

The average fraction of boron in boundary volume for as-rolled samples (Al-protected sample 12AM22 and Ti-protected sample 12AM23), quenched samples (reference sample 12AN15, Al-protected sample 12AM22AA, Ti-protected sample 12AM23AA, Mo-alloyed 13ZZ6ZBM, Al-protected with high hardness 13ZZ9ZBM, and Al-protected with low hardness 13ZZ12ZBM), and quenched and tempered samples (Al-protected sample 12AM24 and Ti-protected sample 12AM25) is shown in Figure 4.85.

Both as-rolled samples 12AM22 and 12AM23 show the lowest fraction of boron in boundary volume approximately 0.02 wt. fraction. Among the three group of heat treatments, the as-quenched samples show the highest average fraction of boron in boundary volume ranging just under 0.04 wt. fraction to nearly 0.06 wt. fraction. After quenching and tempering, both Al-protected 12AM24 and Ti-protected 12AM25 samples show a decreased fraction of boron in the boundary volume. The result for quenched and tempered samples is not as expected where these samples have lots of preferential precipitation on the grain boundaries and possible precipitation in the grains. This method to determine the grain boundary concentration by using the known concentration of 0.008 wt.% B at 900°C is only valid when the boron is in solid solution, whereas the quenched and tempered samples

have lots of possible precipitation in the grains and hence this could explain the discrepancy in the results from those presented in Figure 4.83.

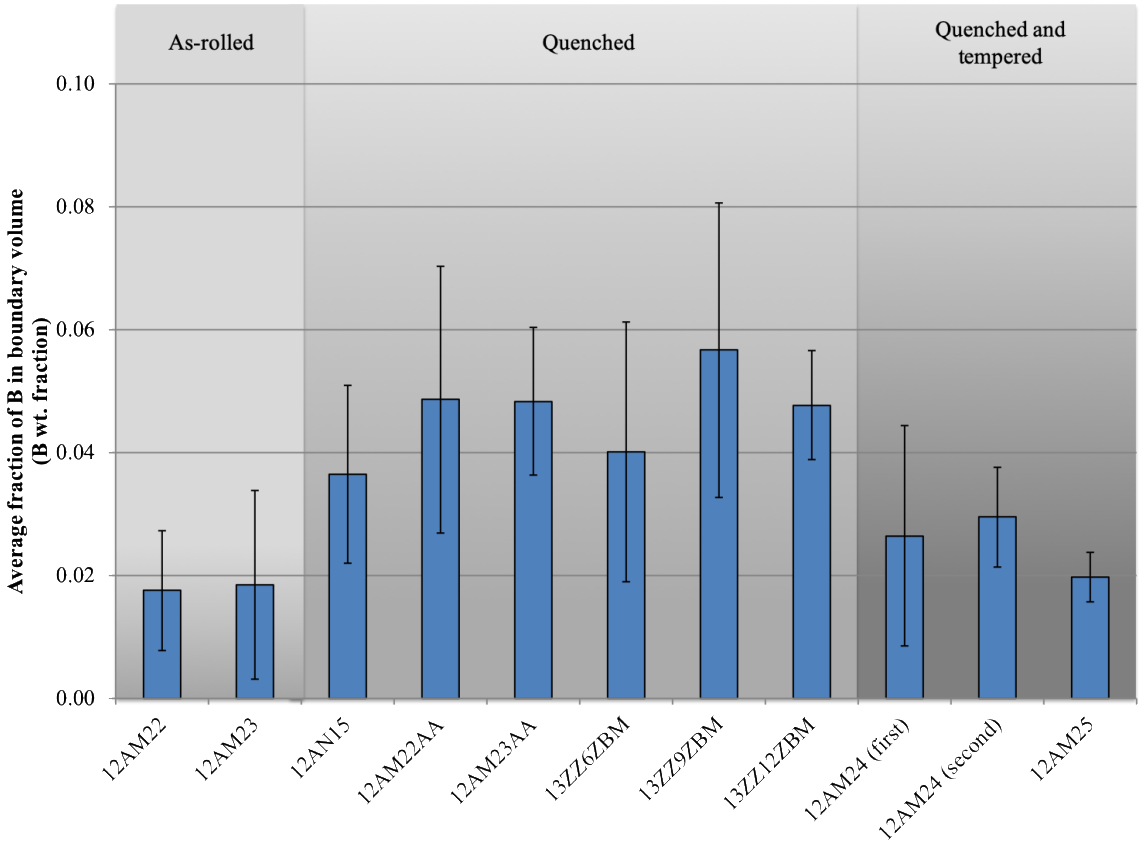


Figure 4.85: Average fraction of B in boundary volume for as-rolled samples (Al-protected sample 12AM22 and Ti-protected sample 12AM23), quenched samples (reference sample 12AN15, Al-protected sample 12AM22AA, Ti-protected sample 12AM23AA, Mo-alloyed 13ZZ6ZBM, Al-protected with high hardness 13ZZ9ZBM, and Al-protected with low hardness 13ZZ12ZBM), and quenched and tempered samples (Al-protected sample 12AM24 first and second, and Ti-protected sample 12AM25).

Both methods of quantification show similar results for as-rolled and as-quenched samples. All the as-quenched samples show higher amount of boron concentration in comparison to the as-rolled samples. However, the method to quantify boron segregation is not accurate in the quenched and tempered samples as tempering heat treatment brings out precipitates on the grain boundaries with possible precipitation in the matrix.

Table 4.19 and Table 4.20 show the data on grain boundary segregation of boron from the first and second methods for quantitation taken from Figure 4.83 and Figure 4.85, respectively. The standard deviation (SD) of the results from each sample is shown, and the relative standard deviation (RSD)

for the results from each sample was calculated by dividing the SD by the average boron concentration. It is well known in polycrystalline metallic materials that the concentration of segregated impurities under any given heat treatment conditions depends on the structure of the individual grain boundaries (Suzuki et al., 1981, Li et al., 2020). As a result, when analytical techniques are used to measure directly the segregation to individual boundaries, there will be a substantial scatter in the data when a relatively small number of individual boundaries are randomly selected in each material, as can be observed from the overall results.

Table 4.19: Quantification data from the first method showing the average B concentration (atoms.nm^{-2}), standard deviation (SD) and relative standard deviation (RSD) of each sample and relating to data in Figure 4.83.

Heat Treatment	Sample	Average B concentration (atoms.nm^{-2})	Standard deviation	Relative standard deviation (RSD) (%)
As-rolled	12AM22	0.61	0.28	47
	12AM23	0.59	0.09	15
As-quenched	12AN15	0.85	0.25	30
	12AM22AA	0.71	0.12	17
	12AM23AA	1.46	0.50	34
	13ZZ6ZBM	1.59	0.49	31
	13ZZ9ZBM	0.77	0.22	28
	13ZZ12ZBM	0.88	0.27	31
Quenched and tempered	12AM24 (first)	0.30	0.06	21
	12AM24 (second)	5.06	1.20	24
	12AM25	2.84	0.41	14

Table 4.20: Quantification data from the second method showing the average fraction of B in boundary volume (B wt. fraction), standard deviation (SD) and relative standard deviation (RSD) of each sample relating to data in Figure 4.85.

Heat Treatment	Sample	Average fraction of B in boundary volume (B wt. fraction)	Standard deviation	Relative standard deviation (RSD) (%)
As-rolled	12AM22	0.02	0.010	56
	12AM23	0.02	0.015	83
As-quenched	12AN15	0.04	0.015	40
	12AM22AA	0.05	0.022	45
	12AM23AA	0.05	0.012	25
	13ZZ6ZBM	0.04	0.021	53
	13ZZ9ZBM	0.06	0.024	42
	13ZZ12ZBM	0.05	0.009	19
Quenched and tempered	12AM24 (first)	0.03	0.018	68
	12AM24 (second)	0.03	0.008	25
	12AM25	0.02	0.004	21

4.5.4 Quantification of Particle Sizes and Size Distributions

Seven steel samples were selected for the quantification of particle sizes and size distributions. These samples are 12AM22 (as-rolled, aluminium protected), 12AM23 (as-rolled, titanium protected), 12AN15 (as-quenched, aluminium protected reference sample), 12AM22AA (as-quenched, aluminium protected), 12AM23AA (as-quenched, titanium protected), 12AM24 (quenched and tempered, aluminium protected) and 12AM25 (quenched and tempered, titanium protected). An area of 30,000 μm^2 was mapped for each of the samples investigated (except 12AN15 which was analysed over 25,000 μm^2).

The $^{11}B^{16}O_2^-$ maps were selected for quantification since this signal gave the largest number of counts, and so the most reliable identification of smaller particles. Images were processed using ImageJ with threshold levels set to distinguish $^{11}B^{16}O_2^-$ ion signals from background noise. The images were scaled and the particle sizes are expressed in diameter (μm). After this point, two methods for quantifying the particle sizes were used. The first method was to let the software automatically count and measure the thresholded images. Particles with size outside the range specified were ignored. However, this method does not seem very accurate, as the software will count any pixel with elevated signal, including the artefacts created from edges and holes. The more accurate method was selecting particles manually. To be considered as a particle, a minimum of five adjoining pixels had to have an elevated $^{11}B^{16}O_2^-$ content.

The resulting size distributions per area are shown in Figure 4.86. The particle size distributions are divided into three groups; as-rolled, as-quenched and, quenched and tempered samples. Blue represents Al-protected samples, red represents Ti-protected samples and green represents as-quenched Al-protected reference sample. Since there was a considerable difference in the numbers of fine and large particles, the results have been analysed in terms of particles larger or smaller than 1μm and are summarised in Figure 4.87.

Particle sizes are largest and the greatest number of particles are observed in the as rolled condition. The aluminium protected as-rolled sample 12AM22 has the highest number of particles per unit area,

7.2 x 10^9 particles/m^2, while the titanium protected as-rolled sample 12AM23 shows a slightly lower number of particles per unit area, but has more big particles than12AM22 which has more small particles.

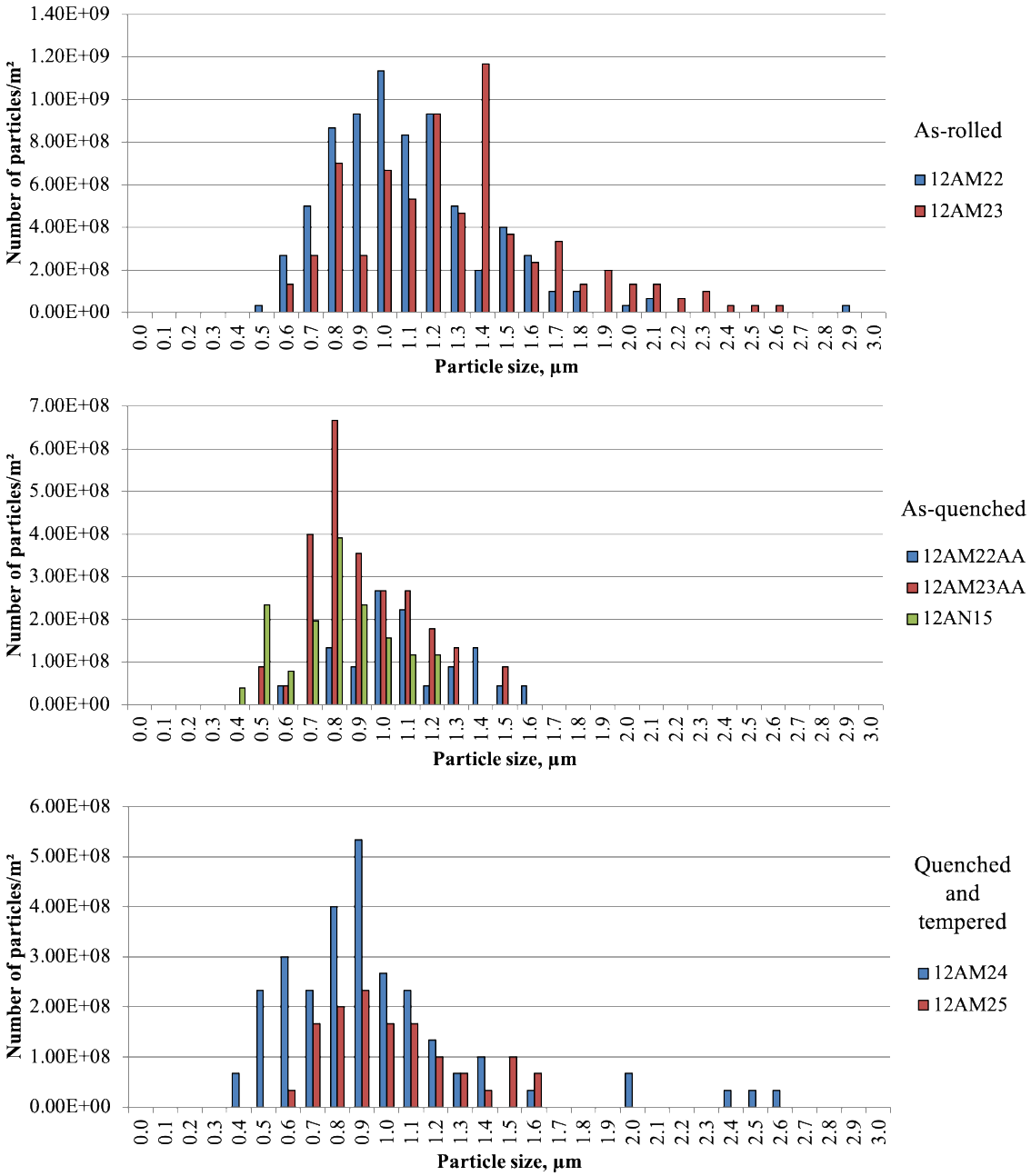


Figure 4.86: Particle size distributions measured from large area NanoSIMS maps for steel samples: As-rolled (Al-protected 12AM22 and Ti-protected 12AM23), as-quenched (Al-protected 12AM22AA, Ti-protected 12AM23AA and reference sample 12AN15), and quenched and tempered (Al-protected 12AM24 and Ti-protected 12AM25).

After quenching, the number of particles dropped significantly as shown in Figure 4.87. Both as-quenched samples 12AM22AA and 12AM23AA show only small numbers of big particles just under 1 x 10^9 particles/m^2. There are more small precipitates in the titanium protected sample 12AM23AA compared to the aluminium protected sample 12AM22AA. The as-quenched reference sample 12AN15 has slightly more total number of particles than 12AM22AA but it has more small particles that are less than 1µm and very few big particles were found in the reference sample. In the as quenched condition, boron is strongly segregated to the grain boundaries, and there appear to be a limited number of particles on these grain boundaries.

After tempering at 600°C, there appears to be numerous fine particles in the aluminium protected sample 12AM24, but the titanium protected sample 12AM25 shows a decrease in the number of precipitates.

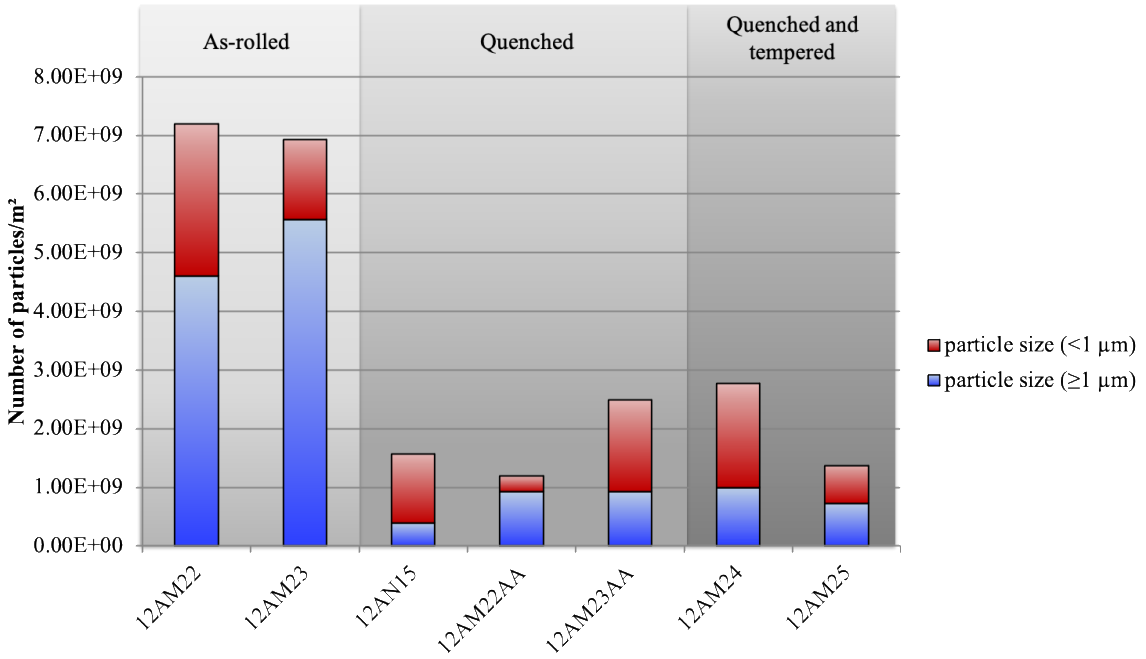


Figure 4.87: Number of particles per unit area of small (< 1 µm) and large (≥ 1 µm) particles detected in each of the steel samples.

SEM and EDX analysis were carried out by Tata Steel to determine BN particle distribution in five samples (as-rolled Al-protected 12AM22 and Ti-protected 12AM23, as-quenched 12AN15, quenched and tempered Al-protected 12AM24 and Ti-protected 12AM25). The analysis was carried

out on a FEI Quanta 600 FEG-SEM. Automatic particle analysis was carried out on sample 12AM22, 12AN15 and 12AM24 for the BN particles. No BN particles were found in either Ti-protected sample, as-rolled 12AM23 and quenched and tempered 12AM25. As the dark BN particle grey level may have been similar to that of any oxides present, it is possible that oxide was also detected, although the size distributions suggest this was unlikely as the oxides are generally in a larger size range.

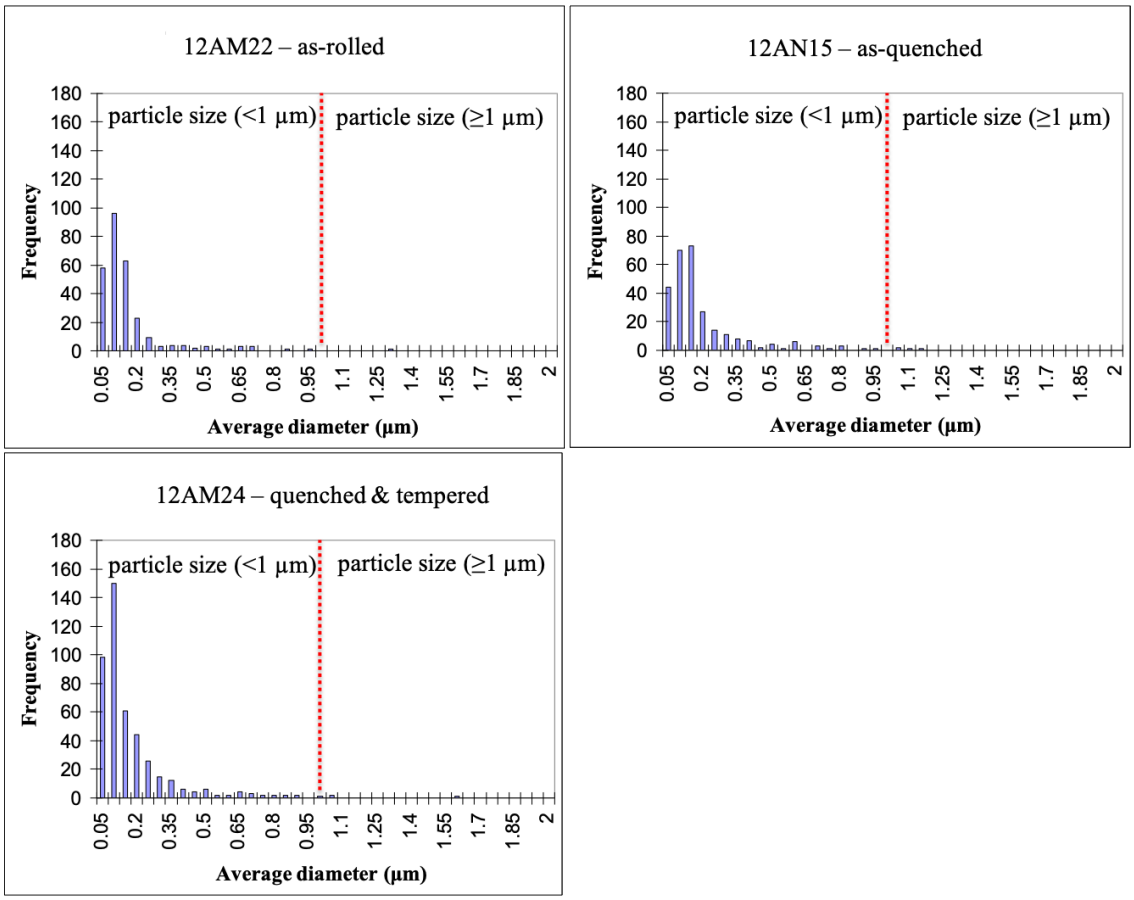


Figure 4.88: Particle size distribution in terms of average diameter (µm) of BN particles on as-rolled sample 12AM22, as-quenched reference sample 12AN15, and quenched and tempered sample 12AM24. The data is courtesy of Tata Steel.

Average diameter frequency distribution histograms of BN particles for samples 12AM22, 12AN15 and 12AM24 measured with SEM by Tata Steel are shown in Figure 4.88. From this data, the number of particles detected in the as-rolled sample 12AM22 and the as-quenched sample 12AN15 are almost the same. However, the as-rolled sample shows higher number of small BN particles with

size below 0.2 µm. The number of BN particles increases after quenching and tempering with lots of fine particles. In Al-protected samples, the smallest BN particle is about 50 nm in diameter and was detected both in the as-rolled 12AM22 and as-quenched 12AN15. The smallest BN particle found in the quenched and tempered sample 12AM24 is 80 in nm diameter.

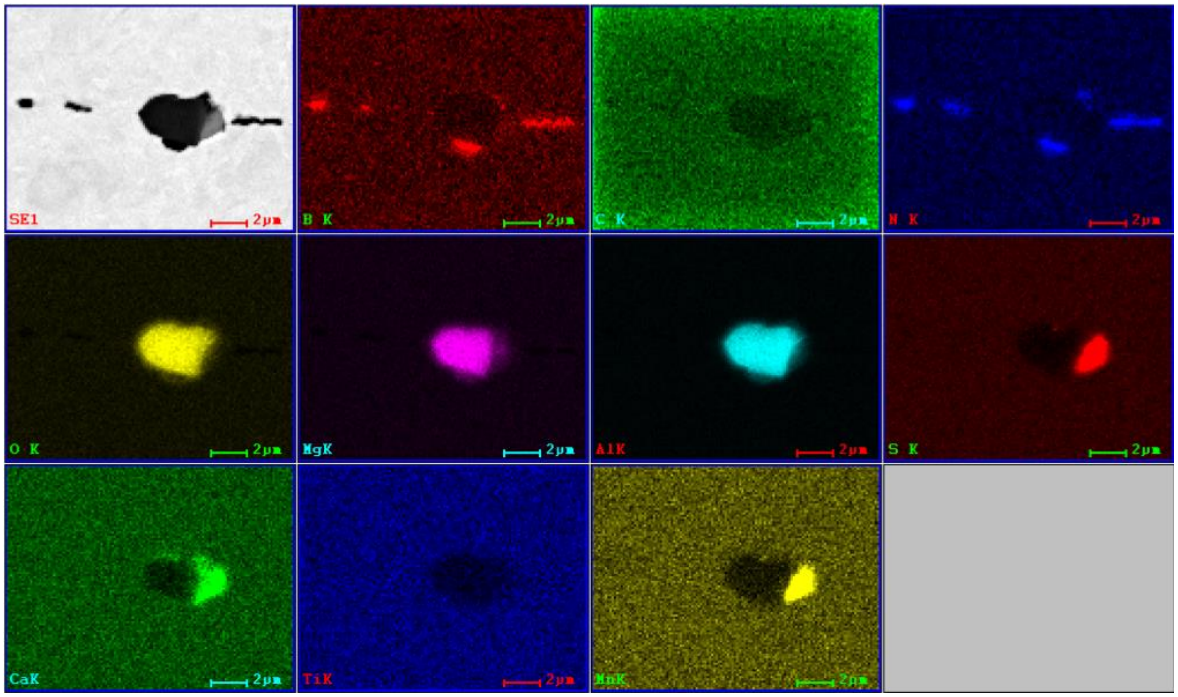


Figure 4.89: X-ray maps on sample 12AN15. BN is present both as free particles and associated with other species. Image courtesy of Tata Steel.

Figure 4.89 shows the example of x-ray maps indicating that BN is present both as free particles and associated with other species in sample 12AN15. It is recognised that quantitative x-ray results from such small, light element particles will not be accurate; however, it may serve to enable basic identification of the particle type.

Figure 4.90 shows a ternary diagram of B, N and Al 'content' on sample 12AM22 that illustrates BN is present, but also a significant Al component is also present. This could be from the two discreet types of precipitate being in close proximity to each other, or one precipitated on the other.

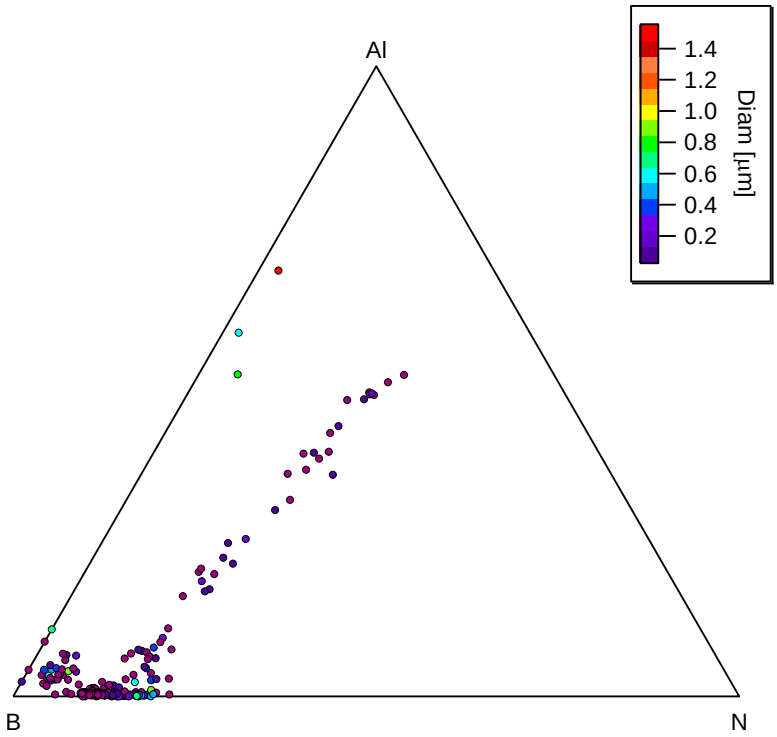


Figure 4.90: Ternary diagram of nitride composition in sample 12AM22. Image courtesy of Tata Steel.

Making a comparison of the data from the two techniques, it is clear from the data reported above that NanoSIMS analysis with an incident beam larger than 50 nm detects with confidence only particles larger than about 0.4 µm while the SEM imaging technique used by Tata Steel has a higher resolution and detects smaller particles down to 50 nm in diameter. The beam broadening effect of the larger primary beam in the NanoSIMS will make all the particles appear to be larger than they really are, and the contrast in the SE images was often so complicated in these samples to make identification of the boron-containing particles difficult.

The SEM analysis detected hardly any BN particles larger than about 1 µm but the NanoSIMS detected larger boron-containing particles especially in the as-rolled samples. However, the NanoSIMS analysis will detect all types of boron-containing particles whereas the SEM contrast method focuses on detecting BN particles. The EDX data in Figure 4.90 and the NanoSIMS images in Figure 4.22 both show different types of precipitate very close to one another, especially along grain boundaries, and this also makes it difficult to separate the types of particle. No BN particles were detected in the Ti-protected samples with SEM analysis but the NanoSIMS could detect lots of boron-containing particles which might be BN or other phases like $Fe_{23}(B,C)_6$ boro-carbides.

Determining exactly what types of precipitate particle are present in these different samples would require confirmation using another technique such as TEM or APT.

4.5.5 Discussion and Summary of Quantitative Analysis

The quantitative analysis of boron in these steels is divided into three parts. First to quantify the total boron counts in the samples, second to quantify boron segregation at the grain boundaries, and lastly to quantify boron particle sizes and size distributions.

Quantification of total boron counts in the samples suggests that, after normalisation by the dose implanted, the minimum and maximum of the total normalised boron lies over a range of almost two orders of magnitude although the actual boron concentrations in these materials are very similar. The spread in the boron counts measured from the steel samples reduces to around one order of magnitude when the boron intensities were normalised by the carbon intensity. This spread means that calibrating boron counts against implanted standards may not be the best way to compare samples analysed many months apart, so a method based on the internal standard offered by the concentration of boron in the grains on either side of a grain boundary was tried instead.

The first method to quantify boron segregation at the grain boundaries used ion implanted standards. This technique can easily control the concentration of implanted elements and produce homogeneous dilute binary alloys (Hashimoto et al., 1987). The boron concentration segregated to the grain boundaries was calculated using the equation adapted from Christien et al. (Christien et al., 2012). The boron concentrations at the grain boundaries calculated using this first method of quantification were in the physically realistic range of 0.6 to 5.1 atoms.nm^{-2} as illustrated by the blue line and left axis in Figure 4.91. As-rolled samples have the lowest segregated boron concentration of around 0.6 atoms.nm^{-2}. The as-quenched samples show a higher amount of boron concentration in the grain boundaries as compared to the as-rolled samples, ranging from 0.7 to 1.6 atoms.nm^{-2}. Quenched and tempered samples show the highest value of grain boundary boron concentration, 2.8 atoms.nm^{-2} (12AM25) and 5.1 atoms.nm^{-2} (12AM24). The reason for higher concentrations in the quenched and

tempered samples is that the tempering heat treatment encourages preferential fine scale precipitation on the grain boundaries. These small precipitates cannot be resolved in the NanoSIMS and hence line profiles will inadvertently cross over them.

The average boron concentration at the grain boundaries in Mo sample 13ZZ6ZBM is 1.6 atoms.nm^{-2} which is slightly lower than reported from APT data on a similar Mo sample, which had a boron excess value of 5.27 atoms.nm^{-2}. Among all of the as-quenched samples, the Mo sample 13ZZ6ZBM shows the highest average B concentration. This is in good agreement with the idea that the addition of Mo retards the precipitation of $Fe_{23}(C,B)_6$ and thus promotes the segregation of B at the grain boundaries (Hara et al., 2004).

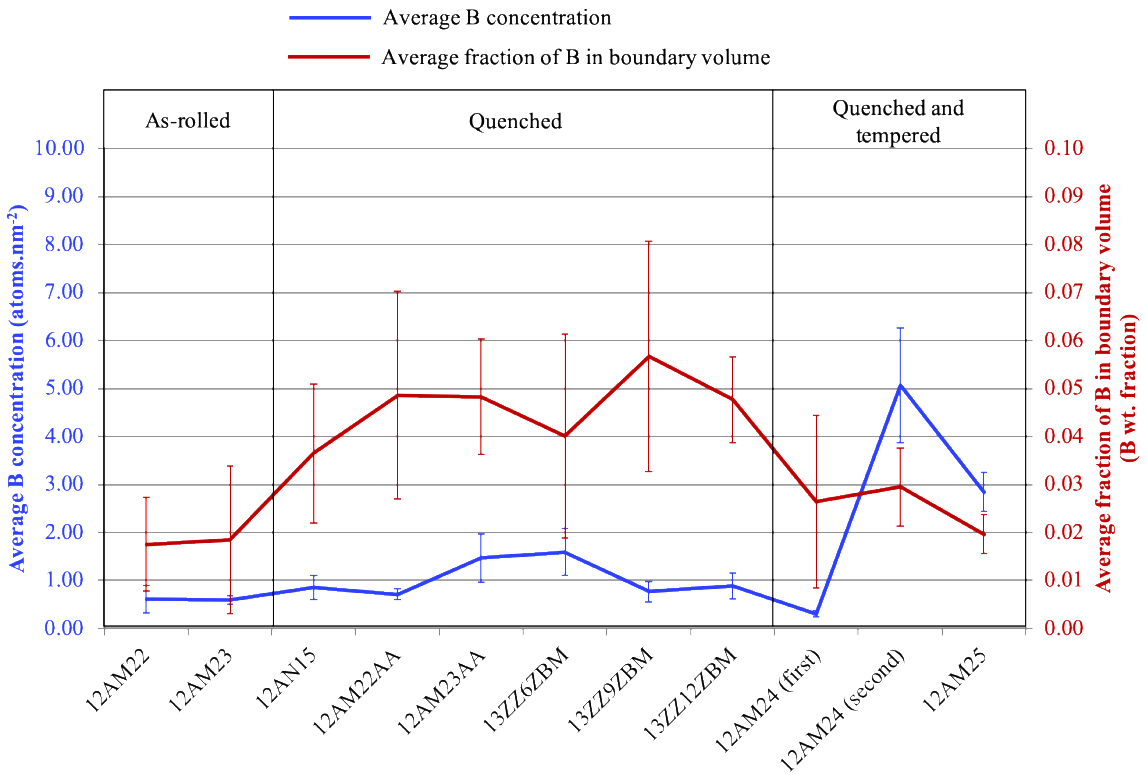


Figure 4.91: Average boron concentrations (blue line, left axis) and average fraction of boron in boundary volume (red line, right axis) for as-rolled, as-quenched and quenched and tempered samples.

The second method to estimate boron grain boundary concentration is by assuming that the background counts arise from a B concentration equal to the solid solution limit at 900°C, which is 0.008 wt.% B in the Fe-B binary phase diagram (Metals, 2007). The boron concentrations calculated

using this second method lie in the range of 0.02 to 0.06 B wt. fraction in boundary volume as illustrated by the red line and right axis in Figure 4.91. The as-rolled samples show the lowest B fraction in boundary volume while the as-quenched samples show the highest average fraction of boron in the boundary volume, ranging from just under 0.04 wt. fraction to nearly 0.06 wt. fraction. After quenching and tempering, both samples show a decreased fraction of boron in the boundary volume. The result for the quenched and tempered samples is not as expected because these samples should have lots of preferential precipitation on the grain boundaries and possible precipitation in the grains. This method to determine the grain boundary concentration by assuming that the alloy concentration is 0.008 wt.% B may only be valid when the boron is in solid solution, whereas the quenched and tempered samples can contain many precipitates in the grains from which the yield may be very different that from the grain interior (matrix effect) and hence this could explain the discrepancy in the results from those presented from the first method.

So, if we assume that the first method of quantification using the ion implanted standard is not very reliable for analysing samples many months apart because of variations in the instrumental performance, an improvement in the protocol might be to perform the calibration with the standard material each time when starting a new set of analyses. This calibration takes about one hour, but should improve the precision of the measurements. The second method of quantification using the known concentration of 0.008 wt.% B at 900°C can be another alternative to estimate boron concentration. Both methods of quantifying boron segregation have reduced accuracy in the analysis of quenched and tempered samples with the NanoSIMS as tempering heat treatment brings out very precipitates on the grain boundaries that are not easy to resolve.

There are not many studies in the literature that quantify boron segregation using SIMS. One of the earliest studies to quantify boron segregation in steel was performed by Hashimoto et al. (Hashimoto et al., 1987) using the ion implanted standard with large error of 200%. Da Rosa et al. (Da Rosa et al., 2020) recently studied boron segregation in high-strength steels by quantifying both concentrations of boron atoms in solid solution in the grains and at the prior austenite grain boundaries using APT and NanoSIMS. They used APT concentration measurements to calibrate the

average NanoSIMS intensity in the grains. Da Rosa et al. pointed out that the RSF value for boron in the grain boundaries could be different from the grains due to the matrix effect on boron ionization, therefore the interfacial excess of solute should not be extracted from SIMS intensity profile across the grain boundary. However, taking this approach would lose the ability to analyse many more boundaries by SIMS than will ever be possible by APT, and also downplays the very considerable calibration and estimation steps in extracting grain boundary segregation data from APT datasets.

Quantitative analysis of boron particle sizes and size distributions was done on some of these using both NanoSIMS and SEM data from Tata Steel. The particle distribution data from the NanoSIMS shows there are lots of boron-rich particles in both the as-rolled samples that are Al-protected and Ti-protected, and that the number of particles decreased after quenching. After quenching and tempering the Al-protected sample shows an increased number of particles, but the Ti-protected sample shows a slight decrease in the number of precipitates. The BN particle distribution data from Tata Steel shows BN particles were detected in Al-protected samples but not in the Ti-protected samples. There are almost the same number of BN particles in both as-rolled and quenched Al-protected samples, then the number of BN particles increased by a factor of almost two after quenching and tempering, with lots of fine particles.

The different results from the particle analysis experiments by NanoSIMS and SEM may be because the NanoSIMS can easily distinguish a large range of boron-rich particles, including BN, and boro-carbides ($Fe_{23}(B,C)_6$, $B_{13}C_2$ or B_4C), which could also be studied by very time-consuming techniques like TEM or APT. No BN particles were detected in the Ti-protected samples by SEM, but with the higher sensitivity of NanoSIMS some of BN particles were detected in both the Al- and Ti-protected as-rolled samples as shown in Figure 4.20 and Figure 4.46, respectively. After quenching and tempering, BN particles were still detected in the Al-protected sample, Figure 4.38, but not in the Ti-protected sample, Figure 4.56. Quantitative x-ray results using SEM and EDX from such small, light element particles may not be accurate, but could be a useful initial identification of particle type before higher sensitivity techniques like NanoSIMS (or APT) were applied.

4.6 Conclusions

The results from Chapter 4 show the capability of the NanoSIMS to analyse boron distributions in a range of high strength steels after the different heat treatments shown in Figure 4.1. The following conclusions can be drawn for Chapter 4:

1. Comparison between the boron distribution in Al-protected steels and Ti-protected steels at three processing stages (as-rolled, as-quenched and quenched and tempered):
    a) In both types of as-rolled samples, aluminium protected 12AM22 and titanium protected 12AM23, high percentages of the total detected boron are in particles rather than segregated to the grain boundaries. The boron content is higher in pro-eutectoid ferrite than in pearlite.
    b) Strong boron segregation at prior austenite grain boundaries was observed in all of the as-quenched samples (12AN15, 12AM22AA, 12AM23AA). Most of the large boron rich precipitates were observed in the Al-protected 12AM22AA sample.
    c) In the quenched and tempered samples (12AM24 and 12AM25), segregation at the prior austenite grain boundaries can just be seen, with small precipitates near the grain boundaries as well as in the grains. Again, it appears in the quenched and tempered samples that small boron-containing precipitates were created during the tempering stage as they were not visible in other samples.
    d) Some BN particles were detected in both the as-rolled Al- and Ti-protected steels.
    e) After quenching and tempering, BN particles were still detected in the Al-protected sample, but not in the Ti-protected sample.
    f) The maximum hardenability can be reached when boron is in solid solution or finely precipitated at grain boundaries by preventing boron precipitating into nitrides. Thus, the addition of Ti as a strong nitride former to the steels can maximise this beneficial effect.

g) Equilibrium segregation seems to have occurred when the samples were homogenised for 15 or 30 minutes at 930°C, and non-equilibrium segregation during water quenching after this homogenisation.

2. Comparison of two Al-protected steel samples at different reheating times in the austenitic region:
   a) Sample 12AM22G which has been treated for 180 minutes at the austenizing temperature has the highest percentage (42%) of boron at the grain boundaries compared to 12AM22AA and 12AM22F. Sample 12AM22F which has been treated for 10 minutes at the austenizing temperature does not show much difference to the as-quenched sample 12AM22AA which has been treated for 30 minutes at the austenizing temperature. The percentage of boron at the grain boundaries in both samples is about 30%. Thus, there does appear to be an advantage in austenizing for longer than 30 minutes.
3. Comparison of direct quenched steel and the conventional as-quenched steel:
   a) Very similar behaviour in terms of boron segregation at the grain boundaries in the direct quenched and the conventional as-quenched steels has been observed. Thus, this direct-quenched approached can be used as an alternative process to reduce costs and increased overall efficiency in the steel making industry while still providing similar results in terms of hardenability in the same type of steel.
4. Comparison between Mo alloyed steel (13ZZ6ZBM) and two other Al-protected steels with different Al concentrations (13ZZ9ZBM – 0.077 wt% Al) and (13ZZ12ZBM – 0.057 wt% Al):
   a) Mo additions did not seem to make much difference in boron distributions observed in this range of steels. All three samples show boron segregation at the grain boundaries, with some big particles with size ranging from 2 to 3 μm. The amount of boron segregated to the boundaries is higher in sample 13ZZ9ZBM which has higher hardness and higher Al content compared to 13ZZ12ZBM.

b) Mo addition to this steel is supposed to retard the precipitation of $M_{23}(CB)_6$ and retain more boron in solution, but the observation from this study does not show this to be the case.

5. Quantitative analysis of boron in steels:

a) Quantification of total boron counts in the samples shows that the minimum and maximum of the total normalised boron can lie over a range of almost two orders of magnitude although the actual boron concentrations in these materials are very similar. This is a result of variations in the instrument parameters and resulting sensitivity at different times. This spread means that calibrating boron counts against implanted standards may not be the best way to compare samples analysed many months apart, so a method based on the internal standard offered by the concentration of boron in the grains on either side of a grain boundary was tried instead.

b) Although the first method of quantification using the ion implanted standard is not very reliable for analysing samples many months apart because of variations in the instrumental performance, an improvement in the protocol might be to perform the calibration with the standard material each time when starting a new set of analyses. The boron concentrations at the grain boundaries calculated using this first method of quantification were in the physically realistic range of 0.6 to 5.1 atoms.nm^{-2}.

c) The second method of quantification using the known concentration of 0.008 wt.% B at 900°C can be another alternative to estimate boron concentrations at grain boundaries. The boron concentrations calculated using this second method lie in the range of 0.02 to 0.06 B wt. fraction in the boundary volume.

d) The particle distribution data from the NanoSIMS shows there are many boron-rich particles in as-rolled samples that are both Al-protected and Ti-protected, and that the number of particles decreases after quenching. After quenching and tempering the Al-protected sample shows an increased number of particles, but the Ti-protected sample shows a slight decrease in the number of precipitates.

e) This is the only extensive quantification of grain boundary segregation performed with NanoSIMS to date, with 100s of grain boundaries analysed.

4.7 References

ASAHI, H. 2002. Effects of Mo addition and austenitizing temperature on hardenability of low alloy B-added steels. *Isij International,* 42**,** 1150-1155.

BANERJEE, M. K. 2017. Heat Treatment of Commercial Steels for Engineering Applications. *In:* HASHMI, M. S. J. (ed.) *Comprehensive Materials Finishing.* Oxford: Elsevier.

BHADESHIA, H. K. D. H. & HONEYCOMBE, S. R. 2006. Formation of Martensite. *Steels: Microstructure and Properties.* Third ed. Oxford: Butterworth-Heinemann.

CALLISTER, W. D. 2001. *Fundamentals of materials science and engineering : an interactive etext,* New York; Chichester, Wiley.

CHRISTIEN, F., DOWNING, C., MOORE, K. L. & GROVENOR, C. R. M. 2012. Quantification of grain boundary equilibrium segregation by NanoSIMS analysis of bulk samples. *Surface and Interface Analysis,* 44**,** 377-387.

DA ROSA, G., MAUGIS, P., PORTAVOCE, A., DRILLET, J., VALLE, N., LENTZEN, E. & HOUMMADA, K. 2020. Grain-boundary segregation of boron in high-strength steel studied by nano-SIMS and atom probe tomography. *Acta Materialia,* 182**,** 226-234.

DRILLET, J., VALLE, N. & IUNG, T. 2012. Nanometric Scale Investigation of Phase Transformations in Advanced Steels for Automotive Application. *Metallurgical and Materials Transactions A,* 43**,** 4947-4956.

FAULKNER, R. G. 1981. Non-equilibrium grain-boundary segregation in austenitic alloys. *Journal of Materials Science,* 16**,** 373-383.

FAULKNER, R. G. 1996. Segregation to boundaries and interfaces in solids. *International Materials Reviews,* 41**,** 198-208.

HAN, F., HWANG, B., SUH, D.-W., WANG, Z., LEE, D. L. & KIM, S.-J. 2008. Effect of molybdenum and chromium on hardenability of low-carbon boron-added steels. *Metals and Materials International,* 14**,** 667.

HARA, T., ASAHI, H., UEMORI, R. & TAMEHIRO, H. 2004. Role of Combined Addition of Niobium and Boron and of Molybdenum and Boron on Hardnenability in Low Carbon Steels. *ISIJ International,* 44**,** 1431-1440.

HASHIMOTO, S., DOI, S., TAKAHASHI, K., TERASAKA, M. & IWAKI, M. 1987. Quantitative analysis of boron in steel by secondary ion mass spectrometry using ion-implanted iron as standard. *Materials Science and Engineering,* 90**,** 119-125.

JAHAZI, M. & JONAS, J. J. 2002. The non-equilibrium segregation of boron on original and moving austenite grain boundaries. *Materials Science and Engineering: A,* 335**,** 49-61.

KARLSSON, L., NORDÉN, H. & ODELIUS, H. 1988. Overview no. 63 Non-equilibrium grain boundary segregation of boron in austenitic stainless steel—I. Large scale segregation behaviour. *Acta Metallurgica,* 36**,** 1-12.

KRAUSS, G. 2015. *Steels: processing, structure, and performance*, ASM International.

KURBAN, M., ERB, U. & AUST, K. T. 2006. A grain boundary characterization study of boron segregation and carbide precipitation in alloy 304 austenitic stainless steel. *Scripta Materialia,* 54**,** 1053-1058.

LARRAÑAGA-OTEGUI, A., PEREDA, B., JORGE-BADIOLA, D. & GUTIÉRREZ, I. 2016. Austenite Static Recrystallization Kinetics in Microalloyed B Steels. *Metallurgical and Materials Transactions A,* 47**,** 3150-3164.

LI, L., KAMACHALI, R. D., LI, Z. & ZHANG, Z. 2020. Grain boundary energy effect on grain boundary segregation in an equiatomic high-entropy alloy. *Physical Review Materials,* 4**,** 053603.

LI, Y. J., PONGE, D., CHOI, P. & RAABE, D. 2015. Segregation of boron at prior austenite grain boundaries in a quenched martensitic steel studied by atom probe tomography. *Scripta Materialia,* 96**,** 13-16.

LIN, H. R. & CHENG, G. H. 1990. Analysis of hardenability effect of boron. *Materials Science and Technology,* 6**,** 724-729.

METALS, K. T. 2007. *Boron in Steel: Part One* [Online]. Available: https://www.totalmateria.com/page.aspx?ID=CheckArticle&site=kts&NM=212 [Accessed 12 December 2018].

MUN, D. J., SHIN, E. J., CHOI, Y. W., LEE, J. S. & KOO, Y. M. 2012. Effects of cooling rate, austenitizing temperature and austenite deformation on the transformation behavior of high-strength boron steel. *Materials Science and Engineering a-Structural Materials Properties Microstructure and Processing,* 545**,** 214-224.

OFFERMAN, S., VAN DIJK, N., REKVELDT, M., SIETSMA, J. & ZWAAG, S. 2002. Ferrite/pearlite band formation in hot rolled medium carbon steel. *Materials Science and Technology,* 18**,** 297-303.

PAJU, M. 1992. Effects of boron protection methods on properties of steel. *Ironmaking & Steelmaking,* 19**,** 495-500.

SUZUKI, S., ABIKO, K. & KIMURA, H. 1981. Phosphorus segregation related to the grain boundary structure in an Fe・P alloy. *Scripta Metallurgica,* 15**,** 1139-1143.

TINGDONG, X., SHENHUA, S., ZHEXI, Y. & ZONGSEN, Y. 1990. Two types of boron segregation at austenite grain boundaries and their mutual relation. *Journal of Materials Science,* 25**,** 1739-1744.

VALLE, N., DRILLET, J., PIC, A. & MIGEON, H. N. 2011. Nano-SIMS investigation of boron distribution in steels. *Surface and Interface Analysis,* 43**,** 573-575.

5 Grain Boundary Analysis in a New Polycrystalline Superalloy

5.1 Introduction

The work reported in this chapter is a study, using high-resolution secondary mass spectrometry (NanoSIMS), of the distribution and behaviour of boron in a new polycrystalline superalloy. It is another example of the capability of the NanoSIMS to provide detailed information on boron distributions over large areas. The combination of high spatial resolution and sensitivity to light elements make NanoSIMS a useful technique for boron analysis in samples that only contain this element in low concentrations. My work has been complementary to parallel SEM, APT and TEM analysis of the same alloys. The large area mapping capability has been particularly valuable to compare with results from APT which can also detect low levels of boron – but only in very small volumes.

5.1.1 Applications of Nickel-based Superalloys

Nickel-based superalloys were developed in the 1950s for high performance applications at high temperatures, typically above 500°C, under conditions where resistance to creep, fatigue and environmental degradation is required. Due to their good properties at elevated temperature, they have been widely used in aerospace applications, and particularly in gas turbines in aircraft and for power generation industrial gas turbines, nuclear and fossil power plants (Donachie and Donachie, 2002).

A gas turbine engine has three main sections; the compressor, the combustion system and the turbine. The air passes through the compressor section and its pressure and temperature increased rapidly. This is where the heat-resistant materials such as nickel-based superalloys are needed. Hot and high-pressure gasses flow from the combustion chamber through the shafts attached to the turbine section, and as these hot gasses expand through the turbine section, they spin the blades. The rotating blades make the compressor draw more pressurised air into the combustion section and power is generated from the spinning turbine (Mouritz, 2012).

The purpose of turbine blades is to extract the kinetic energy from the hot gas stream to turn their turbine discs (Mouritz, 2012, Reed et al., 2009). However, the turbine blades are prone to deformation by creep processes and it is desirable for engine performance and lifetime to keep creep deformation to a minimum (Pollock and Argon, 1992, Pollock and Tin, 2006). Single-crystal superalloys are used for turbine blades which experience the highest temperatures. The absence of grain boundaries in these materials provide the best creep and fatigue properties. However, cheaper polycrystalline nickel-based superalloys are widely used in some components on hot sections of the gas turbine such as casings, guide vanes and the highly stressed rotating disk, where single crystal alloys cannot be cast due to their complicated geometries. These components which experience higher stresses need the combination of high yield strength and fracture toughness that the polycrystalline superalloys can offer (Reed, 2008, Mitchell, 2010).

5.1.2 Metallurgy of Nickel-based Superalloys

The strength of polycrystalline nickel-based superalloys is provided by solid solution strengthening of the face-centred cubic (FCC) gamma (γ) matrix, and precipitation hardening by gamma-prime (γ') or (γ'') and reasonable amount of carbide and boride distributions (Reed, 2008, Mitchell, 2010).

The gamma (γ) phase is a Ni-based solid solution and forms a continuous matrix that contains a high percentage of solid solution elements such as cobalt (Co), chromium (Cr), molybdenum (Mo), tungsten (W), ruthenium (Ru) and rhenium (Re). These elements have an atomic radius very similar to nickel (Ni) and thereby stabilize the γ phase (Reed, 2008).

The gamma prime (γ') phase is usually in the form of a precipitate rich in elements such as aluminium (Al), titanium (Ti), tantalum (Ta) and niobium (Nb). These elements have larger atomic radii and promote the formation of the γ' ordered phase Ni_3 (Al, Ti, Ta). In nickel-iron superalloys which are rich in Nb, the ordered phase γ'' is preferred instead of γ'. It is the γ' that provides significant strengthening and is largely responsible for the elevated temperature strength of the nickel-based superalloys and their remarkable resistance to creep deformation (Reed, 2008, Mitchell, 2010).

Constituents such as sigma (σ), mu (μ) and Laves phases are found in nickel-based superalloys if this material is exposed for long periods at elevated temperatures during heat treatment or in service (Sabol and Stickler, 1969). These compounds have been categorized as having the topologically close-packed (TCP) structure. High concentrations of Cr, Mo, W and Re encourage the precipitation of TCPs (Rae and Reed, 2001, Antonov et al., 2017). They usually form as plate-like or needle-like structures which negatively affect the mechanical properties. They are brittle and undesirable because they act as crack initiators and reduce creep strength (Yang et al., 2007, Wilson, 2017).

5.1.3 Carbon and Boron as Grain Boundary Strengtheners

Polycrystalline Ni-based superalloys also contain elements that strengthen the grain boundaries, such as carbon and boron. Many studies have shown that the high-temperature creep properties of polycrystalline superalloys are improved if carbon and boron are present. This is explained by carbon and boron preferentially residing at γ grain boundaries, and suppressing grain boundary sliding, thus increasing the creep rupture strength, creep ductility and low cycle fatigue behaviour. This is why carbon and boron are often referred to as grain boundary strengtheners (Reed, 2008).

Carbon usually combines with reactive elements such as Ti, Ta and Hf to form MC carbides. $M_{23}C_6$ and M_6C are rich in Cr, Mo and W, and are normally formed at the γ grain boundaries during heat treatment or in service, thus reduce the tendency for grain boundary sliding during deformation (Reed and Rae, 2014). It is also known that carbides can control grain size during thermomechanical processing (Xu et al., 1998, Collins et al., 2013).

High yield strength can be achieved by maintaining the carbon content in the range of 0.05 to 0.14 wt.% C in the superalloys, as a result of pinning grain boundaries by fine carbides and dispersion strengthening of the γ grains. However, carbides with needle or film shapes lead to degradation of the mechanical properties. The needle-shape carbides are formed during heat-treatment and long aging times while film-shaped carbides are formed during solidification and reside along γ grain boundaries (Yang et al., 2011).

During prolonged thermal and stress exposure, decomposition of the MC carbides results in the formation of continuous secondary $M_{23}C_6$ films at grain boundaries. This type of carbide can act as crack initiation sites and leads to a decrease in mechanical properties (Qin et al., 2007). However, fine and discreet $M_{23}C_6$ carbides are only beneficial if they are uniformly distributed along grain boundaries where they can prevent grain boundary migration during deformation and strengthen the grain boundaries (He et al., 2005, Liu et al., 2003).

There is an extensive literature on whether carbides are beneficial or detrimental to the mechanical properties of superalloys, but it is now accepted that in polycrystalline superalloys, carbides are beneficial by increasing rupture strength at high temperature by avoiding grain boundary sliding (Geddes et al., 2010).

Boron is also added to nickel-based superalloys in small quantities (50 to 500 ppm) to strengthen the grain boundaries by retarding the relative motion between grains. Boron tends to segregate to loosely packed regions like grain boundaries during heat treatment due to its low solubility in γ and γ' and its size misfit relative to the nickel matrix. At grain boundaries, it increases the work of cohesion and has a significant effect of improving creep properties, in particular creep ductility (Reed, 2008, Geddes et al., 2010).

Boron can also prevent rapid agglomeration of $M_{23}C_6$ carbides and γ' in grain boundaries due to a reduction in grain boundary diffusivity (Holt and Wallace, 1976, Jena and Chaturvedi, 1984). Rapid agglomeration of these phases leads to depletion of γ' and finally by intergranular micro cracking at grain boundaries transverse to the applied stress (Decker and Freeman, 1958). Most failures initiate at elevated temperature when micro cracks nucleate in the grain boundaries. Therefore, adding minor amounts of boron can alter the grain boundary character and improve creep life in polycrystalline superalloys.

It is now accepted that boron existing either segregated to the grain boundaries or as secondary phase particles such as M_3B_2 or M_5B_3 along the grain boundaries can significantly influence the high

temperature properties of superalloys. In new alloys, it is thus important to study whether the boron is segregated at the grain boundaries or is incorporated into borides.

5.2 Materials and Methods

5.2.1 Materials Composition

The composition of the prototype nickel-based polycrystalline superalloy STAL-15CC used in this study is shown in Table 5.1. Three test-bars were cast with low boron (0.03 at.%B), medium boron (0.05 at.% B) and high boron (0.08 at.% B) content. Castings were made in the form of tapered rods using the casting stock melted by Ross & Catherall and performed at Doncasters Precision Castings Ltd. (Sheffield, United Kingdom).

Table 5.1: Chemical composition of nickel-based polycrystalline superalloy STAL15-CC (at.%)

Alloy	B	C	Co	Cr	Mo	W	Al	Ta	Hf	Si
Low boron	0.03	0.47	5.60	16.43	0.58	1.27	10.11	2.41	0.02	0.06
Medium boron	0.05	0.47	5.50	16.55	0.59	1.26	10.09	2.40	0.02	0.04
High boron	0.08	0.53	5.53	16.64	0.60	1.21	10.01	2.43	0.02	0.08

5.2.2 Heat Treatment

Hot isostatic pressing (HIP) was performed on the as-cast materials to improve mechanical properties. The process was performed at 1195°C for 5 hours under 175 MPa pressure. Two stages of ageing were carried out after the HIP process. The primary ageing was done at 1120°C for 4 hours and followed by air cooling. The second stage of ageing was done at 845°C for 24 hours then followed by air cooling. The heat treatment process is aimed to optimize the grain and precipitate size, morphology and distribution (Kontis et al., 2016).

5.2.3 Sample Preparation for NanoSIMS Analysis

Detailed sample preparation for NanoSIMS analysis was explained in Section 3.2. This project was a collaboration with Paraskevas Kontis and his supervisor Professor Roger Reed. Sample preparation for the materials studied here was carried out by P. Kontis.

The samples were cut into 7.3 x 7.3 x 4 mm pieces and mechanically ground to 1200 grit paper and polished with diamond paste down to a particle size of 1 μm. Figure 5.1 shows how areas of interest were marked with indents using macro-hardness instruments so that grain boundaries were easy to identify during analysis. Prior to NanoSIMS analysis, optical microscope (OM) images of the surface of the samples were captured.

A detailed description of the NanoSIMS analysis, tuning of the instrument and resolving mass overlaps are given in Section 3.7. For this material, $^{12}C^-$, $^{11}B^{12}C^-$, $^{11}B^{16}O_2^-$ and $^{56}Cr^{16}O^-$ signals were collected during the NanoSIMS imaging.

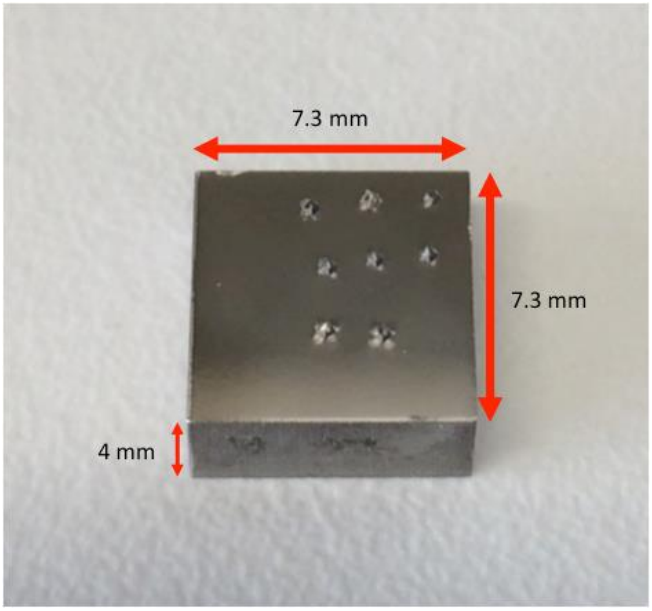


Figure 5.1: Typical NanoSIMS sample with dimensions allowing it to be loaded into the NanoSIMS holder. Marked indents can be seen on the top right of the surface allowing for correlation between NanoSIMS, AFM and optical microscopy.

5.3 Results and Discussion

5.3.1 Microstructure

Figure 5.2 gives an overview of the microstructure of the three boron-containing polycrystalline nickel-based superalloys that have been studied in this chapter. The backscattered SEM images with the descriptive illustration was adapted from Kontis et al. (Kontis et al., 2016). Backscattered SEM images give information based on atomic (Z) number and help to distinguish different phases. Strong compositional contrast is produced using backscattered electrons and the particles of low atomic mass e.g. carbon or boron (M_5B_3-type borides or $M_{23}C_6$-type carbides) appear dark whereas those with higher mass e.g. Ta or W (MC- type carbide) appear light. The microstructure revealed the differing contrast of the carbides and borides and showed that grain boundary γ' appeared larger than the secondary γ' particles precipitated within the grains.

The MC-type carbides in these three samples appear to have a blocky or elongated morphology. In the low boron sample, grain boundaries are decorated mostly by borides and large discrete grain boundary γ'. An elongated MC-type carbide was observed in this sample. Smaller and discrete blocky MC carbides appear at the grain boundary of medium and high boron samples which led to the formation of almost continuous layers of γ' particles at the grain boundaries. Discrete MC carbides formed at the grain boundaries do not provide any easy path for rapid crack propagation and lead to an increase in ductility (Kotval et al., 1972).

Based on general identification of intergranular microconstituents using SEM, it is possible to mistakenly consider the nanosized borides to be $M_{23}C_6$ carbide particles due to their similarity in chemistry and fine size (Zhang and Ojo, 2010). Therefore, it was necessary to identify the phases with complementary techniques such as APT and TEM which can provide atomic-level compositional information and crystallography structure. This analysis is presented in Kontis et.al (Kontis et al., 2016).

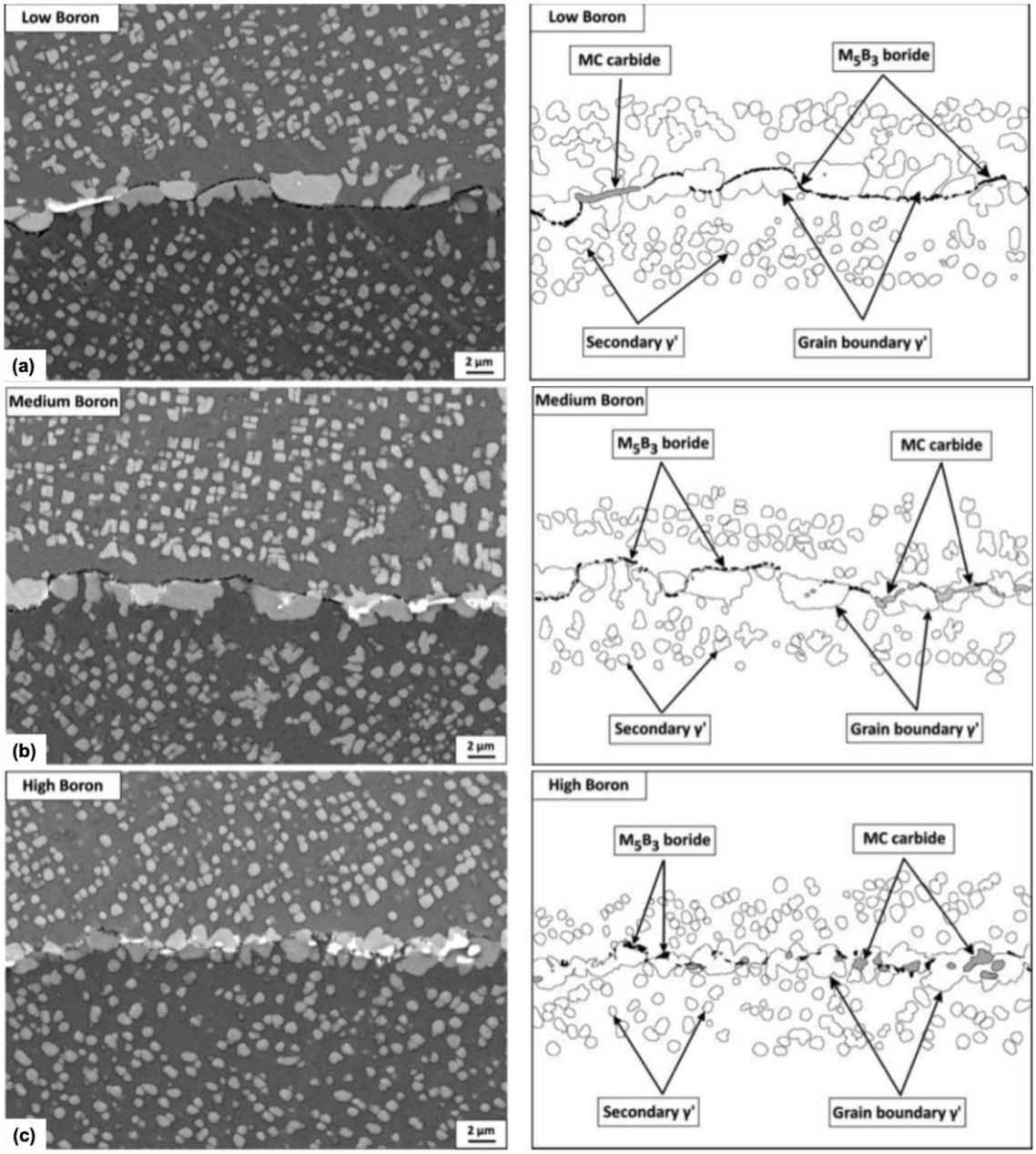


Figure 5.2: Backscattered SEM images (left) of (a) low, (b) medium and (c) high boron superalloy samples with their corresponding descriptive illustrations (right). Images from Kontis et al. (Kontis et al., 2016).

NanoSIMS data cannot give information on the exact composition and the crystallography of the phases. APT and TEM results from all samples show that carbon at the grain boundaries was tied up with Ta that leads to the formation of MC carbides. No Cr-rich $M_{23}C_6$ carbides were found at the grain boundaries, but nano-size plate-like $M_{23}C_6$ carbides were observed at the vicinity of the grain boundaries. The TEM analysis revealed that the crystal structure of the boron rich precipitates was tetragonal which corresponds to M_5B_3. (Kontis et al., 2016).

5.3.2 NanoSIMS Analysis

Three to four images with 50 μm raster size were acquired which followed a series of grain boundaries in order to understand the carbon and boron distribution in three boron containing polycrystalline nickel-based superalloys over a larger area than can be observed by APT or TEM. In order to be able to compare between results from the three different superalloy samples, a fixed counting time for each image was chosen of 1,000 μs/px per image and a total of 30 sequential images were summed which took about 30 minutes for a 256 x 256 pixel image, and a large primary aperture (D1=2) with 300 μm diameter was chosen to give adequate lateral resolution without compromising on sensitivity.

5.3.2.1 Low boron sample

The carbon and boron distribution in the low boron sample are shown in the $^{12}C^-$ and $^{11}B^{16}O_2^-$ maps in Figure 5.3. Boron was observed to be associated with small particles which have precipitated continuously along the grain boundaries, the carbon distribution did not however follow the same distribution. Carbides were localised within the grains with some fine spherical carbides observed in the vicinity of the grain boundaries. Only the top image shows intergranular carbides with plate-like morphology. The boron and carbon signals are not found at similar locations at the grain boundaries.

A 20 by 20 μm^2 area, highlighted in the red box in bottom image of Figure 5.3, was selected for high resolution imaging using a smaller aperture, D1=3. The dwell time was set to 10,000 μs/pixel per image and a total of 11 sequential images were summed. Before analysis was undertaken on these results, the image stack was aligned to correct for drift using the ImageJ software. Summed images of the $^{12}C^-$, $^{11}B^{16}O_2^-$, and $^{52}Cr^{16}O^-$ signals are shown in Figure 5.4. From the summed images, we can see that there was significant drift over the long acquisition as indicated by the black areas on the left and bottom of the image. The distribution of carbon in the $^{12}C^-$ map shows mostly the blocky carbide morphology and some small carbide precipitates in the grains. We can assume the blocky carbides are the MC type carbides as they are depleted in Cr. This type of carbide usually forms

during solidification (Xu et al., 1998). It has been reported that the existence of blocky type MC carbide is beneficial to creep properties (Chen et al., 2002). Scattered boron particles were decorated along the grain boundaries with a high signal of $^{11}B^{16}O_2^-$ from larger borides detected at the lower left region of the grain boundary with some carbon and rich in chromium. Based on the chemical information from the NanoSIMS maps, we can say they are Cr-rich borides. There is no apparent segregation of boron and carbon at the grain boundaries.

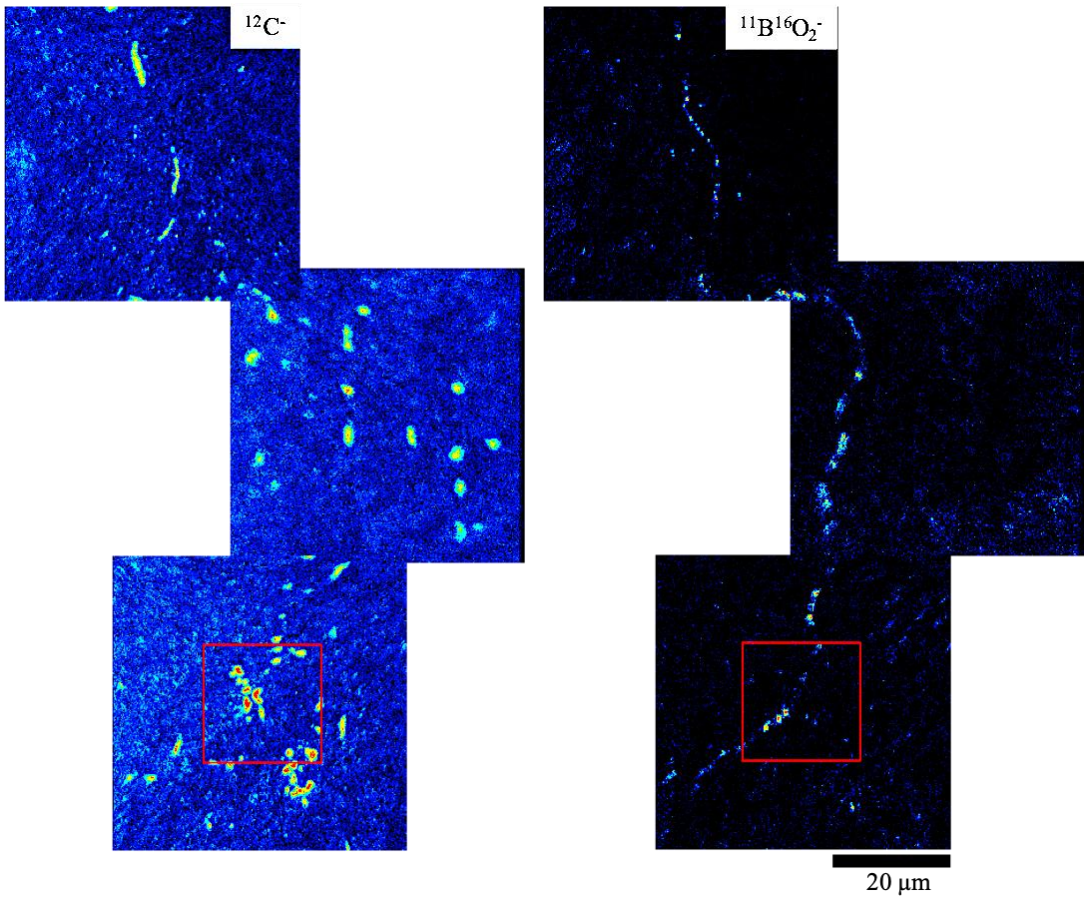


Figure 5.3: Carbon and boron maps showing carbides and borides decorated along grain boundaries on low boron sample. The red square indicates the 20 µm area that was selected for high resolution imaging using the D1=3 aperture shown in Figure 5.4.

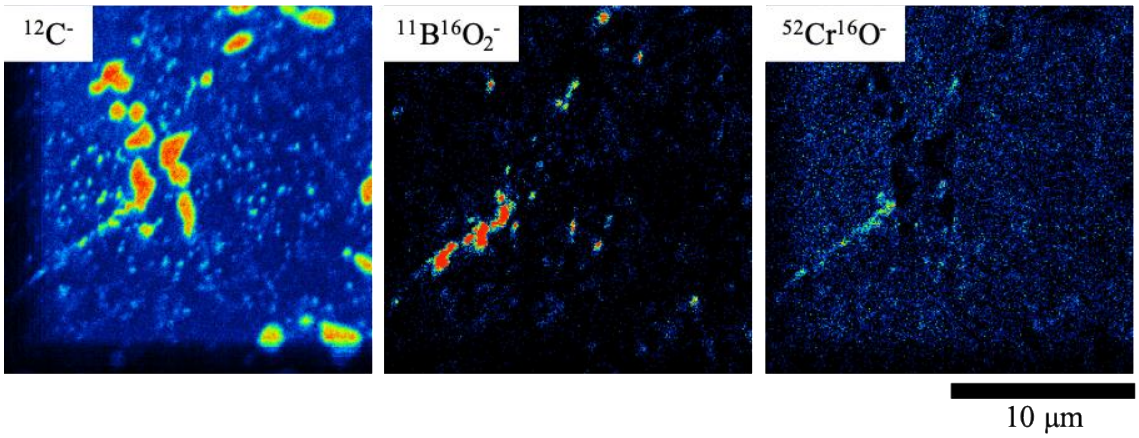


Figure 5.4: High resolution image of $^{12}C^-$, $^{11}B^{16}O_2^-$, and $^{52}Cr^{16}O^-$ maps using D1=3, raster size 20 µm, summed images of 11 slices, dwell time 10,000 µs/px from the red box in Figure 5.3.

Another scan was made in a different area and $^{12}C^-$, $^{11}B^{16}O_2^-$, $^{11}B^{12}C^-$, $^{52}Cr^{16}O^-$ maps and a colour merge image of $^{12}C^-$ and $^{11}B^{16}O_2^-$ are presented in Figure 5.5. The carbon map shows strong signals from intergranular blocky and elongated carbides at the grain boundaries. Fine and continuous boron particles were also decorated along the grain boundaries. Chromium was present throughout the matrix but depleted at the carbide regions. The colour merge image shows $^{12}C^-$ in red and $^{11}B^{16}O_2^-$ in blue indicating that there is very little overlap of carbide and boride particles.

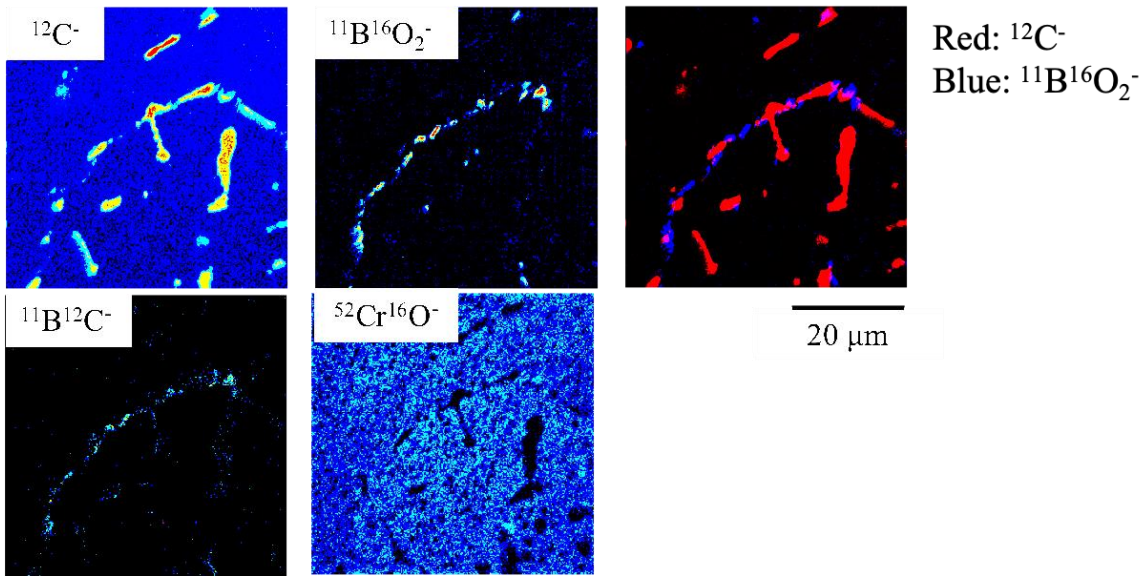


Figure 5.5: Selected area of low boron sample showing NanoSIMS maps of $^{12}C^-$, $^{11}B^{12}C^-$, $^{11}B^{16}O_2^-$ and $^{52}Cr^{16}O^-$. The colour merge image shows $^{12}C^-$ in red and $^{11}B^{16}O_2^-$ in blue.

5.3.2.2 Medium boron sample

From the maps shown in Figure 5.6, serration of grain boundaries (arrows) was present in this sample which is believed to be caused by slow cooling (Blavette et al., 1996). The formation of serrated grain boundaries in nickel-based superalloys is induced by heterogenous nucleation of γ' at the grain boundaries. When primary γ' particles are pinned at a grain boundary, its movement leads to displacement of the local grain boundary segment thus causing serrations (Koul and Thamburaj, 1985).

It can be seen in this sample that the boron precipitates are larger than found in the low boron sample even though the trend does not seem very obvious in the SEM images. Fine carbide precipitates are mostly on the grain boundaries and a few blocky and elongated intergranular carbides were observed at the grain boundaries. Once again, the carbon and boron rich regions were clearly at separate locations along the grain boundary.

Figure 5.7 shows the high-resolution image of $^{12}C^-$, $^{11}B^{16}O_2^-$ and SE maps of the area highlighted in the red box shown in Figure 5.6. The higher resolution scan using the aperture D1=3 was performed on the area of interest with a 20 μm raster size, 15,000 μs/pixel per image and a total of 54 sequential images were summed. Images were drift corrected using ImageJ. Although the drift correction is not perfect, it is still possible to interpret the summed images and get information from the images.

The $^{12}C^-$ map shows a high signal of carbon from the blocky and elongated carbides along the grain boundary and lower signals of carbon from the fine carbide precipitates in the grains. A low signal of carbon was also observed from the boron rich particles on the grain boundary. The morphology of the boron particles in this area are much larger and nearly continuous compared to those found in the low boron sample. The SE image gives an overview that the grain boundary is serrated in this region.

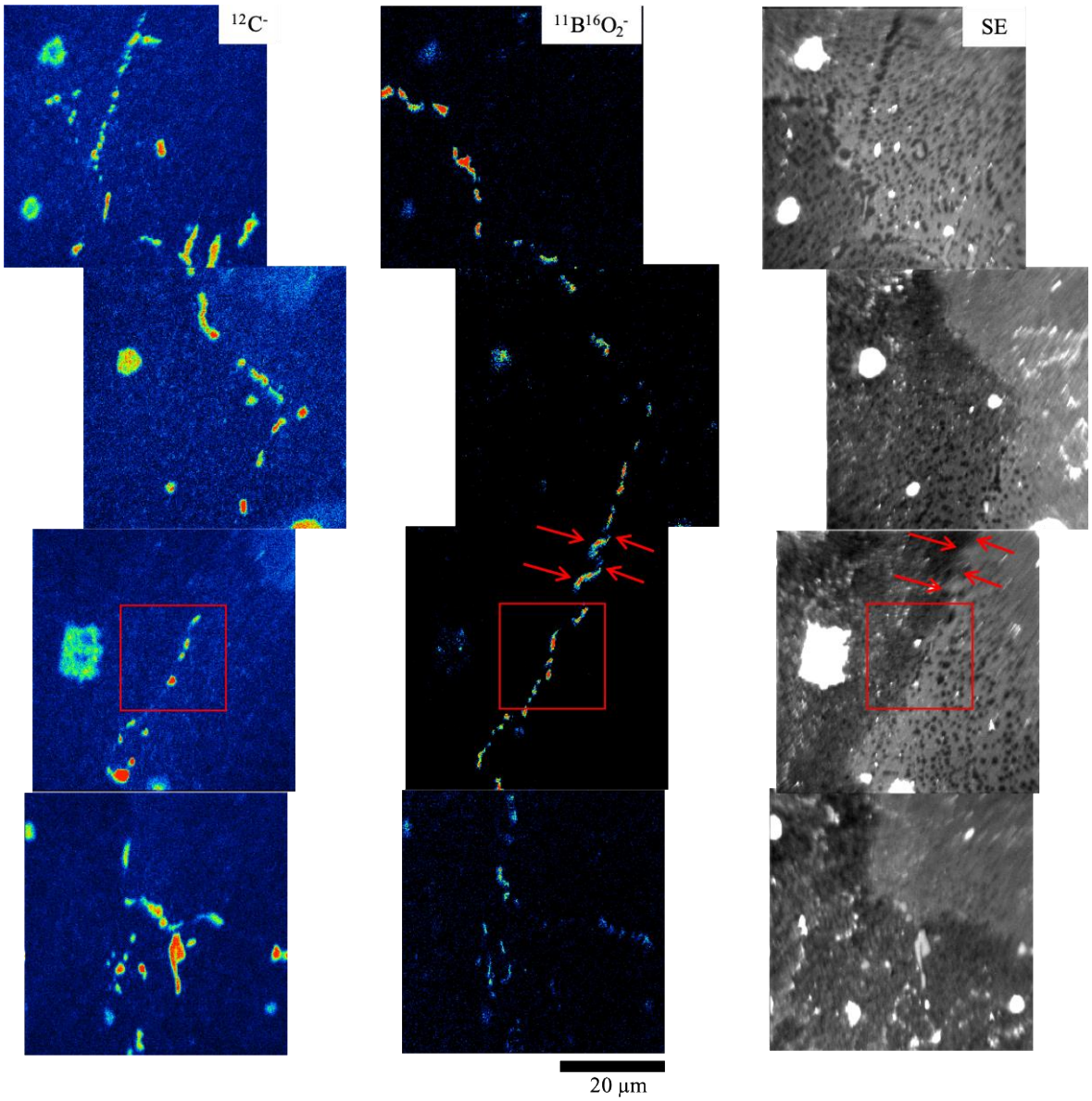


Figure 5.6: Carbon, boron and SE maps showing carbides and borides decorated along grain boundaries in the medium boron sample. Red arrows show the serration of grain boundaries in this sample. The red square indicates the 20 µm area that was selected for high resolution imaging using the D1=3 aperture shown in Figure 5.7.

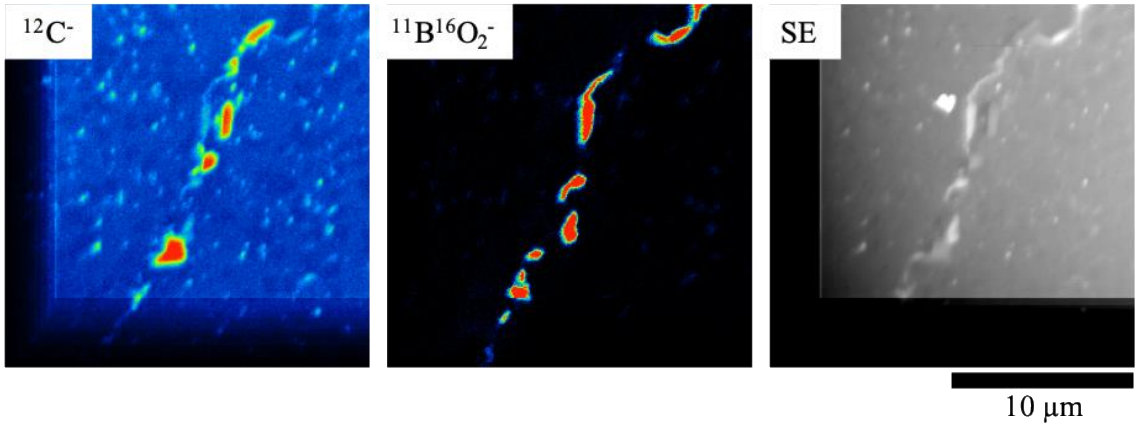


Figure 5.7: High resolution image of $^{12}C^-$, $^{11}B^{16}O_2^-$, and SE maps on medium boron sample using D1=3, raster size 20 µm, summed images of 54 slices, dwell time 15,000 µs/px from the red box in Figure 5.6.

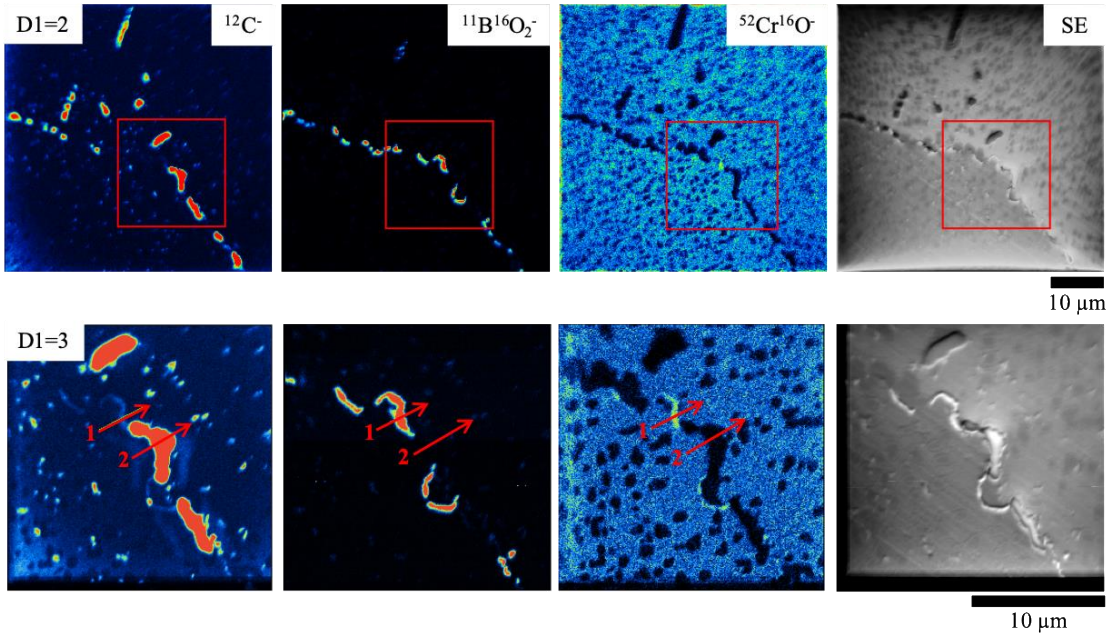


Figure 5.8: Selected area of medium boron sample showing NanoSIMS maps of $^{12}C^-$, $^{11}B^{16}O_2^-$, $^{52}Cr^{16}O^-$ and SE. The top row was scanned with D1=2 aperture with 50 µm raster size. High resolution image of $^{12}C^-$, $^{11}B^{16}O_2^-$, and SE maps. The red square indicates the 20 µm area that was selected for high resolution imaging using the D1=3 aperture. The higher resolution scan at D1=3 is shown in the bottom row. Red arrows indicate the position and direction of the line scan across a Cr-rich boride (line 1) and carbide (line 2).

Another area in this sample is shown in Figure 5.8 and was first scanned using the D1=2 aperture with 50 µm raster size, dwell time 10,000 µm/pixel per image and a total of 74 images were summed. Then a higher resolution scan was performed using a smaller aperture, D1=3, at the 20 x 20 µm area

highlighted in the red box. The dwell time was set to 15,000 μm/pixel per image and a total of 60 images were summed. Two line scans were performed on the higher resolution image over a Cr-rich boride (line 1) and carbide (line 2). The line scans were averaged over 10 pixels width to improve the counting statistics and a step size of 0.08 μm was used along the red arrow shown in the higher resolution image of $^{12}C^-$, $^{11}B^{16}O_2^-$ and $^{52}Cr^{16}O^-$ image in Figure 5.8.

The higher resolution image clearly shows the morphology of the grain boundary in this region are serrated. The distribution of carbon in the $^{12}C^-$ map is similar to that described above, with high carbon signals detected mostly from the blocky and elongated carbides along the grain boundary and lower carbon signals from the fine carbide precipitates within the grains. The carbon and boron rich regions are also clearly at different locations along the grain boundary. The $^{52}Cr^{16}O^-$ signal gives an overview of the γ matrix which is Ni-based solid solution with the FCC structure that contains Cr as one of its solid solution elements. The black regions which are depleted in Cr are the γ' precipitates.

Line scan 1 was performed over a boron particle and shown in Figure 5.9. The boron content is high and the carbon signal much weaker which indicates that it is a Cr-rich boride. The molecular ion $^{52}Cr^{16}O^-$ signal is always rather weak, but the APT analysis on the same material identifies these particles as having compositions close to Cr_5B_3. Line scan 2 was performed on a carbide and shown in Figure 5.10. The carbon signal is very high but the boron and chromium counts from the carbide are extremely low which indicates it is a MC-type carbide. There is some suggestion of boron segregation to both sides of the carbide particle, which is not seen in the APT analysis. The NanoSIMS line scans give information about the compositions but not the exact composition that can be obtained from APT analysis.

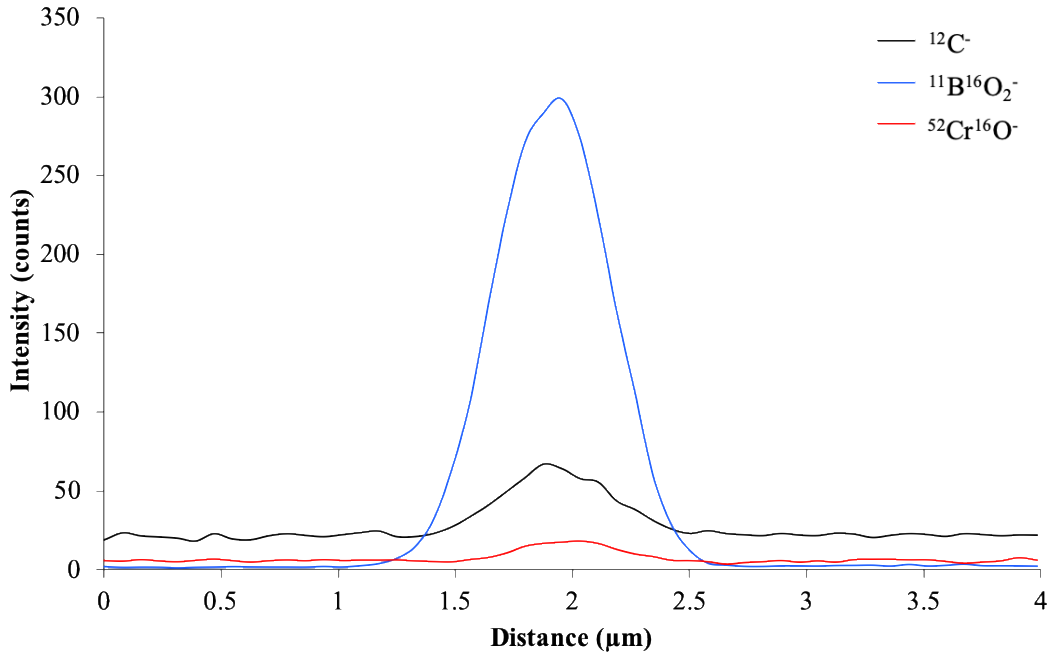


Figure 5.9: Line scans for $^{12}C^-$, $^{11}B^{16}O_2^-$, and $^{52}Cr^{16}O^-$ across a Cr-rich boride in the medium boron sample as indicated by red arrow 1 in Figure 5.8.

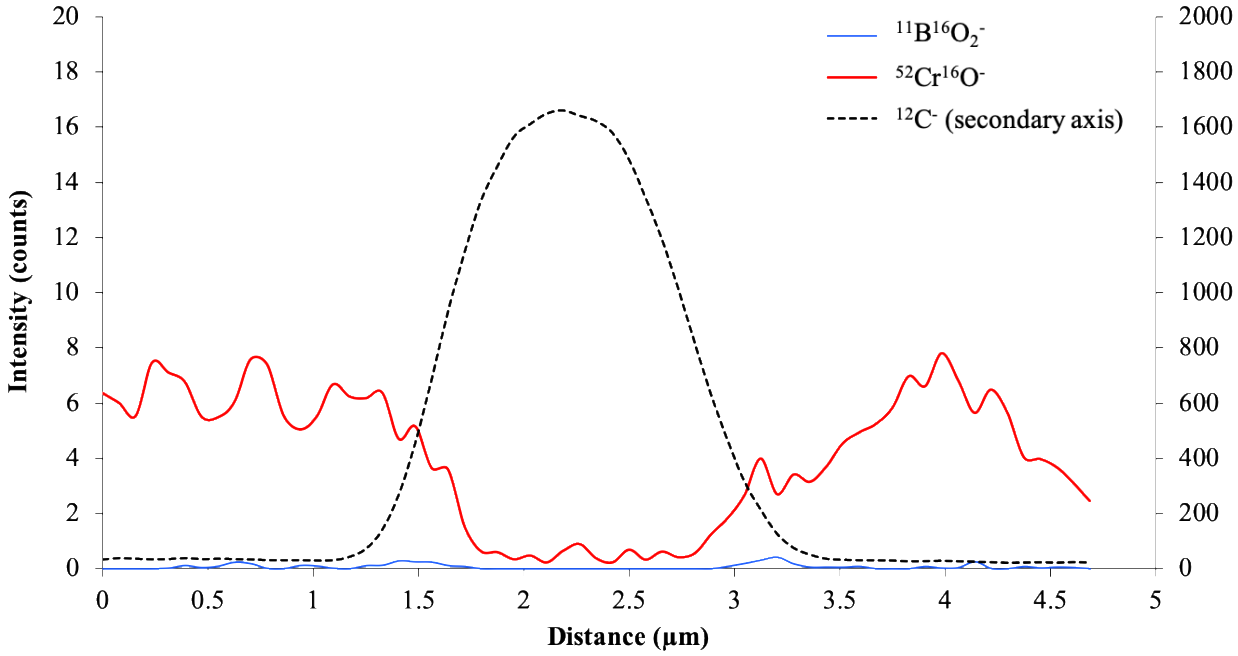


Figure 5.10: Line scans for $^{12}C^-$, $^{11}B^{16}O_2^-$, and $^{52}Cr^{16}O^-$ across a carbide in the medium boron sample as indicated by red arrow 2 in Figure 5.8.

The correlation of NanoSIMS maps of a selected area from medium boron sample with the AFM image of the same area, shown in Figure 5.11, displays the topography of the region scanned by NanoSIMS, clearly revealing the borides and carbides along the grain boundary. The matrix has sputtered faster than the hard borides and carbides which are now left protruding out of the surface. Two line scans were performed on the AFM image over a boride (blue arrow) and a carbide (black arrow). Based on the AFM line scans shown in Figure 5.12, the height of the carbide is higher (100 nm) than the boride (70 nm). The matrix crater depth is about 70 nm after being scanned for around 14 hours. The total dose implanted in this area during this long acquisition was 7 x 10^{16} Cs atoms/cm^2 and the surface is also roughened, following the microstructure, due to the long scan time with increasing dose. It is worth mentioning here that basically the carbides or borides are hard to polish and sputter. From the line scan, the height of the carbide is higher than the unsputtered surface indicating the sample was not flat after polishing.

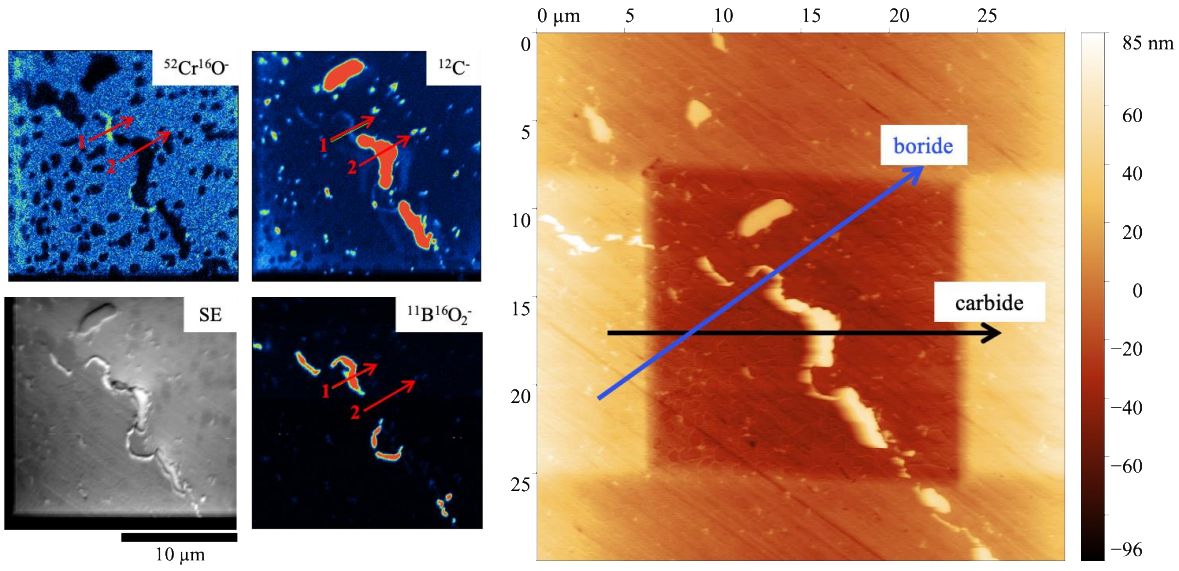


Figure 5.11: Correlation between the same area of NanoSIMS maps with AFM image of medium boron sample on NanoSIMS crater. Line scans were performed across a carbide and a boride.

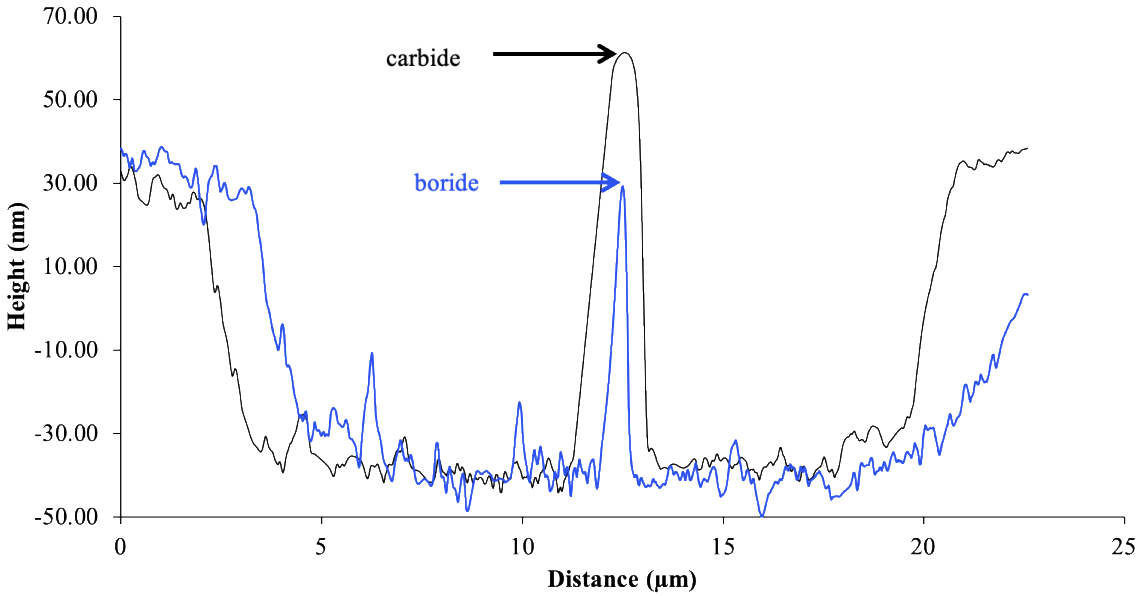


Figure 5.12: AFM line scans on the NanoSIMS crater showing the relative heights of the boride and carbide and the crater depth. The depth of the crater is about 70 nm. The height of the carbide is 100 nm and the boride is 70 nm.

5.3.2.3 High boron sample

Figure 5.13 shows a set of four images of $^{12}C^-$, $^{11}B^{16}O_2^-$ and SE maps along a grain boundary in the high boron sample. It is shown from the maps that this sample also has serrated grain boundaries (arrows). Carbide precipitation is not as obvious in this area as it was from the medium boron sample, with fine particles and some blocky carbides. The morphology of the boron particles is more or less the same as in the medium boron sample, but they are more discrete. As before, the carbide and boride particles seem to be completely separate, and often concentrated in different regions of the grain boundary.

A 20 by 20 μm^2 area highlighted with the red box in the third image of Figure 5.13, was selected for high resolution imaging using a smaller aperture D1=3. The dwell time was set to 15,000 µs/pixel per image and a total of 56 sequential images were summed. Before analysis was undertaken on these results, the image stack was aligned to correct for drift using the ImageJ software. Summed images of the $^{12}C^-$, $^{11}B^{16}O_2^-$, $^{52}Cr^{16}O^-$ and SE maps are shown in Figure 5.14 which clearly shows the substantial drift in this long experiment.

In this area, the distribution of carbon in the $^{12}C^-$ map shows continuous blocky carbide morphology and some small carbide precipitates in the grains. The intergranular blocky carbides are smaller as compared to carbides in the low boron sample. Some of the carbides are depleted in Cr (Figure 5.14) so we can assume them to be MC. Continuous blocky and elongated boron particles decorate the grain boundary. A high $^{11}B^{16}O_2^-$ signal was detected and some amount carbon and chromium. Therefore, these particles should be the same Cr-rich borides as those found in other samples. The $^{52}Cr^{16}O^-$ signal also gives the same observation as other samples where the γ matrix which is Ni-based solid solution contains Cr as one of its solid solution elements. The black regions which are depleted in Cr are the γ' precipitates.

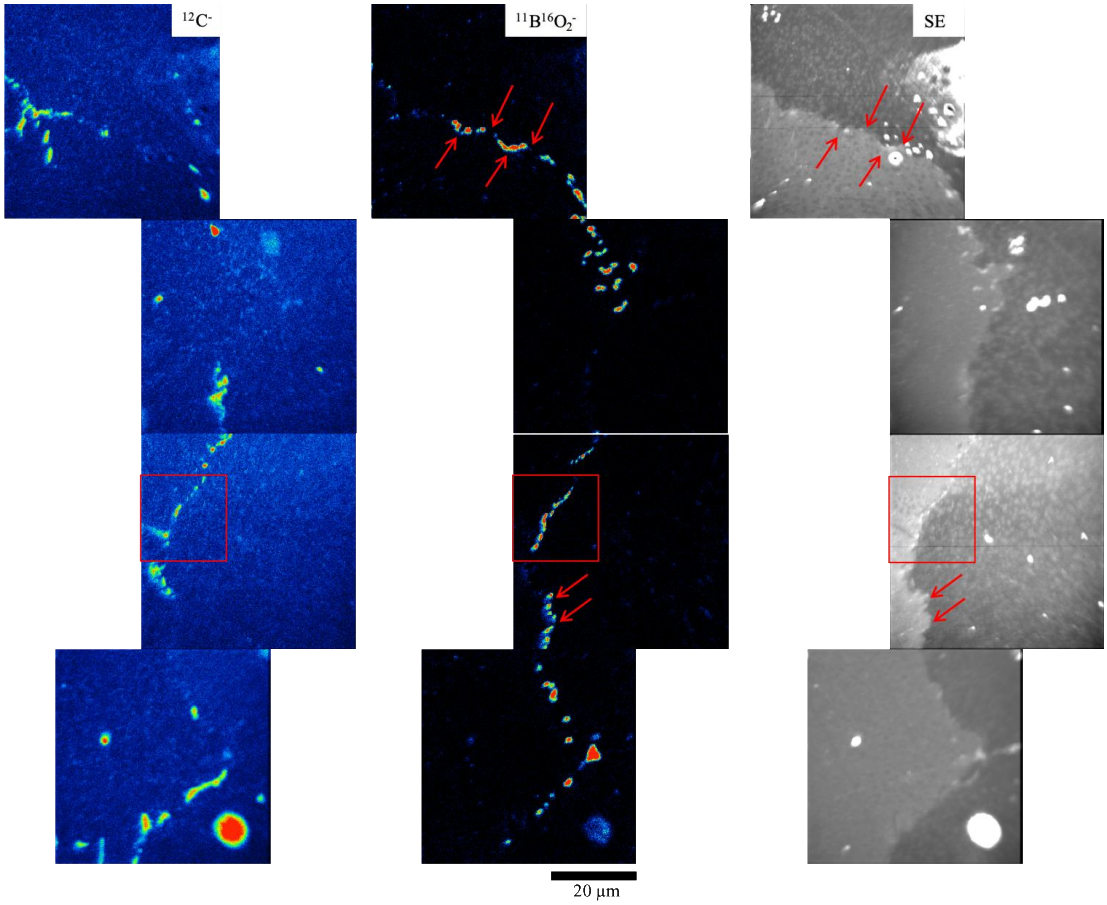


Figure 5.13: Carbon and boron maps showing carbides and borides decorated along grain boundaries in the high boron sample. SE maps clearly show the contrast of two different grains and serrated grain boundaries (arrows). The red square indicates the 20x20 µm^2 area that was selected for high resolution imaging using the D1=3 aperture.

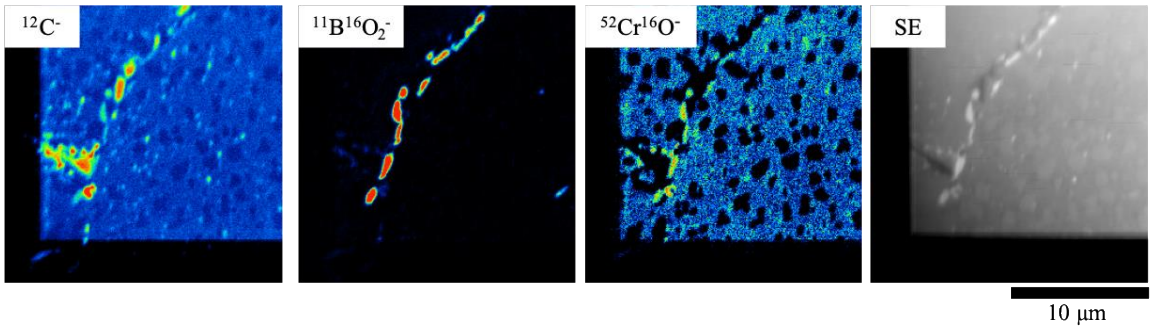


Figure 5.14: High resolution image of $^{12}C^-$, $^{11}B^{16}O_2^-$, $^{52}Cr^{16}O^-$ and SE maps of the region identified in Figure 5.13 using D1=3, raster size 20 µm, summed images of 56 slices, dwell time 15,000 µs/px.

Figure 5.15 and Figure 5.16 show two different areas in this sample that have intragranular carbides with a script-like morphology. Figure 5.15 shows $^{12}C^-$, $^{11}B^{16}O_2^-$, $^{11}B^{12}C^-$, $^{52}Cr^{16}O^-$ maps and two colour merge images combining the $^{12}C^-$ and $^{11}B^{16}O_2^-$ signals and the $^{11}B^{12}C^-$ and $^{52}Cr^{16}O^-$ signals. The first colour merge image shows $^{12}C^-$ in red and $^{11}B^{16}O_2^-$ in blue indicating that there is no overlap of carbide and boride particles. The second colour image shows $^{11}B^{12}C^-$ in red and $^{52}Cr^{16}O^-$ in blue. The overlaps of $^{11}B^{12}C^-$ and $^{52}Cr^{16}O^-$ signals correspond to the pink Cr-rich borides. The carbon maps show intragranular carbide precipitates with script-like morphology at the vicinity of the grain boundary. Some fine intergranular carbide precipitates were also observed at the grain boundaries and in the grains. Chromium is present throughout the matrix but the signal is stronger at the boron rich precipitates.

Figure 5.16 shows $^{12}C^-$, $^{11}B^{16}O_2^-$, $^{52}Cr^{16}O^-$, SE maps and a colour merge image of the $^{12}C^-$ and $^{11}B^{16}O_2^-$ signals. The colour merge image shows $^{12}C^-$ in red and $^{11}B^{16}O_2^-$ in blue. Clear script-like morphology of intragranular carbides can be seen in the colour merge image, and continuous boride precipitates decorated along the grain boundary. A similar observation can be seen in the $^{52}Cr^{16}O^-$ map which has a higher signal at the boron precipitates as compared to the matrix. The contrast of two grains, that can be seen in the SE image, shown the grain boundary morphology.

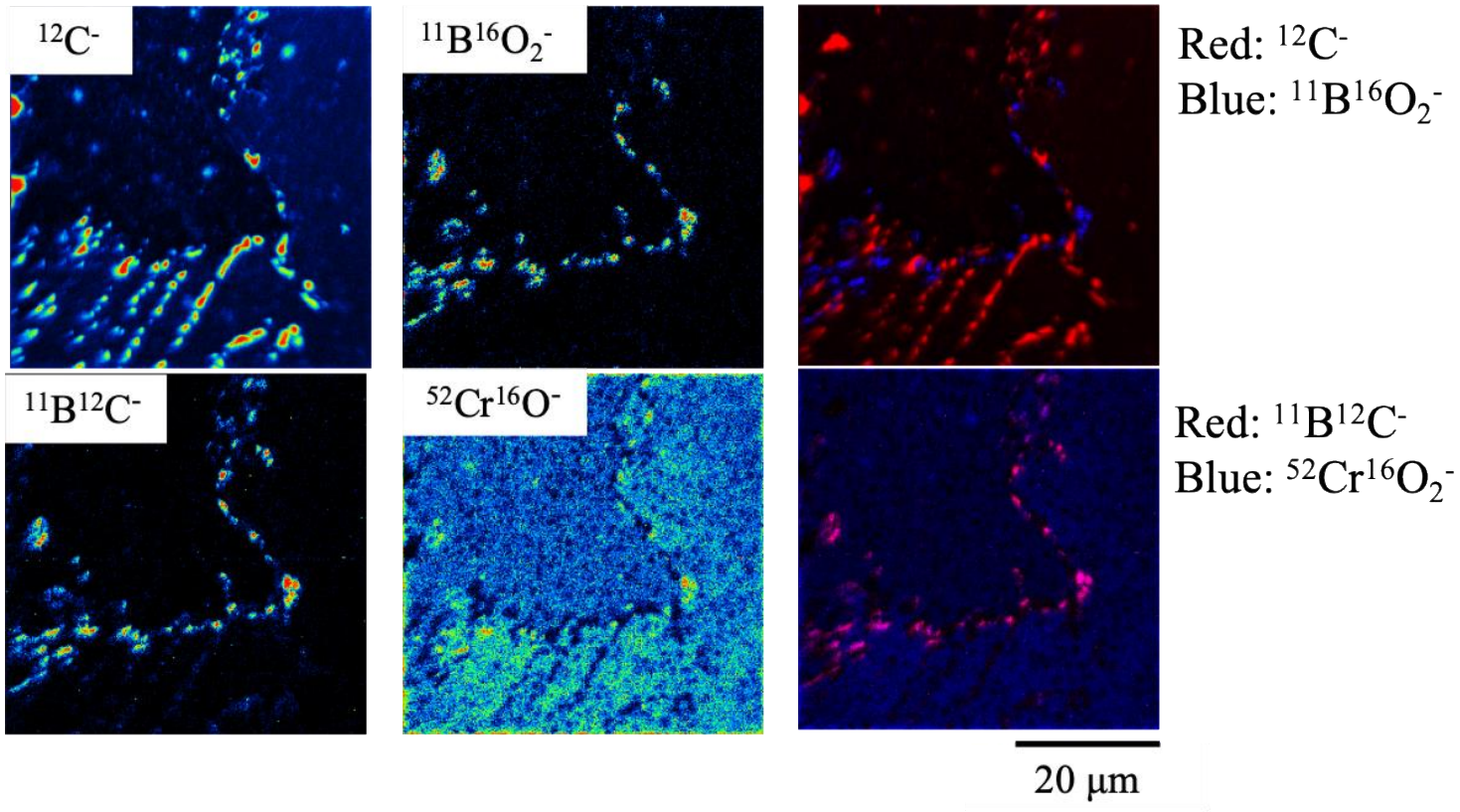


Figure 5.15: Selected area of the high boron sample showing NanoSIMS maps of $^{12}C^-$, $^{11}B^{12}C^-$, $^{11}B^{16}O_2^-$ and $^{52}Cr^{16}O^-$. Top colour merge image shows $^{12}C^-$ in red and $^{11}B^{16}O_2^-$ in blue. Bottom colour merge image shows $^{11}B^{12}C^-$ in red and $^{52}Cr^{16}O^-$ in blue. The overlaps of $^{11}B^{12}C^-$ and $^{52}Cr^{16}O^-$ signals correspond to the pink Cr-rich borides.

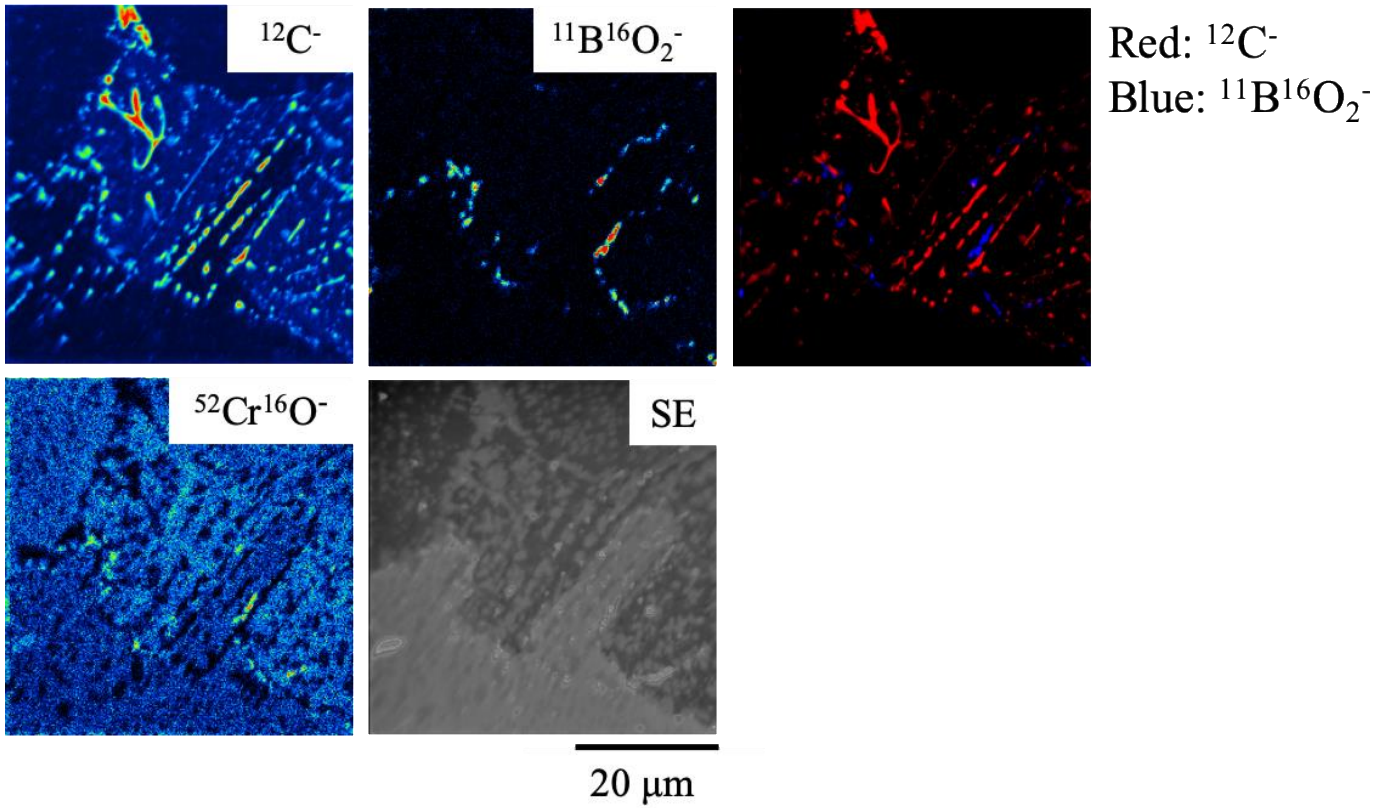


Figure 5.16: Selected area of the high boron sample showing NanoSIMS maps of $^{12}C^-$, $^{11}B^{16}O_2^-$, $^{52}Cr^{16}O^-$ and SE. Top colour merge image shows $^{12}C^-$ in red and $^{11}B^{16}O_2^-$ in blue. Intragranular script like morphology of carbides were observed in the $^{12}C^-$ map and Cr-rich borides decorating along the grain boundary.

5.4 Discussion and Summary

The addition of boron to these new polycrystalline superalloys results in the formation of borides in all of the samples due to its limited solubility in the nickel matrix. The formation of borides is believed to occur during either cooling when no segregation occurs (Karlsson and Nordén, 1988) or during the long holding time during annealing when boron does not desegregate from the grain boundaries (He et al., 1989, Zhang and Ojo, 2010). These borides contain excess Cr in comparison with the nickel alloy matrix. The primary effect of the boron addition is suppression of Cr-rich $M_{23}C_6$ carbide and the formation of Cr-rich M_5B_3 borides. No segregation of boron to grain boundaries was observed in these samples.

The NanoSIMS can also help to map the carbide distributions over large areas. Discrete intergranular MC carbides can lead to formation of continuous layers of γ' particles at the grain boundaries which may prevent easy paths for rapid crack propagation and hence increase the ductility (Kotval et al., 1972). The morphology of the intergranular MC-type carbides is blocky and elongated but intragranular carbides have either a script-like morphology or form fine particles.

It is interesting to compare the results from this study with some of the published studies of the effect of boron in superalloys. Table 5.2 summarised the study of boron in various types of superalloys indicating whether boron is present in solid solution or as borides or carbides. The majority of the studies show boron was found segregated at the grain boundaries (Tytko et al., 2012, Hong et al., 2012, Alam et al., 2012, Lemarchand et al., 2002, Chen et al., 1998, Huang et al., 1997, Letellier et al., 1994, Letellier et al., 1993, Buchon et al., 1991), some other studies observed intergranular borides in the sample (Yan et al., 2008, Zhang and Ojo, 2008, Zhang et al., 2008, Ojo and Zhang, 2008, Cadel et al., 2002). Blavette et al. (1996) found both boron segregation and precipitation of borides in the sample. Some studies have found boron present in MC (Delargy and Smith, 1983) and $M_{23}C_6$ (Tytko et al., 2012) type carbides.

Results from this thesis suggest the boron is contained mostly in precipitates at the boundaries. When designing a new alloy, it is important to consider the amount of Cr and B to add to control the microstructure and either to promote boron segregated at grain boundaries or precipitated as borides.

Table 5.2: Summary of published studies of boron in superalloys showing either boron is present in solid solution at grain boundaries or as a boride or carbide. Adapted from (Kontis et al., 2016)

Material	Boron (at%)	Solid solution	Boride	Carbide	Reference
617B	0.02	Yes	No	Yes	(Tytko et al., 2012)
Alloy 263	0.015	Yes	No	No	(Hong et al., 2012)
718 (WE971/G727)	0.059/0.064	Yes	No	No	(Alam et al., 2012)
Experimental	0.10	No	Yes	Yes	(Yan et al., 2008)
Rene80	0.065	No	Yes	No	(Zhang and Ojo, 2008)
IN738	0.060	No	Yes	No	(Zhang et al., 2008)
Rene80	0.065	No	Yes	No	(Ojo and Zhang, 2008)
N18	0.083	Yes	No	No	(Lemarchand et al., 2002)
N18	0.083	No	Yes	No	(Cadel et al., 2002)
IN718 (Low/High boron)	0.06/0.023	Yes	No	No	(Chen et al., 1998)
IN718	0.016	Yes	No	No	(Huang et al., 1997)
Astroloy	0.11	Yes	Yes	Yes	(Blavette et al., 1996)
Astroloy	0.11	Yes	No	No	(Letellier et al., 1994)
Astroloy	0.11	Yes	No	No	(Letellier et al., 1993)
NA4	0.09	Yes	No	No	(Buchon et al., 1991)
IN939	0.05	No	No	Yes	(Delargy and Smith, 1983)

5.5 Conclusions

The results from Chapter 5 have demonstrated that high-resolution secondary ion mass spectrometry (NanoSIMS) is a useful technique to study the role of boron and carbon in controlling grain boundary character in a new polycrystalline superalloy. The NanoSIMS elemental maps have revealed detailed information on boron and carbon distributions at grain boundaries over large areas. Direct comparison of SEM, APT, TEM and NanoSIMS data on the same samples can give a very precise picture of phase composition and distributions. The following conclusions can be drawn for Chapter 5:

1. NanoSIMS analysis reveals that the additions of boron to this new polycrystalline superalloy promotes the formation of boron rich precipitates along the grain boundaries. According to a complementary study by TEM, these particles have a tetragonal structure which correspond to Cr-rich M_5B_3 borides, in good agreement with the APT datasets.

2. The morphology of the intergranular MC-type carbides is blocky and elongated but intragranular carbides are either script-like morphology or fine particles.
3. Carbide and boride particles seem to be completely separate, and often concentrated in different regions of the grain boundary.
4. No segregation of boron or carbon to the grain boundary was observed in any of the samples.
5. The addition of boron has promoted the serration of the grain boundaries for all these samples.

5.6 References

ALAM, T., FELFER, P. J., CHATURVEDI, M., STEPHENSON, L. T., KILBURN, M. R. & CAIRNEY, J. M. 2012. Segregation of B, P, and C in the Ni-Based Superalloy, Inconel 718. *Metallurgical and Materials Transactions A,* 43**,** 2183-2191.

ANTONOV, S., HUO, J., FENG, Q., ISHEIM, D., SEIDMAN, D. N., HELMINK, R. C., SUN, E. & TIN, S. 2017. σ and η Phase formation in advanced polycrystalline Ni-base superalloys. *Materials Science and Engineering: A,* 687**,** 232-240.

BLAVETTE, D., DUVAL, P., LETELLIER, L. & GUTTMANN, M. 1996. Atomic-scale APFIM and TEM investigation of grain boundary microchemistry in Astroloy nickel base superalloys. *Acta Materialia,* 44**,** 4995-5005.

BUCHON, A., MENAND, A. & BLAVETTE, D. 1991. Phase composition and grain-boundary segregation in a nickel base superalloy: a preliminary TEM-APFIM investigation. *Surface Science,* 246**,** 218-224.

CADEL, E., LEMARCHAND, D., CHAMBRELAND, S. & BLAVETTE, D. 2002. Atom probe tomography investigation of the microstructure of superalloys N18. *Acta Materialia,* 50**,** 957-966.

CHEN, Q. Z., JONES, N. & KNOWLES, D. M. 2002. The microstructures of base/modified RR2072 SX superalloys and their effects on creep properties at elevated temperatures. *Acta Materialia,* 50**,** 1095-1112.

CHEN, W., CHATURVEDI, M. C., RICHARDS, N. L. & MCMAHON, G. 1998. Grain boundary segregation of boron in INCONEL 718. *Metallurgical and Materials Transactions A,* 29**,** 1947-1954.

COLLINS, D. M., CONDUIT, B. D., STONE, H. J., HARDY, M. C., CONDUIT, G. J. & MITCHELL, R. J. 2013. Grain growth behaviour during near-γ′ solvus thermal exposures in a polycrystalline nickel-base superalloy. *Acta Materialia,* 61**,** 3378-3391.

DECKER, R. F. & FREEMAN, J. W. 1958. The mechanism of beneficial effects of boron and zirconium on creep-rupture properties of a complex heat-resistant alloy. United States: University of Michigan, Ann Arbor.

DELARGY, K. M. & SMITH, G. D. W. 1983. Phase composition and phase stability of a high-chromium nickel-based superalloy, IN939. *Metallurgical Transactions A,* 14**,** 1771-1783.

DONACHIE, M. J. & DONACHIE, S. J. 2002. *Superalloys : a technical guide,* Materials Park, OH, ASM International.

GEDDES, B., LEON, H. & HUANG, X. 2010. *Superalloys: alloying and performance*, Asm International.

HE, L. Z., ZHENG, Q., SUN, X. F., GUAN, H. R., HU, Z. Q., TIEU, A. K., LU, C. & ZHU, H. T. 2005. Effect of carbides on the creep properties of a Ni-base superalloy M963. *Materials Science and Engineering: A,* 397**,** 297-304.

HE, X. L., CHU, Y. Y. & JONAS, J. J. 1989. Grain boundary segregation of boron during continuous cooling. *Acta Metallurgica,* 37**,** 147-161.

HOLT, R. T. & WALLACE, W. 1976. Impurities and trace elements in nickel-base superalloys. *International Metallurgical Reviews,* 21**,** 1-2424.

HONG, H. U., KIM, I. S., CHOI, B. G., YOO, Y. S. & JO, C. Y. 2012. On the Mechanism of Serrated Grain Boundary Formation in Ni-Based Superalloys with Low γ′ Volume Fraction. *Superalloys 2012*.

HUANG, X., CHATURVEDI, M. C., RICHARDS, N. L. & JACKMAN, J. 1997. The effect of grain boundary segregation of boron in cast alloy 718 on HAZ microfissuring—A SIMS analysis. *Acta Materialia,* 45**,** 3095-3107.

JENA, A. & CHATURVEDI, M. 1984. The role of alloying elements in the design of nickel-base superalloys. *Journal of Materials Science,* 19**,** 3121-3139.

KARLSSON, L. & NORDÉN, H. 1988. Overview no. 63 Non-equilibrium grain boundary segregation of boron in austenitic stainless steel—IV. Precipitation behaviour and distribution of elements at grain boundaries. *Acta Metallurgica,* 36**,** 35-48.

KONTIS, P., YUSOF, H. A. M., PEDRAZZINI, S., DANAIE, M., MOORE, K. L., BAGOT, P. A. J., MOODY, M. P., GROVENOR, C. R. M. & REED, R. C. 2016. On the effect of boron on grain boundary character in a new polycrystalline superalloy. *Acta Materialia,* 103**,** 688-699.

KOTVAL, P. S., VENABLES, J. D. & CALDER, R. W. 1972. The role of hafnium in modifying the microstructure of cast nickel-base superalloys. *Metallurgical and Materials Transactions B,* 3**,** 457-462.

KOUL, A. K. & THAMBURAJ, R. 1985. Serrated grain boundary formation potential of Ni-based superalloys and its implications. *Metallurgical Transactions A,* 16**,** 17-26.

LEMARCHAND, D., CADEL, E., CHAMBRELAND, S. & BLAVETTE, D. 2002. Investigation of grain-boundary structure-segregation relationship in an N18 nickel-based superalloy. *Philosophical Magazine A: Physics of Condensed Matter, Structure, Defects and Mechanical Properties,* 82**,** 1651-1669.

LETELLIER, L., BOSTEL, A. & BLAVETTE, D. 1994. Direct observation of boron segregation at grain boundaries in astrology by 3D atomic tomography. *Scripta Metallurgica et Materialia,* 30**,** 1503-1508.

LETELLIER, L., CHAMBRELAND, S., DUVAL, P. & BLAVETTE, D. 1993. Grain boundary segregation in nickel base superalloys Astroloy: an atom-probe study. *Applied Surface Science,* 67**,** 305-310.

LIU, L. R., JIN, T., ZHAO, N. R., SUN, X. F., GUAN, H. R. & HU, Z. Q. 2003. Formation of carbides and their effects on stress rupture of a Ni-base single crystal superalloy. *Materials Science and Engineering: A,* 361**,** 191-197.

MITCHELL, R. J. 2010. Polycrystalline Nickel-Based Superalloys: Processing, Performance, and Application. *Encyclopedia of Aerospace Engineering.* John Wiley & Sons, Ltd.

MOURITZ, A. P. 2012. Superalloys for gas turbine engines. *In:* MOURITZ, A. P. (ed.) *Introduction to Aerospace Materials.* Woodhead Publishing.

OJO, O. A. & ZHANG, H. R. 2008. Analytical Electron Microscopy Study of Boron-Rich Grain Boundary Microconstituent in Directionally Solidified RENE 80 Superalloy. *Metallurgical and Materials Transactions A,* 39**,** 2799-2803.

POLLOCK, T. M. & ARGON, A. S. 1992. Creep resistance of CMSX-3 nickel base superalloy single crystals. *Acta Metallurgica et Materialia,* 40**,** 1-30.

POLLOCK, T. M. & TIN, S. 2006. Nickel-based superalloys for advanced turbine engines: chemistry, microstructure and properties. *Journal of propulsion and power,* 22**,** 361-374.

QIN, X. Z., GUO, J. T., YUAN, C., CHEN, C. L. & YE, H. Q. 2007. Effects of Long-Term Thermal Exposure on the Microstructure and Properties of a Cast Ni-Base Superalloy. *Metallurgical and Materials Transactions A,* 38**,** 3014-3022.

RAE, C. M. F. & REED, R. C. 2001. The precipitation of topologically close-packed phases in rhenium-containing superalloys. *Acta Materialia,* 49**,** 4113-4125.

REED, R. C. 2008. *The Superalloys: Fundamentals and Applications,* Cambridge University Press.

REED, R. C. & RAE, C. M. F. 2014. Physical Metallurgy of the Nickel-Based Superalloys. *In:* LAUGHLIN, D. E. & HONO, K. (eds.) *Physical Metallurgy (Fifth Edition).* Oxford: Elsevier.

REED, R. C., TAO, T. & WARNKEN, N. 2009. Alloys-By-Design: Application to nickel-based single crystal superalloys. *Acta Materialia,* 57**,** 5898-5913.

SABOL, G. P. & STICKLER, R. 1969. Microstructure of Nickel-Based Superalloys. *physica status solidi (b),* 35**,** 11-52.

TYTKO, D., CHOI, P.-P., KLÖWER, J., KOSTKA, A., INDEN, G. & RAABE, D. 2012. Microstructural evolution of a Ni-based superalloy (617B) at 700°C studied by electron microscopy and atom probe tomography. *Acta Materialia,* 60**,** 1731-1740.

WILSON, A. S. 2017. Formation and effect of topologically close-packed phases in nickel-base superalloys. *Materials Science and Technology,* 33**,** 1108-1118.

XU, S., DICKSON, J. I. & KOUL, A. K. 1998. Grain growth and carbide precipitation in superalloy, UDIMET 520. *Metallurgical and Materials Transactions A,* 29**,** 2687-2695.

YAN, B. C., ZHANG, J. & LOU, L. H. 2008. Effect of boron additions on the microstructure and transverse properties of a directionally solidified superalloy. *Materials Science and Engineering: A,* 474**,** 39-47.

YANG, J., ZHENG, Q., JI, M., SUN, X. & HU, Z. 2011. Effects of different C contents on the microstructure, tensile properties and stress-rupture properties of IN792 alloy. *Materials Science and Engineering: A,* 528**,** 1534-1539.

YANG, J. X., ZHENG, Q., SUN, X. F., GUAN, H. R. & HU, Z. Q. 2007. Topologically close-packed phase precipitation in a nickel-base superalloy during thermal exposure. *Materials Science and Engineering: A,* 465**,** 100-108.

ZHANG, H., OJO, O. & CHATURVEDI, M. 2008. Nanosize boride particles in heat-treated nickel base superalloys. *Scripta Materialia,* 58**,** 167-170.

ZHANG, H.-R. & OJO, O. A. 2010. Cr-rich nanosize precipitates in a standard heat-treated Inconel 738 superalloy. *Philosophical Magazine,* 90**,** 765-782.

ZHANG, H. R. & OJO, O. A. 2008. TEM analysis of Cr–Mo–W–B phase in a DS nickel based superalloy. *Journal of Materials Science,* 43**,** 6024-6028.

6 Conclusions and Suggestions for Future Work

6.1 Conclusions

6.1.1 High Strength Steels

This work has fulfilled the main aim of the original study plan by demonstrating that high-resolution secondary ion mass spectrometry (NanoSIMS) can be used as a reliable technique to analyse trace elements, and especially light elements such as boron, in the complex microstructure of high strength steels after different heat treatments. The key findings and conclusions of Chapter 4 can be used as answers to the questions stated in the introductory chapter:

1. **Comparison between Al-protected steels and Ti-protected steels at three processing stages (as-rolled, as-quenched and quenched and tempered). What is the role of Al and Ti in the steels? How does boron behave at the early stage of processing (as-rolled), after water quenching from the austenite region (as-quenched), and after the tempering process (quenched and tempered)? Does it exist in solid solution or segregate at the grain boundary or precipitate as a second phase? How do the heat treatments alter the effect of boron on hardenability in these steels?**

At the early stage of processing (as-rolled), boron starts to precipitate out during the hot rolling process resulting in a higher fraction of boron in precipitates rather than in the prior austenite grain boundaries at which the segregation process occurred subsequently during air cooling (Al-protected: Section 4.4.2.1 and Ti-protected: Section 4.4.3.1). The average boron content in the pro-eutectoid ferrite was found to be higher than in the pearlite. Strong grain boundary segregation was observed in all of the as-quenched samples and these samples only contain a small volume fraction of boron-containing particles (Al-protected: Section 4.4.2.2 and Ti-protected: Section 4.4.3.2). Boron is believed to segregate at prior austenite grain boundaries during isothermal heat treatments by equilibrium segregation and also during cooling by non-equilibrium segregation (Tingdong et al.,

1990). The tempering heat treatment encouraged preferential fine scale precipitation on the grain boundaries. Small boron containing precipitates were visible in the quenched and tempered samples (Al-protected: Section 4.4.2.6 and Ti-protected: Section 4.4.3.3).

The maximum hardenability can be reached when boron is in solid solution or as fine precipitates at grain boundaries by preventing boron precipitation into nitrides. Hence, the addition of Ti as strong nitride former to the steels can maximise this beneficial effect. After quenching and tempering, some BN particles were still detected in the Al-protected sample (Section 4.4.2.5), but not in the Ti-protected sample (Section 4.4.3.3).

2. **Comparison of two Al-protected steel samples at different reheating times in the austenite region. Does reheating time at the austenite region have an impact on the behaviour of boron in the steels?**

A longer reheating time of more than 30 minutes at the austenite region resulted in higher boron segregation at the prior austenite grain boundaries (Section 4.4.2.4).

3. **Comparison of direct quenched steel and the conventional as-quenched steel. Do the processing conditions play a significant role in controlling the location of boron in these steels?**

The direct quenched method can be an alternative to reduce costs and increase overall efficiency in the steel making industry as it shows a similar boron segregation behaviour by conventional thermomechanical process. The direct quenched sample also shows strong boron segregation at the grain boundaries and less boron in particles (Section 4.4.4.2).

4. **Comparison between Mo alloyed steel and two other Al-protected steels with different Al concentrations. What is the effect of Mo on boron distribution in the steel?**

The addition of Mo was intended to retard the precipitation of $M_{23}(CB)_6$ and retain more boron in solution, but the observation from this study does not show this to be the case (Section 4.4.5.1).

Samples with higher Al content showed a higher amount of boron segregation and had a higher hardness (Section 4.4.5.2).

5. How can NanoSIMS data be used for quantitative analysis of boron in steels?

NanoSIMS elemental maps can reveal detailed segregation of boron at grain boundaries and small particles over a large area, improving the reliability of the data. For the first time, NanoSIMS quantitative analysis of boron segregation on these high strength steels has been carried out with 100s of grain boundaries analysed, thus improving the statistics of this kind of analysis in comparison to other analytical techniques such as TEM and APT, but at somewhat lower spatial resolution. Quantification of total boron counts in these samples shows that calibrating boron counts against implanted standards may not the best way to compare samples analysed many months apart due to variations in the instrument performance and resulting sensitivity at different times (Section 4.5.2). The boron concentrations at the grain boundaries using the first method of quantification using the ion implanted standard were in the range 0.6 to 5.1 atoms.nm^{-2}. The second method of quantification using the known concentration 0.008 wt.% B at 900°C can be another alternative to estimate boron concentrations at grain boundaries. The boron concentrations calculated using this second method lie in the range of 0.02 to 0.06 B wt. fraction in the boundary volume (Section 4.5.3).

Quantification of boron particle sizes and distributions was conducted using NanoSIMS and SEM data from Tata Steel. NanoSIMS can easily detect all types of boron-containing precipitates whereas the SEM contrast method focusses on detecting BN particles. The SEM analysis detected hardly any BN particles larger than about 1 µm but the NanoSIMS detected larger boron-containing particles especially in the as-rolled samples. No BN particles were detected in the Ti-protected samples with SEM analysis but the NanoSIMS could detect lots of boron-containing particles which might be BN or other phases like $Fe_{23}(B,C)_6$, $B_{13}C_2$ or B_4C boro-carbides (Section 4.5.4). However, to determine exactly what type of precipitates there are requires confirmation using TEM or APT.

Overall, more than 100 grain boundaries can be analysed in a sample using the NanoSIMS in approximately two days, improving the statistics of this kind of analysis in comparison to other

analytical techniques such as TEM and APT, but at somewhat lower spatial resolution. It is also shown that estimated lateral resolution can be as good as 100 nm when using the smallest aperture D1=4, which is sufficient to analyse grain boundary segregation and to distinguish segregation from precipitation for all but the smallest precipitates. The same elemental maps can be used to detect, count and size the distribution of boron-containing precipitates, in a manner complementary to SEM-based techniques that rely on contrast in the image, but the NanoSIMS can also directly detect differences in composition by mapping different ionic species such as BO^-, BC^- and BN^- instead of just relying on greyscale contrast.

6.1.2 Polycrystalline Ni-based Superalloys

Based on the progress made in learning how to carry out high resolution boron analysis on these steel samples, a new project was proposed in collaboration with Dr. Paraskevas Kontis and Prof. Roger Reed in another set of experiments to understand the distribution and role of grain boundary segregating elements (boron and carbon) in a new polycrystalline Ni-based superalloy, and to provide complementary information to that being gathered by other experiments using SEM, APT and TEM. It was found that the analytical protocols that had been developed for the steel samples were also suitable to obtain reliable mapping data from these new alloys. The key conclusions of Chapter 5 can be summarised as follows:

NanoSIMS analysis reveals that the additions of boron in this new superalloy promotes the formation of boron-rich precipitates and suppression of Cr-rich carbides (Section 5.3.2). Results from a complementary study by TEM and APT shows that these particles correspond to Cr-rich M_5B_3 borides and Cr-rich $M_{23}C_6$ carbides. The morphology of the intergranular MC-type carbides is blocky and elongated but intragranular carbides are either script-like morphology or fine particles. The NanoSIMS data showed that carbide and boride particles are often concentrated in different regions of grain boundary and seem to be completely separated. No significant segregation of boron or carbon was observed in the samples. Finally, the addition of boron promotes the serration of the grain boundaries.

This thesis has demonstrated that several kinds of data can be obtained using the high- resolution ion mass spectrometry analysis on two important engineering materials, high-strength steels and polycrystalline Ni-based superalloys. The data obtained from this study can be added to more conventional techniques to make a useful contribution to the development of materials for industrial applications and the effects that heat treatments have on microstructure and materials properties.

6.2 Future Work

Matrix effects complicate the interpretation of data from all SIMS techniques applied to the analysis of metallurgical samples, leading to changes in ionization yield and variable sputter rates, and must be carefully studied to ensure consistent interpretation. For instance, the topography of the material must be examined using AFM before and after NanoSIMS analysis to interpret factors causing matrix effects and understand the effect of crystallographic sputtering on quantification.

From the NanoSIMS maps, significant differences in the amount of boron segregated at different grain boundaries is revealed, and this may correlate with grain boundary misorientations; certain misorientations being more favourable for boron segregation. Therefore, further studies to relate the effect of grain boundary orientation on quantitative segregation data using EBSD is suggested. This may be the only combination of techniques that can generate a statistically significant data set on this important correlation.

One of the problems that arose from the attempt in this thesis to perform quantitative analysis using the ion implanted calibration standard is that the protocol is not very reliable for analysing samples many months apart because of inevitable variations in the instrumental performance. So, an improvement in the protocol might be to perform the calibration with the standard material each time when starting a new set of analyses. This calibration takes about one hour, but should improve the precision of the measurements, and would be a valuable addition to help obtain more reliable quantitative data on a large number of grain boundaries.

6.3 References

TINGDONG, X., SHENHUA, S., ZHEXI, Y. & ZONGSEN, Y. 1990. Two types of boron segregation at austenite grain boundaries and their mutual relation. *Journal of Materials Science,* 25**,** 1739-1744.